U.PORTO
FACULDADE DE CIÊNCIAS
UNIVERSIDADE DO PORTO

FACULDADE DE
CIÊNCIAS E TECNOLOGIA
UNIVERSIDADE NOVA DE LISBOA

universidade
de aveiro

PhD

Assembly of graphene-based nanomaterials on solid surfaces: physical characterization and charge transfer studies

Paula Maria do Vale Fernandes

PhD thesis submitted to
Faculdade de Ciências da Universidade do Porto,
Faculdade de Ciências e Tecnologia da Universidade Nova de Lisboa,
Universidade de Aveiro
2021

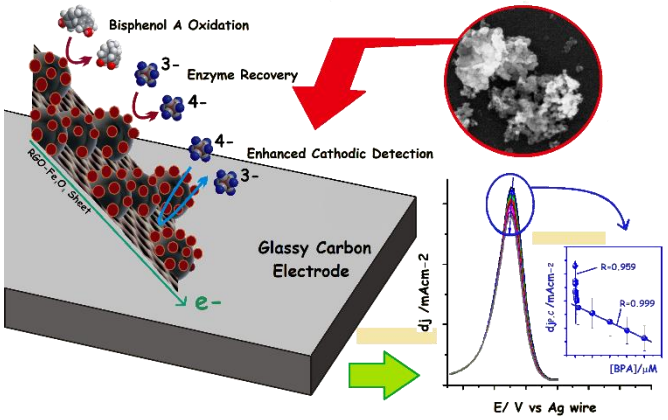

Assembly of graphene-based nanomaterials on solid surfaces: physical characterization and charge transfer studies

Paula Maria do Vale Fernandes
Doutoramento em Química Sustentável
Departamento de Química e Bioquímica
2021

Orientador
António Fernando Sousa da Silva
Professor Catedrático
Faculdade de Ciências da Universidade do Porto

Coorientador
José Miguel Campiña Pina
Investigador
Faculdade de Ciências da Universidade do Porto

This work was supported by the PhD fellowship (contract: SFRH/BD/111274/2015) granted by FCT – Fundação para a Ciência e a Tecnologia financed under POPH – Advanced Training subsidized by the European Union and national MCTES funds.

Acknowledgements

I would like to express my sincere and full gratitude to all people that direct or indirectly helped me in the course of this PhD thesis.

First of all, I would like to acknowledge my supervisor, Professor António Fernando Sousa da Silva, for the opportunity he gave me to do research, for all interesting scientific discussions and constructive suggestions. It was a privilege for me to learn from his great scientific knowledge.

I would like to acknowledge my co-supervisor, Doctor José Miguel Campiña, for all his guidance, support, pertinent advices, endless encouragement, constructive suggestions, and for all interesting scientific discussions that allowed me to see science in a better way.

I also thanks to Professor Carlos Pereira, for his help and support during this thesis.

I am thankful to RG4 - Physical Analytical Chemistry & Electrochemistry of the Centro de Investigação em Química da Universidade do Porto (CIQUP), for providing all material and conditions to do my research work.

I would like warmly thank Pr. Elby Titus and Dr. Rahul Krishna (Universidade de Aveiro)for their kind donation of a samples of the hybrid conjugates.

My special thanks to all laboratory members, especially to Elisabete, Iullia, José, Nuno, Renata, Tatiana, Tânia, Thacilla, Teresa. I thank them for all their friendship, help, support, companionship, and for providing a friendly and collaborative working environment. I also thank the good leisure moments spent together that helped me to relax and to overcome some difficult moments.

I would also like to thank to my colleagues in the doctoral program: Carla, Ricardo and Sarmento for all their friendship and companionship. I really enjoyed all moments in these four years. “Folgados” forever.

I wish to thank all my closest friends for their attention, support, patience, friendship, and for always listening me along these years. I would especially like to thank João for all his support and companionship.

At last, but not least, I would like to express my sincere gratitude to my parents and my brother for their great support, motivation, encouragement, unconditional love and especially for believing in me. without which I would not have come this far.

THANK YOU ALL!

Abstract

Graphene, a single atomic layer thin two-dimensional (2D) carbon nanomaterial, has received considerable attention from the scientific community due to its extraordinary physical, chemical and electrical properties. One area of particular interest is electrochemistry, where graphene has been widely used as an electrode material in sensing and energy related devices.

In this thesis, the fundamentals of electron capture and transfer through electrodes modified with graphene-based nanomaterials (GNMs) were investigated. In this regard, two simple and well-known forms of 2D graphene (graphene oxide (GO) and reduced graphene oxide (rGO)) plus two conjugated with nanoparticles (NPs) (rGO-iron oxide (Fe_3O_4) NPs and rGO-Nickel (Ni) NPs) were chosen to modify a glassy carbon electrode (GCE). The optimal degree of coverage, nanosheet packing density, structural phase, and/or range of film thicknesses, that lead to faster electron transfer processes through different GNMs, were evaluated. For these purposes, a broad range of characterization methods were used, including electrochemical techniques (cyclic voltammetry (CV) and electrochemical impedance spectroscopy (EIS)), atomic force microscopy (AFM), scanning electron microscopy (SEM), attenuated total reflectance Fourier transform infrared (ATR-FTIR) spectroscopy, X-ray photoelectron spectroscopy (XPS), and energy-dispersive X-ray (EDX) spectroscopy.

Afterwards, the optimal conditions of each of the hybrid reduced graphene oxide-nanoparticles' conjugates (rGO-Fe_3O_4 NPs and rGO-Ni NPs) was used to independently deposit such films onto a glassy carbon electrode further functionalized with a chitosan biopolymer and enzyme (laccase and glucose oxidase, respectively) layers, thus leading to the envisioned biosensors. Subsequently, the two assembled films were characterized by SEM, ATR-FTIR, XPS and electrochemical techniques, namely CV and EIS, both denoting an excellent electroanalytical performance with a wide linear range, high sensitivity, and very low detection limits, thus holding great potential to be used as biosensors.

Keywords: Graphene-based nanomaterials, conducting films, modified electrodes, supramolecular assembly, electrochemical sensors & biosensors, charge transfer studies, electrochemical impedance spectroscopy, Cyclic voltammetry.

Resumo

Grafeno, o primeiro material ordenado, estritamente bidimensional, com a espessura de um único átomo, isolado e medido, tem recebido interesse por parte da comunidade cientifica devido às suas excelentes propriedades físicas, químicas e elétricas. Uma área que manifesta particular interesse pelo uso deste extraordinário material é a eletroquímica, em que o grafeno tem sido bastante utilizado como material de elétrodo para a construção de sensores, entre muitas outras aplicações.

Nesta tese investigou-se os fundamentos da captura e transferência eletrónica através de elétrodos modificados com nanomateriais à base de grafeno. Com este intuito, duas formas simples e bem conhecidas de grafeno 2D (oxido de grafeno (GO) e oxido de grafeno reduzido (rGO)) mais duas formas conjugadas com nanopartículas (NPs) (rGO-Fe_3O_4 NPs e rGO-Ni NPs) foram escolhidos para modificar elétrodos de carbono vítreo. De forma a perceber quais as condições ideais que favorecem os processos de transferências eletrónica através destes filmes, propriedades como o grau de cobertura do elétrodo, densidade de empacotamento das nanopartículas, orientação e espessuras dos filmes foram estudadas. O processo de transferência eletrónica foi estudado na presença de hexacianoferrato (sonda eletroquímica) por técnicas eletroquímicas, tais como a Voltametria Cíclica (CV) e a Espectroscopia de Impedância Eletroquímica (EIS). A Microscopia de Força Atómica (AFM), a Microscopia Eletrónica de Varrimento (SEM), a espectroscopia no Infravermelho com Transformada de Fourier e Refletância Total Atenuada (ATR-FTIR), Espectroscopia de Fotoeletrões de Raios X (XPS) e a análise de Raios X dispersiva em Energia (EDX) complementaram o estudo com informação estrutural.

Posteriormente, cada um dos conjugados de óxido de grafeno reduzido com nanopartículas (rGO-Fe_3O_4 NPs e rGO-Ni NPs) foram usados como base para a construção de um biossensor. Cada elétrodo modificado com rGO-Fe_3O_4 NPs e rGO-Ni NPs foi funcionalizado com uma camada de biopolímero de quitosana e enzima (lacasse e glicose oxidase, respetivamente), levando aos biossensores previstos. De seguida, os dois filmes montados foram caracterizados por SEM, ATR-FTIR, XPS e por técnicas eletroquímicas, nomeadamente CV e EIS, A sua aplicação como biossensor foi explorada, mostraram ambos um excelente desempenho eletroanalítico com uma ampla gama linear, elevada sensibilidade e apresentam limites de deteção muito baixos.

Palavras-chave: Grafeno baseado em nanomateriais, filmes condutores, elétrodos modificados, montagem supramolecular, sensores & biossensores eletroquímicos, estudos de transferência de carga, espectroscopia de impedância eletroquímica, voltamétrica cíclica.

Table of Contents

List of Figures

Chapter 1 - Graphene: Structure, Synthesis, Properties and Applications

Chapter 2 - Techniques

Chapter 4 - Assembly of Thin Graphene Films on Electrode Surfaces: Conformation, Impedance, and Electron Transfer Studies

Chapter 5 - A Layered Nanocomposite of Laccase, Chitosan, and Fe3O4 Nanoparticles-Reduced Graphene Oxide for the Nanomolar Electrochemical Detection of Bisphenol A

Chapter 6 - Reduced Graphene Oxide-Nickel Nanoparticles/Biopolymer Composite Films for Sub-Millimolar Detection of Glucose

List of Tables

Chapter 5 - A Layered Nanocomposite of Laccase, Chitosan, and Fe3O4 Nanoparticles-Reduced Graphene Oxide for the Nanomolar Electrochemical Detection of Bisphenol A

Chapter 6 - Reduced Graphene Oxide-Nickel Nanoparticles/Biopolymer Composite Films for Sub-Millimolar Detection of Glucose

List of Symbols and Abbreviations

AA – Ascorbic acid

AB – Acetate buffer

AU – Uric acid

APCVD - Ambient Pressure Chemical Vapour Deposition

AFM – Atomic Force Microscopy

ATR-FTIR – Attenuated Total Reflectance Fourier Transform Infrared

BPA – Bisphenol A

BDG – Boron-doped graphene

CPE – Constant phase element

C – Capacitance

C_{dl} – Double layer capacitor

Chit95 – Chitosan

CA – Chronoamperometry

CC - Catechol

CV – Cyclic Voltammetry

CVD – Chemical Vapour Deposition

CNTs – Carbon nanotubes

DD – Degree deacetylation

DO – Degree of oxidation

DR – Degree of reduction

ΔEp – Potential differences

DP – Dissolution-precipitation

DSD – Direct Surface Deposition

DFT – Density functional theory

DLEG – Direct laser-engraved graphene

EDs – Endocrine disruptors

ET – Electron transfer

$E_{1/2}$ – Half-wave potential

E^0 – Standard potential

EDX – Energy Dispersive X-Ray

EIS – Electrochemical impedance spectroscopy

Eraα; ERβ; ERRy – estrogen receptors

EpG - Epitaxial growth

EG – Epitaxial Graphene

EGR – Exfoliated graphene

FAD – Flavin adenine dinucleotide

FESEM – Field Emission Scanning Electron Microscopy

FRET – Fluorescence Resonance Energy Transfer

FETs – Field-effect Transistors

FLG – Few Layers Graphene

FIB – Focused ion bean

FTO – Fluorine-doped tin oxide

fcc – Face centered cubic

GCE – Glassy Carbon Electrode

GO – Graphene Oxide

GOx – Glucose Oxidase

GNMs – Graphene-based nanomaterials

GR – Graphite

GRO – Graphite Oxide

GNR – Graphene Nanoribbon

GQDs – Graphene quantum dots

GFETs Graphene field-effect transistors

HRP – Horseradish peroxidase

HRTEM – High-resolution transmission electron microscopy

HOPG – Highly Oriented pyrolytic Graphite

HDGs Heteroatom-doped graphene

ITO – Indium-doped tin oxide

j – Current density

j_{pa} – Anodic current density

j_{pc} – Cathodic current density

LES – Laccase-based electrochemical sensors

LOD – Low Limit of Detection

LPCVD – Low pressure vapour deposition

LEDs Light-emitting diodes

LIBs – Lithium ion batteries

MWCNTs – Multi-Walled Carbon nanotubes

MSE – Standard error of the mean

MOSFETs – Metal oxide Field-effect transistors

MNPs – Metal nanoparticles

NPs – Nanoparticles

NMR – Nuclear magnetic resonance

NIR – near Infrared

NDG – N-doped graphene

ORR – Oxygen reduction reaction

PBS – Phosphate Buffer

PC – Polycarbonate

PEEK – Polyether ether Ketone

PG – Pristine Graphene

PECVD – Plasma-enhanced Chemical Vapour Deposition

PVCs – Photovoltaic cells

PIS – Potential interfering spices

rGO – Reduced Graphene Oxide

R_S – Solution resistance

R_1 – Electron transfer resistance

RSD – Relative Standard Derivation

RTIL – Room Temperature Ionic Liquid

SWV – Square Wave Voltammetry

SLG – Single Layer Graphene

S – Sensitivity

SEy – Standard error of the y-interception

SPEs – Screen-printed electrodes

SGD – sulphur-doped graphene

SIBs – Sodium ion batteries

STM - Scanning Tunneling Microscopy

TYRs – Tyrosinases

TvL – Laccase from Trametes Versicolo

UA – Uric Acid

UFF – Universal force field

UHVCVD – Ultrahigh Vacuum Chemical Vapour Deposition

XPS – X-Ray photoelectron spectroscopy

W – Warburg element

Preface

This thesis is organized in four parts containing seven chapters:

Part A (Introduction): It is composed of one chapter (*Chapter 1*) in which a general overview of the scope, concepts, and motivations underlying the work presented in this thesis is given.
In *Chapter 1*, a brief introduction to the field of graphene and graphene derivatives is addressed. The general concepts, methods of synthesis, properties, and the main areas and applications of this promising field are presented.

Part B (Experimental Section): It is composed of two chapters (*Chapters 2 and 3*). This part presents a detailed description of the experimental techniques, setups, reagents and solutions used in this work.
In *Chapter 2*, an overview of the experimental techniques used in this work is provided. Techniques such as Cyclic Voltammetry (CV), Electrochemical Impedance Spectroscopy (EIS), Atomic Force Microscopy (AFM), Scanning Electron Microscopy (SEM) are described together with their experimental setups and instrumentation.
Chapter 3 presents a detailed description of the reagents and solutions used in the course of this work. Additionally, the preparation of the samples and surfaces, and its further modification for the characterization studies is also addressed in this chapter.

Part C (Results & Discussion): It is composed of three chapters (*Chapters 4–6*) in which the results obtained through the electrochemical techniques and microscopic techniques are presented and discussed. In the end of each chapter the main conclusions are also provided.
Chapter 4 describes the modification of glassy carbon electrode (GCE) surface with graphene oxide (GO), reduced graphene oxide (rGO) and reduced graphene oxide-based nanoparticles (rGO-NPs) is widely studied in order to try and improve electron transfer kinetics and surface interactions. After its characterization by ATR-FTIR, FESEM, EDX, the different concentrations of graphene related materials has been deposited on glassy carbon electrode and electrochemically characterized using a potassium hexacyanoferrate(II)/(III) as electrochemical redox probe. The electrochemical response of the graphene oxide is compared with the glassy carbon electrode bare, where the GO

shows a blocking of the capacitive current with increasing concentration. The opposite behaviour is found for modifications with the reduced graphene oxide.

Chapter 5 describes the preparation, characterization and application (that the enzymatic biosensor) of a hybrid conjugate of reduced graphene oxide/ferrous-ferric oxide nanoparticles (rGO-Fe_3O_4 NPs). This hybrid conjugate was characterized and immobilized on a glassy carbon electrode (GCE) with a chitosan biopolymer (containing the enzyme laccase). Subsequently its characterized by SEM, ATR-FTIR, XPS, and several electrochemical techniques. Then, the modified electrode was interrogated in the presence of aqueous bisphenol A in proof-of-concept electrochemical studies. The biosensor showed an excellent electroanalytical performance with a wide linear range, high sensitivity, and very low detection limits.

Chapter 6 describes the synthesis and physical characterization of a hybrid conjugate of reduced graphene oxide and nickel nanoparticles (rGO-Ni NPs). The conjugate was further deposited onto a glassy carbon electrode as a nanocomposite film of chitosan and glucose oxidase. The electrochemical response and morphology of the films were investigated by SEM, CV, and EIS, and their applications as a glucose biosensor were explored for the first time in proof-of-concept tests.

Part D (Concluding Remarks & Future Perspectives): Consists of one chapter (*Chapter 7*) in which the main conclusions and remarks regarding the whole work carried out during this PhD thesis are presented. Besides, suggestions for future work are also provided

.

Part A - Introduction

Chapter 1 - Graphene: Structure, Synthesis, Properties and Applications

Graphene is the first two-dimensional (2D) crystalline material which is truly stable under room conditions. This chapter describes the progress made in the preparation of 2D graphene and its derivatives since being first isolated by Geim and Novoselov in 2004. Its outstanding properties and the prospects of technological applications in different fields are reviewed with the focus being primarily set on the development of electrochemical sensor

1.1. From Bulk Graphite to Single/Few-Layer Graphene

During the last decade, new applications for the most diverse nanostructures in the fields of renewable energy, photochemistry, biotechnology, portable and flexible electronics, nanobiomedicine, theranostics, and many others, have continuously poured headlines in the scientific literature. Among other 2D nanomaterials, graphene and its derivatives constitute one of the most important additions to the box of nanotools for the development of potentially disruptive nanotechnologies[1]. By definition, graphene consists of a flat 2D mesh of pure carbon with a single-atom thickness that can be isolated from the corresponding stack of sheets that make up natural graphite (GR) as shown in Fig. 1.1[2]. C atoms in graphene occupy the vertices of a hexagon in what is often referred to as the hexagonal honeycomb lattice (Fig. 1.1.b).

Hybridization of their $2p_X$, $2p_Y$, and 2*s* orbitals yields 3 sp^2 orbitals of the same energy with trigonal planar symmetry. In-plane sp^2 orbitals of two adjacent atoms may overlap face-to-face to form a covalent σ bond. Thereby, each C in the hexagonal lattice forms 3 σ bonds with their neighbors. The σ-bonding determines the C-C distance in graphene to be about 0.142 nm (Fig 1.1.b). Interestingly, every C atom retains one unhybridized $2p_Z$ orbital perpendicular to the σ plane. Side-to-side overlapping of parallel $2p_Z$ orbitals (above and below the nodal plane of the nuclei) results in the formation of covalent π bonds. The lower degree of orbital overlapping in this configuration (plus its strong sensitivity to rotation around σ bonds), determine the weaker strength of π bonds (~256 vs the 347 kJ mol^{-1} of σ bonds)[3, 4]. Moreover, π-bonding electrons are highly delocalized around the ring and that plays a key role in determining the electronic properties of graphene[5, 6].

In three-dimensional (3D) GR, the individual sheets of graphene stack upon each other by the action of non-covalent Van der Waals dispersion forces (particularly aromatic π-π interactions). Due to the weak nature of these interactions, the interlayer distance (*aka* the d-spacing) in GR is more than twice the C-C bond length in the individual sheets (about 0.335 nm, Fig.1.1) [2]. The structure of 2D graphene can be regarded to result from the extrapolation of extremely planar polycyclic aromatic molecules to an infinite size. Thus, graphene can be considered the basic structural unit for other carbon allotropes such as GR, carbon nanotubes (CNTs), and fullerenes [6].

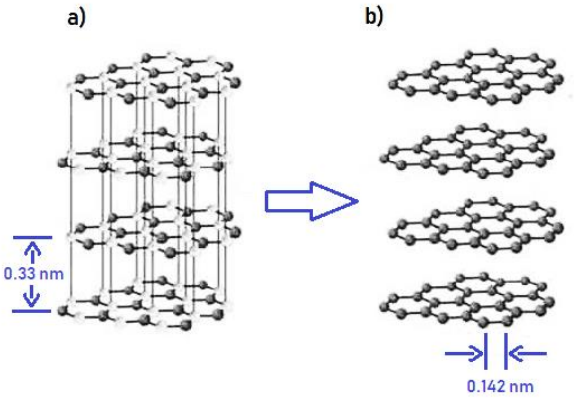

Fig. 1. 1: *Schematic diagram of (a) Graphite and (b) Four layers of graphene from graphite (adapted from reference [2]).*

2D sheets of graphene can be rolled-up into nanometer-sized one-dimensional (1D) CNT cylinders. Fullerenes are zero-dimensional (0D) structures that derive, structurally speaking, from graphene by introducing pentagons into its hexagonal lattice (Fig 1.2) [7].

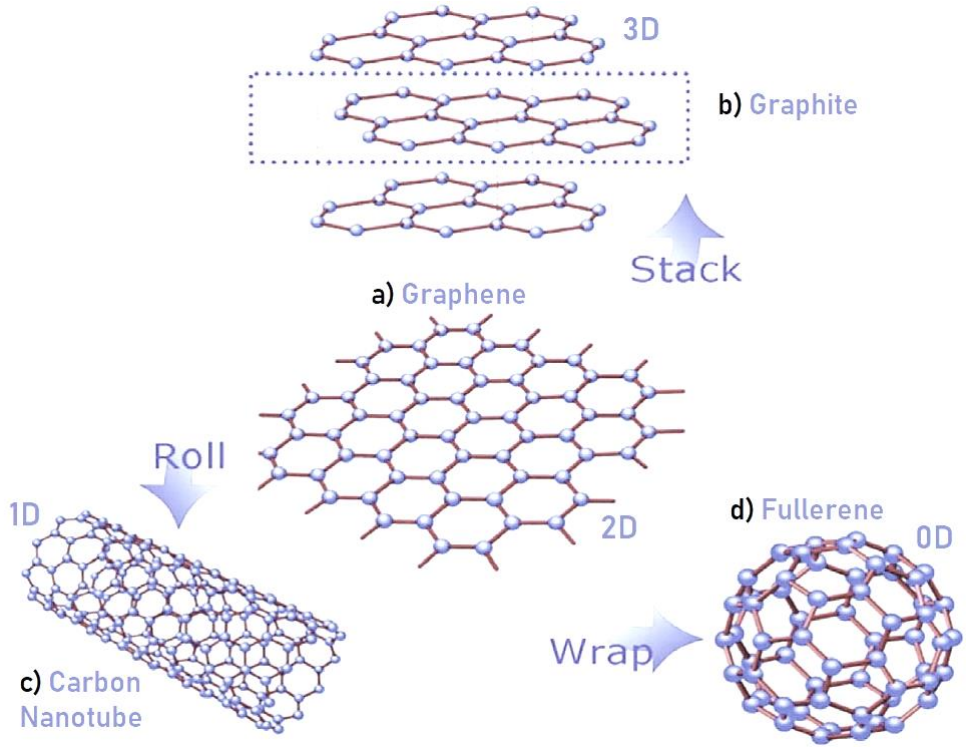

Fig. 1. 2: *a) Graphene: the mother building block of other carbon allotropes, b) graphite (3D), c) Carbone nanotube (1D) and d) fullerene (0D) (adapted from reference [7]).*

Graphene was theoretically discussed for the first time by Philip Russell Wallace in 1947 [8]. Wallace was a theoretical physicist at McGill University in Montreal (Canada) interested in studying the electronic structure of GR. In his research, Wallace developed a 2D analogue (graphene) from which he extrapolated the properties of 3D GR. For several decades, the study of graphene remained only at the level of theory because many

scientists believed that 2D materials could not exist as free-standing materials due to its very unstable nature [9-11].

The term graphene was first used by Boehm and co-authors to describe carbon flakes which were single or multilayer [12]. According to Boehm: "a single carbon layer of the graphitic structure can be considered as the final member of this series and the term graphene should therefore be used to designate the individual carbon layers in graphite intercalation compounds" [13].

In 2004, Andre Geim and Konstantin Novoselov (Manchester University, UK) developed a mechanical method that allowed for the isolation and physical characterization, using the atomic force microscope (AFM), of one-atom-thick single-layer graphene (SLG) (Fig 1.3) [14]. The method consisted of the mechanical exfoliation of small mesas of highly oriented pyrolytic graphite (HOPG) by repeated peeling to obtain thin layers of GR. The peeling was done with Scotch tape and the layers were transferred to a silicon substrate (SiO_2) for inspection. For this pioneering work, they received the Nobel Prize in Physics in 2010 [15]. Although the method is very clever, cheap, and simple; its yield is very low and that turned very hard to achieve high-quality industrial production levels.

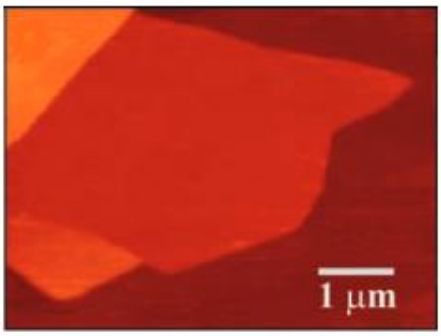

Fig. 1. 3: *Atomic force microscopy image of single-layer graphene on SiO_2 surface (dark-brown) (adapted from reference [14]).*

1.2. Methods of Synthesis

To continue studying the properties of graphene and its integration in different nanotechnologies, it was first necessary to develop alternative methods for its synthesis and processing. Then, following the work of Geim and Novoselov, research activities on graphene expanded quickly. While most of the efforts were devoted to obtaining high-quality graphene in high yield, other important goals as gaining control over the physical properties or reducing the production costs, have also been pursued [16, 17]. As a consequence, the number of graphene-related publications has followed an exponential increase since 2004 (reaching more than 40 publications per day in 2013) [1, 18]. For the preparation of graphene nanomaterials in the laboratory, researchers have explored two

general pathways consisting of top-down and bottom-up synthetic strategies (see Fig 1.4)[19].

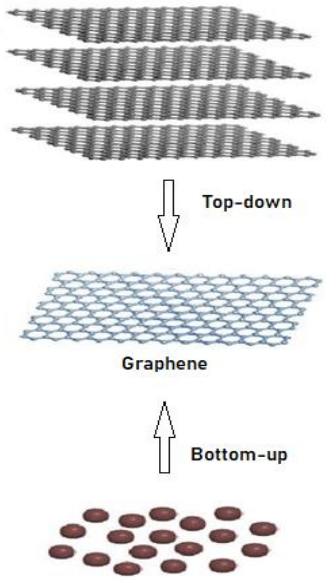

Fig. 1. 4: *Schematic illustration of bottom-up and top-down graphene synthesis methods (adapted from reference [20]).*

Fig 1.5 summarizes the most common methods reported so far, based on both types of approaches.

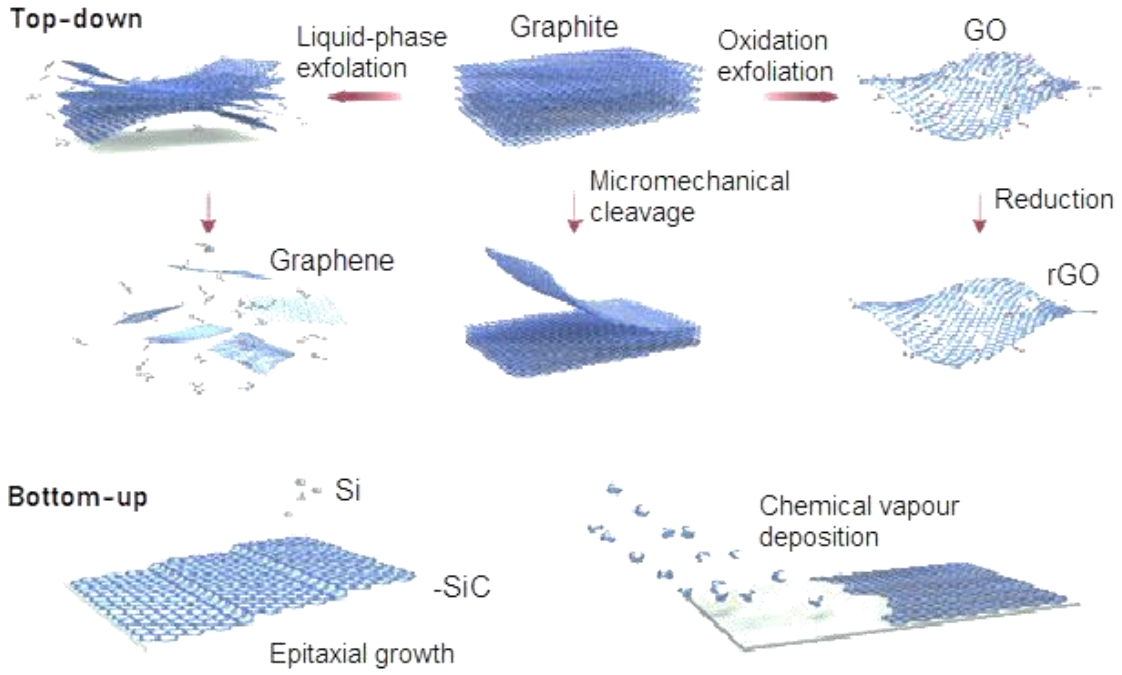

Fig. 1. 5: *Schematic illustration of the different types of methods to prepare Graphene (adapted from reference [21]).*

1.2.1. Bottom-Up Approach

In materials science, bottom-up synthetic strategies involve the building of materials through the assembly (or self-assembly) of the basic structures that form it (which can be atoms, molecules, or nanostructures). When the building blocks are atoms, the process is also known as atom-by-atom fabrication or atomically precise manufacturing. The methods of assembly can be either physical or chemical. The main advantage of this group of techniques is the high structural integrity and crystallinity of the synthesized materials (which are usually characterized by a very low density of defects, missing atoms, impurities, etc). As it is detailed in the following sections, bottom-up approaches to graphene rely on the individual deposition of C atoms from different sources [20].

1.2.1.1. Chemical Vapour Deposition

Chemical vapor deposition (CVD) is a vacuum-based method used in the preparation of planar ultrathin films which are typically characterized by a superior structural quality and high thickness uniformity. For these reasons, CVD is a well-recognized tool in atomic layer deposition [22]. For these purposes, the supporting substrate is typically exposed to volatile precursors at low pressure (LPCVD) or ultrahigh vacuum (UHVCVD). Precursors react, and/or decompose, on the substrate surface to form deposits ranging from one- to few-atoms in thickness. It has been used to deposit materials such as silicon (dioxide, carbide, nitride, etc), carbon, fluorocarbons, metal dichalcogenides, tungsten, amongst others, in a wide variety of forms (monocrystalline, polycrystalline, amorphous, epitaxial) [23].

For the thermal CVD preparation of graphene (hereinafter CVDG), metal catalysts such as Cu or Ni are used as substrates. Hydrocarbons such as methane (CH_4), ethylene (C_2H_4), or acetylene (C_2H_2) are some of the typical sources of C. Two main types of mechanisms have been described in the literature: (a) Dissolution-precipitation (DP), and (b) Direct surface deposition (DSD) [24]. The hydrocarbons are typically decomposed at the catalyst surface at high temperatures (850-1150 ºC) (Fig 1.6) [25-27]. The diffusion of carbon to the bulk occurs in metals with high carbon solubility at these temperatures (e.g. Ni). When the metal is cooled-down, the stored carbon diffuses to the surface initiating the growth of SLG/FLG (DP mechanism). In some cases, this mechanism has been found to promote epitaxial growth (e.g. in Ru single-crystal substrates under UHV) [27].

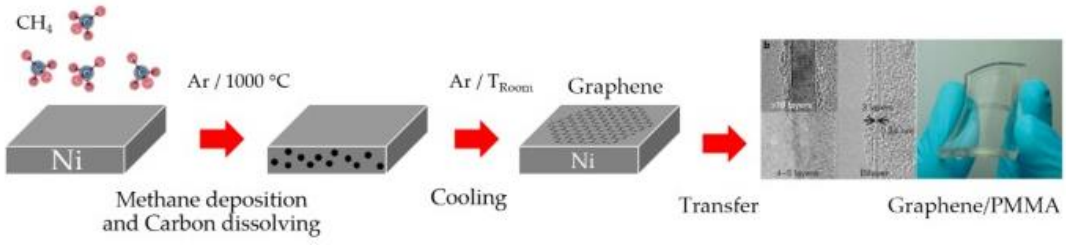

Fig. 1. 6: *Schematic illustration of graphene growth using chemical vapour deposition and the transferred graphene to poly(methyl methacrylate)(adapted from reference[28]).*

DSD growth of graphene on metal catalysts can be also accomplished by lowering the operating temperatures to 500-700 ºC (e.g. in both Ni and Ru)[29, 30] or using metals with negligible carbon solubility at high temperatures (such as Cu) [31]. Metallic thin films can be used to fabricate graphene films in ambient pressure CVD (APCVD) through the DP mechanism [32]. The advent of plasma-enhanced CVD (PECVD) has enabled the growth of graphene on those metals, or even on dielectric surfaces (Si/SiO_2, quartz glass, etc)[32, 33], at low temperatures. This is very important when devising routes towards industrial-scale production of graphene, as it may lead to reduced environmental footprints (less energy is consumed in the synthesis) and more affordable products.

Hydrogen gas (H_2) is usually required to promote carbon deposition on the substrate. If the hydrocarbon/H_2 gas flow rate ratio is not appropriate, undesirable results will be obtained [34]. By corroding the amorphous C-based structures H_2 improves the quality of CVD graphene. Nonetheless, an excess of H atoms will also corrode graphene sheets.

In 2006, Somani *et al.* reported on the first forms of graphene (thin layer films) grown by the CVD method [35]. In this work, graphene was synthesized on Ni substrates from a natural, eco-friendly, and low-cost precursor such as camphor. After that publication the CVD method became the most popular and effective way to produce graphene films [36-38]. CVDGs are characterized by their large areas and high structural quality (i.e. by a very low density of defects) [25].

However, due to their low thickness (SLG) and the need to transfer the sheets to other substrates, conserving the large areas of CVDGs in the transferred films is quite challenging [37, 39, 40]. The high production costs, low throughput, and the need of further purification to remove residue catalyst, are other disadvantages of the method [41]. In any case, the impact of some of these issues can be minimized by growing graphene on dielectric substrates using the PECVD method.

1.2.1.2. Epitaxial Growth

When the organization of a film grown onto a substrate matches the crystalline order of the latter, the process is referred to as epitaxial growth (EpG). EpG can proceed from gas or liquid precursors, but the first case is the most common, and the vapors for EpG are typically generated in a CVD chamber or by laser ablation. Applied to the synthesis of graphene, the CVD-EpG method stands out of the rest because it allows direct growth on silicon carbide (SiC). SiC is an indirect semiconductor that has gained great prominence in the transistor industry due to the higher blocking voltage, lower on-state resistance, and higher thermal conductivity (κ) of their metal oxide field-effect transistors (MOSFETs), compared to silicon (Si) [42]. Besides, its band gap can be reduced (indirect-to-direct transition) by chemical functionalization.

The CVD-EpG technique proceeds through the thermal decomposition of hexagonal SiC substrates at 1200-1800 °C under ultra-high vacuum [43]. At such temperatures Si atoms sublimate from the surface, thus, leaving over the surface a network of sp^2-hybridized C atoms that induce the subsequent epitaxial growth of graphene by CVD (Fig 1.7) [44, 45]. Thus, thermally-induced CVD-EpG on SiC looks like a promising way to prepare large-scale SLG/FLG with high crystalline quality for applications in transistor devices. Unfortunately, yields are not that high and the technique relies on the use of expensive SiC wafers and UHV facilities which consume vast amounts of energy.

On top of these issues, the CVDGs prepared in this way still lack enough homogeneity. The orientation of the resulting layers is defined by the crystal lattice on the substrate. Therefore, the CVDGs grown on Si- or C-terminated faces have different characteristics. In the first case, SLG sheets of several microns in width are easily obtained [46]. However, on the C-terminated face, forms of FLG (with sheets rotated 0 or 30 degrees from each other) are found. Following this method, Mitsuhashi *et al*. prepared bilayer CVDG with excellent carrier mobility of up to 95,000 $cm^2\ V^{-1}s^{-1}$ [47].

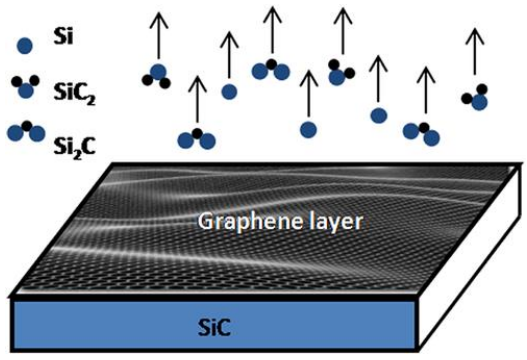

Fig. 1. 7: *Illustration of epitaxial graphene growth on a silicon carbide (SiC) by sublimation of Si atoms (adapted from reference [44]).*

1.2.2. Top-Down Approaches

Top-down strategies are based on the physical separation of the stacked GR layers to unleash single graphene sheets. For these purposes, the weak π-π stacking Van der Waals forces must be overcome. The principal top-down routes include micromechanical cleavage, liquid-phase exfoliation, and the intercalation of GR [21].

Compared to the main bottom-up methods described in the previous sections, larger amounts of graphene can be produced via physical/chemical exfoliation of bulk GR. These constitute a simple and inexpensive way to prepare graphene, but they also present important disadvantages like, for instance, the occurring of defects during the separation of the layers or the possible agglomeration of the isolated sheets [20]. On top of that, these are tedious procedures with typically low reaction yields. In this respect, GR intercalation has proven to be effective in increasing the exfoliation yields.

1.2.2.1. Micromechanical Exfoliation

Micromechanical exfoliation, *aka* micromechanical cleavage, has been used for decades by crystallographers. In 1999, Rodney S. Ruoff and his co-workers (Washington University, USA) reported a method for the controlled exfoliation of HOPG to yield micrometer-sized GR islands made up of several atomic layers [48]. In this work, the authors also speculated on the idea that mechanical rubbing of GR against flat surfaces could be a valid route towards few-atom-thick, or even one-atom-thick, graphene sheets. The validity of this concept would be confirmed a few years later by Geim and Novoselov using the scotch tape method [14], the most popular procedure based on micromechanical cleavage for the isolation of graphene thus far. Their technique consists of the repeated peeling of GR until a single layer of graphene is obtained (Fig.1.8) [28].

Mechanical exfoliation can also be implemented through the use of scanning probe imaging equipment. In this regard, the atomic force microscope (AFM) has been routinely applied in the last decades for the investigation of tribological phenomena in the nanoscale. The use of AFM tips for the micromechanical cleaving of GR plates was also reported for the first time in Ruoff´s paper [48]. AFM manipulation of GR can be performed either on the original HOPG substrate or after transferring the plates to different substrates.

In general, micromechanical exfoliation produces high-quality graphene that can be electrically isolated for fundamental studies. However, it is not a suitable approach for large scale production thus far. Other issues include difficulties to keep individual single-layers away from aggregation and to control the number of atomic layers.

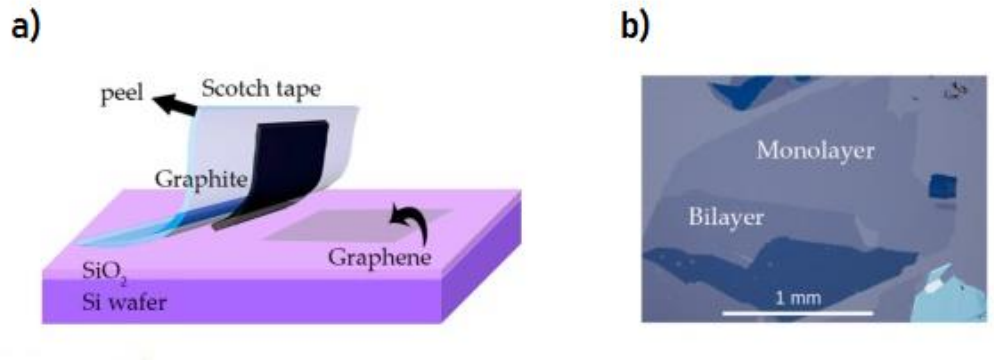

Fig. 1. 8: *a) graphene sheet is left on top of a silicon oxide wafer exfoliated by scotch-tape technique, b) the real monolayer and bilayer graphene (adapted from reference [28]).*

1.2.2.2. Liquid-phase Exfoliation

Liquid-phase exfoliation of GR is another possible route towards graphene. Under such an approach, bulk GR is directly exfoliated into liquid media by physical means to produce a range of products going from single-layer (SLG) to few-layers graphene (FLG).

For instance, graphene flakes can be obtained by sonicating bulk GR in appropriate organic solvents. Exfoliation occurs through the strong interactions established between the basal planes of GR and the solvent molecules. The ideal solvent would be one that minimizes the interfacial tension between the liquid and the graphene flakes. In this context, solvents with surface tension around 40 mN m^{-1}, such as N-methyl-pyrrolidone (NMP), N,N-dimethylformamide (DMF), or γ-butyrolactone (GBL), are typically used in absence and presence of surfactants (Fig.1.9) [49,50].

Unfortunately, these solvents are highly volatile, toxic, and not very friendly to the environment. To improve the sustainability, research efforts have focused on the development of greener methods. J.-H. Ding *et al*. (Ningbo Institute of Materials Technology and Engineering, China) recently reported a cost-effective procedure to produce FLG in pure water without any chemicals or surfactants [51]. The method consists in the preparation of edge hydroxylated graphene by an easy liquid exfoliation approach with the assistance of a vapor pretreatment. The resulting graphene was dispersed in water to obtain an ultrathin conductive film. Another example of eco-friendly exfoliation is provided by J. Chen *et al.* from the Wuhan University of Technology (China) [52]. The authors developed a method consisting of the ultrasonication of GR in presence of a degradable, and water-soluble, polymer modified with chloramine. The method produced defect-free FLG in high yield.

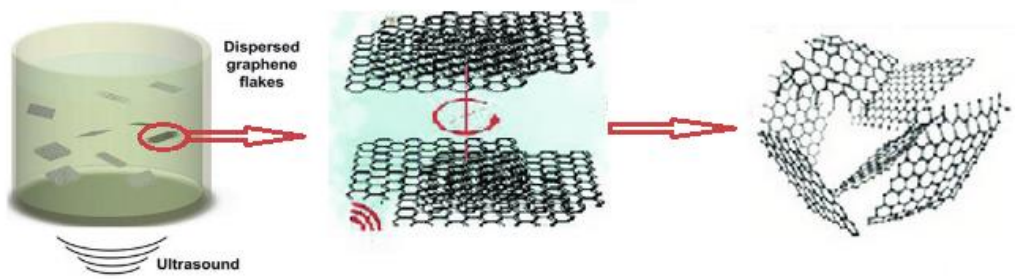

Fig. 1. 9: *Schematic illustration of graphene preparation by liquid-phase exfoliation (adapted from reference [53]).*

Indeed, the principal advantage of graphene produced by exfoliation in the liquid phase is their high structural quality. This was evidenced, for instance, by the registration an electron mobility as high as 95 $cm^2\ V^{-1}s^{-1}$ for SLG sheets obtained through this method [54]. As shown in sections 1.2.2.3 and 1.2.2.4, most of these methods have been also applied to forms of GR previously expanded by physical or chemical means. In this respect, the exfoliation of GR (EGR) intercalated with supercritical fluids is another route explored in the literature. In this technique, the intercalated fluid is quickly expanded by brief ultrasonication in proper solvent to push the graphene layers apart. The method is very fast and yields pristine graphene (PG) sheets. When DMF, NMP, and ethanol, were used; well-dispersed solutions mainly consisting of sheets of less than 10 layers (with about a 10% being SLG) were obtained [55]. The fraction of SLG was improved to 60% using 1-pyrene sulfonic acid sodium salt as a surfactant during the expansion [56].

1.2.2.3. Chemical Exfoliation

This is one of the most promising approaches to synthesize large-scale graphene. The covered methods typically consist of two main stages. In the first step, GR is chemically oxidized to graphite oxide (GRO). In such a process, the stacked layers are readily intercalated with vast amounts of solvent molecules, ions, and oxygen-containing functional groups. As a result, the d-spacing increases substantially, and π-π stacking forces are weakened [57]. These changes favour the physical exfoliation of the plates in the second stage which is often carried out by ultrasonication in a suitable solvent or rapid heating (more details in Section 1.2.2.4). The method produces sheets of graphene oxide (GO) with thickness varying from single to few layers. Because of the massive presence of functional groups (carbonyls, carboxyls, hydroxyls, etc) [58, 59], GO can get dispersed in polar protic solvents such as water what greatly facilitates its processing.

The first synthesis of GRO was reported by Brodie in 1859. For these purposes, GR was treated with a mixture of potassium chlorate ($KClO_3$) and nitric acid (HNO_3) [60]. In

1957 Hummers and Offeman developed a safer, quicker, and more efficient process using sodium nitrate ($NaNO_3$) and potassium permanganate ($KMnO_4$) as an alternative oxidizer to $KClO_3$ (which evolves to the toxic gas ClO_2) [61]. Under this strategy, HNO_3 is formed in situ in the reaction mixture instead of being used directly as a solvent. Today, the so-called Hummer´s method and small variations of it are the most common procedures for the oxidation of GR in the preparation of GO. The introduction of O-groups in GR involves changes in the hybridization of C atoms from sp^2 to sp^3. Hence, a mixture of both types of C is typically found in GRO and GO. Furthermore, the physical disaggregation of the layers introduces a variety of defects (Stone-Wales, lattice vacancies, dislocations, etc.) [62]. These aspects have profound implications for the properties of graphene and explain, for instance, the poor electrical properties of GO.

Interestingly, the modification of graphene properties can also lead to new functionalities that broaden its range of applications. In this regard, the high density of functional groups and defective sites in GO confer it with good (electro)catalytic properties which are in sharp contrast with the weak catalytic activity found for PG [63]. Although the mechanical properties are also compromised to some extent, these are still good enough that GO has been primarily explored as a mechanical reinforcer in membranes and composite materials [64, 65].

Aiming to repair the honeycomb lattice and restore the aromaticity of PG, GO is often reduced by chemical, electrochemical, or thermal means [66, 67]. The most common chemical routes reported in the literature involve the use of reducing agents such as hydrazine (N_2H_4) and its derivatives [68, 69], $NaBH_4$ [70, 71], sulfur-containing compounds [72], metal powders [73, 74], vitamin C [75], or hydroxylamine [76], in-situ generated hydrogen [77], amongst others. Although each process has advantages and disadvantages, it is noteworthy that metal powders have produced reduced graphene oxide (henceforth referred to as rGO) at low temperature with the highest C/O atomic ratio (up to 33.5) [78, 79]. Most of the O-groups are removed in these treatments and the resulting rGO presents improved electrical and thermal properties compared to GO (Fig 1.10) [80].

Unfortunately, the complete reduction of GO is hard to achieve, even under harsh conditions [78], and a certain amount of functional groups and defects remains always in the structure [81]. As discussed in section 1.3, structural lattice defects degrade the properties of graphene and deteriorate the performance of their corresponding devices. Hence, unavoidably, the extraordinary properties found for graphene samples of high lattice perfection cannot be achieved by rGO. Nonetheless, the unique combination of electrical/electrocatalytic properties, arising from the partial recovery of the honeycomb structure of PG and the retention of a small density of oxygen groups and defects from the

starting GO, turns rGO into a better-balanced material for the modification of electrodes to serve, for instance, in electrochemical applications.

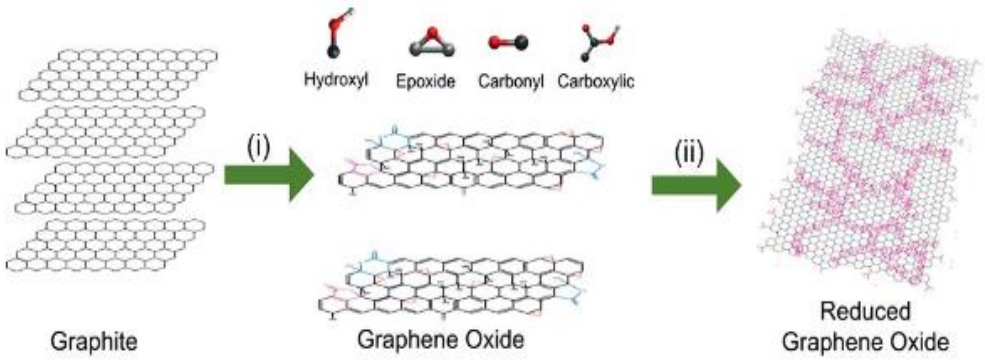

Fig. 1. 10: *GO synthesis and reduction which involve (i) oxidation of graphite to graphene oxide layers where the flakes are functionalized with epoxy, hydroxyl, carbonyl groups and (ii) conversion of GO to rGO through chemical and/or thermal treatment.* (*adapted from reference[80]).*

1.2.2.4. Thermal Exfoliation

Thermal methods are used to exfoliate GRO. Heat causes the functional groups to decompose and produce gases that build up pressure between the adjacent graphitic layers. Exfoliation occurs when this pressure exceeds the van der Waals stacking forces [82]. Hence, for the successful build-up of pressure, the starting forms of GR must be significantly functionalized. In this sense, EGR and GR intercalation compounds (GICs) are less functionalized than GRO (which exhibits a C/O atom ratio as low as 2) but their d-spacing is yet enough expanded to undergo direct thermal exfoliation. It is worthy to note that when applied to GRO, thermal methods usually result in a simultaneous exfoliation and reduction of the layers to a certain extent.

Thermal treatments are capable of achieving near-complete exfoliation into single-layer materials. Compared to mechanical exfoliation, it also brings certain advantages. In the first place, these processes are much faster (often completed within seconds) [82]. Secondly, most of them operate in the absence of liquid which is advantageous for applications that require dry graphene (e.g. the construction of electrodes for lithium-ion batteries). Rapid heating is one of the most widely used thermal strategies in the exfoliation of GRO, EGR, and GICs. Schniepp *et al.* reported for the first time on the exfoliation of GRO to single-layer sheets [83]. The starting material was loaded into a quartz tube and inserted into a furnace preheated to 1050 ºC. The product was characterized as wrinkled sheets with a minimum thickness of 1.1 nm (with up to 80% of single-layer flakes) and

surface area in the range 700–1500 m^2 g^{-1}. Following the same procedure, Wu *et al.* determined that the smaller the lateral size and the lower the crystallinity of the starting GR, the better the exfoliation [84].

Li *et al*. investigated the exfoliation of EGR by rapid heating at 1000 ºC in a gas mixture (3% hydrogen in argon) [85]. Ribbon and sheet forms of SLG and FLG were found after dispersion of the product. The very low yield obtained (~0.5%) was improved by further intercalation of the thermally exfoliated products (step 1) with oleum (fuming sulfuric acid) and subsequent exfoliation by ultrasonication in DMF (step 2) [86]. The resulting suspension contained up to 90% of SLG sheets of high structural quality. A similar two-steps strategy, based on rapid heating at 900 ºC followed by ultrasonication of the re-intercalated products in liquid phase, was applied to exfoliate GICs intercalated with concentrated sulfuric acid and hydrogen peroxide into (up to 50% of obtained sheets) [87]. Other rapid heating methods include microwave (MW) irradiation, arc discharge, solvothermal methods, and the detonation of explosives [88-92].

GRO pre-activated in KOH was exfoliated in about 1 min under MW heating to yield graphene with surface areas of 3100 m^2 g^{-1} [88]. The technique was also used by Janowska *et al.* to exfoliate EGR in aqueous ammonia at temperatures of 120–200 ºC [89]. The treatment produced FLG flakes of less than 10 layers. The hydrogen arc discharge method has also been efficiently applied to the exfoliation of expanded GRs. The electrical discharge instantly raises the temperature to more than 2000 ºC. By doing so, the pressure between the layers quickly exceeds the stacking forces. Wu *et al*. used this method to exfoliate GRO yielding, after proper dispersion and centrifugation of the products, up to 80% of SLG sheets with thickness around 0.9–1.1 nm [90]. Qian *et al*. reported on the synthesis of single- and bi-layer graphene sheets by solvothermal exfoliation of EGR in acetonitrile [91]. EGR was also successfully exfoliated via another solvothermal method based on oleylamine as a solvent and intercalating agent [92].

Up to 60% of the obtained sheets were identified as SLG with individual surface areas as large as 300 μm^2. For GRO, thermal exfoliation in the air at much lower temperatures, 200-550 ºC, has also shown to be efficient. Sheets exfoliated by this method exhibited specific surface areas in the range of 328-418 m^2g^{-1} (the higher the temperature, the greater the surface) [93]. Exfoliation of GRO was further reported in argon (at 275-295 ºC) [94] and hydrogen (200 ºC) [95]. The latter yielded a specific surface area of 442 m^2g^{-1}, which is close to the values obtained in the air. In an attempt to enhance the exfoliation yields at 200 ºC, exfoliation was conducted in a vacuum oven (<1 Pa) [96]. This strategy was expected to increase the d-spacing to facilitate the exfoliation. Statistical analysis showed that over 60% of the sheets were SLG. Following this method, graphene with an even higher surface area (759 m^2g^{-1}) was obtained at 135 ºC [97].

1.2.2.5. Others Methods

Besides the well-studied mechanical and thermal exfoliation methods, other approaches (based on alternative ways of peeling GR materials or on totally new concepts which start from different carbon sources) have been developed. For instance, GR has also been exfoliated by electrochemical means. For these purposes, a certain bias is applied between two graphite electrode rods immersed in a conductive electrolyte. The anode corrodes yielding graphene flakes which are functionalized by the solvent. This constitutes a versatile approach for the simultaneous exfoliation and functionalization of graphene which is implemented quickly (within 1 hour in most cases) and introduces lower amounts of lattice defects compared to thermal or ultrasonication methods.

N. Liu *et al*. conducted the electrochemical exfoliation of GR in the room temperature ionic liquid (RTIL) methyl imidazolium hexafluorophosphate [98]. The method produced imidazolium-functionalized SLG sheets dispersible in organic solvents, with an average thickness of 1.1 nm, and with better electrical properties than GO and low reduced GO. The method has also been applied in RTIL-water electrolytes [99] or liquids like sulfuric acid [100]. In the first case it was found that the higher the water content, the larger the amount of oxygen-containing functional groups and the wider the variety of graphene materials obtained. In the second case, graphene nanosheets with large lateral size in the μm scale and thinner than 3 nm (more than 60% of the sheets were bi-layer) were obtained. Although partially oxidized, the electron mobility still exceeded that measured in most rGOs.

Janowska *et al*. developed a completely different approach to produce graphene based on the oxidative opening of CNTs. The method consisted of the coating of single-wall and multi-wall CNTs (SW- and MWCNTs, respectively) with Pd nanoparticles (NPs) to induce their catalytic unzipping in oxygen-containing aqueous media [101]. Under MW irradiation, Pd NPs generate reactive oxygen species which act as a pair of scissors to cut the CNTs lengthways. The method produced FLG sheets with yields of up to 8 wt% and oxygen-containing functional groups (i.e. –CO, –COR, –COOH) on its surface as confirmed through XPS analysis.

All the synthetic methods described above (both bottom-up and top-down) have their advantages and disadvantages. These characteristics are properly summarized and compared in Table 1.1. All forms of graphene investigated in this thesis (both prepared in the laboratory and purchased from commercial suppliers) were synthesized through top-down approaches. These are not the best in terms of structural quality and physical properties but their good process ability in liquid solvents (for the preparation of modified

electrodes), and their lower cost than those coming from CVD methods, were the main points pushing the balance towards such a choice of materials.

Table 1. 1 *A Comparison of Approaches for Synthesis of Graphene*

Synthesis method	Precursor	Advantages	Disadvantages
Micromechanical exfoliation	graphite	- Low cost - Impurity free - Simple	- Low yield - Time consuming
Liquid-phase exfoliation	graphite	- High quality	- Existence of defects - Low quality
Chemical oxidation + exfoliation	graphite	- High yield - Scalable to industrial level - Efficient	- Existence of defects - Low quality
Chemical vapour deposition	Hydrocarbon gases	- High quality - High growth rates - Good reproducibility	- High temperatures -Difficulty in controlling number of layers - high Cost
Epitaxial growth	SiC wafer	- simple -High quality and controllable	- High temperature - High vacuum - Existence of defects

1.3. Properties of Graphene

Since its first isolation, SLG has exhibited unique properties such as superb electrical conductivity (carrier mobility at room temperature higher than 200000 $cm^2V^{-1}s^{-1}$)[102], high Young's modulus (about 1 TPa) and great stretch abilities up to 25%[103], very large specific surface area (~2630 m^2g^{-1})[104], excellent transparency (only a 2.3% of the incident visible light is absorbed[105], and excellent thermal conductivity (2000–5000 $Wm^{-1}K^{-1}$)[3, 106], amongst others. Under the light of these characteristics, graphene has been described as the thinnest, strongest, and most flexible material ever made.[7] Fig.1.11 illustrate some of its exceptional properties that have been established to date. As a consequence, it has been extensively investigated as a filler and mechanical reinforcement in (nano)composites,[107, 108] but also in electronic devices such as photovoltaic solar cells[109], organic light-emitting diodes[110], field-effect transistors[111], photodetectors[112] and touch screens[113].

Supercapacitors[114], lithium-ion batteries[115] and sensors[116] are other applications of graphene as an excellent electrode material.

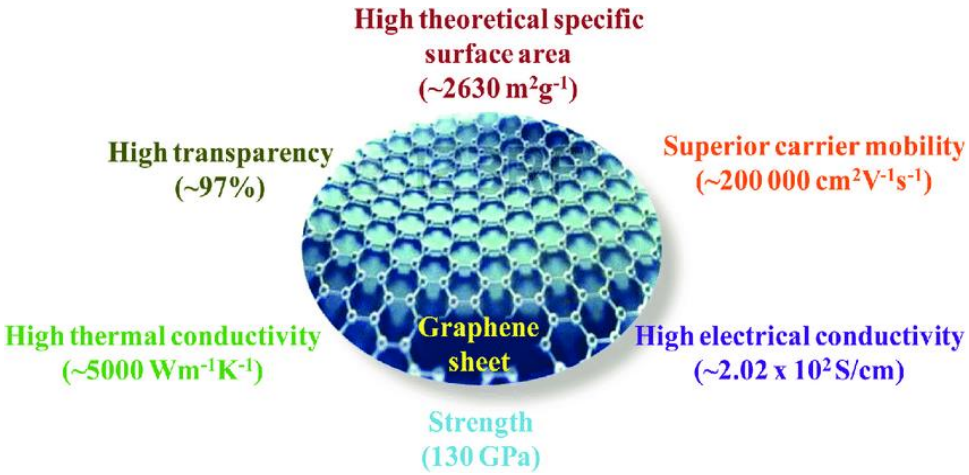

Fig. 1. 11: *Schematic illustration summarizing the most important properties found for SLG (adapted from reference[117]).*

1.3.1. Mechanical

The exceptional mechanical properties of graphene and its composites are, to a large extent, related to the great stability of the sp^2 bonds in the hexagonal honeycomb crystal lattice[118]. Hone and his co-authors published the first study on the mechanical properties of free-standing and defect-free SLG[103]. Using AFM-based nanoindentation methods, intrinsic strength of 42 Nm^{-1} and Young´s modulus of 1.0 TPa were measured. [103, 119, 103] These values portray graphene as the strongest material ever made to date. Regarding the stiffness, slight discrepancies have been found in the literature and attributed to deviations in the free-standing structure of SLG. Under real experimental conditions, free-standing graphene is never flat but inevitably goes rippled, crumpled, and/or wrinkled[17, 118]. These deformations can influence the mechanical behaviour of graphene.

For instance, Nicholl *et al*. observed that graphene is significantly softened by out-of-plane crumpling[120]. In these respect, the values of in-plane stiffness measured at room temperature fell within the range 20-100 Nm^{-1}, thus, being much smaller than the expected for flat graphene (340 Nm^{-1}). The effect of wrinkle deformation in CVDG was also studied by Raman spectroscopy[121]. The authors found that, during deformation, the broadening and shift in wavenumbers per strain unit followed by the 2D band were <25% and ~75%, respectively, of those found for flat graphene. In line with these findings, Young's modulus declined from 1.0 TPa to only 250 GPa. Because of its potential impact on applications,

the deformation of graphene from its flat structure is an important aspect that has captured the attention of researchers[122-129].

Another important property of graphene is its fracture toughness. This parameter describes the ability of a crack-containing material to resist fracture. To predict the mechanical behaviour of real materials for engineering applications, fracture toughness is more relevant than the intrinsic strength in perfect graphene sheets. P. Zhang *et al*. developed the first tensile test for SLG using nanoindentation measurements in an AFM[130]. A crack was induced through the focused ion beam technique (FIB). The fracture toughness was, then, measured as 4.0±0.6 MPa $m^{1/2}$. This result is in good agreement with those found in other literature studies [131, 132] and allows concluding that the possible introduction or natural occurrence of weak links, from which failure might initiate, has a heavy influence on the fracture toughness of graphene.

1.3.2. Electrical

With an electron mobility slightly over $2x10^5$ $cm^2V^{-1}s^{-1}$ at carrier densities of ~$2x10^{11}$ cm^{-2} (nearly 140 times the mobility of silicon and twice that of carbon nanotubes)[102], current densities up to $1x10^9$ A cm^{-2} (10^3 times higher than copper), and a sheet resistance of only 31 Sm^{-1}; freestanding SLG sheets are the best electrical conductor at room temperature[133]. As mentioned earlier in Section 1.1, the hexagonal honeycomb structure of graphene consists of sp^2-hybridized C atoms. Every atom in the lattice is bonded through three in-plane σ bonds. However, each C atom retains one unhybridized $2p_Z$ orbital (perpendicular to the sp^2 plane) which overlaps with their neighbours side by side (π bonds) to form a delocalized network with the electron density mainly concentrated above and below the plane of the nuclei. The strong C-C sp^2 bonding and the delocalized nature of π-electrons are ultimately responsible for the outstanding properties referred to above[134].

Besides, graphene is a 2D zero-gap semiconductor in which the conduction and valance bands (CB and VB) are symmetric and exhibit conical shape. These bands intercept in the so-called Dirac points. These correspond to six locations in momentum space (on the edge of the Brillouin zone) which can be divided into two sets of three non-equivalent points typically referred to as K and K´ (Fig.1.12)[134]. The Fermi level (E_F) is set at the intersections of the CB and VB cones as long as there is no doping. Thus, the populations at both bands follow the Fermi-Dirac statistics (same density of electrons and holes) and electrons at the highest occupied molecular orbital (HOMO) of the VB may flow

towards the lowest unoccupied molecular orbital (LUMO) of the CB as massless relativistic Dirac fermions[3].

Mass-less behaviour results in unusual outstanding properties including ballistic charge transport (collision-free) and anomalous quantum Hall effect at room temperature[135-137]. A minimum conductivity in the order of the quantized unit of electrical conductance ($4e^2h^{-1}$; where *e* is the elementary charge and *h* the Planck´s constant) has been consistently measured. Conductivity never goes below this value even if the density of carriers approaches zero near the Dirac points[138]. The origin of this residual conductivity remains unclear. Some authors have ascribed it to the presence of impurities, others to thermally-induced carriers, substrate-related effects and/or impurities, etc. Unfortunately, these outstanding electrical properties are readily affected by factors such as the number of graphene layers, size restrictions in one dimension (e.g. graphene nanoribbons, GNRs), or the nature of the supporting substrate.

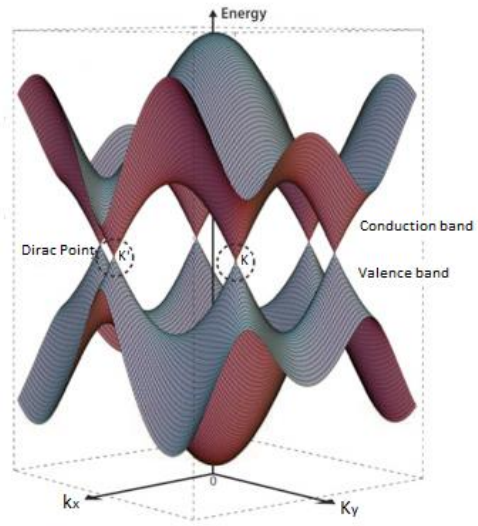

Fig. 1. 12: *The band structure of graphene. Conductance band touches valence band at K and K' points (adapted from reference [134]).*

Calculations reported by X-Y. Fang *et al*. demonstrated that the resistivity of FLG sheets increases from 1.4 to 8.2 μΩ cm^{-1} when the number of layers is raised from 1 to 9[139]. On the other hand, Y. Xu *et al.* observed changes in the electronic states of SLG supported on Si(100) substrates[140]. However, those were completely suppressed after passivation with hydrogen to yield Si (100)-H surfaces. The limiting effect of the substrate can also be inferred from the behaviour reported for field-effect Transistors (FETs) of graphene on SiO_2 substrates (SiO_2 GFETs). The best room temperature carrier mobility measured for these devices fall in the range 1-4x10^4 $cm^2V^{-1}s^{-1}$ [141]. These values are excellent compared to the 1400 $cm^2V^{-1}s^{-1}$ reported for silicon[142], but still 5-20 times lower

than the record mobility measured for SLG suspended 150 nm over Si/SiO_2[143]. In these devices, carrier mobility has shown to be almost independent of the temperature in the range 10-100 K, hence, pointing to defect scattering as the governing transport mechanism. Nonetheless, most SLGs prepared through bottom-up methods are nearly perfect crystals with a negligible density of defects compared to other semiconductors[144]. Although the pseudo-spin conservation rule ensures that complete backscattering is forbidden, this only contributes to rising the mobility by two-fold as large-angle scattering is yet allowed. Hence, the high mobility found at room temperature must be explained by a different type of phenomenology. In other conventional semiconductors (e.g. Si), optical phonon scattering dominates at room temperature.

In SLG, optical phonons are too energetic to participate at room temperature. Hence, the interactions between electrons and acoustic phonons (i.e. modes of vibration in its lattice) must govern its electrical behaviour. Acoustic phonons are known to cause the resistivity to increase linearly with the temperature at the rate of 0.1 $\Omega\ K^{-1}$. Thereby, pure electron-phonon scattering would intrinsically limit the room temperature mobility of SLG to a value of $2x10^5\ cm^2V^{-1}s^{-1}$ (at the limit carrier density of $1 \times 10^{12}\ cm^{-2}$)[145]. However, the exceptionally higher mobility found in suspended SLG[143], suggested that carrier scattering in supported graphene must also contain contributions from substrate features such as charge traps, interfacial phonons, substrate stabilized ripples, or fabrication residues[141, 144, 146].

In this respect, the adsorption of water and oxygen molecules leads to non-repetitive and large-hysteresis I-V curves for GFETs, thus, forcing electrical measurements to be conducted in a vacuum. Surface passivation with silicon nitride, hexagonal boron nitride, poly(methyl methacrylate), or aluminum oxide, is an efficient strategy to limit the interactions with underlying substrate features and impurities[147]. Through the modulation of electron-phonon interactions, different regimes of superconductivity can also be accessed by graphene. Theoretical studies by M. Calandra *et al*. showed that surface doping with alkaline metal ad-atoms may lead to the observation of superconductivity[148]. Another valid route towards superconductivity consists in the deposition of SLG onto electron-doped d-wave superconductors, such as $Pr_{2-X}Ce_XCuO$[149].

1.3.3. Optical

Graphene can absorb radiation from different regions in the electromagnetic spectrum through unique optical transitions. This ability comes from its particular electronic structure which includes the lack of bandgap and the interaction between radiation and

Dirac fermions in the sheets. Indeed, it is the absence of discrete energy band levels (like in most semiconductors) that ensures radiation being absorbed independently of its frequency. While radiation in the visible (Vis) to near-infrared (NIR) region is known to induce intra-band transitions, absorption in the far-infrared (FIR) occurs through either intra-band transitions or free carrier absorption mechanisms. Atomically thin graphene is known to be highly transparent in the Vis. Nair *et al*. illuminated individual sheets of suspended SLG under a white beam and found that up to 97.7% of the incident light was transmitted through them[105].

Although it may seem poor, this is a still remarkable absorption considering that SLG sheets are only 0.335 nm thick. Furthermore, the authors demonstrated that absorption is merely determined by the fine structure constant ($a=e^2/hc$, with c being the speed of light); a fundamental parameter in quantum electrodynamics that accounts for the coupling between light and relativistic electrons. As might be predicted, the optical transparency of graphene is highly sensitive to the number of layers in the sheets/flakes. As shown in Fig 1.13, opacity increases linearly as the number of layers is raised. Nair and his co-authors also found that each atomic layer in FLG contributes to an additional 2.3% increase in absorbance[105]. This finding has inspired the development of microscopy/optical spectroscopy methods for the counting of graphene layers on transparent substrates[150].

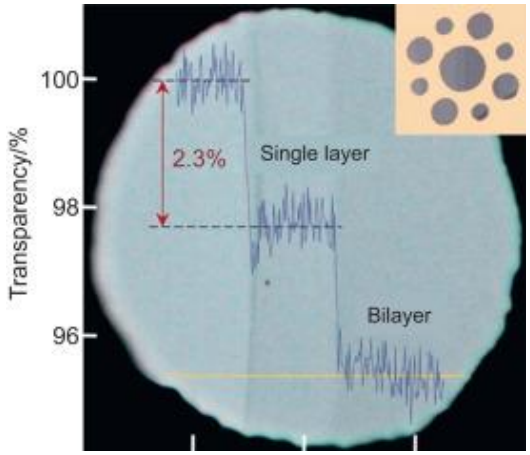

Fig. 1. 13: *Transparency of graphene (adapted from reference[105]).*

Optical transitions in graphene may also be induced by electric fields (*aka* gate-dependent optical transitions often used in electronics to modulate the current)[151]. Under an applied field, the low density of states near the Dirac point causes the Fermi level to shift. This change dictates how much radiation is absorbed in the IR by graphene. This mechanism allows for the tuning of the optical transmission of an electromagnetic radiation source and is more relevant to SLG (as discussed above, the presence of more than one atomic layer significantly alters the absorption properties and the ability to tune the

absorbance). PG can also undergo photoluminescence upon illumination with NIR lasers. This was an exciting finding as common photoluminescence mechanisms involve the excitation of electrons to a higher energy band (during the absorption of radiation) and their return to the ground state through the release of photons.

However, in zero-gap graphene, the broad emission of light emerges as a direct consequence of femtosecond laser excitation. The high temperatures induce a transient regime in which the electron distribution is driven strongly out of equilibrium, thus, creating thermalized carriers. Hot electrons interact with strongly coupled optical phonons (through phonon absorption and/or emission mechanisms) and, then, decay to the ground state emitting radiation[152]. For non-pristine graphene, only conventional photoluminescence can be observed whether a bandgap is opened through chemical functionalization or cutting it to smaller sheets exhibiting quantum confinement (usually referred to as graphene quantum dots, GQDs)[153]. Because of the great combination of high transparency and excellent conductivity, SLG and FLGs have become a valid alternative to conventional transparent electrodes such as indium- or fluorine-doped tin oxide (ITO and FTO, respectively) to serve in optoelectronic devices like light-emitting diodes (LEDs), photovoltaic cells (PVCs), etc. On the other hand, their unique optical transitions and the ability to absorb radiation over a wide range of frequencies have shown a great potential in optical and photonic applications (from saturable absorbers to high-bandwidth photodetectors, etc)[154].

1.3.4. Thermal

As with mechanical and electrical properties, heat conduction is also highly anisotropic in graphene. In this sense, the flow of heat through the basal plane of SLG is about 100-fold greater than the out-of-plane flow.[155] The main reason for explaining such behaviour is the weak interfacial coupling that rules in that direction (as opposed to the strong sp^2 bonding governing in the plane). As discussed in section 1.3.2, the high mobility of carriers at room temperature in SLG results from the interaction between electrons and lattice vibrations. But phonons are also involved in the mechanism of heat conduction in the basal plane (more specifically long-wavelength phonons). Their mean free path is only limited by the sample size and exceptionally high values in the range 100-600 nm have been measured for supported/suspended samples of SLG in the submicron scale.[156, 157,158]

As a consequence, a significant fraction of the theoretical ballistic heat flow limit becomes achievable at room temperature for suspended SLG (>80% in samples with a length below 235 nm)[155] and a maximum in-plane thermal conductivity of 5.3×10^3 $Wm^{-1}K^{-1}$

has been measured.[106] This value is about twice the conductivities reported for some of the best thermal conductors such as CNTs or individual diamond crystals[159, 160] and exceeds those found for materials like graphite or copper by about 10-fold[110]. Hence, graphene is postulated as one of the best materials available for thermal management. Unfortunately, the heat flow decreases when the sheets are in contact with a substrate (supported SLG), size-confined (as in GNRs), or present more than one layer (FLG). This behaviour is not unexpected, given that phonon propagation is very sensitive to surface or edge perturbations.

In line with this reasoning, SiO_2-supported SLG has exhibited in-plane thermal conductivities around 600 $Wm^{-1}K^{-1}$[1161]. Such a large decline emerges from the coupling and scattering of graphene phonons with substrate vibrational modes and the consequent reduction of the mean free path[162]. In GNRs, phonon scattering with boundaries and edge roughness is responsible for an even more pronounced decay to values in the order of 80 $Wm^{-1}K^{-1}$ (as measured for 20 nm wide GNRs)[163, 164]. Molecular dynamics simulations by F. Hao *et al.* illustrated how the introduction of only a 2-4% of monatomic and Stone-Wales vacancies in the plane may induce a reduction in thermal conductivity of up to 95%[165]. Despite all these effects, atomically thin graphenes still retain a relatively high thermal conductivity at a size regime where other materials cannot conduct heat as effectively (e.g. lower thermal conductivities of 25 and 2 $Wm^{-1}K^{-1}$ have been reported for silicon and silicon nanowires, respectively)[166, 167].

1.3.5. Chemical

As discussed in previous sections, the strong in-plane covalent sp^2 bonding imparts high mechanical and thermal stability. These properties evoke thoughts of very limited chemical reactivity at perfect graphene sheets. However, graphene also has the highest ratio of edge atoms amongst all carbon allotropes. Edge, functionalized, and/or defective sites are known to present enhanced chemical reactivity compared to those at the perfect basal plane[168]. Moreover, like in no other solid material, the unhybridized p_Z orbitals of every C atom in the structure are fully available for chemical functionalization on both sides of the sheets.

As a consequence of these characteristics, SLG has been shown to burn at temperatures as low as 350 ºC[169]. In the same context, G. Diankov *et al*. found that SiO_2- and mica-supported SLG are about 100 times more reactive to ionized hydrogen plasma than their bi-layered and thicker counterparts[170]. While SLG suffered from severe isotropic hole formation in the plane and etching from the edges, a negligible impact was shown for

FLG treated at 400 ºC. As detailed in the next subsections, a wide variety of derivatives have been prepared via chemical functionalization of graphene with oxygen (O), nitrogen (N), sulfur (S), and other heteroatoms.

1.4. Graphene Derivatives

1.4.1. O-Doped Graphenes: GO & rGO

As described in section 1.2.2.3, GO is an oxygenated analogue of PG which can be produced and processed from solution, thus, constituting one of the 2D materials with greater potential for industrial applications. From a structural point of view, it consists of a single sheet of GRO containing a mixture of sp^2- and sp^3-hybridized C. The content of O-groups in GO is highly dependent on the preparation methods and the experimental conditions. Most of these methods cannot control the extent of the oxidation processes locally and yield non-uniform distributions of O-groups at the surface. For these reasons, an unambiguous consensus model that accurately describes the chemical structure of GO has yet to emerge. Earliest models were based on repeat units forming regular lattices (Fig 1.14)[171].

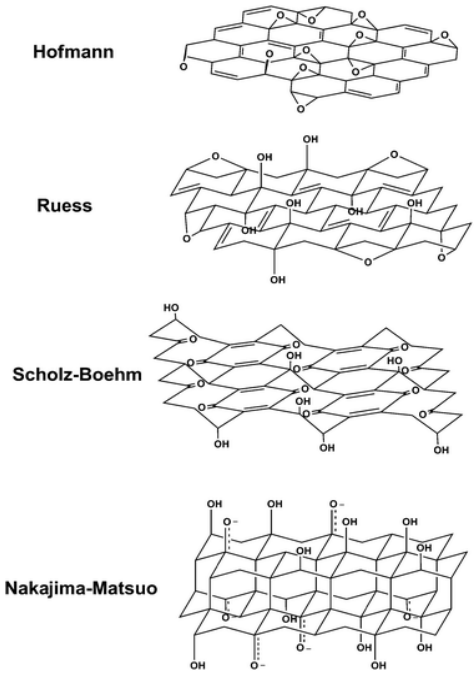

Fig. 1. 14: *Evolution of the structural models proposed for GO (adapted from reference [171]).*

This concept was abandoned and contemporary models have focused more on the non-stoichiometric and amorphous nature of the material. Amongst them, the most widely accepted was proposed by Anton Lerf and Jacek Klinowski (Fig 1.15). By reacting GO with

different species, and analyzing the products with solid-state nuclear magnetic resonance (NMR) spectroscopy, they outlined most of the fundamental structural features of GO[172, 173]. Cross polarization/magic angle spinning (CP/MAS) experiments displayed broad 13C NMR peaks at 60 and 70 ppm which were assigned to tertiary alcohols and epoxy (1,2-ether) groups, respectively[172]. In a posterior revision, -COOH groups were also incorporated in the periphery of the graphitic platelets[173]. Nonetheless, slight modifications have been introduced during the last decades under the light of recent observations.

During the first stages of GR oxidation, epoxy (-COC-) and -OH groups are preferentially attached to C atoms in the basal plane (and, to a less extent, also to peripheral atoms)[174-177]. Using atomic layer deposition of TiO_2, XPS, and TEM data, D. S. Shin *et al.* concluded that these groups do not distribute uniformly on the plane but in the form of islands[178]. Further analysis by density functional theory (DFT) unveiled that the particularities of the binding energetics determines this behaviour. As the oxidation proceeds, ether groups (-C-O-C-) are introduced in the plane and semiquinones can be found at edge and/or defective sites. The continuous increase of the ether-to-epoxy ratio during the oxidation process has led to suggest that –C-O-C- are introduced in the plane through the unzipping of –COC- groups (a process that would be driven by the local strain induced by O adatoms)[174].

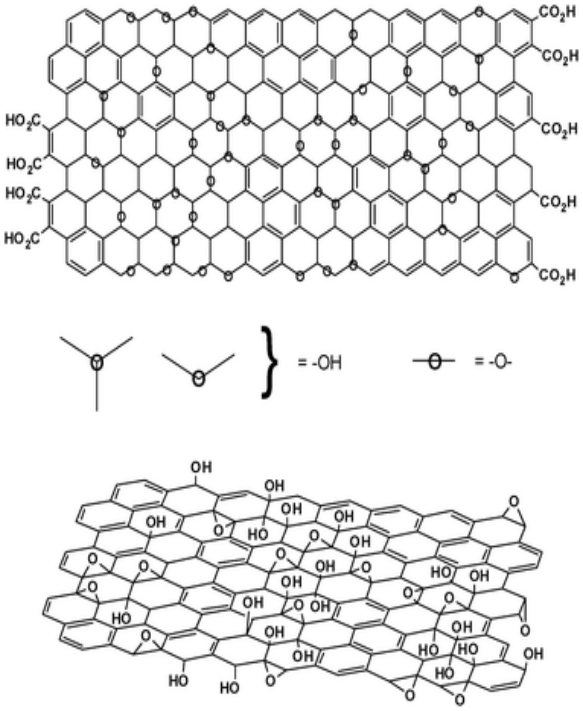

Fig. 1. 15: *Two representations of the model proposed by Lerf and Klinowski for GO (adapted from reference[171]). The structure at the bottom corresponds to the model as originally proposed in 1996.[172] The top structure shows a revision published shortly after.[173]*

In addition to the peripheral -COOH groups considered in the first revisions of the Lerf–Klinowski model (top illustration in Fig 1.15), edge sites are also prone to be

functionalized with >=O, -C-O-C-, cyclic esters (-CO-O-), and –OH groups.[171, 175-177, 179] In 2013, A. M. Dimiev *et al*. stated that none of the structural models proposed before could adequately explain the acidity found for aqueous solutions of GO[150]. To tackle this question, they proposed that the O-composition is not static but instead dynamic. The experimental evidence showed that GO does not contain significant amounts of preexisting -COOH groups. In such a dynamic model, -COOH groups are gradually formed and, in general, the O-content is constantly changing due to interactions with water molecules. O-groups modify the nature of the Van der Waals interfacial interactions turning GO into a much more hydrophilic material than PG[180].

First-principles calculations by J. J. Hernández-Rosas *et al*. have shown that the dipole moment of PG grows from 0.02 to about 6.5 D after decoration of the structure with only a 0.5% of O-groups[181]. Such an improved hydrophilicity allows for GO to form stable aqueous dispersions and establishing stronger interfacial interactions (e.g. with polymer matrices)[182]. This is an important advantage for applications in drug delivery[183, 184], sensors[185, 186], capacitors[187], photocatalysis[188, 189], batteries[190] and structural nanocomposites[191, 192]. The calculations also pointed out that the introduction of -OH and -COOH groups in the basal plane trends to bend the surface of the sheets slightly compared to PG (Fig 1.16).

DFT calculations by S. Abdelaal *et al*. using the universal force field (UFF) potential went further to demonstrate that O-groups affect the local surface flatness in their vicinities[193]. The induced undulations were shown to extend along the surface for distances of up to 50 nm (depending on the introduced O- groups). Interestingly, this effect is screened in the surrounding of H atoms at –COOH and –OH groups (see Fig 1.17). As it has been discussed, O-functionalization reduces the ratio of sp^2-to-sp^3 atoms which, unavoidably, affects the physical properties of graphene by different extents. Electrical properties are dramatically affected to the point that GO behaves as an insulating material with sheet resistances as high as 9 GΩ sq^{-1})[171, 194, 195]. The thermal conductivity is also reduced by a 50% compared to PG[196].

As pointed in the calculations of Hernández-Rosas *et al*. the electronic structure of GO can be slightly tweaked through the control of the O- composition. The bandgap was proven to be either increased or reduced by selective removal of >=O and -OH groups, respectively. Thereby, transitions from semi-metallic to semiconductor behaviour (and vice versa) could be potentially induced in GO. Unfortunately, as noted above, most of the available thermal and chemical experimental methods are not selective enough in terms of the introduced groups and, thus, do not allow fine-tuning its composition. Regarding the mechanical properties, the decline is less dramatic. This is well illustrated by the reduction in Young´s modulus towards the 200 GPa, which is still higher than most materials and

justifies the extensive exploration and massive application of GO as a mechanical reinforce in (nano)composites.

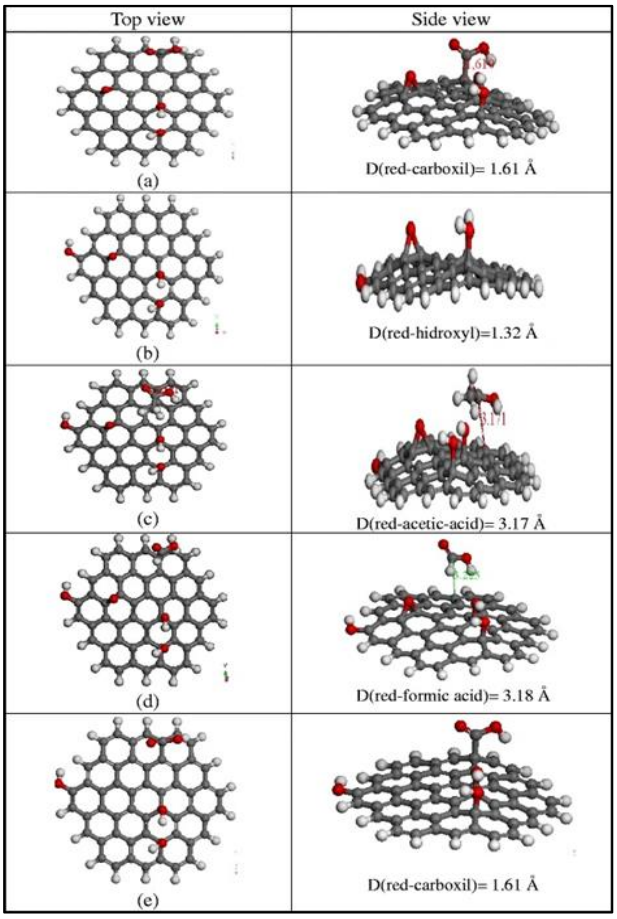

Fig. 1. 16: Optimized DFT structures of GO containing different distribution of O-groups (adapted from reference [181]).

Hernández-Rosas´s calculations also confirmed that GO is more chemically reactive than PG[181]. Regions surrounding edge -COOH groups were shown to be more susceptible to receive electrophilic attacks than those on the basal plane. This finding was explained by the electron-withdrawing character of -COOH and reveals that chemical reactivity is strongly localized at the periphery of the system. More recently, S. Abdelaal *et al*. reported kinetic measurements on the reactivity of GO towards Ni^{2+}, Cd^{2+}, and Pb^{2+} (pH range: 2-9)[193]. Surface saturation was reached at pH 6.0 for all three cases (hydroxides precipitate at higher values). Considering that minimum values of zeta-potential were also reported to fall at pH~6[197], this finding was interpreted as indicating that surface reactivity is governed by the O-composition.

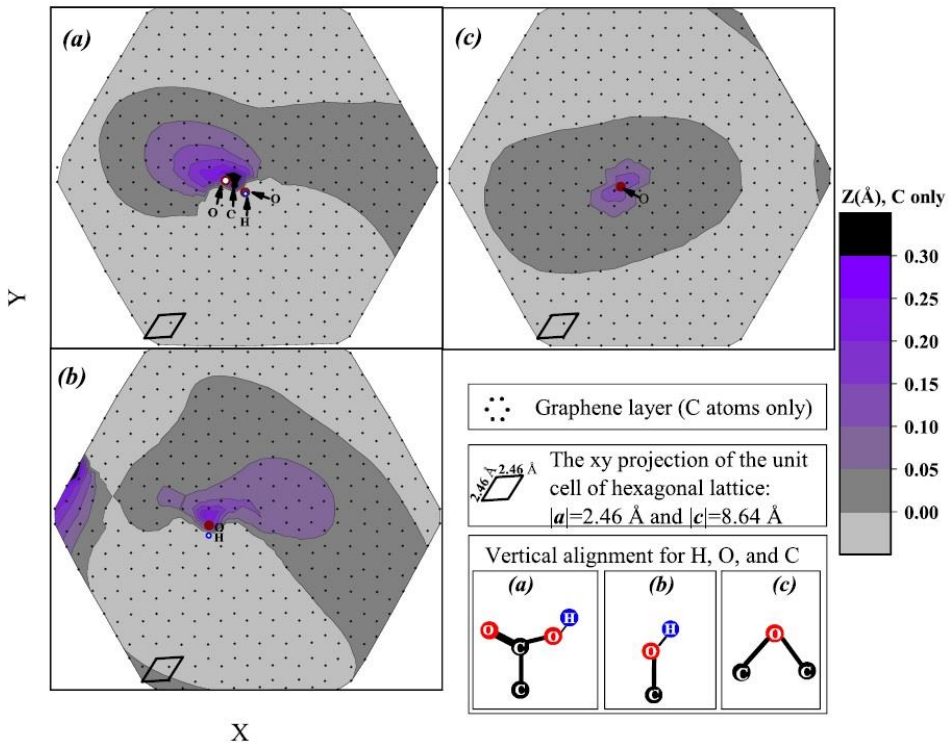

Fig. 1. 17: *Optimized DFT structures for SLG containing isolated O-groups. The configurations were calculated using the universal force field, UFF, potential (adapted from reference [193]).*

It was also argued whether the saturation loadings would rise by increasing the degree of oxidation (DO) of GO because of the introduction of greater amounts of active sites (i.e., O-groups deprotonated and negatively charged at such pH). This reasoning would be backed by the decrease observed in zeta-potential after rising the O-content from 23% (-35 mV at pH 6.0) to 34% (-50 mV)[197]. D. V. Stergiou *et al*. (University of Ioannina, Greece) investigated the electrocatalytic properties of GO towards the oxidation of ascorbic acid (AA*, aka* vitamin C)[198]. Using a glassy carbon electrode (GCE) coated with GO (GCE/GO), the oxidation over potential was lowered by up to 350 mV compared to GCE/rGO, GCE/DLEG, and bare GCE. The C/O atomic ratio was shown to be a critical parameter determining the electrocatalytic behaviour.

Accordingly, the GO with the lowest O-content exhibited the highest catalytic activity towards AA. Similar behaviour was found for GR screen printed electrodes (SPEs) modified with GO towards β-nicotinamide adenine dinucleotide (NADH) and AA[199]. The electrocatalytic properties were ascribed to–OH, >=O, and –COOH residues. Although these groups were already present in the as-prepared GO, it was demonstrated that only became active when the electric resistivity was decreased significantly. To this end, the authors diminished the O-content in the sheets (just as pointed in the work of Stergiou *et al*. by electroreduction of SPE/GO to SPE/rGO. It is worth mentioning that

electrochemical methods allow for a more precise control of the DO than other thermal or chemical procedures[198].

In conclusion, although O-groups are needed to exhibit meaningful catalytic or electrocatalytic properties, the electrical conductivity of the sheets must be also recovered to some extent. For these reasons, rGO was described in section 1.2.2.3 as a better-balanced material than GO, or even PG, for (electro)catalytic and electrochemical applications. rGO exhibits intermediate properties between those of PG and GO (with the reduction process strongly influencing the outcome)[200]. As discussed in ref.[198, 199, 201], the electrical properties can be tuned through the control of the degree of reduction (DR) of GO: i.e. the more O-groups on the sheets the higher the electrical resistivity and vice versa. Analogously, the optical properties can also be tweaked through the control of either the DR of GO or the DO of exfoliated graphenes and/or rGO.

The latter approach was implemented by Md T. Hasan *et al*. by ozone-induced oxidation of rGO[171]. By increasing the time of exposure to the ozone gas, an increase in solubility and concomitant alterations in the optical properties of rGO were observed. The changes involved the continuous bleaching of absorption in the Vis and the appearance of the broad fluorescence emission centered in the green (λ~520 nm). The intensity of emission and the position of the absorption transitions were controlled by adjusting the time of exposure to ozone and successfully reversed via thermal processing. R. Maiti *et al*. investigated the controlled reduction of GO via photothermal reduction using NIR radiation[202]. With increasing the reduction time and the power density, the intensity of the yellow-red fluorescent emission (found at ~610 nm for the starting GO and ascribed to the –OH and –COC- groups), was found to decrease progressively.

All this evidence proves that the reduction of GO has a strong impact on its electrical properties and optical behaviour. Carrier mobility is recovered to values of 0.5-200 $cm^2\ V^{-1}s^{-1}$ (as a function of the method and the DR)[62]. These figures are about 100-fold lower than those obtained for supported CVDGs but are still competitive with those exhibited by DLEGs (and certainly much better than those for GO). On the other hand, mechanical and thermal properties are very slightly affected by its reduction to rGO. AFM-based nanoindentation measurements indicated that the average Young´s modulus of single-layer rGO falls within the same order of magnitude than GO (0.25 vs 0.2 TPa) and is only half of that reported for FLG (0.5 TPa)[175].

R. Aradhana *et al.* recently published an interesting paper investigating the roles of GO and rGO as additives in epoxy nanocomposite adhesives[176]. The mechanical, thermal and electrical properties of the composites were determined as a function of their graphene content. The results showed very similar improvements in the mechanical and thermal properties of the adhesive by incorporation of either 0.5 wt% of GO or rGO. For

instance, the adhesive strength (evaluated from shear strength data) was improved by 50 and a 44%, respectively. The tensile strength at break rose from 47.5 MPa for the pristine adhesive to 72.05 MPa (52% higher) and 62.02 MPa (31%) for the GO- and rGO-containing samples, respectively. Interestingly, while GO increased the volume and surface resistivity of the composites at any wt%, rGO induced a decrease of 26% and 83% in both parameters.

The thermal properties followed similar trends. In good agreement, the enhancement measured in the conductivity at 30 ºC was only slightly higher for the GO-containing adhesive ($\kappa_{30ºC}$ increased by 211% vs the 139% registered for the rGO sample). This behaviour was verified at different temperatures in the range 30-90 ºC. Hence, although GO seems the best choice when targeting improved mechanical and thermal properties in composites, rGO is also good enough for those purposes but also brings enhancements in the electrical properties. For this reason, rGO must be a better choice in applications where high electrical conductivity matters.

The structure of rGO prepared with low-to-moderate DR (C/O ratio in the range 8-100) is known to consist of nanometric sp^2-graphitic islands isolated amongst domains of oxidized graphene[203]. Thus, it may behave like an insulator for low DR or like a conductor for moderate-to-high DR (C/O ratio in ranging from 100 to 240)[203, 204]. SEM and TEM images have shown that, contrary to the few-layer and curved nature of GO, rGO sheets are layered, flat and entangled with each other, and often do form stacked lamellar superstructures[177, 205]. As discussed in section 1.2.2.3, rGO can be synthesized from GR through a variety of approaches (see Fig.1.14). But despite the great efforts to achieve perfect conditions to prepare rGOs with the closest properties to bottom-up PG, producing single-layer and low-defect forms of rGO in bulk quantities is just quite hard[79, 84].

1.4.2. Other Heteroatom-Doped Derivatives

The structure and properties of carbon materials can be effectively tailored through doping with heteroatoms. The replacement of C by nitrogen (N), sulfur (S), or Boron (B) atoms in the lattice has the potential to significantly alter the properties and performance of graphene-based materials. Heteroatom-doped or co-doped graphenes (HDGs) have gained increasing attention due to its enhanced physical, chemical, and biological properties compared to PG. The synthesis of N-doped graphene (NDG) was first reported by two independent groups from the United States and China[182, 194]. In the first study, K. Gong *et al*. found an excellent catalytic activity towards the oxygen reduction reaction (ORR) in the cathode of fuel cells. This finding suggested potential applications in the

replacement of scarce catalysts (such as Pt and Pd noble metals) in fuel cells[194] and stimulated novel lines of research for heteroatom-doped 2D materials.

The most common procedures for the synthesis of NDG are classified in one-step (CVD, solvothermal, flame treatment, etc) and two-steps methods (thermal annealing, pyrolysis, wet chemical synthesis, and microwave-assisted approaches)[183]. Typical precursors employed in the CVD methods include NH_3 (N source), pyridine or polypyrrole (C sources), and metal catalysts (Ni or Cu). The N-contents achieved by this method vary from 0.25 to 16.7 at%[184]. Three common configurations are usually obtained in the doping of graphene with nitrogen: pyridinic N, pyrrolic N, and graphitic N. The pyridinic N structure becomes more favorable as the N-content increases and that plays a major role on the enhancement of the electrocatalytic activity and energy storage performance[185]. Owing to its simple and scalable characteristics, thermal annealing of GO in ammonia (NH_3) or urea atmospheres is also employed.

Under this approach, the N-content is directly correlated with the annealing temperature and reaches typical values in the range 1.1-10 at%[183]. Reduction of GO by N_2H_4 is another suitable route towards NDG. N-contents as high as 7.2 at% have been achieved and even exceeded (8.9 at%) whether a mixture of NH_4OH and N_2H_4 is used as source of N[186]. Autoclave-based hydrothermal and solvothermal methods using NH_3 and other precursors (e.g. urea, lithium nitride or cyanuric chloride) have become popular because of its potential to yield NDGs with superior N-contents of up to 28 at%[187, 188]. These methodologies have been adapted for the synthesis of other doped or co-doped HDGs. For instance, sulfur-doped and boron-doped graphene (SDG and BDG, respectively) can be synthesized via CVD, thermal, or solvothermal procedures.

For the synthesis of SDG, typical precursors include H_2S, SO_2, or CS_2 in gas phase[189, 190] and liquid species such as thiourea, dibenzyl disulfide, ammonium thiocyanate, or dimethyl sulfoxide[191, 192]. In the case of BDG, the most common procedures are based on thermal and solvothermal methods in presence of boric acid or borane as the B source[195, 206, 207]. Co-doping can be achieved through the control of the ratio of the different sources of heteroatoms[191, 195]. Due to the changes induced in the electronic structure, surface site geometry, and morphology of PG; HDGs have exhibited improved performance in electroanalysis[203], electronics (GFETs[201, 205], LEDs[208], etc), energy storage[204, 207], charge transport[200], and other applications[209]. In particular, applications as electrocatalysts for the ORR process in renewable energy devices have been widely discussed[189, 194, 210, 211].

DFT simulations showed that N-sites in NDGs are endowed with higher spin and/or charge density (n-doping) which increase the electrocatalytic activity towards ORR[210],

S-sites in SDGs behave similarly. Because S has more electrons than C (and N) enhanced n-doping effects can be expected.

On the other hand, B-doping can be regarded as a type of p-doping[201]. Q. Liu *et al*. showed that NDG can catalyse ORR at levels equivalent to those of Pt/C in alkaline medium and very close to Pt/C in acid medium[211]. In line with these observations, Qu *et al*. recorded current densities 3 times higher than those at a Pt/C electrode (Fig 1.18)[212]. It is also worthy to note that HDGs are significantly more stable than Pt/C catalysts against methanol oxidation[206, 211]. Co-doped graphenes (mainly those of N with B or S) have also been applied as metal-free electrocatalysts for ORR and other catalytic processes of interest[213-215].

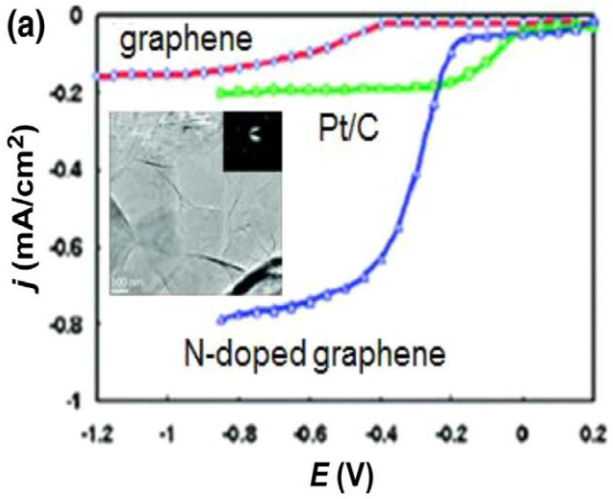

Fig. 1. 18: *Cathodic scans recorded at 1000 rpm and 0.01 V s^{-1} for NDG- and Pt/C-modified rotating ring-disc electrodes (RRDE) in air-saturated 0.1 M KOH (adapted from reference [212]).*

Often HDGs serve as supporting materials for other nanostructures (e.g. Pt, MnO, TiO_2, or Fe_3O_4 NPs). Their roles in these hybrid conjugates consist of enhancing the electrical conductivity, prevent aggregation phenomena, and improve the structural integrity of the nanomaterials. Examples of applications of HDGs as electrocatalysts in relevant reactions other than ORR[206, 216, 217] and in lithium-ion and sodium-ion batteries (LIBs and SIBs)[195, 201, 218, 219] are also abundant in the literature. For instance, LIBs equipped with NDG- and SDG-based anodes have exhibited reversible discharge capacity as high as 1043 and 870 mA·h·g^{-1} (at charge/discharge rates of 50 and 370 mA·g^{-1}, respectively) which is 2-3 times higher than that found using PG-based anodes.[204, 206] Besides providing good conductivity, the properties of NDG and SDG allow for an enhanced anchoring of Li^+ via intercalation with doped sites (e.g. at pyridinic and pyrrolic N-sites at NDG)[204].

This turns NDGs into superior anode materials for LIBs compared to other conventional anode materials[204, 217]. Early studies also pointed that B-substituted carbons can store more Li^+ than pristine carbons[218]. However, the electrophilic nature of B-sites

(compared to N or S-doped sites) results in a weaker adsorption of Li ions. To illustrate this point, a discharge capacity of 548 $mA \cdot h \cdot g^{-1}$ was registered at 100 $mA \cdot g^{-1}$ for a LIB prepared with a BDG anode (B-content: 5.9 at%)[195]. Such a performance falls below the capacities mentioned above for NDG or SDG-based LIBs (at similar rates). Analysis of the results obtained at higher rates of 1 $A \cdot g^{-1}$ indicated a higher capacity for the BDG-cell compared to the PG-cell (231 vs 139 mAh g^{-1}, respectively). Nonetheless, when graphene is co-doped with N and B (BNDGs), enhanced storage performances are registered as reported by Panchakarla and his co-workers[219]. After B-N co-doping, the systems exhibit a combination of *p*-/*n*-type semiconducting behaviour[220]. The radius of Na^+ is about a 55% larger than that of Li^+[221]. which turns the rapid intercalation/extraction of Na^+ more difficult in HDGs and may compromise their structural integrity in SIBs[222].

3D HDGs have also been used as anode materials in SIBs with excellent performance. Different authors have reported unusually high initial reversible capacities of up to 852.6 $mA \cdot h \cdot g^{-1}$ at 500 $mA \cdot g^{-1}$ (with long-life cycle stability)[223-225]. Such a superb performance was attributed to the synergistic effects converging at these materials. The combination of a 3D mesoporous structure and the physicochemical properties endowed by N-doping do facilitate the diffusion of the large-size Na^+ ions, enhance their storage, and minimize detrimental volume expansion effects during discharge–charge processes.

HDGs have also found applications as supercapacitors. Due the high surface-to-volume ratio of graphene and the changes introduced in its electronic structure by H-doping, applications have focused in the fabrication of double-layer capacitors. The defective nature and the enhanced electron density of N- and S-sites in n-doped NGDs and SDGs favors the adsorption of positively charged species (or cations), thus, enhancing the materials capacitance. On the other hand, the more electrophilic nature of B-sites can be exploited for an increased storage of electrons (or anionic species). Jeong *et al*. prepared supercapacitors based on NDG through a facile plasma process[226]. The measured capacitance was about 4 times larger than that for an analogous PG supercapacitor. However, all the synthesis methods cannot produce NDGs suitable to serve in double-layer capacitors. Qiu *et al*. demonstrated that the more defective the NDG the higher capacitance are achieved[227]. Hence, thermal or hydrothermal doping methods are preferred for these purposes.

1.5. Analytical Applications

Since the discovery of graphene and its remarkable electrical, mechanical, and chemical properties, graphene and its derivatives have been extensively applied in a

plethora of fields of science and technology, including as sensors, transistors, flexible electronics, energy storage, water purification membranes, anode for li-ion battery, supercapacitors, solar cells, composite materials and so many others applications[228]. In the following section, we emphasize the use of graphene and its derivatives towards the development of electrochemical biosensors.

1.5.1. Graphene in Biosensors

According to the International Union of Pure and Applied Chemistry (IUPAC), a chemical sensor is a device that transforms a chemical event into a signal of analytical utility[229]. Chemical sensors contain two main elements: the chemical recognition system, also known as the receptor, and a physicochemical transducer that converts the chemical information into a measurable physical signal. Receptors can be made of any organic or inorganic material that specifically interacts with a single analyte or a family of them, from organic/inorganic molecules and macromolecules to whole cells or microorganisms. In the case of biosensors, the receptor is often a biomolecule (e.g. DNA, aptamers, antibodies, enzymes, etc.) that has a high affinity for certain types of compounds. Therefore, a biosensor is a chemical sensor in which the recognition of the analyte occurs through a biochemical process (Fig. 1.19)[230].

In recent decades, most efforts have been devoted to improving the performance of chemical biosensors. Due to its excellent properties, graphene has been investigated as a new transducer material in electrical (GFETs, photodetectors), electrochemical, and optical (bio)sensors. To convert the interactions between receptor and analyte into a measurable signal, the receptor must be in contact with the transducer´s surface so that efficient transfer of charge/mass/radiation occurs between both of them[231, 232]. In this context, the most common methods to immobilize biomolecules on the surface of graphene can be covalent, such as in the case of antibodies and DNA (through the wise use of click chemistries such as that based on EDC/NHS activation) or by mere physical adsorption without the formation of new bonds (as usual in the case of enzymes)[230, 231].

The fabrication of biosensors incorporating graphene and derivatives (GO, rGO, HDGs, etc.) has been widely researched due to the large surface area (ideal for the immobilization of large amounts of receptors: enhanced loading capacity) and high electrical conductivity expected for these materials[233]. The high density of carriers in the hexagonal lattice of PG facilitates the transfer of electrons between the transducer and the receptor, thus, producing very sensitive signals for applications in electrochemical sensing[231, 234, 235]. Furthermore, the use of graphene as a transducer may also improve the

compatibility with active biomolecules. For instance, it is well-known that proteins readily lose their functional structure after contact with metal and other material surfaces and, thus, graphene could act a powerful material in keeping the functional features of proteins[236, 237].

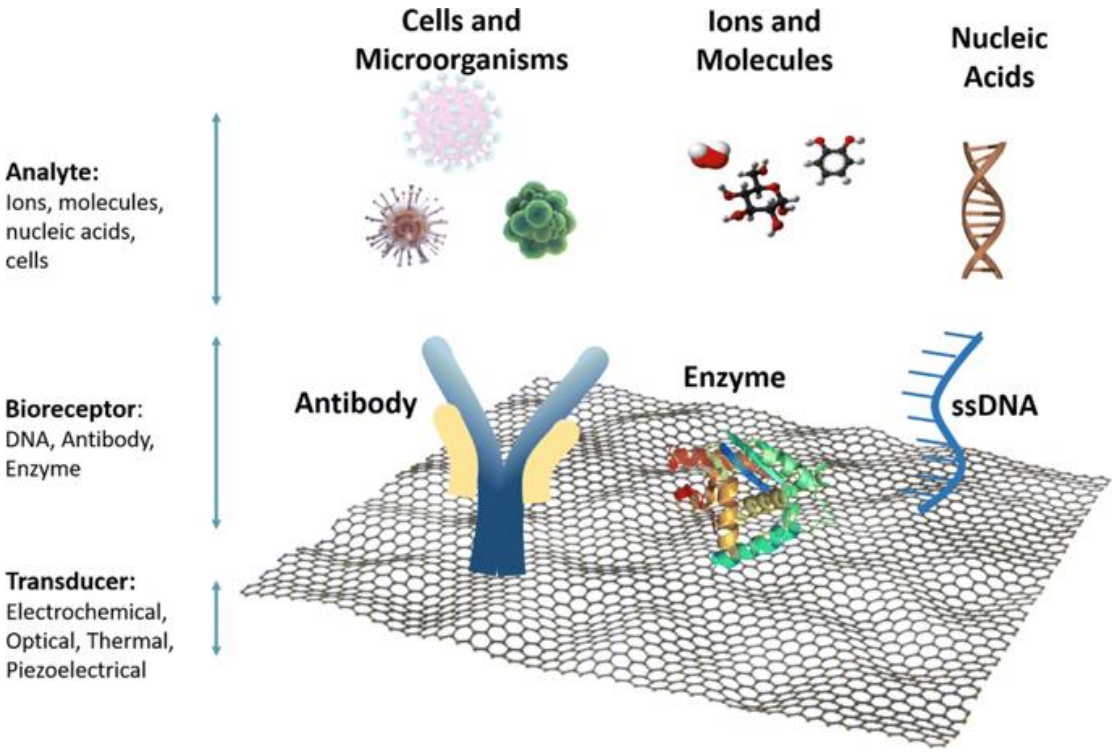

Fig. 1. 19: Examples of biosensors build from different building blocks on a graphene platform (adapted from reference [230]).

The particular properties of each derivative must be taken into account since it may affect the outcome of the sensors:[230]

- The density of defects and functional groups, arising from the different methods of preparation and/or doping, will intrinsically affect the sensor performance.

- Functional groups at graphene sheets may interact directly with the target molecule. Hence, the inhibition of the unspecific binding of the analyte to the transducer could be relevant.

- Intimate bonding between the receptor and graphene sheets could be affected by parameters such as the number of layers, the degree of functionalization, and the redox states of the functional groups.

- The physical orientation of the immobilized receptors is another parameter that can affect the selectivity and sensitivity of the sensor.

When all these factors are taken into consideration, graphene-based biosensors usually exhibit high sensitivity and selectivity, as well as good stability and fast response times.

1.5.2. Electrochemical Biosensors

The development of ultrasensitive and highly selective biosensors for accurate analyte monitoring has received much attention in recent years due to its great potential in the fields of healthcare, environment, food safety, among others. In the last decades, sensors with various forms of detection, including spectroscopic, chromatographic, colorimetric, photochemical, electrical, or electrochemical processes, have been widely developed. Electrochemical sensors figure prominently among the aforementioned detection methods due to their intrinsic capabilities, namely rapid analysis, great robustness, ease of use and simplicity, low cost, and excellent sensitivity. Moreover, they are also highly advantageous since require small sample aliquots[238]. Electrochemical biosensors convert the physicochemical interactions between analyte and receptor biomolecules into electrical signals. Depending on the registered parameter, these can be classified as:

- Amperometric (electric current);
- Potentiometric (electrode's potential);
- Impedimetric (electrode's impedance for electron transfer);
- Conductometric (medium conductivity).

The application of nanomaterials and nanocomposite materials in analytical platforms has contributed significantly to the development of biosensors. Due to their chemical and electrical properties, graphene derivatives (e.g. GO, rGO, HDGs, etc.) are prominent materials for applications in electroanalysis. In fact, the performance of these devices can be further improved by conjugation with other nanomaterials, including metal or metal oxide NPs. George *et al.* have recently discussed a wide variety of examples in which the performance of different graphene-based electroanalytical devices is enhanced by conjugation with different types of NPs (e.g. Au, Pt, MnO_2, ZnO, ZrO_2, etc.)[239].

Recently, new electroanalytical platforms based on graphene nanocomposites and their derivatives have been proposed. In particular, GO and rGO have been widely used for the design and development of biosensors due to their high content in O-groups and surface defects. These characteristics allow for the controlled nucleation and growth of metals, metal oxides, and semiconductors[240]. The following table summarizes the recent developments while using GO and rGO as the basis of electrochemical sensors.

***Table 1. 2**: Some examples of the recent studies that resort to GO and rGO-based nanocomposites for the development of electrochemical sensors*

Catalytic material utilised	Analytical target	Method	Linear detection Range	LOD	Ref.
nMo$_3$Se$_4$-rGO nanocomposite	cardiac troponin I biomarker	electrochemical	1 fM -100 nM	1 fM	[241]
rGO/AuNPs	L-tryptophan	electrochemical	0.5–500 µM	0.39 µM	[242]
g-C$_3$N$_4$-GO	pesticide	electrochemical	0.045–213 µM	8.3 nM	[243]
PtPdNPs-CP5[a]-RGO	bisphenol A	electrochemical	0.01 - 1000 µM	3.3 nM	[244]
PDA[b]-rGO)/Pd nanocomposite	Acetaminophen	Electrochemical	0.28 - 100 µM	0.087 µM	[245]
AuNPs/rGO	nitrite	Electrochemical	0.1 nM - 7 µM	0.1 nM	[246]
PANI-graphene microflowers	Cholesterol	Electrochemical	1.93 - 464.04 mg dL^{-1}	1.93 mg dL^{-1}	[247]
Graphene-β-Cyclodextrin	Cholesterol	Electrochemical	1 - 100µM	1µM	[248]
GO–MIP	Cholesterol	Electrochemical	0.1 M - 1 nM	0.1 nM	[249]
Graphene-NiO	Cholesterol	Electrochemical	2 - 40µM	0.13 µM	[250]
ZnO/rGO composite	catechol	Electrochemical	15 to 225 µM	47 nM	[251]
Graphene-Pcys[c]/Ni(OH)$_2$ nanocomposites	Glucose	Electrochemical	1.0 µM - 0.10 mM	0.35 µM	[252]
PtNPs-rGO	Glucose	Electrochemical	0.003 - 7.72 mM	1.8 µM	[253]
Mn$_3$O$_4$NPs/N-rGO	Glucose	Electrochemical	1.0 - 329.5 µM	0.5 µM	[254]
Au/CuONPs-rGO	Glucose	Electrochemical	1 µM - 12 mM	0.1 µM	[255]
SnS nanosheets - graphene	Cu^{2+}	Electrochemical	1.5 - 36.0 µM	0.02 µM	[256]
Fe$_3$O$_4$-rGO nanocomposite	DNA	Electrochemical	10 aM - 1 nM	2 aM	[257]
pyronin Y-graphene	Dopamine (DA)	Electrochemical	0.5 - 1020 µ*M*	0.15 µ*M*	[258]
rGO/Mn-TPP[d] nanocomposite	DA	Electrochemical	0.3 - 188.8 µM	8 nM	[259]

Catalytic material utilised	Analytical target	Method	Linear detection Range	LOD	Ref.
NiO/GO nanocomposite	DA UA AA	Electrochemical	2.0 - 60 μM 2.0 - 120 μM 40 - 700 μM	0.10 μM 0.14 μM 5.50 μM	[260]
rGO-AgNPs	H_2O_2	Electrochemical	0.002 - 20 mM	0.73 μM	[261]
PdNPs/TNM[e]-rGO nanocomposite	H_2O_2	Electrochemical	up - 12 mM	0.0025 μM	[262]
Graphene-CeO_2/AuNPs	H_2O_2	Electrochemical	1.0×10^{-3} mM - 10.0 mM	2.6×10^{-4} mM	[263]
rGO/FeNPs nanocomposite	H_2O_2	Electrochemical	0.1 μM - 2.15 mM	0.056 μM	[264]
AgNPs-rGO/CeO_2	H_2O_2	Electrochemical	0.5 μM - 12 mM	0.21 μM	[265]
GO/Nafion nanohybrid	lobetyolin	Electrochemical	1.0×10^{-7} - 1.0×10^{-4} M	4.3×10^{-8} M	[266]
AuNPs-rGO	methylmercury	Electrochemical	3 - 24 μM	0.12 μM	[267]
rGO-RuNPs	Methylparaben	Electrochemical	5.00×10^{-7}– 3.00×10^{-6} M	2.40×10^{-7} M	[268]
Pd/Fe_3O_4/polyDOPA-rGO	Nitrite	Electrochemical	2.5 - 6470 μM	0.5 μM	[269]
Co_3O_4/rGO/chitosan	Pb(II)	Electrochemical	1.0 - 200.0 nM	0.35 nM	[270]
AuNPs-rGO	sulfite	Electrochemical	$2.0 \times 10^{-7} - 2.3 \times 10^{-3}$ M	4.5×10^{-8} M	[271]
Nd_2O_5 NPs-GO	anti-cancer (raloxifene) drug	Electrochemical	0.03 - 472.5 μM	18.43 nM	[272]

[a] cationic pillar [5] arene (CP5); [b] PDA – polydopamine; [c] Pcys-poly cysteine; [d] TPP- tetraphenylporphyrin; [e] TNM- tert-nonyl mercaptan;

The conjugation of either GO or rGO with nanoparticles has been shown to extensively improve the performance of electrochemical biosensors since this platform exhibits excellent electrochemical behaviour, namely high surface area and active electron transfer sites[232, 273]. Many of these platforms were used to immobilize biomolecules, such as enzymes, antibodies and DNA to produce highly selective and sensitive of biosensors.

1.5.2.1. Enzyme-based electrochemical biosensors

Enzymes are biomolecules capable of catalysing a biological reaction that are composed of amino acids that generate globular proteins with 3D structure[274]. These biomolecules are present in the metabolism of all organisms and catalyse a large number

of reactions with excellent selectivity and efficiency. Due to these characteristic, enzymes have been the first molecular recognition elements used in biosensing[274].

An enzymatic biosensor can be defined as an analytical device that combines an enzyme as a bioreceptor with the physical transducer to produce a measure signal with high catalytic activity, selectivity, and specificity[274, 275].

Enzyme-based biosensors are usually of electrochemical nature since they have advantages over other types of sensors. For example, they have quick response without damaging the sample. The fundamental principle of an enzymatic electrochemical biosensors is based on two mechanisms for detection: the first consists in converting the undetectable form of an analyte to a detectable signal through the catalytic properties of the enzymes, and the second consists in the detection of analyte which inhibit or moderate the activity of the enzyme[230, 276]. Both mechanisms generate a detectable electrical signal at the sensor, permitting the quantification of a specific analyte. This detectable electrical signal corresponds to the concentration of the analyte molecule. This concentration signal can be determined by potentiometric (potential), impedimetric (charge) and amperometric (current) techniques. Fig 1.20 represents an example of an enzymatic biosensor[230].

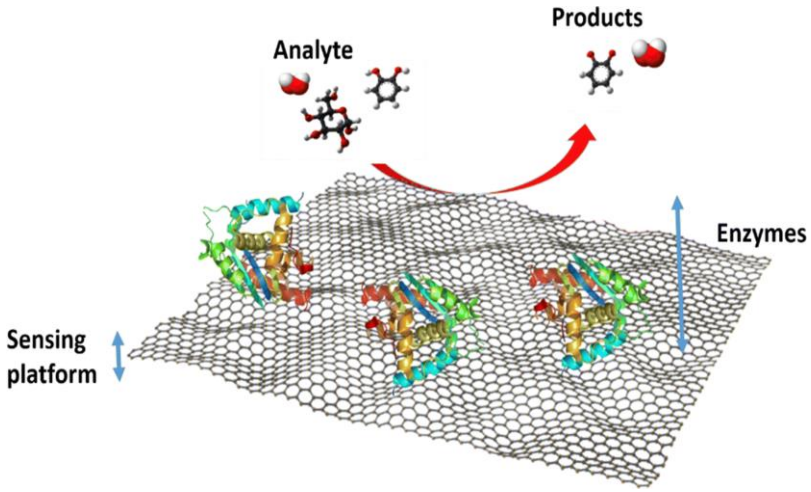

Fig. 1. 20: *Example of an enzyme biosensor (adapted from reference [230]).*

The performance of an enzymatic biosensor depends on the electron transfer between the electrode surface and the active site of the enzyme. Electron transfer can be performed directly or indirectly as showed in Fig.1.21. In order to achieve the direct electron transfer, an enzyme can be directly immobilized on the electrode's surface without the participation of a mediator or other reagents. However, the direct electrochemistry of redox enzymes on the electrode's surface is very difficult because the active site of most redox enzymes is located deeply in a hydrophobic cavity of the molecule and it can lead to the denaturation of the enzymes and, thus, affect the biosensor's response[277]. In order

to address this issue, nanomaterials have been widely used as mediators between the enzyme and the electrode, thus improving the stability, enzyme adsorption and enhance the direct electron transfer.

Graphene-based nanomaterials have exhibited excellent electrochemical behaviour as mediators for constructing enzymatic biosensors due to their outstanding properties, such as high electrical conductivity, large surface area, enhanced electrocatalytic activity and excellent electron transfer sites[273, 277, 278]. The use of GO and rGO-based nanomaterials as a transducer have shown to be an excellent material to allow the electron transport between the enzyme and the electrodes surface, as an optimum subtract to improve the stability and activity of the enzymes.

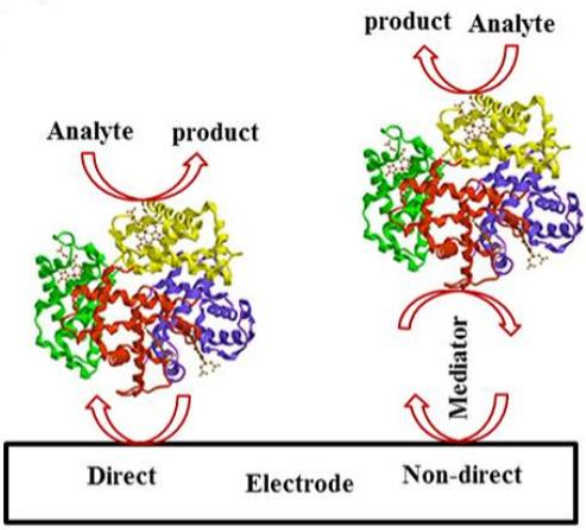

Fig. 1. 21: *Schematic representation of an enzymatic biosensor (adapted from reference [277]).*

1.5.2.2. Immobilization of enzymes onto graphene

Enzyme immobilization is characterized by the process of fixing this biomolecule on a solid support such as an electrode in the case of electrochemical biosensors. In order to allow the sensitive, repetitive and continuous detection of the target analyte, the immobilization process should not affect the catalytic activity of the enzyme. As such, it is essential to avoid the exposure of enzymes to adverse conditions, such as the use of harsh chemical treatments or high temperature[274]. The immobilization of the enzymes on GNMs ensures suitable platforms for the preparation of enzymatic biosensors with high selectivity, sensitivity and stability. The use of GNMs is in fact prominent for the successful construction of an enzyme biosensor because that allows the direct transfer of the electrons from the redox center of enzyme to the transducer. Several methods have been

used to immobilize enzymes on graphene's surface to fabricate an enzymatic biosensor. The most common strategies to successfully enable the immobilization of an enzyme in an efficient manner are physical adsorption and covalent immobilization[279].

Physical adsorption: also termed as noncovalent immobilization, is a simple physical adsorption method to immobilize enzymes on graphene and its derivatives by physical forces such as van der Waals, ionic and hydrophobic interactions. This approach, consists in the simple deposition of the enzyme on graphene's surface. The physical adsorption method is considered to be the simplest and most widely used strategy for the immobilization of enzymes on graphene derivatives, because it does not require the use of harsh chemical treatments, thus preserving the activities and functional features of enzymes[279].

Covalent immobilization: different organic binding molecules are used to modify graphene surfaces for further enabling direct covalent binding to enzymes. The functionalization of the graphene surface is essential because some enzymes are not stable when directly adsorbed into pristine graphene. The covalent immobilization reactions involve two main steps: (a) activation of graphene surface by adding a bifunctional cross-linker, and (b) the conjugation of enzymes onto functionalized graphene. The activation of graphene surface occurs by covalent bonding between the organic groups, such as amines and carboxylic groups and the oxygenated groups of GO[240]. In general, the most common cross-linker used for functionalization of graphene is 1-ethyl-3-(3-dimethylaminopropyl) carbodiimide hydrochloride (EDC)/N-hydroxysuccinimide (NHS) for carboxylated graphene and glutaraldehyde for amino-functionalized graphene[240]. The use of a multifunctional cross-linker can improve the stability and efficacy of enzyme–graphene conjugates.

Unlike physical adsorption, the covalent immobilisation prevents the inactivation of catalytic functions of the enzymes and electrically wires the active sites of the enzymes to the GO surface. However, the covalent immobilization affects the electronic properties of graphene because it changes the native lattice structure of graphene, by converting carbon bonding from sp^2 to sp^3.

1.5.2.3. Application of enzymatic electrochemical biosensors developed from graphene nanocomposite-based electrodes

Enzyme-based electrochemical biosensors have been extensively used in multiple scientific areas, including healthcare, environmental monitoring and food safety. The main area where enzymatic biosensors are applied is in healthcare. Once can find many studies

in the literature that report the use of enzymatic biosensors to monitor blood glucose levels. Moreover, the reliable detection of urea is another important topic of enzymatic biosensors in healthcare due to its potential application in patients suffering from renal disease. In the environmental level, the enzymatic biosensors have been widely applied to the detection of phenolic compounds, which are known to raise toxicity concerns. In the food safety, the application of enzymatic biosensors is mainly used for monitoring food processing procedures to detect concentrations of fermentative end products.

The use of GNMs as transducers in enzymatic biosensors have been widely reported for the detection and determination of biomolecules such as glucose, hydrogen peroxide (H_2O_2), deoxyribonucleic acid (DNA), phenols, etc., as summarized in Table 1.3.

Table 1. 3 *Some recent examples of enzymatic electrochemical biosensors developed from graphene nanocomposite-based electrodes and their immobilization platform, target, detection method, linear detection range, and limit of detection (LOD).*

Enzyme	Immobilization platform	Target	Detection method	Linear detection Range	LOD	Ref
GOx[a]	rGO-Fe_3O_4	Glucose	Electrochemical	0.05 - 1 mM	0.1 µM	[280]
GOx	Silk-graphene field effect transistor	Glucose	Electrochemical	0.1 - 10 mM	0.1 mM	[281]
GOx	AuNP/PANI/rGO/NH_2-MWCNTs	Glucose	Electrochemical	1 - 10 mM	64 µM	[282]
GOx	AuNPs-graphene	Glucose	Electrochemical	0.1 nM - 5 mM	0.1 nM	[283]
GOx	Graphene-PANI	Glucose	Electrochemical	10 µM - 1.48 mM	2.769 µM	[284]
GOx	Chitosan/Nafion/Pt NPs/SGGT[b]	Hydrogen peroxide, glucose	Electrochemical	3 - 300 µM, 0.5 µM - 1 mM	≤ 0.5 µM	[285]
GOx	3D GO-PANI	Glucose	Electrochemical	0.07 - 1.10 mM	0.045 mM	[286]
GOx	AuPd-polyimide-rGO	Glucose	Electrochemical	0.0008 - 0.28 mM	0.0005 mM	[287]
GOx	rGO - AuNPs	Glucose	electrochemical	2 - 10 mM	0.9 nM	[288]
GOx	rGO-PtNPs-chitson	Glucose	Electrochemical	0.002 - 10 mM	2 µM	[289]
GOx	GO-Ph-AuNPs	Glucose	Electrochemical	0.3 - 20 mM	0.3 mM	[290]
GOx	rGO	Glucose	Electrochemical	0.1 - 1 mM	5.8 µM	[291]
GOx	rGO	Glucose	Electrochemical	1.4 - 9.5 mM	13.4 µM	[292]
GOx	PANI-modified SnO_2-3D rGO	Glucose	Electrochemical	0.1 nM - 5 µM	0.26 nM	[293]
GOx	Graphene-MnO_2	Glucose	Electrochemical	0.04 - 2 mM	10 µM	[294]
GOx	rGO-polyethyleneimine (PEI)	Glucose/ cholesterol	Electrochemical	0.1 - 15.5 mM/ 2.5 - 25 µM	5 µM/ 0.5 µM	[295]

Enzyme	Immobilization platform	Target	Detection method	Linear detection Range	LOD	Ref
GOx	rGO-Fe_3O_4	Glucose	Electrochemical	0.5 - 10 mM	106.5 µM	296
GOx	3D graphene	Glucose	Electrochemical	0.3 - 6 mM	0.2 mM	297
GOx	Graphene-CNTs/AuNPs	Glucose	Electrochemical	10 µM - 2 mM	4.1 µM	298
GOx	rGO/β-cyclodextrin	Glucose	Electrochemical	50 µM - 3.0 mM	12 µM	299
GOx	rGO/fullerene	Glucose	Electrochemical	0.1 - 12.5 mM	35 µM	300
GOx	GO-TiO_2-OISL[c]	Hydrogen peroxide	Electrochemical	1 - 120 µM	46 nM	301
Lacc[d]	rGO-rhodium nanoparticles	17β-estradiol	Electrochemical	0.9 - 11 pM	0.54 pM	302
Lacc	rGO-Palladium-copper nanocages	Phenol	Electrochemical	0.005 -1.155 mM 1.655 -5.155 mM	1.5 µM 2.0 µM	303
Lacc	PANI-graphene composites	Hydroquinone	Electrochemical	0.4 - 337.2 µM	2.94 µM	304
Lacc	Graphene-cellulose microfiber	Catechol	Electrochemical	0.085 - 209.7 µM	0.085 µM	299
Lacc	MoS_2-graphene quantum dots	Caffeic acid	Electrochemical	0.38 - 100 µM	0.32 µM	305
HRP[e]	$CaCO_3$ microspheres encapsulated with a graphene capsule	Hydrogen peroxide	Electrochemical	0.01 - 12 mM	3.3 µM	306
HRP	rGO	Hydrogen peroxide	Electrochemical	0.039 - 0.78 µM	0.02 µM	307
HRP	3D graphene/methylene blue-CNTs	Hydrogen peroxide	Electrochemical	0.2 µM - 1.1 mM	58.0 nM	308
HRP	1-aminopyrene-rGO	Hydrogen peroxide	Electrochemical	1.5 - 28.5µM	0.5 µM	309
ChOx[f]	rGO-PPy	cholesterol	Electrochemical	0.01 - 6 mM	3.78 µM	310
ChOx	Chitosan-graphene	cholesterol	Electrochemical	0.005 - 1.0 mM	0.715 µM	311
ChOx	TiO_2 nanowires-3D graphene	cholesterol	Electrochemical	0.05 - 8.0 mM	6 µM	312
BOx[g]	GONPs-NiNPs	bilirubin	Electrochemical	0.01 - 600 µM	0.15 nM	313
ADH	Au-AgNPs-P(L-Cys)-rGO	NADH	Electrochemical	0.017 - 1.84 µM	5 µM	314
Uricase	Chitosan-graphene - PB[h]	uric acid	Electrochemical	0.0025-0.40 mM	2.5 µM	315

[a] Glucose oxidase (GOx), [b] solution-gated graphene transistors (SGGT), [c] Organic-Inorganic Supporting Ligand (OISL), [d] Laccase, [e] horseradish peroxidase (HRP), [f]cholesterol oxidase (ChOx), [g] bilirubin oxidase (BOx), [h] Prussian blue (PB)

Graphene-based nanocomposites have been widely used to construct enzymatic electrochemical biosensors. The most commonly used enzyme for the fabrication of these biosensors is glucose oxidase (GOx). This enzyme has been widely for the development of biosensors for detection of glucose levels, which is essential in biomedicine [280 -296]. In the last few years, several efforts have been made to improve the sensitivity of the developed biosensors. The immobilization of GOx in different sensing platforms, such as oxide nanoparticles decorated graphene and therein derivatives[180,] silk fibroin film on a

graphene field effect transistor[281], metallic nanoparticles modified graphene and derivatives[288, 290], nanostructured graphene based conducting polymers composite[284, 286, 294], among others, is key to the success of the sensors. Additionally, GOx have also been immobilized on a hybrid rGO–Fe_3O_4 based substrate for the detection of glucose[280, 296]. This hybrid nanomaterial is an attractive substrate for construction of biosensors because it takes advantage of the properties of rGO.

Others enzymes also used for the development of biosensors include laccase, horseradish peroxidase (HRP), cholesterol oxidase (ChOx). Laccase is an oxygen-reducing enzyme, which has been used for development of an electrochemical biosensors. For example, laccase has been widely used for the detection of phenols and catechols[299, 303, 305]. Additionally, laccase was used together with reduced graphene oxide-rhodium nanoparticles for the design of a sensitive electrochemical biosensor for the detection of 17β-estradiol, which is an important natural hormone classified as an emerging contaminant affecting humans and aquatic life)[302].

HRP has been widely used for the determination of hydrogen peroxide concentrations. For example, HRP has been immobilized on 1-aminopyrene and reduced graphene oxides for the detection of intracellular hydrogen peroxide[309]. Another example of the use of HRP on the determination of hydrogen peroxide consists in the immobilization of this enzyme on porous calcium carbonate microspheres encapsulated with graphene[306]. ChOx has been used for the determination of cholesterol, an indispensable steroid present in the human body[310-312]. Pramanik *et al.* reported a single step fabrication of a graphene conjugate by simultaneous electro-polymerisation of pyrrole and co-deposition of rGO and ChOx aimed for cholesterol quantification[310]. The gathered results denoted an excellent sensitivity, larger linear response and lower detection limit of the developed biosensor.

In summary, all of these sensory platforms showcase the versatility that graphene and its derivatives have in being integrated with other nanomaterials such as inorganic nanoparticles, organic polymers or hydrogels for the detection of a wide variety of (bio)analytes. Moreover, these platforms show that graphene and its derivatives are excellent electrode materials for the development of biosensors with superior performance that can improve the sensing not only in the biomedical field but also in other applications such as food, environmental and agriculture industries monitoring.

Part B - Experimental Section

Chapter 2 - Techniques

In this chapter a brief overview of the experimental techniques used in this work is presented. Techniques such as Cyclic Voltammetry (CV), Electrochemical Impedance Spectroscopy (EIS), Atomic Force Microscopy (AFM), Scanning Electron Microscopy (SEM), XPS and ATR_FTIR spectroscopy will be described together with their experimental setups and instrumentation.

2.1. Electrochemical techniques

Electrochemical techniques are concerned with the interaction between electricity and chemistry, namely the measurements of electrical quantities, such as potential, current or charge and their relationship to chemical parameters such as concentration[316]. In contrast to many chemical processes that involve homogeneous bulk solutions, electrochemical processes occur at the electrode/electrolyte solution interface.

Electrochemical processes involve chemical phenomena associated with charge separation, usually in liquid media. This charge separation often leads to charge transfer, which occurs heterogeneously on electrode surfaces. The heterogeneous redox reactions are separated in space and usually occur at different electrodes immersed in the electrolyte solution in an electrochemical cell[316, 317]. In order to ensure the electroneutrality of the solution, an oxidation reaction and a reduction reaction must be carried out simultaneously. Thus, the overall chemical reaction consists of two independent chemical half-reactions, which describe the real chemical changes.

Most of the charge transfer processes involve the transfer of electrons during the redox process. Thus, the simplest system to be considered is the reversible electron reaction:[318]

$$O + ne^- \rightleftharpoons R \qquad \textbf{(Equation 2.1)}$$

where O and R are the oxidized and reduced forms of the redox couple, respectively. This reaction will occur in a potential region that makes the electron transfer thermodynamically or kinetically favorable.

In an electrochemical reaction, the application of a well-defined potential to the working electrode leads to the electrostatic attraction of charged species to the electrode surface. Furthermore, other species available in the solution can interact with the surface of the working electrode by adsorption. In this way, during a heterogeneous electron transfer reaction one needs to consider not only the transport of the electroactive species to and from the bulk solution to the electrode surface but also the electrode reaction itself.

2.1.1. Electrochemical cell

The electrochemical cell consists of a device where oxidation-reduction reactions occur. The most common electrochemical cell has three electrodes (working electrode,

reference electrode, and counter electrode) that are immersed in the electrolyte solution (figure 2.1).

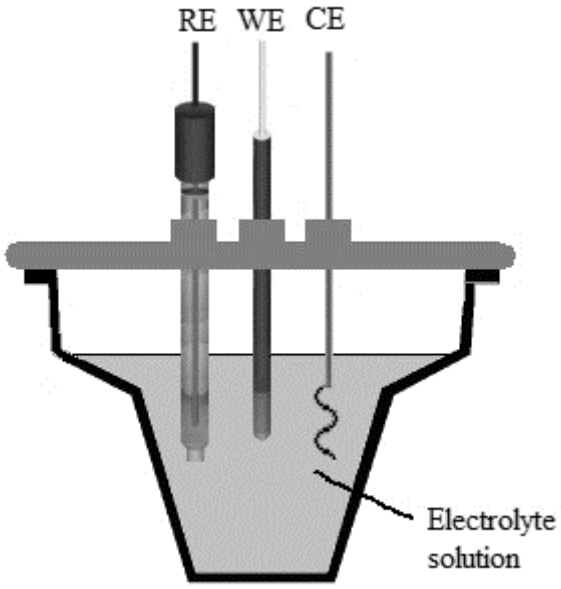

Fig. 2. 1: *Simplified schematic representation of the Electrochemical three electrodes cell.*

The working electrode (WE) is where the electrochemical reaction of interest occurs; the reference electrode (RE) is an electrode which maintains a stable and well-known potential along the experiments with the help of a potentiostat, and it is used as a point of reference in the electrochemical cell for the potential control and measurement; and the counter electrode (CE), also known as auxiliary electrode, is responsible for supplying electrons required by the WE. It is used to close the current circuit in the electrochemical cell, and the reaction that occurs in the CE should not interfere with the studied reaction. Indeed, the total surface area of the CE must be higher than the area of the WE so that it will not be a limiting factor in the kinetics of the electrochemical process under study. The RE is, generally, kept separately from the WE, being as close as possible by the presence of a Luggin-Haber cappilary, which decreases the uncompensated resistance (so-called ohmic loss) of the electrolyte solution. This solution is composed by solvent and support electrolyte and can contain electroactive species.

In an electrochemical cell, the movement of the species, called mass transport, can occur due to three effects:[317, 318]

- *Diffusion*: involves the thermal movement of charged and neutral species in solution (without electric field effects) under the influence of concentration gradients (*i.e.* from regions of high concentration to

regions of low concentration) aiming to minimize concentration differences;

- *Convection*: transport of species to the electrode by physical movement (fluid mechanical movement);
- *Migration*: only movement of charged species along an electrical field effect.

These different modes of mass transport are illustrated in Figure 2.2.

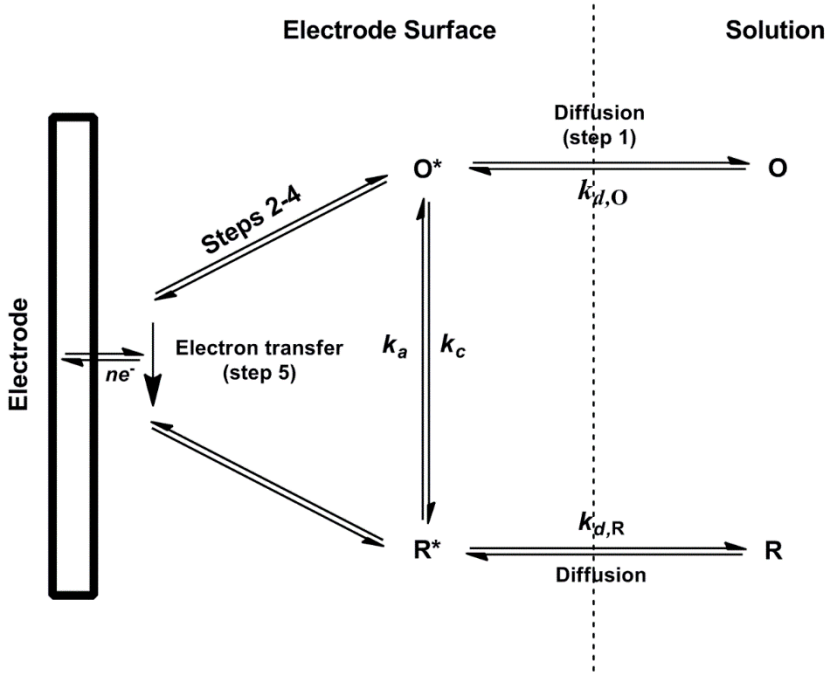

Fig. 2. 2: *Simplified schematic representation of the electron transfer process on an electrode surface (adapted from reference[318]).*

In Figure 2.2 is possible to distinguish some relevant parameters such as:[317]

a) $k_{d,O}$ and $k_{d,R}$, which are the mass transfer coefficients of the oxidized (O) and reduced (R) species (considered both to be soluble) that are associated to the diffusion process described by the Fick's law.[319] Generally, these coefficients are influenced by the thickness of the diffusion layer and can be controlled through the type of experiment and experimental conditions used, such as varying the force convection.

b) (k_c) and anodic (k_a), which represent the charge transfer rate constant of the cathodic and anodic reactions, respectively, and include the adsorption of reagents on the electrode surface.These constants can be determined by using the Butler-Volmer expressions:[320, 321]

$$k_c = k_0 \exp[-\alpha_c nF(E - E^{O})/RT] \quad \textbf{(Equation 2.2)}$$

$$k_a = k_0 \exp[\alpha_a nF(E - E^{O})/RT] \quad \textbf{(Equation 2.3)}$$

where k_0 is the standard rate constant of the electrochemical reaction; α_c and α_a are the cathodic and anodic charge transfer coefficients, respectively; n is the number of electrons involved in the reaction process; F is the Faraday's constant; E is the applied potential; E^O is the formal potential of the system; R is the ideal gas constant; and T is the temperature.

The values of k_c and k_a depend on the applied potential (E) and on the value of the standard rate constant (k_0). In this regard, two extreme situations can be considered:[317, 318]

- $k_0 >> k_d$ - *reversible reaction*, which means that at any potential the system is always at equilibrium at the electrode surface and, thus, it is possible to apply the Nernst equation at any potential. The current is determined only by the electronic energy differences between the electrode and the donor or acceptor species in solution and their rate of supply;
- $k_0 << k_d$ - *irreversible reaction*, which means that when a high potential is applied (in order to overcome the activation barrier and allow the reaction to occur), the mass transport does not influence the electron transfer kinetic constant and consequently the process is controlled by the slowest kinetic reaction.

c) The presence of the *electrical double layer* also affects the kinetics of electrode reactions[322]. The *electrical double layer* can be defined as the interfacial region between the electrode and the aqueous solution. The basic concept of "double layer" consist of a spatial distribution of charges at the electrode surface and of a distribution of equal number of opposite charges in the solution in order to neutralize the charge of the electrode. The *electrical double layer* term starts to be used with the development of the classical models such as the Helmholtz[323], Gouy-Chapman[324, 325] and Stern[326] models widely used to gather relevant information about the molecular structure at the electrode/electrolyte solution interface. Thenceforth, many modifications and improvements have been made to these early models, and the latest approaches use molecular dynamics simulations to

elucidate the structure and dynamics of the electrical double layer at the electrode surface.

2.1.2. Cyclic Voltammetry

Cyclic Voltammetry (CV) is the most widely, simple, fast and perhaps straightforward used technique for acquiring qualitative and quantitative information about any electroactive specie (*i.e.* specie that can be oxidized and/or reduced) involved in the electrochemical reactions. CV is also invaluable to study electron transfer- initiated chemicals reactions, which includes catalysis. The power of cyclic voltammetry results from its ability to rapidly provide considerable information on the thermodynamics of redox processes, on the kinetics of heterogeneous electron-transfer reactions, and on coupled chemical reactions or adsorption processes.

Cyclic voltammetry is often the first experimental approach performed in an electroanalytical study, since it offers rapid location of redox potentials of the electroactive species and convenient evaluation of the effect of media upon the redox process.

2.1.2.1. Basic principles of Cyclic Voltammetry

A cyclic voltammogram is obtained by applying a linear potential sweep (*E*),), at a scan rate υ, to the working electrode, between the limits E_{min} (minimum potential) and E_{max} (maximum potential), and measuring the resulting electric current (*I*). The application of a potential sweep to the working electrode is controlled *versus* a reference electrode and usually has a triangular waveform as shown in Figure 2.3[317].

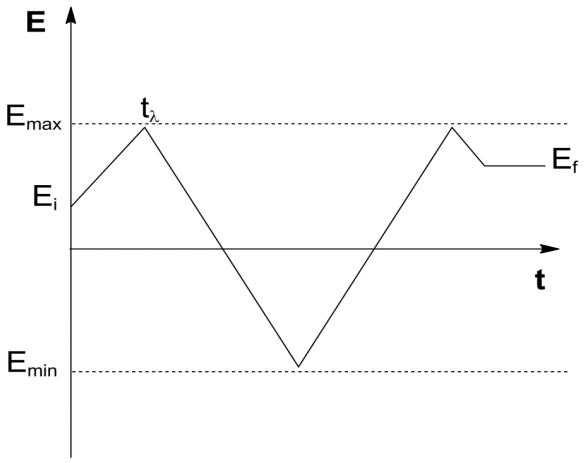

Fig. 2. 3: *Variation of the applied potential to the working electrode with time in cyclic voltammetry: E_i – initial potential; E_f – final potential; E_{min} – minimum potential; E_{max} – maximum potential (corresponds to the reverse potential); t_λ – switching time. The fact that the initial sweep is positive is simply illustrative (adapted from reference [318]).*

The sweep or scan rate (v = dE/dt) indicates the rate at which the potential is changed with time. When a single anodic (*i.e.* oxidizing) or cathodic (*i.e.* reducing) sweep is performed, the technique is usually referred as *linear potential sweep method*, whereas when both sweeps are performed in a repetitive way, the method is referred as *cyclic voltammetry*.

The response, electric current *versus* potential is called a *cyclic voltammogram* and has different characteristics as a function of the type of system involved. A brief description of the most common types of systems that can be observed in a voltammetric experiment is provided below.

2.1.2.2. Reversible Systems

In the CV of reversible systems (O + ne^- ⇄ R), *i.e.*, those in which the kinetics of the couple O/R is fast enough (relative to the time-scale of the sweep) to keep the electron transfer process in equilibrium, the product of the initial oxidation or reduction is then reduced or oxidized, respectively, on reversing the scan direction. Figure 2.4 shows a typical cyclic voltammogram of a reversible system and the main characteristic parameters that can be easily obtained graphically.

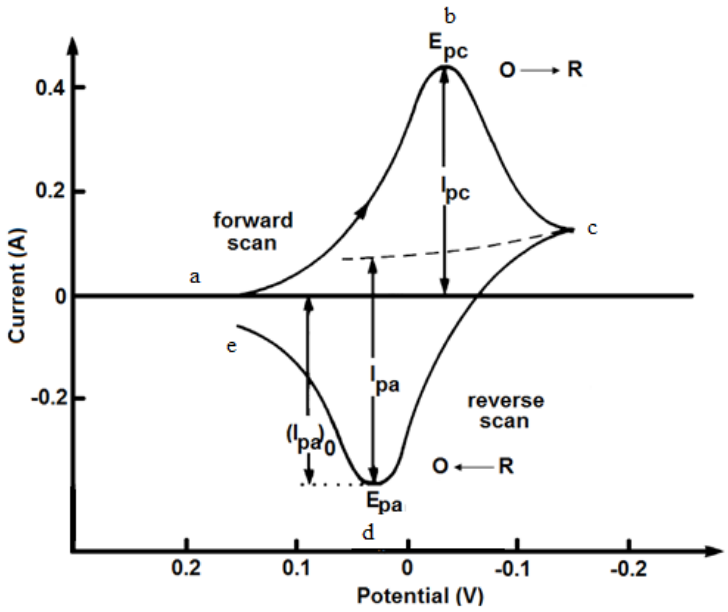

Fig. 2. 4: *Typical cyclic voltammogram for a reversible system of the type O + ne^- ⇄ R (adapted from reference [318]).*

Figure 2.4 illustrates the usual response of a reversible redox process during a single potential cycle. The reduction process occurs from (a) the initial potential to (c) the switching potential. In this region the potential is scanned negatively to cause a reduction.

The resulting current is called cathodic current (i_{pc}). The corresponding peak potential occurs at (b), and is called the cathodic peak potential (E_{pc}). The Epc is reached when all of the substrate at the surface of the electrode has been reduced. After the switching potential has been reached (c), the potential scans positively from (c) to (e). This results in anodic current (I_{pa}) and oxidation to occur. The peak potential at (d) is called the anodic peak potential (E_{pa}), and is reached when all of the substrate at the surface of the electrode has been oxidized. These cathodic and anodic characteristic peaks of the cyclic voltammograms are generated by the formation of the diffusion layer near the electrode surface. Although the cyclic voltammograms are almost always plotted in this way, (see Figure 2.4) the axes can be reversed[318].

The first theoretical analysis of the wave shape for a reversible system was achieved in the early 194y Randles[327] and Sevcik[328]. The Randles-Sevcik equation (at 25 ºC) allows obtaining the peak current (I_p):

$$I_p = (2.69 \times 10^5) n^{3/2} A C D^{1/2} \nu^{1/2} \qquad \textbf{(Equation 2.4)}$$

where n is the stoichiometric number of electrons involved in the reaction process, A is the electrode surface area (cm^2), D is the diffusion coefficient of the specie ($cm^2\ s^{-1}$), C is the bulk concentration of the specie ($mol\ cm^{-3}$), v is the scan or sweep rate ($V\ s^{-1}$), and I_p is the peak current (A).

From the analysis of equation 2.4 it is possible to infer that the peak current for the oxidized or reduced species is directly proportional to the concentration of the species and to the square root of the scan rate, and is commonly measured by extrapolating the preceding baseline current.

The position of the peaks on the potential axis (E_p) is related to the formal potential of the redox process (E^O). For a reversible process, the formal potential can be estimated according to the following equation:

$$E^{\mathrm{O}} = \frac{E_{pa} + E_{pc}}{2} \qquad \textbf{(Equation 2.5)}$$

The information provided by the Randles-Sevcik equation can be presented in the form of a diagnostic tool for cyclic voltammograms of reversible systems:[317]

- $I_p \propto v^{1/2}$;
- E_p independent of v;
- $|E_p - E_{p/2}| = (1.1RT/nF) = 56.6/n$ (mV at 25 ºC);

- $\Delta E_p = |E_{pa} - E_{pc}| \neq 0 = (2.3RT/nF) = 59.0/n$ (mV at 25 ºC);
- $|I_{pa}/I_{pc}| = 1$

When these conditions are verified, the peak separation can be used to determine the number of electrons involved in the electron transfer process of reversible systems. If one of the above conditions is not verified, the system cannot be considered as reversible, and should be considered as quasi-reversible or irreversible, depending on the extension of the irreversibility.

2.1.2.3. Irreversible and Quasi-Reversible Systems

In the case of irreversible reaction of the type O + ne^- → R, linear potential sweep and cyclic voltammetry lead to the same voltammetric profile, since no reverse peaks appear on changing the sweep direction (some at times with a very weak reverse peak), which means that re-reduction or re-oxidation cannot occur (Figure 2.5 A). This process is usually due to slow electron exchange or slow chemical reactions at the electrode surface. In an irreversible electrode process, the mass transfer step is very fast as compared to the charge transfer step

.

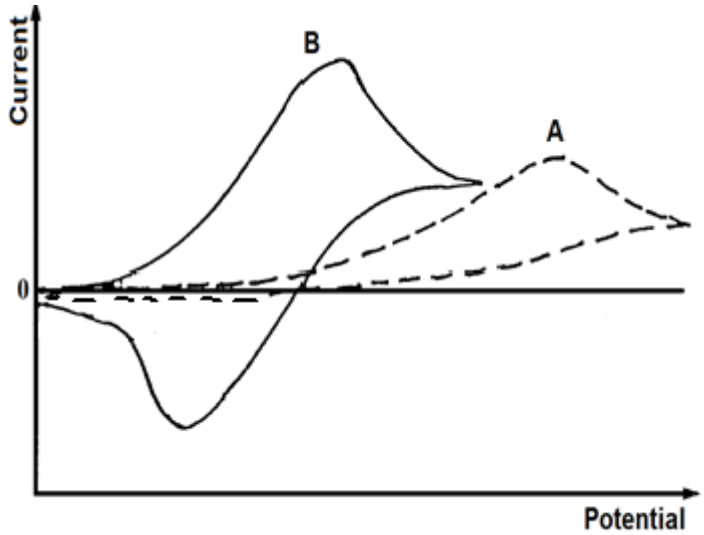

Fig. 2. 5: *Typical cyclic voltammograms for irreversible* ***(A)*** *and quasi-reversible* ***(B)*** *systems (adapted from reference [316]).*

In the completely irreversible voltammograms the peak current (I_p) is given by:

$$I_p = (2.99\times10^5)\alpha^{1/2}n^{3/2}ACD^{1/2}v^{1/2} \qquad \textbf{(Equation 2.6)}$$

From the analysis of equation 2.6 it is clear that the peak current (I_p) for the oxidized or reduced species is still directly proportional to the concentration of the specie (C) and to the square root of the scan rate ($v^{1/2}$), but is lower in height (depending upon the value of α) when compared to the reversible systems.

From the information provided by this equation it can be also deduced the following diagnostic criteria for cyclic voltammograms of totally irreversible systems:[317, 318]

- $I_p \; \alpha \; v^{1/2}$;
- E_p dependent of v;
- $|E_p - E_{p/2}| = 47.7/\alpha n$ (mV at 25 ºC);
- $\Delta E_p = |E_{pa} - E_{pc}| > 59.0/n$ (mV at 25 ºC);
- $|I_{pa}/I_{pc}| = 1$

However, electrode processes are not always easy and fast (reversible systems) or very sluggish (irreversible systems), and sometimes we must consider the whole voltammogram characteristics. A quasi-reversible process is intermediate between reversible and irreversible systems. The current due to quasi-reversible processes is controlled by both mass transport and charge transfer kinetics. The process occurs when the relative rate of electron transfer with respect to that of mass transport is insufficient to maintain Nernst equilibrium at the electrode surface. In these systems the reverse peak appears but is smaller than the forward peak. The voltammograms of a quasi-reversible system (Figure 2.5 B), are more drawn out and exhibit a larger separation in peak potentials compared to a reversible system[318]. which means that $\Delta E_p = |E_{pa} - E_{pc}| > 59.0/n$ (mV). For electrochemically quasi-reversible reactions, the surface concentrations are controlled both by kinetics and diffusion processes[318].

2.1.2.4. Adsorbed Species

CV can also be used to evaluate the interfacial behaviour of electroactive components. When both adsorption species (reactant and product) are involved in the reaction mechanism there is a change in the shape of the cyclic voltammogram obtained for reversible systems, and an adsorption isotherm (one of the most used is the *Langmuir adsorption isotherm* which is only applicable to a monolayer coverage level and assumes that there is no interaction between adsorbed species) has to be chosen in order to solve the corresponding equations or alternatively, one has to assume that there is adsorption equilibrium before the experiment begins.

The mathematical expressions to calculate the voltammetric profile of the cyclic voltammograms are available and well-described in the literature[318]. In the presence of electroactive species, the peak current (I_p) is given by:[318]

$$I_p = \frac{n^2 F^2 \Gamma A \nu}{4RT} \qquad \textbf{(Equation 2.7)}$$

where n is the number of electrons involved in the process, F is the Faraday's constant, A is the area of the electrode surface, v is the scan rate, R is the ideal gas constant, T is the temperature, and Γ is the surface concentration of the adsorbed specie (O/R).

The peak current (I_p) is directly proportional to the surface concentration of the adsorbed specie (Γ) and to the scan rate (v). Figure 2.6 shows a typical CV for a reversible system of species adsorbed at the electrode surface[318].

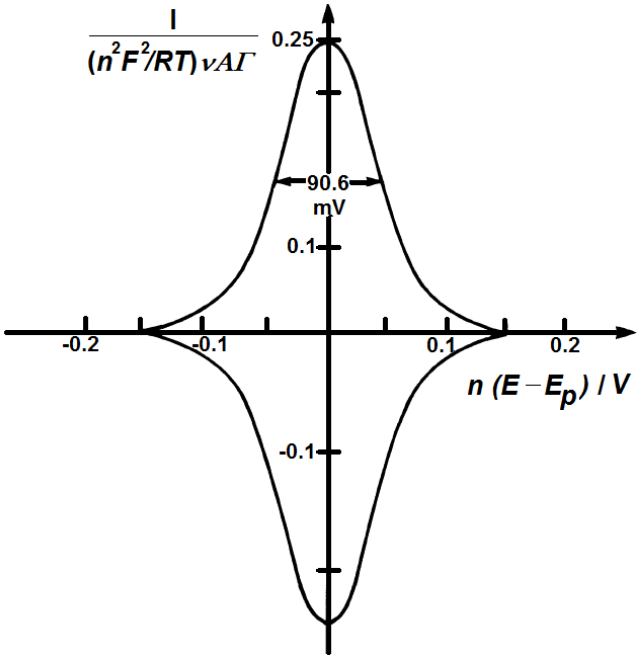

Fig. 2. 6: *Ideal cyclic voltammogram for a reversible system of species adsorbed at the electrode surface. If O and R species are adsorbed with the same strength, $E_p = E^O$ (adapted from reference [318]).*

Ideal Nernstian behaviour is clearly observed in this figure by symmetrical CV peaks ($\Delta E_p = 0$) due to the fixed amount of reactant adsorbed on the surface, *i.e.*, the value of E_p is the same for oxidation and reduction, as well as a peak width at half-height of

90.6/*n* (mV at 25 ºC). Ideal behaviour is achieved for relatively slow scan rates and for an adsorbed layer that shows no intermolecular interactions and fast electron transfer.

The peak area at saturation, *i.e.*, the quantity of charge consumed during the reduction or adsorption of the adsorbed layer (*Q*), can be used to calculate the surface concentration of the adsorbed species, as follows:

$$Q = nFA\Gamma \qquad \textbf{(Equation 2.8)}$$

This equation can be used to calculate the area occupied by the adsorbed molecule which allows predicting its orientation on the surface[318].

2.1.2.5. Description of the Experimental Setup and Instrumentation

CV measurements were performed on a Voltalab PGZ301 Potentiostat (from Radiometer Analytical) controlled by Voltamaster 4 software (see Fig 2.7 A). All electrochemical experiments were carried out under a soft stream of N_2 in a conventional three-electrode electrochemical cell (enclosed in a grounded Faraday cage) equipped with a Ag wire electrode as the reference electrode, a large area helix-shaped Pt wire as the counter electrode, and a glassy carbon electrode (GCE) as the working electrode (Fig 2.7B).

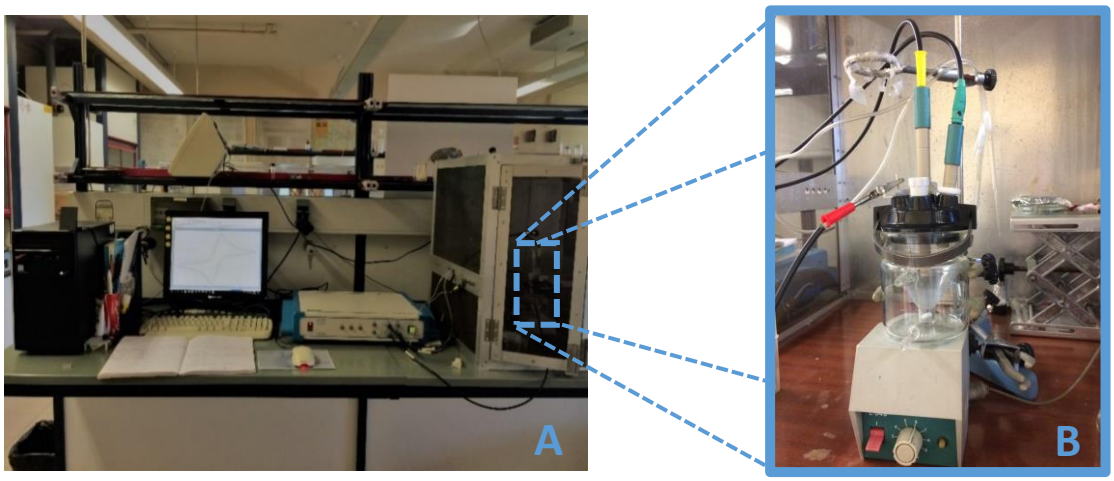

Fig. 2. 7: (A) *Illustration of the experimental setup used for electrochemical measurements* ***(B)*** *Electrochemical cell used for electrochemical measurements*

2.1.3. Electrochemical Impedance Spectroscopy

Electrochemical Impedance Spectroscopy (EIS) is one of the most effective and consistent technique for the characterization of electrochemical systems, including double-layer capacitance, diffusion impedance, determination of the charge transfer and charge storage processes, charge transport processes, and solution resistance[329]. It has widespread application in the field of characterization of materials and it is a powerful tool with great interest for the detection of relevant chemical and biological species. It is normally used in the characterization of coatings, fuel cells, batteries and passivity and corrosion studies. It has also been used extensively as a tool for investigating mechanisms in electrodeposition, diffusion of ions across membranes, study of semi-conductor interfaces and biosensors. EIS has the advantage of not causing any damage or disturbance to the analyzed surface of the electrochemical system[329, 330].

In EIS, the system under investigation (typically in the equilibrium state) is excited by a small amplitude ac sinusoidal signal of potential or current in a wide range of frequencies and the response of the current or voltage is measured. Since the amplitude of the excitation signal is small enough for the system to be in the (quasi-)equilibrium state, EIS measurements can be used to effectively evaluate the system properties without significantly disturbing them. Frequency sweeping in a wide range from high-to low-frequency enables the reaction steps with different rate constants, such as mass transport, charge transfer, and chemical reaction, to be separated[330].

Mathematically, impedance has been expressed as a complex number comprising resistance (real part) and reactance (imaginary part). The electrical resistance is a very well-known concept, being defined as the ability of a circuit element to resist the flow of electrical current. Ohm's law (Equation 2.9) defines resistance (*R*) in terms of the ratio between voltage (*E*) and current (*I*), as follows:[330, 331]

$$R = \frac{E}{I} \qquad \textit{(Equation 2.9)}$$

where the impedance of the system (Z) can be calculated by means of an expression similar to the previous Ohm's law, being Et the applied potential and It the resulting current:

$$Z = \frac{E(t)}{I(t)} \qquad \textit{(Equation 2.10)}$$

The applied potential E(t) can be expressed as a function of time:

$$E(t) = E_0 \sin(\omega t) \qquad \textbf{(Equation 2.11)}$$

where $E(t)$ is the applied voltage at a time t, E_0 is the oscillation amplitude of the excitation signal, and ω is the angular frequency of the sinusoidal excitation (rad s^{-1}). ω is 2π times higher than the conventional frequency (Hz), *i.e.*:

$$\omega = 2\pi f \qquad \textbf{(Equation 2.12)}$$

In a linear system, the current response (I), which has different oscillation amplitude (I_0) and is shifted in phase (ϕ) relatively to the excitation signal, is expressed by:

$$I(t) = I_0 \sin(\omega t + \phi) \qquad \textbf{(Equation 2.13)}$$

The electrical impedance of the system (Z) is defined as the proportionality factor between the applied potential perturbation and the current response. Using an expression analogous to the Ohm's law, one can calculate the impedance of the system as:

$$Z = \frac{E(t)}{I(t)} = \frac{E_0 \sin(\omega t)}{I_0 \sin(\omega t + \phi)} = Z_0 \frac{\sin(\omega t)}{\sin(\omega t + \phi)} \qquad \textbf{(Equation 2.14)}$$

where the impedance (Z) is characterized by the magnitude (Z_0) and phase angle (ϕ).

If we plot the applied sinusoidal signal E(t) on the X-axis of a graph and the sinusoidal response signal I(t) on the Y-axis, the result is an oval (Fig 2.8). This oval representation is known as a "Lissajous Figure". Analysis of Lissajous Figures on oscilloscope screens was the accepted method of impedance measurement before the availability of modern EIS instrumentation[330, 331].

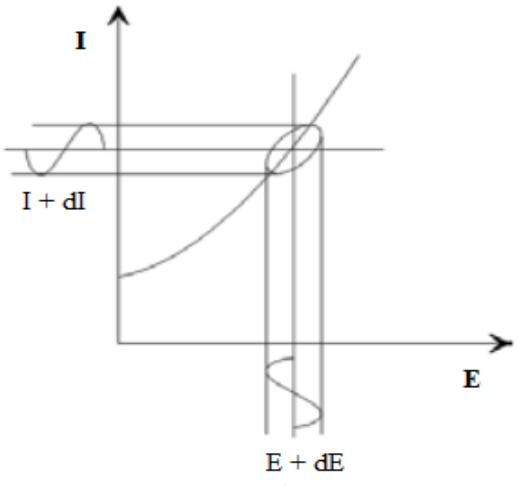

Fig. 2. 8: *Origin of Lissajous Figure.* (*adapted from reference [331]).*

Remembering Euler's equation:

$$\exp(j\phi) = \cos(\phi) + j\sin(\phi) \qquad \textit{(Equation 2.15)}$$

It is possible to express the impedance as a complex function. In this way, the potential is described as:

$$E(t) = E_0 \exp(j\omega t) \qquad \textit{(Equation 2.16)}$$

where j is the imaginary number defined as $j = (-1)^{1/2}$. In the same way, the current response is defined as:

$$I(t) = I_0 \sin(j\omega t - \phi) \qquad \textit{(Equation 2.17)}$$

Thus, the impedance (Equation 2.18) can be represented as a complex number:

$$Z = Z_0 \frac{\exp(j\omega t)}{\exp[j(\omega t - \phi)]} = |Z| \exp(j\phi) = |Z| (\cos\phi + j\sin\phi) \qquad \textit{(Equation 2.18)}$$

Equation 2.19 states that in the complex plane (Argand diagram), the impedance is composed of a real ($Z' = Z_0 \cos\phi$) and an imaginary ($Z'' = Z_0 \sin\phi$) parts at any value of ω as follows:

$$Z = Z' + jZ'' \qquad \textit{(Equation 2.19)}$$

If the real part is plotted on the X-axis and the imaginary part is plotted on the Y-axis of a chart, a Nyquist plot is obtained (see Figure 2.8). It is important to bear in mind that in this plot the Y-axis is negative and each point is the impedance at one specific angular frequency (ω).

As it has been indicated in Fig 2.9, low frequency data are on the right side of the plot and higher frequencies are on the left (it is only valid for electric circuits in EIS data where impedance usually falls as frequency rises). Furthermore, on the Nyquist plot the impedance can be represented as a vector of length |Z|. The angle between this vector and the X-axis, generally called as phase angle, is defined as $\phi = arg\ Z$.

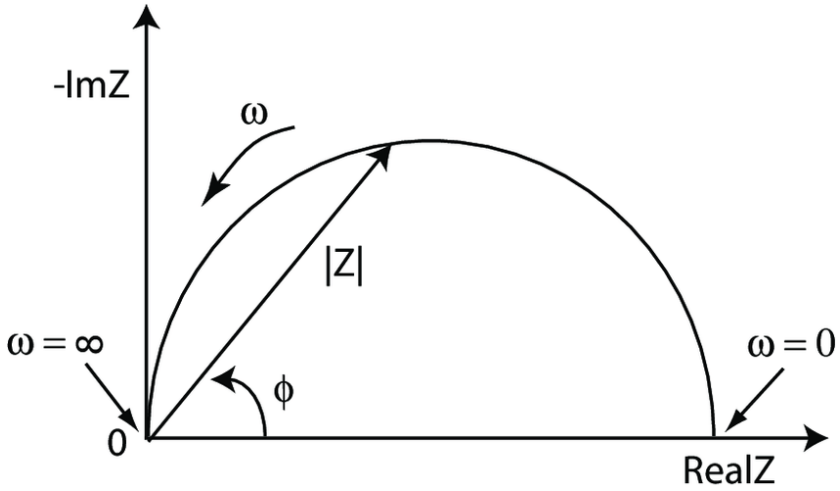

Fig. 2. 9: *Nyquist plot that illustrates both the real (Z') and imaginary (Z") components of impedance at each ω (adapted from reference [331]).*

The advantage of the Nyquist plot representation is that it gives a fast overview of the data and one can make some qualitative interpretations. However, Nyquist plots have one major shortcoming, *i.e.*, when we look at any data point on the plot, we cannot tell what frequency was used to record that point, which means that one loses the frequency dimension of the data. In order to overcome this limitation, one can always label the frequencies on the curve. The semicircle presented in this figure is characteristic of a simple equivalent electrical circuit (Fig 2.10) with a single time constant (*τ*).

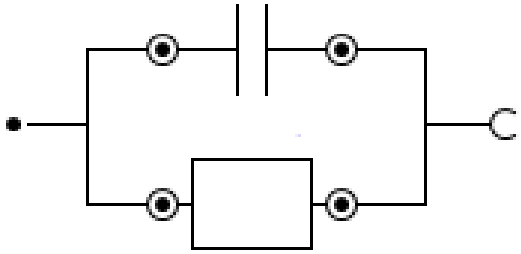

Fig. 2. 10: *Simple equivalent electrical circuit for a system characterized by a single semicircle (single resistive process), i.e., with a single time constant (τ) (adapted from reference [331]).*

Although, electrochemical impedance plots often contain several semicircles, *i.e.*, more than one time constant, usually only a portion of one or more semicircles is seen. A more complete way of presenting impedance data involves the use of Bode plots (Fig 2.11) in which the impedance is plotted with logarithm of the frequency on the X-axis and both the absolute values of the logarithm of the impedance ($\log |Z| = \log Z_0$) and the phase-shift on the Y-axis[331].

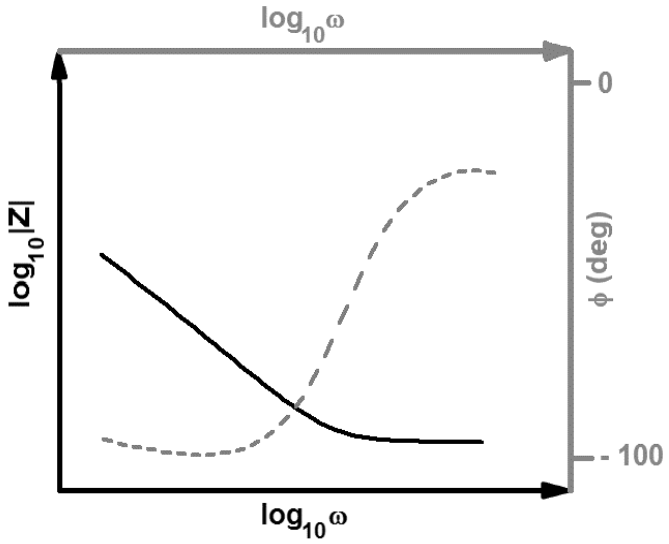

Fig. 2. 11: *Typical Bode modulus (black straight line) and Bode phase (blue dashed line) plots of an electric circuit with a single time constant (adapted from reference [331]).*

The Bode modulus (black straight line) and the Bode phase (gray dashed line) plots for a simple equivalent electrical circuit with a single time constant are shown in Fig 2.10. Unlike the Nyquist plot, the Bode plots clearly show the frequency values at each point [331].

2.1.3.1. Electrical Circuit Elements

EIS data are commonly analysed by fitting to an equivalent electrical circuit model. Most of the circuit elements in the model are common electrical elements such as resistors (R), capacitors (C), inductors (L) and distributed elements such as, constant phase element (*CPE* or *Q*) and Warburg impedance (*W*). These elements can be combined in series and parallel to give complex circuits. A certain physical meaning is then assigned to the various elements of the equivalent electrical circuit. As an example, most models contain a resistor that models the solution resistance of the electrochemical cell[331].

Some knowledge of the impedance of the standard circuit components is therefore quite useful. Table 2.1 lists the common passive and distributed electrical circuit elements together with their impedance (*Z*) and admittance (*Y = 1/Z*) expressions.

Looking at the table, the impedance of a resistor (Z_R) it doesn´t dependent of the angular frequency (ω) and has no imaginary component (j). The current through a resistor stays in phase with the voltage across the resistor. However, the impedance of a capacitor (Z_C) have an imaginary impedance component and Z_C decreases as the angular frequency is higher. The current through a capacitor is phase shifted 90 degrees with respect to the voltage. Inductor also have only an imaginary impedance component and an impedance

od an inductor (ZL) increases as the angular frequency increases. The current through an inductor is phase-shifted -90 degrees with respect to the voltage[331].

Table 2. 1: *Common passive and distributed electrical circuit elements used in the models, and their impedance and admittance expressions.*[331]

Element	Impedance	Admittance
Resistor (R)	$Z_R = R$	$Y_R = 1/R$
Capacitor (C)	$Z_C = 1/j\omega C$	$Y_C = j\omega C$
Inductor (L)	$Z_L = j\omega L$	$Y_L = 1/j\omega L$

Although all electrochemical cells can be represented by an equivalent electrical circuit model (few can be modeled by using only a single equivalent circuit element). EIS models usually consist of a number of elements in a network. These elements can occur in serial and parallel combinations. Providentially, there are simple formulas that describe the impedance of circuit elements in both series (Fig 2.12) and parallel (Fig 2.13) combinations[331].

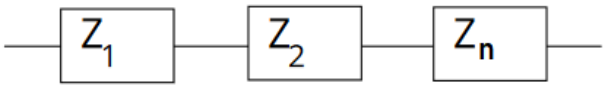

Fig. 2. 12: *Impedances in Series*

For *n* linear impedance elements in series, the equivalent impedance can be calculated as:

$$Z_{eq}^{series} = Z_1 + Z_2 + Z_3 + \ldots + Z_n = \sum_{i=1}^{n} Z_i \qquad \textbf{(Equation 2.20)}$$

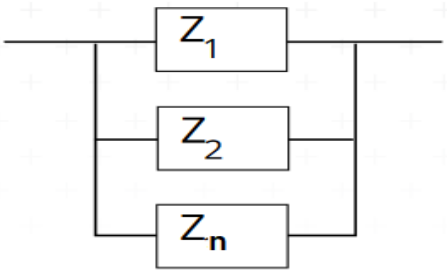

Fig. 2. 13: *Impedances in Parallel*

For *n* linear impedance elements in parallel, the equivalent impedance can be calculated from:

$$Z_{eq}^{parallel} = \frac{1}{Z_1} + \frac{1}{Z_2} + \frac{1}{Z_3} + \ldots + \frac{1}{Z_n} = \sum_{i=1}^{n} \frac{1}{Z_i} \qquad \textit{(Equation 2.21)}$$

2.1.3.2. Common Equivalent Electrical Circuit Models

The characterization of the electrochemical systems with impedance spectroscopy requires the interpretation of the data with the help of suitable equivalent circuit models. These models are regressed to experimental data in order to estimate the parameters that can describe, interpret and fit the impedance data adequately and can also be used to predict the behaviour of the system under different conditions[331].

The most common equivalent electrical circuit models will be described in this section. The individual elements that constitute the following equivalent circuits were summarized in Table 2.1 together with their respective equations for both the impedance (Z) and admittance (Y = 1/Z).

2.1.3.2.1. Purely Capacitive Coating: RC Equivalent Circuit

A metal covered with an undamaged coating behaves like an ideally polarized electrode (ideal capacitor) and generally has a very high impedance. The equivalent electrical circuit for such a situation is a RC equivalent circuit (Fig 2.14 A). This type of circuit includes a solution resistance (R_s) in series with the coating capacitance (C). Fig.2.14 B shown an example of a Nyquist plot for this model in which were assigned the following values: R_s = 500 Ω (a bit high but realistic for a poorly conductive solution); C = 200 pF (realistic for a 1 cm^2 sample, a 25 μm coating, and ε = 6); frequency range between 100 kHz and 0.1 Hz. Analysing the Nyquist plot is possible to estimate the value of the solution resistance by the interception of the curve with the X-axis. Although, the capacitance value can be determined by curve fitting or can be estimated from the analysis of the Bode plots representation (Fig 2.14 C). In the Bode phase plot (Fig 2.14 C_2), the phase angle (ϕ) remains around 90 degrees for a wide range of frequencies.

However, most of the times the surface under investigation is not homogeneous (the coating does not behave ideally), and a CPE is included instead of C, resulting in a RQ equivalent electrical circuit.

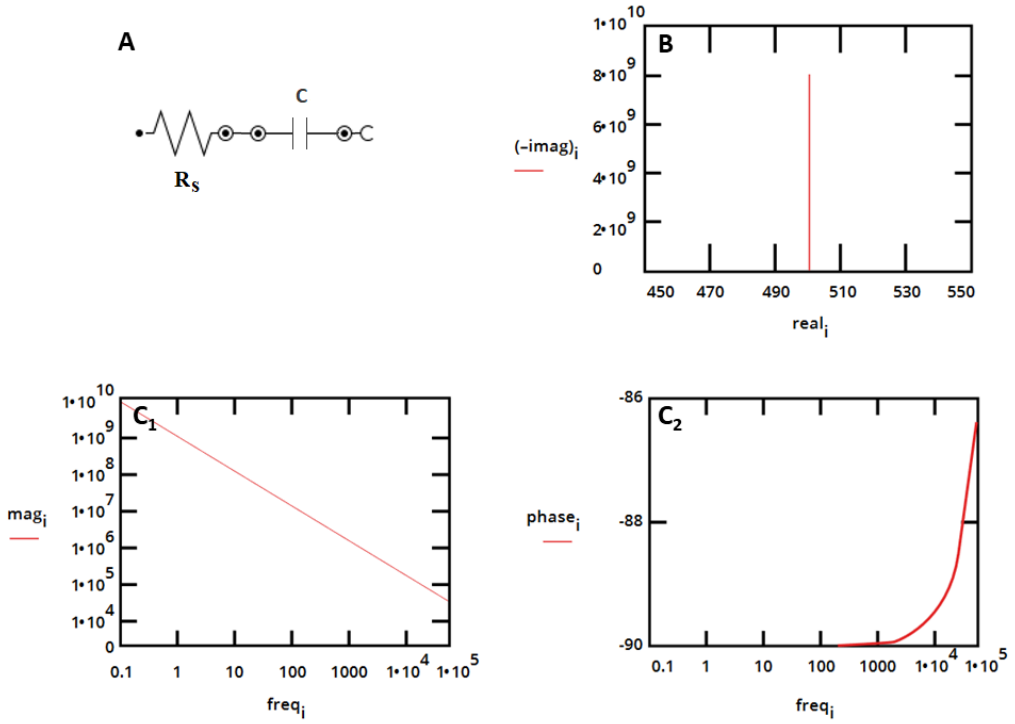

Fig. 2. 14: (A) *Typical RC equivalent electrical circuit for a purely capacitive coating;* ***(B)*** *Typical Nyquist plot for an excellent coating (RC equivalent electrical circuit);* ***(C)*** *Typical Bode modulus* ***(C_1)*** *and Bode phase* ***(C_2)*** *plots for an excellent coating (RC equivalent electrical circuit) (adapted from reference [331]).*

2.1.3.2.2. Randles Equivalent Circuit: The R(CR) Equivalent Circuit

The Randles equivalent circuit, *R(CR)*, is one of the simplest and most common equivalent circuit models. The simplified Randles equivalent circuit, *R(CR)*, is shown in Fig.2.15 A. It includes a R_s, a double layer capacitor (C_{dl}) or a constant phase element (*CPE*) in parallel with and a charge transfer resistance (R_1). An example of a Nyquist plot for this model is shown in Fig 2.15, in which were assigned the following values: R_s =520 Ω and C_{dl} = 2 μF, assuming a 1 cm^2 electrode undergoing uniform corrosion at a rate of 1 mm $year^{-1}$ [330]. The Nyquist Plot for a simplified Randles equivalent circuit is always a semicircle. Through this diameter is possible to estimate the value of the charge transfer resistance. The R_s can be estimated by reading the real axis value at the high frequency intercept. The real axis value at low frequency is the sum of the solution resistance and the charge transfer resistance (R_s + R_1). Fig 2.15 C shows the Bode plots for the same circuit. In the Bode phase plot (Fig. C_2), the phase angle (ϕ) does not reach 90 degrees as it would do for pure capacitive coatings. The phase shift would approach 90 degrees as more widely separated were the values of R_s and R_1[331].

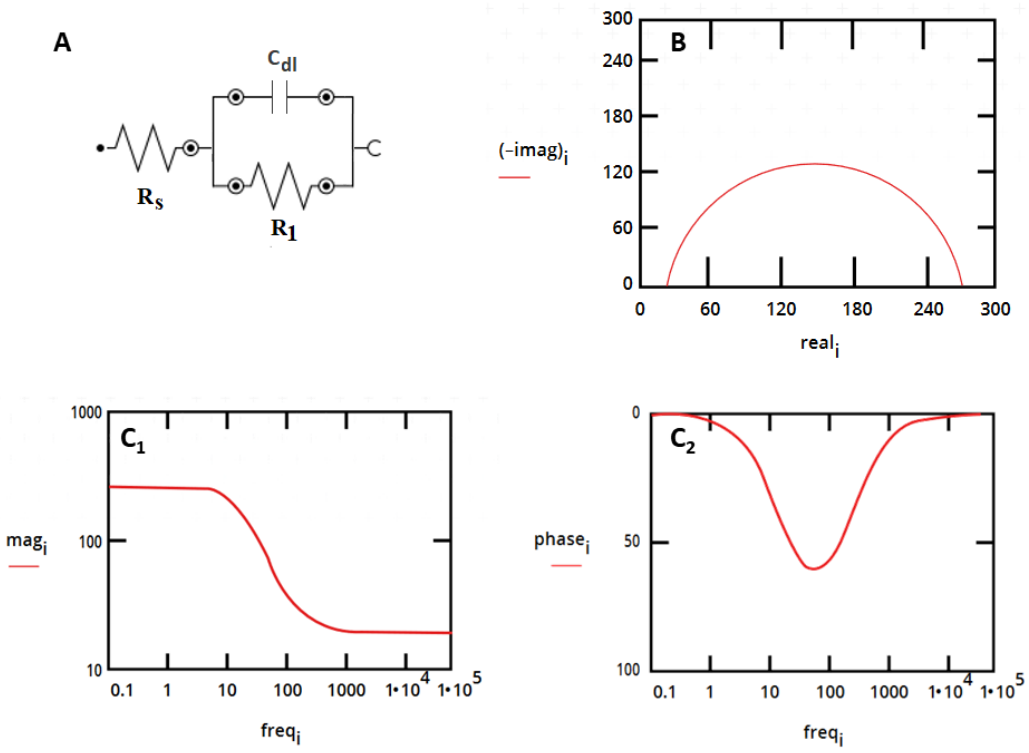

Fig. 2. 15: ***(A)*** *Typical simplified Randles equivalent circuit: R(CR);* ***(B)*** *Typical Nyquist plot for a simplified R_s(CR1) Randles equivalent circuit;* ***(C)*** *Typical Bode modulus* ***(C_1)*** *and Bode phase* ***(C_2)*** *plots for a simplified Randles equivalent circuit (adapted from reference[331]).*

When the capacitor is substituted for a CPE the Nyquist plots show a semicircle which is depressed by angle of (n-1) 90 degrees. In these cases, the double layer capacitance can be calculated by the equation suggested by Hsu and Mansfeld:

$$C_{dl} = Y^0(\omega_{max})^{n-1} \qquad \textbf{(Equation 2.22)}$$

With w_{max} corresponding to the frequency that can be extracted from a maximum in the semi-circle region of the Nyquist plot Fig. 2.9).

When the charge transfer process is very irreversible, no semi-circle is usually observed in the Nyquist plots but a sight curvature at low frequencies. In these cases, the proposal of Brug *et al.* is more adequate to use:

$$C_{dl} = (Y^0)^{1/n}\left(\frac{1}{R_{CT}} + \frac{1}{R_\Omega}\right)^{1-n/n} \qquad \textbf{(Equation 2.23)}$$

2.1.3.2.3. Mixed Kinetic and Diffusion Control: The [R(C[RW])] Equivalent Circuit

A simple kinetics electrode reaction in which both interfacial electron transfer kinetics and the semi-infinite diffusion processes are rate determining steps, is defined as mixed kinetic and diffusion control process. This model system is similar to the simplified Randles equivalent circuit described previously, but incorporates a Warburg impedance (Z_W) in series with the apparent R_1 and in parallel with the C_{dl} or a CPE. Furthermore, this circuit is also composed by a resistance, R_s (accounting for the ohmic resistance of the electrolyte solution), in series with the circuit elements formed by the CPE (or C_{dl}), R_1 and W. This model Randles-type equivalent circuit is schematically represented as $[R_s(C[R_1W])]$ or $[R_s(Q[R_1W])]$ and is shown in Fig 2.16A. R_s and W components represent the bulk properties of the electrolyte solution and diffusion of the applied redox probe, respectively, and are not affected by chemical transformations occurring at the electrode interface. The other two components of the circuit, i.e., CPE and R_1, depend on the dielectric and insulating features at the electrode/electrolyte solution interface. An example of a Nyquist plot for this model is shown in Fig 2.16B, in which were assigned the following values: R_s = 950 Ω; C_{dl} = 800 nF; R_1 = 8.79 kΩ; σ = 150 Ω $s^{-1/2}$. The Nyquist Plot for this Randles-type equivalent circuit presents a semicircle feature in the high-medium frequency region (ω→∞), where the total impedance is controlled by the interfacial charge transfer resistance ($R_1 >> Z_W$), and a linear region at low frequencies where the semi-infinite linear diffusion governs the process (Z_W). Generally, the semicircle is offset on the real axis at the high frequency intercept (ω→∞) by a value corresponding to the magnitude of the R_S. This is the intercept near the origin of the plot. The extrapolation of the semicircle in the real axis at the low frequency intercept (ω→0) corresponds to the sum of the solution resistance and the charge transfer resistance ($R_s + R_1$). The diameter of the semicircle is therefore equal to the charge transfer resistance (in this case 8.79 kΩ). For very fast electron transfer processes (very small R_1 value), the Nyquist plot reveals a very small semicircle and mainly the linear diffusing part of the impedance spectrum. In contrast, if the electron transfer process is the rate determining step (high R_1 value), the impedance spectrum only shows a large and well-defined semicircle (associated to irreversible or hindered electron transfer processes) without a straight line at low frequencies. The inclusion of a CPE element instead of an ideal capacitor slightly influences the Nyquist plot by presenting a slightly depressed semicircle. Fig 2.16C shows the Bode plots for the same circuit. In the Bode phase plot (Fig 2.16C_2), the phase angle (ϕ) approach a maximum

value of 45 degrees at relatively low frequencies. The phase shift would approach 90 degrees as more widely separated were the values of R_s and R_1 [331].

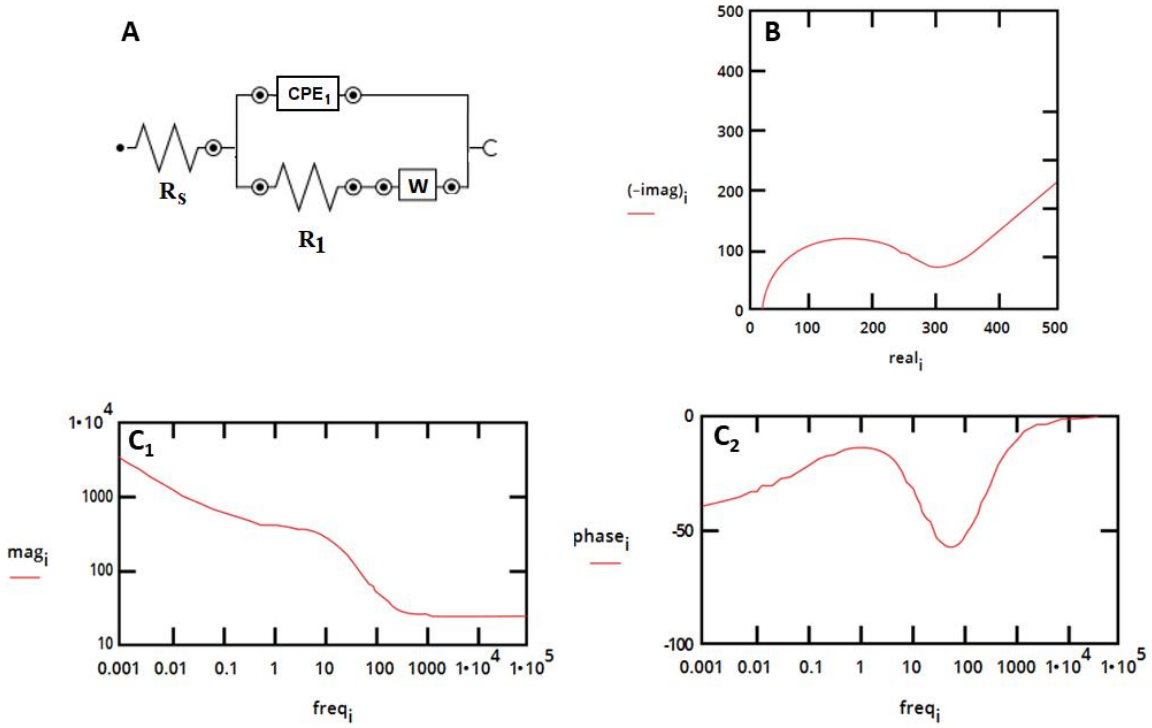

Fig. 2. 16: **(A)** Schematic representation of a Randles-type equivalent circuit for mixed kinetic and diffusion control: $[R_s(C[R_1W])]$; **(B)** Typical Nyquist plots for a Rundles-type equivalent circuit, $[R_s(C[R_1W])]$; **(C)** Typical Bode modulus **(C_1)** and Bode phase **(C_2)** plots for a $[R_s(C[R_1W])]$ Randles-type equivalent circuit (adapted from reference [331]).

2.1.3.2.4. Circuits with two time constants

The Nyquist plot showed in the Fig 2.17 two semicircles are observed which indicate the presence of two time constants in the system. This type of the diagram is characteristic of the most paint coatings degrade with time. In these cases, water penetrates into the coating and forms a new liquid/metal interface under the coating. Corrosion phenomena can occur at this new interface, resulting in more complex behaviour with a different time constant. The interpretation of this impedance data can be very complicated and some models can be used. Fig 2.17A illustrates an example of a circuit that can be used to fit an impedance curve with two time constants. The model consists of two circuits in series from R_1Q_1 and R_2Q_2 parallel combinations and the two are in series with the R_s between the alloy surface and the reference electrode[331].

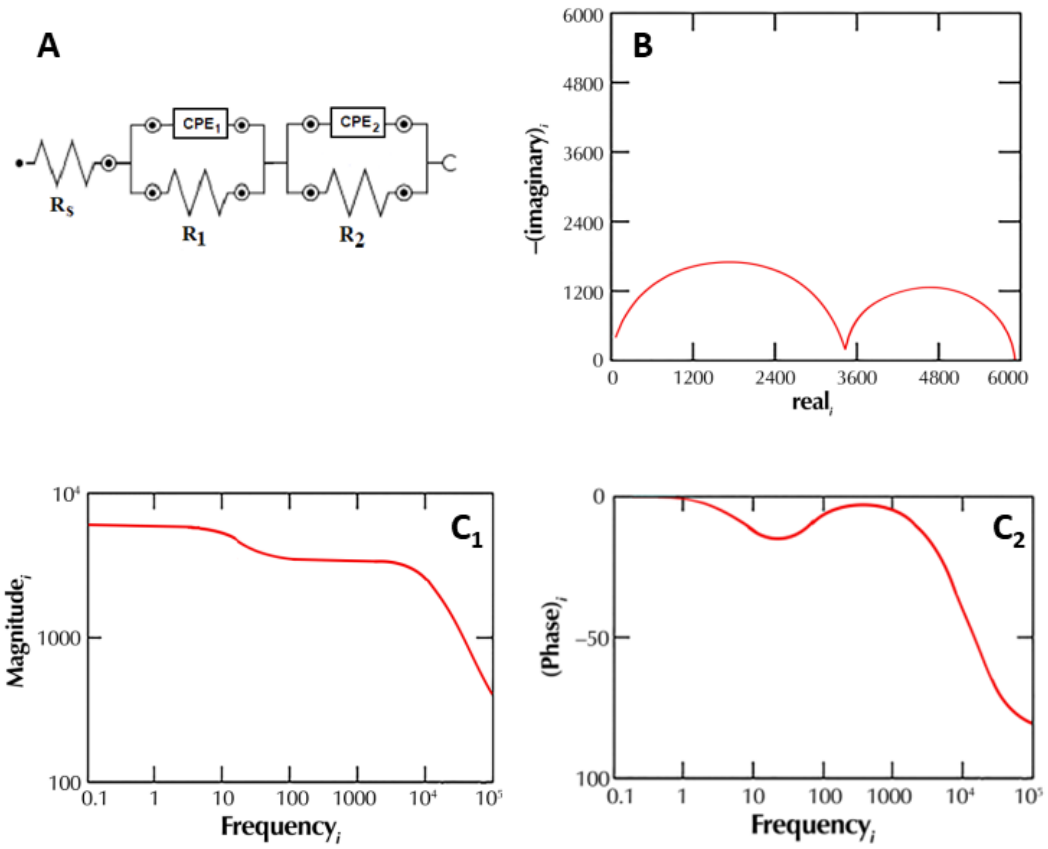

Fig. 2. 17: *(A) Schematic representation of a circuit with time constant: [Rs(R_1Q_1)(R_2Q_2)]; Typical Nyquist plots for a two time constant;* ***(C)*** *Typical Bode modulus* ***(C_1)*** *and Bode phase* ***(C_2)*** *plots for a: [Rs(R_1Q_1)(R_2Q_2)] circuit (adapted from reference [331]).*

2.1.3.3. Description of the Experimental Setup and Instrumentation

The experimental setup and instrumentation used for EIS measurements were the same previously described in the section *2.1.2.5.* for CV.

Impedance data were registered in the frequency range between 10 kHz and 0.1 Hz, using a single sine wave amplitude of 10 mV, and at the half-wave potential (+0.150 V) determined from the CVs in the presence of hexacyanoferrate redox probe. The impedance data were fitted to some equivalent circuit described in the previous section, using the Eco Chemie Frequency Response Analyzer (FRA) integrated in the GPES software.

2.2. Morphological Techniques

2.2.1. Atomic Force Microscopy

Atomic Force Microscopy (AFM) is an image technique to investigate surface properties and structure of materials in nanometric scale[332]. The AFM technique was developed by Binnig, Quate and Gerber in 1986, as a result of the improvement of the first Scanning Tunneling Microscopy (STM), intended to extend the possibilities of STM to insulating samples[333]. AFM allow to get images showing the arrangement of individual atoms or to see the structure of individual molecules. This technique can provide important information about the structure, and morphology of the surfaces modified with biological molecules. In addition, compared to conventional scanning electron microscopy, samples may be studied in a more natural state, as there is no requirement to scan in vacuum or for a conductive coating[332, 334, 335].

2.2.2. The basic working principle of the AFM

A typical AFM consists of a cantilever with an atomic dimensional tip (probe) at the free end, a laser, a photodetector and a scanner (Fig 2.18).

The basic working principle of AFM consists in maintaining a sharp probe in close contact with the sample surface by a feedback mechanism as it scans over the surface of the specimen[336]. The movement of the probe to stay at the same probe-sample distance is taken to be the sample's topography. As the tip approaches the surface, the atoms of the tip interact with the atoms and molecules of the sample, leading to the deflection of the cantilever. Two types of forces (short and long-range) are established between the interaction of tip and the surface. The short-range force that involves mainly quantum-chemical forces between the atomic orbitals of the tip and of the surface. The long-range interactions consist principally in van der Waals forces but also electrostatic, capillary, and magnetic forces[337]. The AFM measures the forces acting between a fine tip and a sample surface, carefully maintaining the force between the tip and surface at a set, low level, according to Hooke's law:

$$F = -k\,x \qquad \textit{(Equation 2.24)}$$

The vertical deflection of the cantilever (*x*) is directly proportional to the force exerted by the tip on the sample's surface (*F*), and depends on the cantilever's spring constant (*k*).

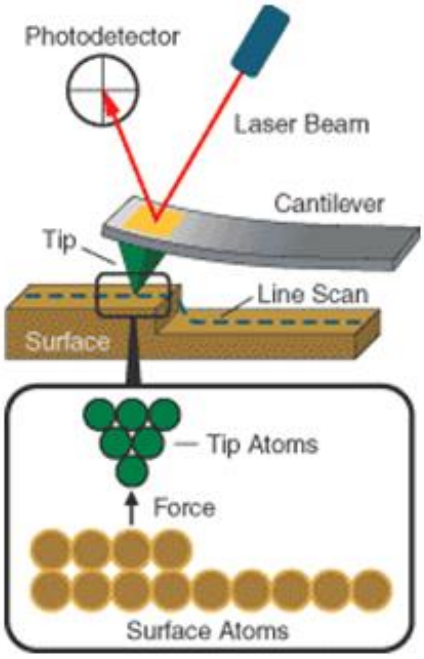

Fig. 2. 18: *Schematic representation of the basic working principle of the AFM in which the sample is scanned by a tip situated at the end of the cantilever. The resolution is limited by the shape of the tip (Adapted from reference [336]).*

The tip is attached to the free end of a cantilever and is brought very close to a surface. Attractive or repulsive forces due to the interactions between the tip and the surface will cause a positive or negative bending of the cantilever. This bending is detected by a laser beam, which is reflected from the backside of the cantilever[337].

Usually, the probe is formed by a silicon or silicon nitride cantilever with a sharp integrated tip, and the vertical bending (deflection) of the cantilever due to forces acting on the tip is detected by a laser focused on the back of the cantilever. The laser is reflected by the cantilever onto a distant photodetector. The movement of the laser spot on the photodetector gives a greatly exaggerated measurement of the movement of the probe. This set-up is known as an optical lever. The probe is moved over the sample by a scanner, typically a piezoelectric element, which can make extremely precise movements. The combination of the sharp tip, the very sensitive optical lever, and the highly precise movements by the scanner, combined with the careful control of probe-sample forces allow the extremely high resolution of AFM[336, 337].

2.2.2.1. Operating Principles of the Common Imaging Modes

When working with AFM, and depending on the application, normally consider two primary modes of operation, (a) static (also called contact mode) and (b) dynamic (non-contact mode, and tapping mode) modes, according to the kind of voltage (DC or AC) is driving the cantilever.

During scanning in the contact mode, the tip is in a soft physical contact with the surface with a specific height or under a constant force. The movement is strongly influenced by frictional and adhesive forces that can cause damage to the sample. When the spring constant of cantilever is less than surface, a constant bend in the cantilever is maintained. The force on the tip is repulsive. By maintaining a constant cantilever deflection (using the feedback loops) the force between the probe and the sample remains constant and an image of the surface is obtained[337].

In non-contact mode, the tip does not touch the sample, the cantilever oscillates just above the specimen during the scan. The tip-surface separation and the oscillation amplitude are in the order of 1 nm to 10 nm, which is the main difference to the tapping mode, where the oscillation amplitude of the tip is in the range of 20 nm to 200 nm. This operational mode is less destructive than contact mode. The cantilever oscillates nearby its resonance frequency. An electronic feedback loop provides the oscillation amplitude remaining constant so that a constant tip-sample interaction is conserved during the scan. Tapping mode is a key advance in AFM. This mode allows high resolution topographic imaging of samples that are easily damaged, loosely hold to their substrate, or difficult to image by other AFM modes. The tapping mode is very useful for soft surfaces, especially biological samples[337].

2.2.2.2. Description of the Experimental Setup and Instrumentation

AFM measurements were performed in air using a CSInstruments products Nano-Observer Atomic Force Microscope operating in dynamic tip deflection mode (Acoustic Alternating Current, AAC) (see Fig 2.19). An intermittent contact regimen (tapping mode) was selected in order to minimize typical tip sticking problems.

The AFM's experimental setup used in this work consisted of: an isolation chamber that offers thermal, acoustic, and atmospheric isolation to the AFM system; CSI AFM that holds the laser, photodiode detector, AFM scanner, AFM probe (cantilever and tip),

sample's plate, and the stepper motor; AC mode controller, Computer and NanoSolution 1.36.0.2908 software. Silicon cantilevers (ACT-SS-50, AppNano, USA) with a pyramidal shaped tip with height in the range of 14-16 μm, radius of curvature (ROC) lower than 5 nm, spring constant of 13-77 N/m, and a typical resonance frequency in the range 200-400 kHz were used for these purposes.

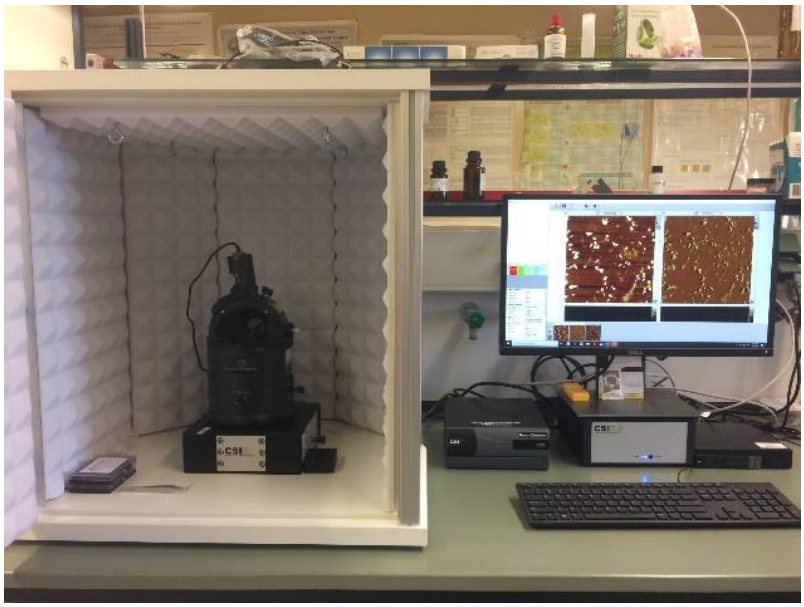

Fig. 2. 19: *Illustration of the experimental setup used for AFM measurements.*

2.2.3. Scanning Electron Microscopy

Scanning Electron Microscopy (SEM) is a widely technique used to investigate the micro-structure and chemistry of a range of materials.[338] SEM is another technique where only milligram quantities of material may be used to determine particle size, shape, and texture[339, 340].

2.2.3.1. The basic working principle of the SEM

The main components of the SEM include a source of electrons, electromagnetic lenses to focus electrons, electron detectors, sample chambers, computers, and displays to view the images (Fig 2.20)[338, 341].

Electrons are produced at the top of the column, accelerated down and passed through a combination of lenses to produce a focused beam of electrons which hits the surface of the sample. The position of the electron beam on the sample is controlled by scan coils situated above the objective lens. These coils allow the beam to be scanned over the surface of the sample. This beam scanning enables information about a defined

area on the sample to be collected. As a result of the electron-sample interaction, a number of signals are produced. These signals are then detected by appropriate detectors[337, 341].

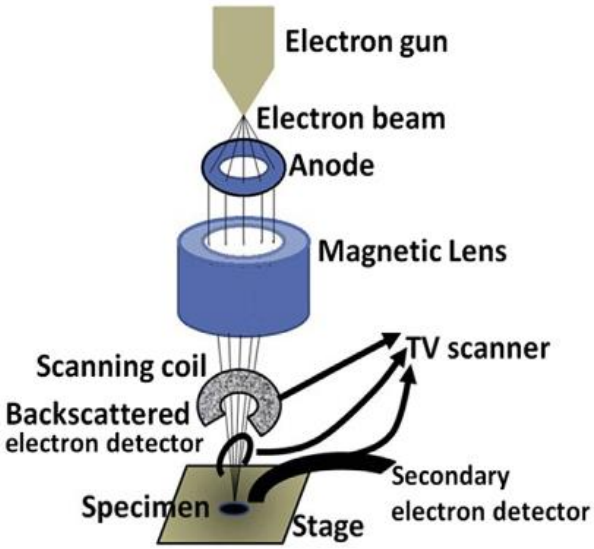

Fig. 2. 20: *Components of scanning electron microscopy (SEM) (adapted from reference [338]).*

SEM allows to obtain information about the samples being used by focusing a monochromatic beam of high-energy electrons, which is accelerated by a positive electric field, to generate a variety of signals at the surface of the sample. The electrons interact with the sample, they produce secondary electrons, backscattered electrons, and characteristic X-rays. The signals that derive from electron-sample interactions reveal information about the sample including topographic (texture of the sample's surface), morphologic (size and shape of the sample's surface), chemical composition (elemental and relative abundance) and crystallographic (atomic arrangement of the different components of the sample) information[340, 341]. In addition to topographical, morphological and compositional information, SEM can detect and analyze surface fractures, provide information in microstructures, examine surface contaminations, reveal spatial variations in chemical compositions, provide qualitative chemical analyzes and identify crystalline structures. SEM has a variety of applications in a number of scientific and industry-related fields, especially where the characterization of solid materials is of great relevance[334, 335, 340].

2.2.3.2. Description of the Experimental Setup and Instrumentation

SEM images were taken at CEMUP (Centro de Materiais da Universidade do Porto, Portugal), and acquired in the secondary electrons (SE) and backscattered electrons (BSED) modes with a field emission scanning electron microscope (Type FEI Quanta 400 FEG, see Fig 2.21) operating under high vacuum at accelerating voltages of 10 and 20 kV and working distances (WD) between 8.5 and 10.8 mm.

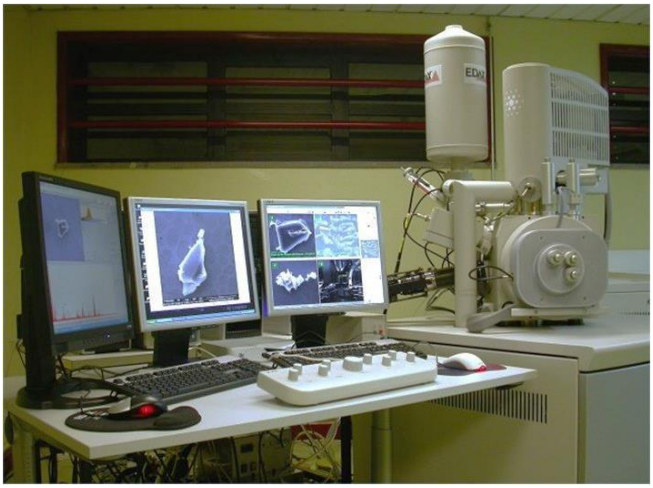

Fig. 2. 21: Illustration of the experimental setup used for SEM measurements.

The SEM's experimental setup used consisted of: an electron gun, vacuum chamber, anode, condenser and objective lens, electron beam, and sample chamber that includes the sample holder and the secondary, backscatter and X-ray detectors.

2.3. Spectroscopic Techniques

Spectroscopic techniques are extensively used in the study of the optical and electronic properties of different materials through studying the interaction between the radiated energy and materials. The different spectroscopic techniques are based on measuring absorption, scattering or emission of light that contains information about the properties of the materials[342].

2.3.1. ATR-FTIR spectroscopy

Fourier transform infrared (FTIR) spectroscopy is a technique to quantify and qualify organic substances in the solid, liquid, or gaseous state. Attenuated total reflectance (ATR) is one of the most used sampling techniques in FTIR spectroscopy because it is allowing to obtain high-quality spectra without requiring complex preparations of solid or liquid samples, unlike many other sampling techniques[343].

2.3.1.1. Principles of ATR-FTIR

The basic principle of ATR-FTIR is shown in Figure 2.22. The ATR crystal comprises an IR transparent material with a high refractive index and polished surfaces. The sample is in contact with the ATR crystal.

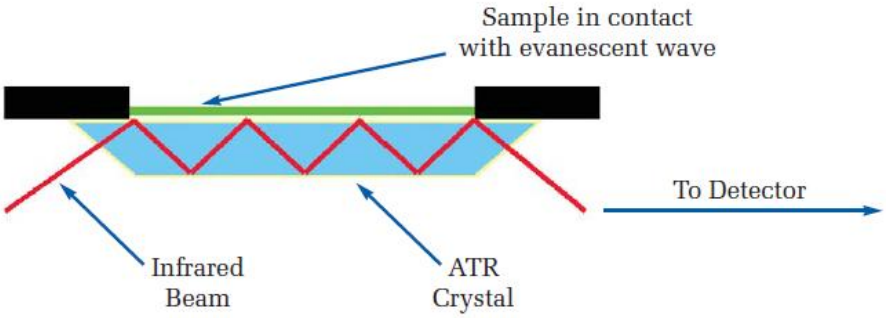

Fig. 2. 22: *The basic principle of the ATR-FITR (adapted from reference [343]).*

ATR FTIR spectroscopy is based on total internal reflection. The infrared (IR) radiation travels through the crystal and interacts with the sample on the surface in contact with the ATR crystal. Total internal reflection occurs due to the differences in refractive indices between the crystal and sample. The total internal reflection forms the so-called "evanescent wave" which extends into the sample. Based on the sample's composition, a small part of the infrared light is absorbed when the evanescent wave interacts with the sample, resulting in a slightly attenuated total reflection[342, 343]. After this process, an attenuated radiation is directed from the crystal to the normal beam path in the spectrometer, being measured by the detector, thus originating the sample spectrum.
In order to achieve a high quality of spectra, some aspects must be considered:[343, 344]

- Good contact between sample and ATR crystal because the evanescent wave penetrates only up to a specific number of microns into the sample.

- The refractive index of the crystal must be significantly higher than that of the sample (the typical refractive indices for ATR crystals are around 2 - 4 and typical values for organic substances such as polymers range from ca. 1.2 to 1.5, a large number of IR-active samples can be measured).

2.3.1.2. Description of the Experimental Setup and Instrumentation

ATR-FTIR spectra were taken using a Bruker Tensor 27 spectrometer (Fig 2.23). In order to characterize the nanocomposites of graphene, ATR-FTIR spectroscopic measurements were performed at room temperature (≈ 20 ºC) in the wavelength range between 600 to 2000 cm^{-1}.

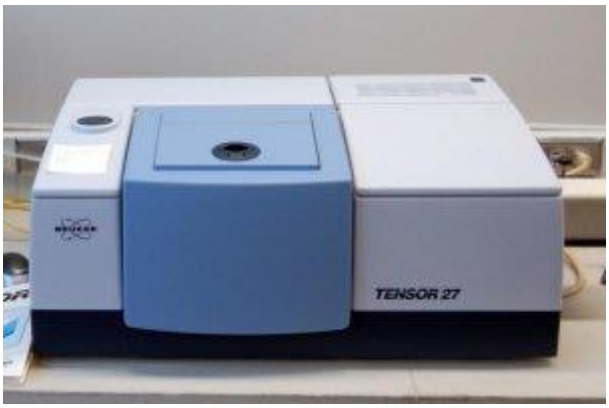

Fig. 2. 23: *Illustration of the experimental setup used for ATR-FITR measurements.*

2.3.2. X-ray Photoelectron Spectroscopy - XPS

X-ray Photoelectron Spectroscopy (XPS) is the most widely used surface analysis technique which analyses the average surface chemistry of a sample up to a depth of approximately 3-5nm. This quantitative spectroscopy technique allow measures the elemental composition, empirical formula, atomic concentrations and chemical states of elements present at a samples surface[345].

2.3.2.1. Principle of XPS

The principle of XPS involves a single electron process which is based on the photoelectron effect[343]. X-ray Photoelectron Spectroscopy uses an irradiation of a soft

X-ray (monochromatic Aluminum Kα or non-monochromatic Magnesium Kα x-rays) on the sample surface, and measuring the kinetic energy of the photoelectron emitted from an atom at the sample's surface. The binding energy of these electrons are measured and are characteristic of the elements and associated chemical bonds (chemical state) in the top few atomic layers of the material[343, 345].

The electrons ejected are analysed in the XPS detector through measuring the electrons kinetic energy which provides the information to determine the kind of elements present in the sample. Fig 2.24 illustrates the schematic representation of the x-ray photoelectron process[346].

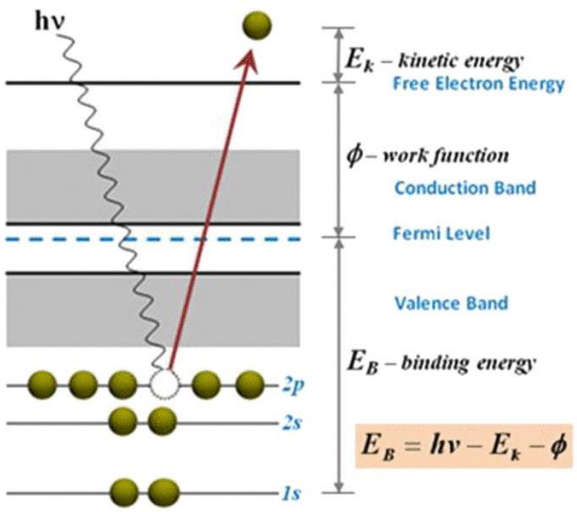

Fig. 2. 24: *Schematic representation of the X-ray photoelectron process (adapted from reference [346]).*

The kinetic energy of the ejected electrons is named E_k, and it is determined by the following equation:

$$E_K = h\upsilon - E_b - \phi \qquad \textbf{(Equation 2.27)}$$

Where the binding energy of an electron is represented by E_b, the energy of a photon is given by hυ where h represents the plank's constant and υ is the frequency of a photon. The work function is represented by the symbol ϕ which is the minimum energy needed to remove an electron from a solid[345, 346].

XPS spectra exhibitions a number of emitted electrons against their kinetic energy. This surface analysis technique requires high vacuum (P ~ 10^{-8} millibar) or ultra-high vacuum (UHV; P < 10^{-9} millibar) conditions, although a current area of development is ambient-pressure XPS, in which samples are analysed at pressures of a few tens of millibar. The XPS method has been extensively used on solid surfaces and as non-destructive method of analysis of compounds.

2.3.2.2. Description of the Experimental Setup and Instrumentation

X-ray Photoelectron Spectroscopy (XPS) was performed in two different spectrometers. In the case of GO and rGO (chapter 4) and rGO-Fe_3O_4 NPs conjugate (chapter 5), X-ray photoelectron spectroscopy, was performed at CEMUP (Centro de Materiais da Universidade do Porto). A Kratos Axis Ultra HSA equipped with an achromatic Al (K_α) X-ray source (15 kV, 90 W) and a 500 mm Rowland circle monochromator was used for XPS measurements (Fig 2.25). The spectra were analyzed with the Casa XPS software (v.2.3.18PR1.0) using Shirley-type backgrounds.

Fig. 2. 25: *Illustration of the experimental setup used for XPS measurements.*

For the characterization of rGO-Ni NPs Conjugate (chapter 6), the XPs was taken in an ESCALAB 200A spectrometer (VG Scientific, UK) equipped with an achromatic Al (Kα) X-ray source of 15 kV (300 W) and operated in CAE mode (20 eV pass energy). The analysis of the spectra was done with the XPS Peak 4.1 software (Gaussian–Lorentzian peak shape). For deconvolution, a non-linear least squares fitting routine (plus Shirley-type background subtraction) was used.

Chapter 3 – Reagents, Solutions, sample preparation and surface modification

In the Chapter 3 a complete description of all the reagents, solutions, samples and surfaces prepared for the characterization studies will be given. A detailed description of the experimental techniques used in this work is presented too.

3.1. Chemicals

The chemicals used in this experimental work are shown in Table 3.1, together with the information about their purity and supplier. All the chemicals were analytical grade and used as received without further purification. Nitrogen gas (N_2, Air Liquide, purity ≥ 99.999%) was used to remove oxygen from the electrochemical cell, and to dry the electrode surface.

Table 3. 1: *List of all the reagents used in the course of this work.*

Chemicals	***Formula***	***Purity***	***Supplier***
Ethanol	C_2H_5OH	*96% vol.*	*Aga S.A.*
Acetone	CH_3COCH_3	*n.a.**	*VWR*
Sodium dihydrogen phosphate	NaH_2PO_4	*≥ 99%*	*Fluka*
Sodium hydrogen phosphate	Na_2HPO_4	*≥ 99%*	*Sigma- Aldrich*
Sodium chloride	*NaCl*	*≥ 99%*	*Sigma- Aldrich*
Potassium hexacyanoferrate (II) tryhidrate	$[K_4Fe(CN)_6]•3H_2O$	*≥ 99.5%*	*Fluka*
Potassium hexacyanoferrate (III)	$[K_3Fe(CN)_6]$	*> 99%*	*Merck*
Sulfuric acid	H_2SO_4	*95-97%*	*Fluka*
Hydrochloric acid	*HCl*	*> 37%*	*Sigma- Aldrich*
Hydrogen peroxide	H_2O_2	*30% (v/v)*	*Sigma- Aldrich*
Potassium chloride	*KCl*	*99%*	*Fluka*
Glacial acetic acid (AcH)	CH_3COOH	*≥ 99%*	*Sigma- Aldrich*
Sodium acetate (NaAc)	CH_3COONa	*> 99%*	*Merck*
Chitosan, 95% of degree of deacetylation (Chit95)	$(C_8H_{15}NO_6)_{0.05}(C_6H_{13}NO_5)_{0.95}$	*n.a.**	*Primex, Iceland*

Chemicals	Formula	Purity	Supplier
Iron (III) acetylacetonate	$Fe(ACAC)_3$	97%	Sigma- Aldrich
Oleic Acid	$(C_{18}H_{34}O_2)$	≥99%	Sigma- Aldrich
1, 2-hexadecanediol	$(CH_3(CH_2)_{13}CHOHCH_2OH)$	90%	Sigma- Aldrich
Oleylamine	$CH_3(CH_2)_7CH=CH(CH_2)_7CH_2NH_2$	70%	Sigma- Aldrich
Phenyl ether	$(C_6H_5)_2O$	99%	Sigma- Aldrich
n-hexan	$H_3C(CH_2)_4CH_3$	n.a.*	VWR
Graphite powder	n.a.*	n.a.*	Sigma- Aldrich
Sodium nitrate	$NaNO_3$	99%	Sigma- Aldrich
Potassium permanganate	$KMnO_4$	99%	Sigma- Aldrich
Sodium hydroxide	NaOH	97%	Sigma- Aldrich
Citric acid	$HOC(COOH)(CH_2COOH)_2$	99.5%	Sigma- Aldrich
L-ascorbic acid	$C_6H_8O_6$	99%	Sigma- Aldrich
Nickel chloride hexahydrate	$NiCl_2.6H_2O$	99.9%	Sigma- Aldrich
Sodium borohydride	$NaBH_4$	99.99%	Sigma- Aldrich
Hydrazine hydrate	$NH_2NH_2 \cdot xH_2O$	60-67%	Sigma- Aldrich
Graphene oxide	CxOyHz	n.a.*	Graphenea
Reduced Graphene Oxide	CxOyHz	n.a.*	Graphenea
D-glucose	$C_6H_{12}O_6$	≥99.5%	Merck
Uric Acid	$C_5H_4N_4O_3$	≥99%	Sigma-Aldrich
Catechol	$C_6H_6O_2$	≥99%	Sigma-Aldrich
Glucose oxidase	$C_{17}H_{26}Cl_2N_2O_3$	n.a.*	Fluka

Chemicals	Formula	Purity	Supplier
Laccase	$C_{44}H_{69}N_{11}O_{20}$	n.a.*	Sigma-Aldrich
Bisphenol A	$C_{15}H_{16}O_2$	≥99%	Aldrich
Naphthol-(1)	$C_{10}H_7OH$	≥99%	Riedel-de-Haen
Benzene	C_6H_6	99.8%	Merck
4 - Nitrophenol	$C_6H_5NO_3$	≥99%	Sigma-Aldrich
Di-n-butyl phthalate	$C_{16}H_{22}O_4$	99%	Sigma-Aldrich
Gold Nanoparticles	AuNPs	n.a.*	Nanovex
Alloyed Gold-Silver Nanoparticles	AuAgNPs	n.a.*	Nanovex

** n.a.: not available*

3.2. Solutions

All the solutions used in this work were prepared following standard procedures are described in Table 3.2, together with their pH and concentration. All the aqueous solutions were prepared in ultrapure water with a resistivity of 18 MΩ.cm (at 25 ºC) obtained from a Milli-RO 3 Plus coupled with a Milli-Q water purification system and stored at 4 ◦C. Ultrapure water was also used for rinsing procedures. A Methrom 654 pH Meter was used for pH measurements in all the cases.

Table 3. 2: *List of all the solutions used in this work, and their corresponding pH and concentration.*

Solute	Solvent	pH	Concentration
Na_2HPO_4	*Ultrapure water*	*7.4*	*50 mM*
NaH_2PO_4			*50 mM*
NaCl			*150 mM*

Solute	Solvent	pH	Concentration
$[K_4Fe(CN)_6]•3H_2O$	*Na_2HPO_4 / NaH_2PO_4 50 mM buffer + 150 mM NaCl*	*7.4*	*2 mM*
$[K_3Fe(CN)_6]$		*7.4*	*2 mM*
NaAc AcH	*Ultrapure water*	*5.0*	*0.1 M*
NaAc AcH	*Ultrapure water*	*4.5*	*0.1 M*
Chit95	*NaAc / AcH 0.1 M buffer in ultrapure water*	*5.0*	*5 mg/mL*
Glucose oxidase	*Na_2HPO_4 / NaH_2PO_4 50 mM buffer + 150 mM NaCl*	*7.4*	*1 mg/mL*
Laccase	*NaAc / AcH 0.1 M buffer in ultrapure water*	*4.5*	*10 mg/mL*
Citrate	*Ultrapure water*	*6.5*	*2 mg/mL*

3.3. Synthesis

3.3.1. Synthesis of Graphene oxide (GO)

Graphene oxide was synthesized by Dr. Rahul Krishna and Prof. Elby Titus (University of Aveiro) following the modified Hummers method, described in the litherature[61]. In this method, 250 mg of graphite flakes was dispersed in ice cooled conc. H_2SO_4 (12 mL) by stirring for 30 min. Then, 200 mg of $NaNO_3$ and 1.5g $KMnO_4$ were then added slowly into the solution. This mixture was stirred for 2 h and the temperature of the reaction was maintaining lower than 35 °C. After this time, the temperature was increased to 35 °C and excess Milli Q water was added into the solution. Subsequently, the suspension was heated to 98 °C for 30 min. To eliminate excess of $KMnO_4$, 5 mL of H_2O_2 (30% v/v) was dropped slowly and stirred for 10 minutes. The resultant suspension was

centrifuged (3000 rpm), filtered and washed with Milli Q water and diluted HCl (until the pH of the filtrate was neutral) to remove remaining impurities and oxidizing agents. The resulting filter power was re-dispersed in ethanol to make the 0.5 mg/mL dispersion[347].

3.3.2. Synthesis of Fe_3O_4NPs

The synthesis of Fe_3O_4 NPs (nanoparticles) was produced by Dr. Rahul Krishna and Prof. Elby Titus (University of Aveiro) following a method previously described in the literate[347, 348]. 1,2-hexadecanediol, oleic acid, cis-1-amino-9-octadecene, and iron (III) acetylacetonate were placed in a 4-neck round bottom flask at 1.7:1:1:0.3 molar ratio with 22 mL of phenyl ether (PE) and stirred for 15 min under N_2 flow at room temperature (RT). After that, the mixture was heated to 200 ^oC for 30 min and further heated up to reflux point of PE (265 ^oC) for more 45 min. The reaction was performed under N_2 atmosphere and stirring. After, a black-brown mixture appeared inside of glass flask indicated the formation of Fe_3O_4 NPs. At this point, the black-brown dispersion was cooled down and ethanol was added to the mixture to precipitation the black material. Then, the product was separated by centrifugation (15000 rpm – relative force, RCF=25155 x g) in a Beckman centrifuge equipped with a TA-15-1.5 rotor (maximum radius: 100 mm) and 2-3 times treated with ethanol to ensure the removal of impurities.

3.3.3. Synthesis of Fe_3O_4/rGO nanocomposite

The nanocomposite was synthesized by Dr. Rahul Krishna and Prof. Elby Titus (University of Aveiro) following a method previously described in the literature[347]. According to it, GO sheets and Fe_3O_4 NPs were pre-synthesized and submitted to alkaline reduction in one pot (Scheme 1).

The synthesized Fe_3O_4 NPs were re-dispersed under sonication in a 0.5 mg/mL dispersion of GO (pre-synthesized from graphite flakes – section 3.3.1) in ethanol. Later, 100 mg of the citric acid and 100mg of the L-ascorbic acid were added to the mixture and, then, the mixture was stirred at 55 ^oC for 12 h under N_2 atmosphere. At this point, 50 mL of NaOH 1 M were added and the solution was stirred for another 6 h at 95 ^oC. The product was finally centrifuged at 10000 rpm (RCF=1118 x g), the solid was filtered, washed with ethanol and doubled-distilled water and, then vacuum dried for 24 h to obtain the hybrid rGO-Fe_3O_4 NPs composite.

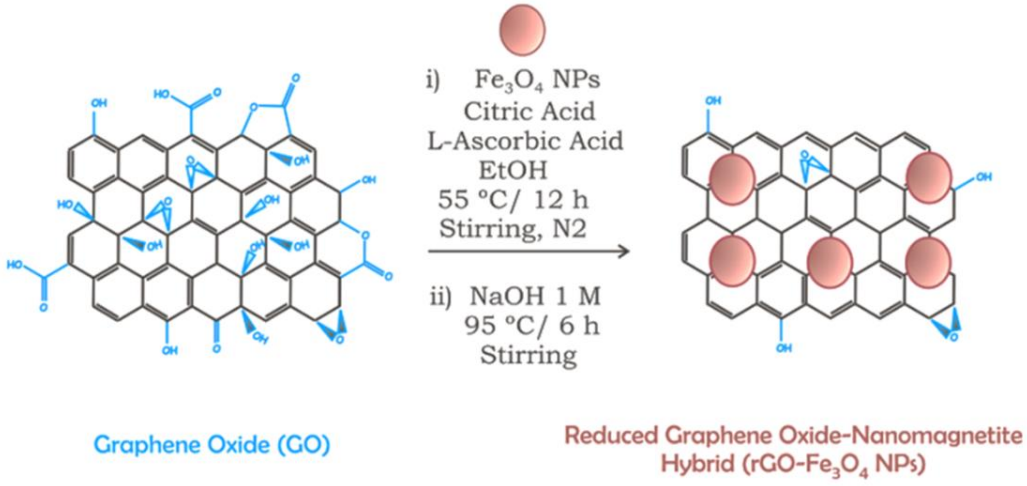

Scheme 1: *Modified Hummers method was followed to synthesize the rGO-Fe_3O_4 NPs hybrid conjugate*

3.3.4. Synthesis of Ni/rGO nanocomposite

GO was synthesized from graphite powder through a modified Hummers method describe in the section 3.3.1. The nanocomposite was synthesized by Dr. Rahul Krishna and Prof. Elby Titus (University of Aveiro) following a method previously described in the literature[116]. Ni/rGO hybrid sheets were grown in situ as follows: 100 mL of GO aqueous dispersion (1.0 mg/mL) were placed in a 4-neck round bottom flask and mechanically stirred at RT. Subsequently, 600 mg of nickel chloride hexahydrate ($NiCl_2.6H_2O$) were added and the temperature was gradually increased to 85 ºC. Then, 18 mL of hydrazine hydrate (65%) were slowly poured into the reaction mixture and stirred for 25 min in Ar atmosphere. Afterwards, 450 mg of sodium borohydride (NaBH4) were very slowly added under stirring. Finally, 25 mL of a 1 M sodium hydroxide (NaOH) solution were added and stirred for further 2h (Scheme 2). The product was filtered and washed with ethanol and doubled-distilled water to remove impurities. Then, it was vacuum-dried at 100 ◦C for 3 h to obtain the Ni/rGO nanocomposite powder.

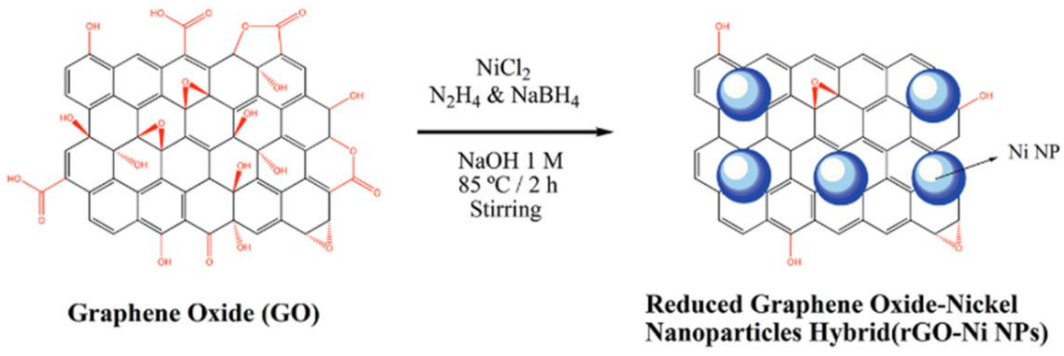

Scheme 2: *Modified Hummers method was followed to synthesize the rGO-Ni NPs hybrid conjugate.*

3.4. Experimental Setup & Instrumentation and Sample Preparation

3.4.1. ATR-FITR Spectrophotometric Analysis

Attenuated total reflectance Fourier transform infrared (ATR-FTIR) spectra were taken using a Bruker Tensor 27 spectrometer. In order to characterize the nanocomposites of graphene, ATR-FTIR spectroscopic measurements were performed at room temperature (≈ 20 ºC) in the wavelength range between 600 to 2000 cm^{-1}.

Before the characterization of the graphene derivatives, the ATR-FITR spectrometer was calibrated according to the following steps: initially the white line was drawn and then the solid sample of the conjugate was placed on the surface of the ZnSe crystal. The solid sample was pressed in order to guarantee perfect contact between the sample surface and the crystal. The spectrum was obtaining.

3.4.2. AFM and SEM Surface Preparation and Modification

AFM and SEM measurements were performed by using the previously modified GCE. In summary, after the modification of each layer, the GCE was rinsed with ultrapure water, dried under a soft stream of N_2, and placed in the microscope holder to be visualized by AFM or SEM.

3.4.3. Electrochemical Surface Preparation and Modification

Electrochemical measurements were performed on a Voltalab PGZ301 potentiostat (Radiometer Analytical) controlled by Voltamaster 4 software. All electrochemical experiments were carried out under a soft stream of N_2 in a conventional three-electrode electrochemical cell system (enclosed in a grounded Faraday cage to reduce electrical noise). Pt and Ag wires were used as counter and pseudo-reference electrodes and a glassy carbon electrode (GCE, Metrohm, 6.1204.300, area: 0.06 cm^2) was used as working electrode. The electrochemical measurements were carried out in 0.05 M PBS (pH 7.4) and PBS + 2 mM $K_4[Fe(CN)_6]\cdot 3H_2O$ + 2 mM $K_3[Fe(CN)_6]$ and CV was performed at 0.05 $V\cdot s^{-1}$ in the potential range -0.8/+0.9 V and -0.3/+0.6 V, respectively. The presence of the $[Fe(CN)_6]^{4-/3-}$ probes allowed for the internal calibration of the pseudo-

reference electrode. In this sense, the half-wave potential ($E_{1/2}$) showed, in all cases, excellent agreement with the tabulated standard potential (E° vs Ag/AgCl/NaCl sat.). The impedance spectra were registered at +0.15 V. A sine wave of 10 mV amplitude and frequency decreasing from 10^4 to 10^{-1} Hz, was used in the experiments.

For the electrochemical experiments, GCE was previously cleaned following a procedure based on the combination of mechanic polish and electrochemical cycling. GCE was polished with 3 F µm Polycrystalline diamond suspension to a mirror finish and washed in water and ethanol. Then, cyclic voltammetry was performed in H_2SO_4 0.5 M and the result compared to the typical response of clean GCE. The CV of clean GCE was compared with other CVs registered for a clean profile until the electrochemical reproductively performance was found. At this point, the cleaned GCE was ready to further modifications.

3.4.3.1. Preparation of GO, rGO and rGO-Fe_3O_4 NP films

Thin films of GO, rGO and rGO-Fe_3O_4 NPs (used in the chapter 4) were deposited onto the surface of a GCE by the drop-casting method (scheme 3). GO dispersion (0.5 mg·mL^{-1}) and rGO powder were purchased from Graphenea (San Sebastián, Spain) and used without further purification. rGO-Fe_3O_4 NP was synthesized according the procedure in the section 3.3.3. GO dispersion was diluted in water (concentration range between 0.1 to 500.0 µg/mL) and rGO was dispersed in DMF in the same range of concentrations used for GO. The rGO-Fe_3O_4 NPs was dispersion in ethanol (concentration range 0.20-20.0 mg/mL). Then, 10µL of GO, rGO and rGO-Fe_3O_4 NPs dispersion were spread onto the GCE surface and air dried. At this point, the GCE-modified was ready to used.

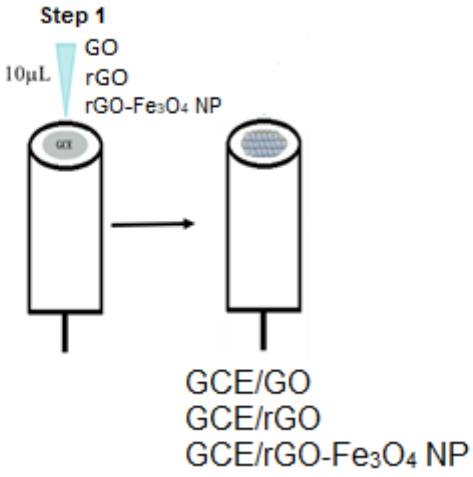

Scheme 3: *Schematic showing the different steps used for the preparation of the GO, rGO and rGO-Fe_3O_4 NP films onto a clean GCE.*

3.4.3.2. Preparation of Fe_3O_4/rGO/Chit95/TvL Films

Fe_3O_4/rGO/Chit95/TvL nanocomposite film was mounted on it following a sequential drop-casting procedure (scheme 4). In first place, 10 µL of the rGO-Fe_3O_4 NPs dispersion in ethanol (concentration range 0.20-20.0 mg/mL) were spread and dried in the air. In the second step, 10 µL of a 5 mg/mL dispersion of chitosan (degree of deacetylation: DD=95%, average molecular mass: 150-200 kDa, Primex, Iceland; hereinafter Chit95) in 0.1 M acetate buffer (AB) pH 5 were subsequently casted. Once dried, 10 µL of a 10 mg/mL solution of laccase from Trametes versicolor (>0.5 $U \cdot mg^{-1}$, Sigma Aldrich; hereinafter TvL) in 0.1 M AB (pH 4.5) were dropped on it and dried in the air. At this point, the GCE-modified was ready to used (chapter 5).

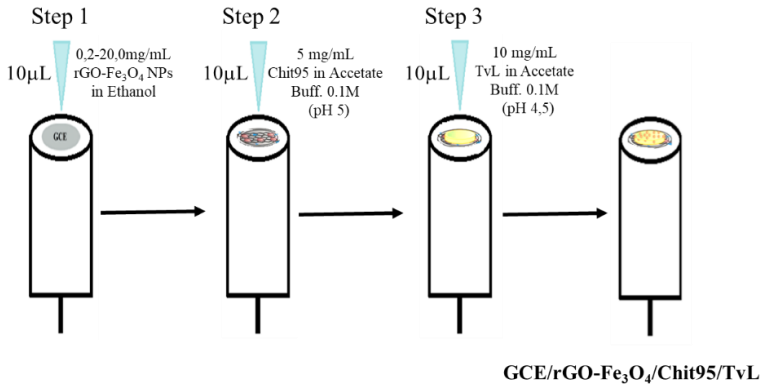

Scheme 4: *Schematic showing the different steps used for the preparation of the rGO-Fe_3O_4/Chit95/TvL nanocomposite film onto a clean GCE.*

3.4.3.3. Preparation of Ni/rGO/Chit95/GOx Films

Ni/rGO/Chit95/GOx nanocomposite film was deposited onto a GCE following a sequential drop-casting procedure. GCE was modified in three steps (scheme 5). In the first, 10 µL of a 1 $mg \cdot mL^{-1}$ rGO-Ni NPs dispersion in ethanol were spread on it and air dried. Afterwards, 10 µL of a 5 $mg \cdot mL^{-1}$ dispersion of chitosan (deacetylated to a degree of DD=95%, average molecular mass: 150-200 kDa, Primex, Iceland; hereinafter referred to as Chit95) in acetate buffer 0.1 M (pH 5; AB) were casted. Once dried, 10 µL of a 10 $mg \cdot mL^{-1}$ solution of glucose oxidase, GOx in 0.05 M phosphate buffer + 0.15 M NaCl (pH 7.3; PBS) were dropped. To enhance the enzyme loading, GOx was casted twice. At this point, the GCE-modified was ready to used (chapter 6).

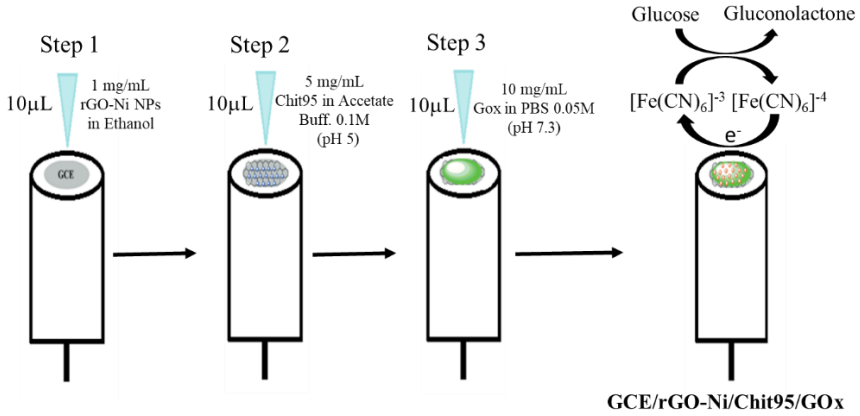

Scheme 5: *Schematic showing the different steps used for the preparation of the rGO-Ni/Chit95/GOx nanocomposite film onto a clean GCE.*

Part B - Results & Discussion

Chapter 4 - Assembly of Thin Graphene Films on Electrode Surfaces: Conformation, Impedance, and Electron Transfer Studies

This chapter explores the links between structure, morphology, and the electron transfer (ET) properties of solid electrodes modified with 2D GNMs. After characterization of the GO, rGO, and rGO-NPs materials used in the modification, thin films of those were deposited onto a freshly prepared GCE from aqueous dispersions. The films were assembled since a wide range of concentrations and subsequently studied by AFM, SEM, and electrochemical methods in presence of $Fe(CN)_6^{3-/4-}$ redox probes. While increasing the load of GO resulted in a progressive blockage of the ET processes; the modification with rGO exhibited a couple of changes in the redox response of the electrodes.

The results shown in this chapter will be subject of an article to be published in a peer-reviewed journal. The student performed the all experimental part, as well as writing the first draft of the paper.

4.1. Contextualization

Carbon-based electrodes have been extensively studied in both analytical and industrial electrochemistry due to their good electronic conductivity, large potential window, and electrocatalytic activity for many important redox reactions[349]. For the preparation of these electrodes, usually an inert substrate, such as glassy carbon (GC) is used. The modification of GC electrode substrates with different carbon materials such as carbon nanotubes (CNTs)[350] and graphene and derivatives[351], is carried out to improve the electrochemical characteristics and performance of the fabricated electrode. The use of graphene as an electrode material has been widely studied due to its extraordinary physical, electrical, and chemical properties and its advantageous behaviour for a wide variety of electrochemical applications[352]. However, it must be noted that fundamental reports have emerged demonstrating that graphene might not provide a significant advantage as an electrode material as first thought[353, 354]. Pumera *et al.*[354] shows that single-, few-, and multi-layer of graphene does not provide a significant advantage in terms of sensitivity and repeatability over graphite microparticles to the electro-analytical detection of uric acid. The fundamental understanding of the ET at graphene is the key role to understand this contradictory behaviour.

Several studies demonstrated that the origin of ET in graphene is through from two heterogeneous structural contributions, namely the peripheral edge plane and basal plane-like sites/defects[355, 356], where the ET kinetics of the edge defect sites is anomalously faster over that of the basal sites, which in comparison can be regarded as relatively electrochemically inert[357, 358], The distinct morphology of graphene can originate different ratios of edge to basal plane content and this gives rise to unique electronic properties that dictate the electrochemical responses. Brownson *et al.*[353] studied the effect of the different ratios of edges, basal planes, and layer numbers of CVD graphene on a conductive substrate. The results showed that graphene exhibits slow ET towards the electrochemical probes studied, effectively blocking underlying ET of the supporting electrode substrate likely due to its large basal and low edge plane content[356]. The focus of this work is to study the electrochemical performance of graphene derivatives as an electrode material and to understand the effect that the arrangement of the sheets has on the electrochemical response.

4.2. Results and discussion

4.2.1. Characterization of GO and rGO

4.2.1.1. ATR-FTIR Spectroscopy

The commercial forms of graphene employed for the preparation of the ultrathin films were previously characterized by different techniques. In the first place, powder samples of GO and rGO were analyzed by ATR-FTIR. As shown in Fig. 4.1, the spectrum of GO (black solid line) exhibits a broad band around 3300 cm^{-1} (attributed to O-H stretching in hydroxyl groups and/or adsorbed water) plus a series of peaks due to different vibrations: 1730 cm^{-1} (symmetric C-O stretching in carbonyl moieties); 1622 cm^{-1} (asymmetric O-C-O stretching in deprotonated carboxylic acids); 1226 cm^{-1} (C-O-C stretching in epoxy groups); 1049 cm^{-1} (C-O stretching in hydroxyl-substituted C atoms); and 976 cm^{-1} (asymmetric ring deformation in epoxides)[359, 360]. The intensity of some of these peaks decreases dramatically (while others entirely disappear) in the spectrum of rGO (red line). As discussed in Chapter 1, the chemical reduction of GO involves the extensive removal of O-groups and the partial restoration of sp^2-hybridized C-C bonds in the sheets. Hence, the ATR-FTIR evidence in the figure strongly supports that the rGO investigated in this work presents a relatively high degree of reduction compared to its commercial GO counterpart.

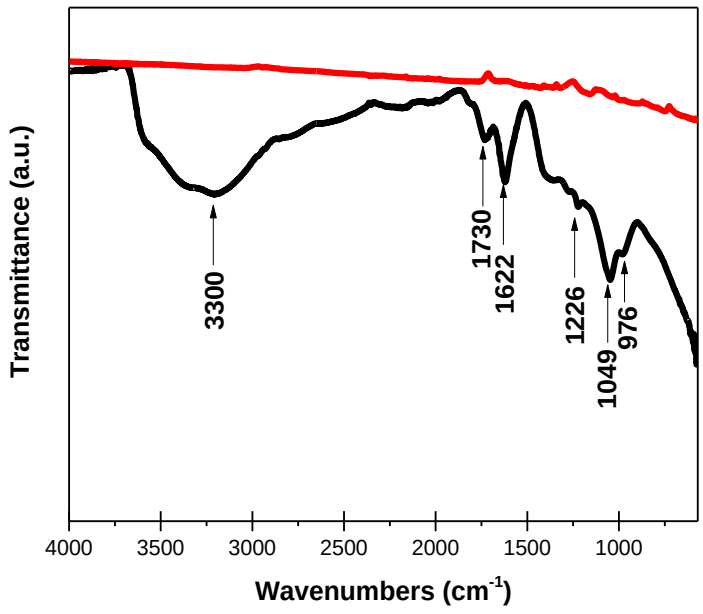

Fig. 4. 1: *ATR-FITR spectra recorded for GO (black line) and rGO powder samples (red line).*

4.2.2. Drop-Casting of GO and rGO Films

4.2.2.1. Microscopy and EDX Studies

Fig 4.2 shows a collection of AFM images taken in amplitude for the surface of the different GCE/GO electrodes (panels B-J). For the sake of comparison, the image captured for the bare GCE is also included (panel A). The latter depicts a relatively smooth surface (R_{MS}=5.5 nm; Table 4.1) with some linear scratches reflecting its history of usage. At first glance, the evidence already shows how proceeding with a 10^3-fold increase in [GO] triggers very significant changes in the morphological aspect of the surfaces. For low [GO] in the range 0.5-5.0 μg·mL^{-1} (Figs 4.2B-4.2D), a series of bright particles are spotted lying on the glassy carbon, GC, surface (darker background). Their amount and size rise slightly with the increase of [GO] to a maximum of 3-4 μm. As a consequence, the roughness, given as the R_{MS}, increased continuously up to a value of 37.5 nm. Based on the high O-content unveiled in section 4.2.1, GO sheets must wear a negative net charge under the working conditions (pH>7). Repulsive electrostatic interactions established between neighbor sheets must prevent from significant aggregation. Therefore, the small bodies imaged in this range must correspond to individual sheets of GO or very small aggregates.

The surface scratches noticed for the GCE in Fig 4.2A are easily found in the backgrounds of Figs 4.2B-4.2F and, with more difficulties, also in Figs 4.2G & 4.2H (as indicated by the white arrows). This proves that even at [GO] over 50 μg·mL^{-1}, large regions of the original electrode surface remain unmodified. For [GO] in the range 10-100 μg·mL^{-1} (Fig 4.2E-4.2H) the background becomes increasingly coated with islands of a wrinkled appearance. In simultaneous with these changes, the R_{MS} oscillates between 24 and 55 nm. The oscillations suggest the establishment of roughening-smoothing loops that concatenate as the surface gets loaded with additional material. A height profile was extracted along the blue line in panel F. It unveiled that these islands are relatively thin (~70 nm with peaks around 130 nm) and likely formed by the agglomeration of individual GO sheets. For the highest concentrations investigated, the islands coalesced into a relatively uniform, thick, and wrinkled film coating the entire surface (Figs 4.2I & 4.2J). In fact, no further increase in the maximum R_{MS} was registered. The whole body of evidence suggests that the GCE surface only gets fully covered at levels over 100 μg·mL^{-1} GO.

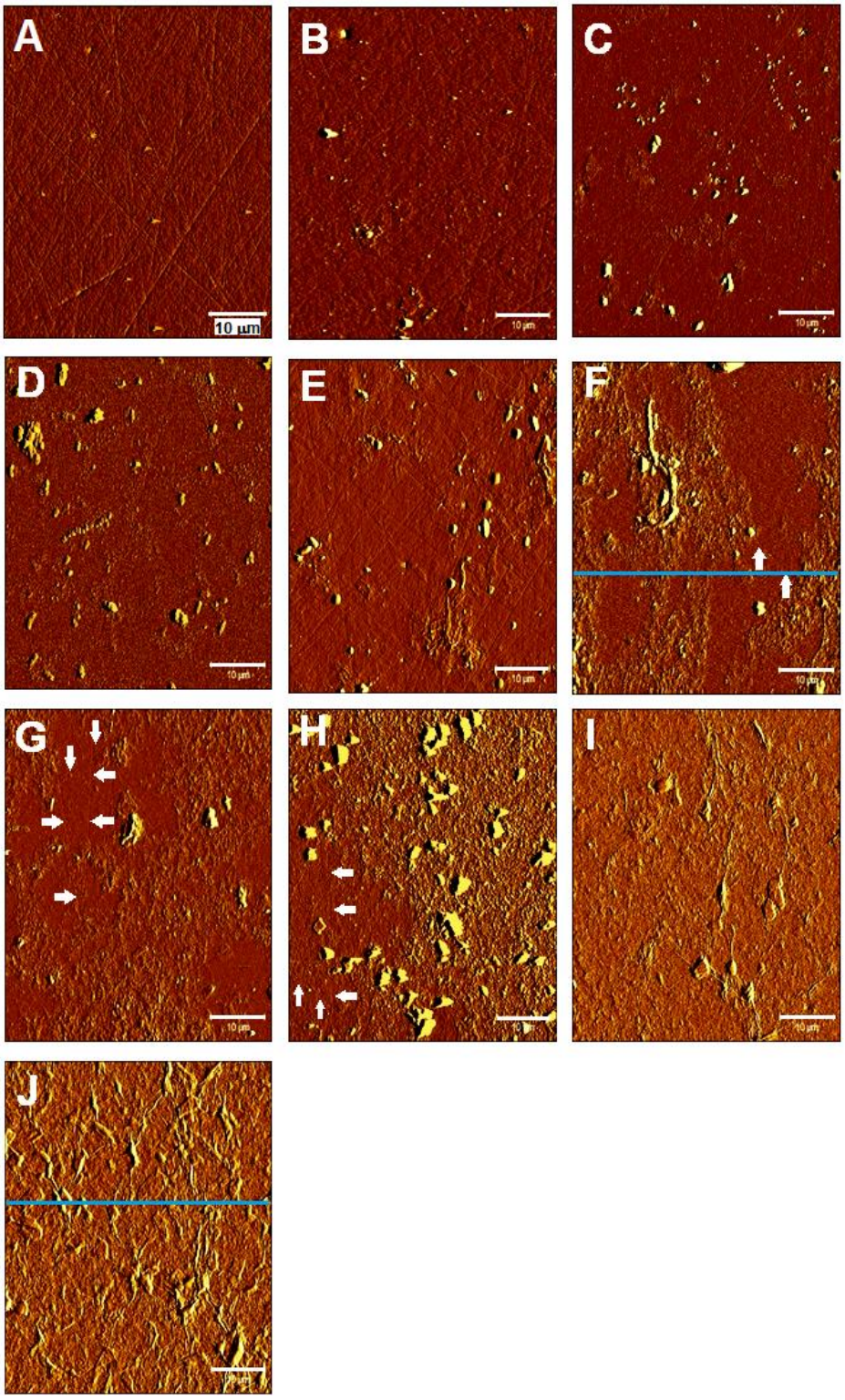

Fig. 4. 2: *Amplitude 50 µm × 50 µm AFM images registered in tapping mode for the surfaces of the different GCE/GO electrodes prepared from dispersions of the following concentrations:* ***(B)*** *0.500,* ***(C)*** *1.00,* ***(D)*** *5.00,* ***(E)*** *10.0,* ***(F)*** *25.0,* ***(G)*** *50.0,* ***(H)*** *100,* ***(I)*** *250, and* ***(J)*** *500 µg·mL^{-1} GO. White arrows indicate the paths of surface scratches. Height profiles were extracted along the blue lines. The scale bar is 10 µm. The image obtained for the bare GCE* ***(A)*** *is also included for better comparison.*

Table 4. 1: *Root-mean-square surface roughness (R_{MS}) measured for the bare GCE and the different GCE/GO and GCE/rGO electrodes from their corresponding topographic AFM images.*

[GO] / µg·mL^{-1}	*R_{MS} / nm*	*[rGO] / µg·mL^{-1}*	*R_{MS} / nm*
0	5.50	0	5.50
0.5	7.80	0.5	6.30
1.0	21.3	1.0	9.30
5.0	37.5	5.0	10.8
10.0	24.2	10.0	16.0
25.0	55.5	25.0	16.1
50.0	36.6	50.0	71.3
100.0	44.9	100.0	84.2
250.0	26.4	250.0	102.8
500.0	50.0	500.0	187.1

In line with this view, no surface scratches are found in those images. The highest load of material was achieved for the sample prepared from the 500 µg·mL^{-1} GO dispersion (Fig 4.2J). Another height profile extracted from the latter image shows an internal structure consisting of two incomplete layers (thickness around 78 and 74 nm, respectively) settling on top of a complete base layer (thickness ~70 nm). Such a structure determines the wrinkled topography seen under the scanning probe microscope and allows us to ascribe the brightest features in Figs 4.2I & 4.2J to the tallest regions of the multilayered film. This particular electrode was further investigated by FESEM (Fig 4.3). A top view of the GCE/GO surface is presented in Fig 4.3A (magnification factor, MF: 1,000 X). In strong agreement with the AFM evidence in Fig 4.2J, the SEM image displays a surface uniformly covered with a densely packed, relatively homogeneous, and wrinkled film, with no apparent signs of aggregation. A random region was enlarged using 10 times higher MF. The zoomed image (Fig 4.3B) reveals the outermost structure of the film in greater detail. As shown, irregular, defect-free, and flat sheets of 10-15 µm seem to stack on top of each other in lying-down configuration.

To investigate the local composition, an EDX spectrum was taken over that exact location (Fig 4.3E). The results showcase two intense peaks at 0.27 and 0.52 keV which are ascribed to C and O atoms, respectively. The local C:O atomic ratio, estimated as the quotient of intensities for both peaks (I_C/I_O), is 1.3. Such a low value evidences a high content in O-groups. Taking into account the high homogeneity of the film, this could also be true for any other region thereof. Unlike GO, extensively reduced rGO sheets should have a small or even negligible negative net charge at the working pH. This should translate into a greater impact of aggregation issues on the morphology of rGO films. To gain insights into the most important structural differences between both types of films, GCE/rGO electrodes prepared in the same range (0.500-500 µg·mL^{-1} rGO) were also inspected using the AFM (Fig. 4.4).

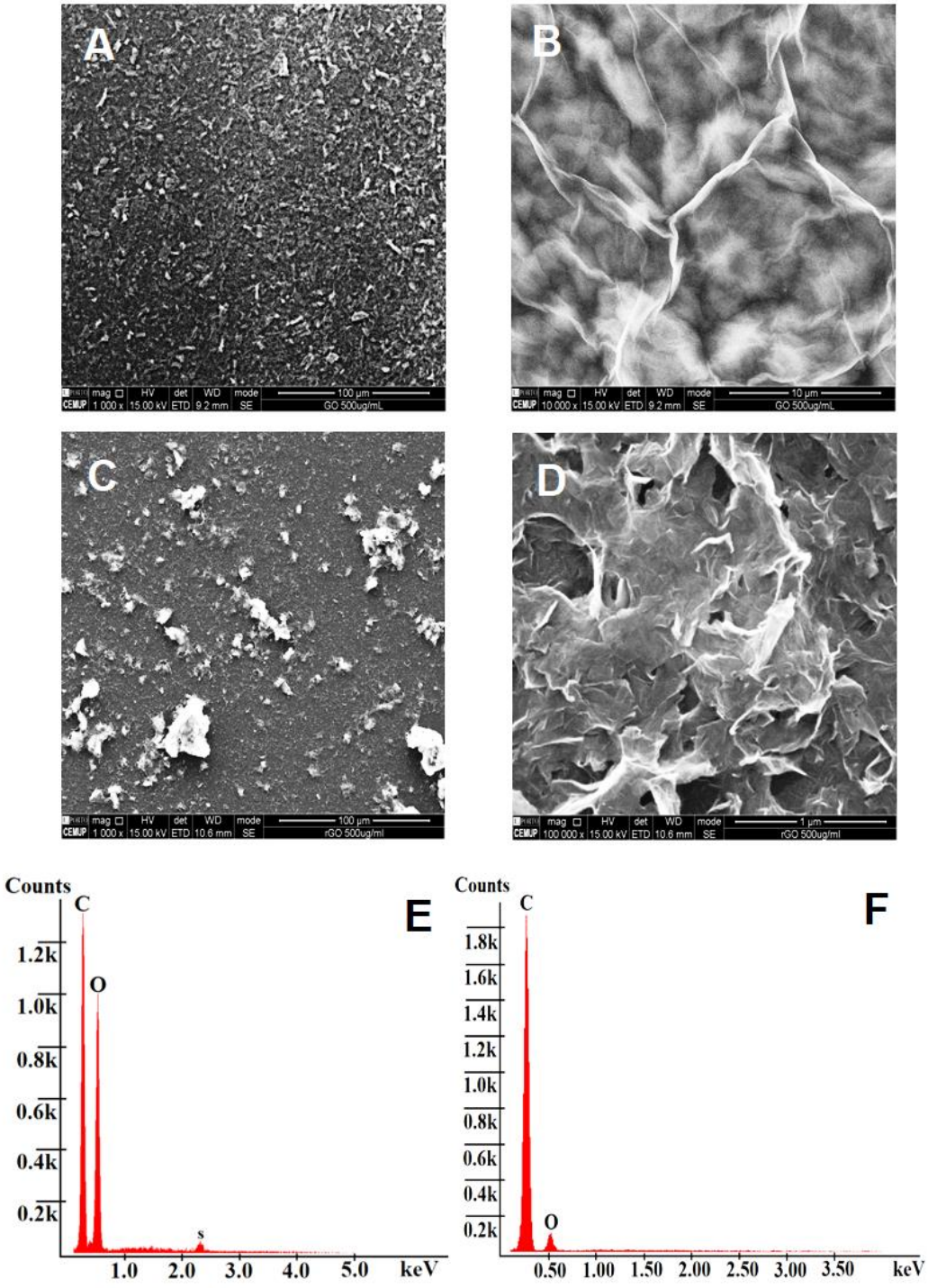

Fig. 4. 3: *Top-view FESEM images taken for the surfaces of the GCE/GO (A) and GCE/rGO electrodes (C) in secondary electrons (SE) mode. The magnification factor, MF, was 1,000 X. Panels B and D showcase a couple of regions investigated in higher detail with MF 10,000 X and 100,000 X, respectively. The EDX spectra taken at those regions are shown in panels E and F.*

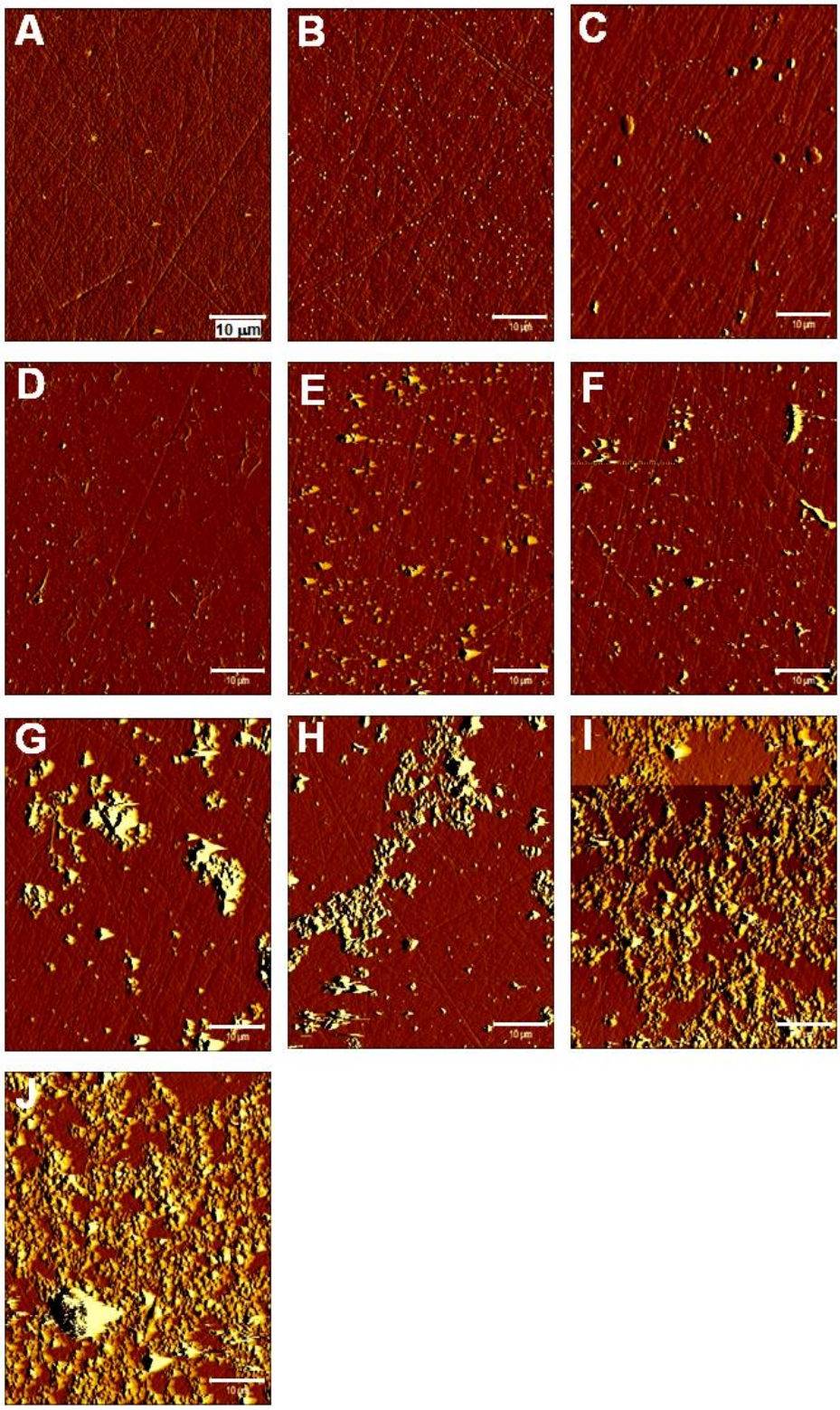

Fig. 4. 4: *Amplitude 50 µm × 50 µm AFM images registered in tapping mode for the surfaces of the different GCE/rGO electrodes prepared from dispersions of the following concentrations:* ***(B)*** *0.500,* ***(C)*** *1.00,* ***(D)*** *5.00,* ***(E)*** *10.0,* ***(F)*** *25.0,* ***(G)*** *50.0,* ***(H)*** *100,* ***(I)*** *250,* ***(J)*** *500 µg·mL^{-1} rGO. The scale bar is 10 µm. The image obtained for the bare GCE* ***(A)*** *is also included for better comparison.*

The first meaningful difference in respect to the GCE/GO system is that the glassy carbon (GC) surface scratches are visible in the background of all the registered images

(even in the most concentrated). That is the best confirmation that the GC surface is never fully covered with a homogeneous film of rGO.

For low [rGO] up to 1 μg·mL^{-1} (Figs 4.4B & 4.4C), the pictures resemble those discussed above for the GCE/GO electrodes and show a nearly empty (and scratchy) GC surface decorated with small particles of 1-3 μm (isolated rGO sheets or their small aggregates). In the range 5-25 μg·mL^{-1} rGO, the density of particles slightly overtakes that observed for their GO counterparts. However, in contrast to that found in Figs 4.2E & 4.2F, no signs of island film-growth are detected either in Fig 4.4E or 4.4F. This is further supported by the smaller values of R_{MS} (with a maximum of 16 nm vs the 55 nm measured for the GCE/GO electrodes). The impact of aggregation becomes more evident from [rGO]>25 μg·mL^{-1}. In good agreement, the R_{MS} undergoes a steeped increase to 71 nm at 50 μg·mL^{-1} and reaches 103 nm at 250 μg·mL^{-1} rGO (Table 4.1). These values are not only much higher than those for their analogous GCE/GO electrodes but, contrary to the oscillations registered for the latter, rose linearly in the whole range of [rGO] investigated. This is behaviour is related to the lack of growth of any form of uniform film as evidenced in the amplitude images.

Contrary to the roughening-smoothing mechanism leading to the formation of the uniform GO film, the rGO film emerges from the deposition of spherical aggregates of increasing size in increasing degrees of coverage. However, as no smoothening takes place, full coverage is never reached and no continuous film is formed at any stage of the modification process investigated. This is seen in the images of the highest concentrations investigated (Figs 4.4I & 4.4J) which show holes in the structure unveiling the scratchy surface of GC. The further growth of R_{MS} to a maximum of 187 nm also supports this view. FESEM images were also taken for the 500 μg·mL^{-1} rGO electrode (Fig 4.3). In good agreement with the evidence in Fig 4.4J, Fig 4.3C displays a distribution of big aggregates on a widely uncovered GC surface. As the inspected area is much larger here (>200 x 200 μm^2), one may infer that the uncoated fraction of the surface is greater than suggested by the AFM data. The structure of the aggregates is examined by zooming on one of them with a 10^2-fold higher MF (Fig 4.3D). As observed for GO in Fig 4.3B, individual rGO sheets also appear to stack on top of each other. Nevertheless, these look a lot more defective and corrugated than their GO counterparts. Such a finding makes perfect sense since, as well known, graphite oxide reduction methods introduce massive amounts of defects in the basal plane of GO[68, 81]. In summary, the microscopic evidence indicates that by increasing the concentration in both the GO and the rGO dispersions, greater amounts of these materials are generally deposited on the surface of the GCE However, while increasing [GO] leads to relatively thin and uniform films of wrinkled morphology formed upon stacking of large, defect-free, and freestanding sheets of GO (and showing a small

impact of sheet aggregation); no uniform film of rGO is deposited. In striking contrast with the homogeneous coverage of the GCE surface detected for concentrations over 50.0 $\mu g \cdot mL^{-1}$ GO, rGO deposits under the form of spherical microparticles of increasing size that never coat the GC surface entirely. Such differences in the structure and morphology are extremely relevant and will certainly determine the electrical and electrochemical properties of these electrodes.

4.2.2.2. Electrochemical Studies

4.2.2.2.1. GCE/GO Electrodes

We have investigated the electrochemical response of the modified electrodes using potentiodynamic and potentiostatic methods. Fig 4.5 shows some of the CVs and impedance spectra measured for the GCE/GO electrodes (coloured solid curves) in pure PBS (panels A & B) and in PBS + $[Fe(CN)_6]^{3-/4-}$ (C & D).

The blank voltammetric response registered in PBS for the bare GCE (the so-called sample GO#0) presents a capacitive double-layer current with no distinctive Faradaic peaks (black dashed curve in Fig 4.5A). The deposition of increasing loads of GO did not produce significant changes in the shape of the voltammograms (coloured curves). Fig 4.5B presents the Nyquist plots recorded at +0.15 V for the same electrodes. The impedimetric response was linear in all cases and the curves overlapped each other showing no particular trend. It is worth noting that the typical $-Z_i$ *vs.* Z_R plot for a pure capacitor is usually linear and exhibits very high slopes, just as seen in the figure[361]. Hence, we must conclude that coating the GCE surface with a homogeneous film of GO (as those seen in Figs 4.2J and 4.3A) does not introduce significant variations in the double-layer capacitance of the electrodes.

This behaviour could have been anticipated to some extent if both, the absence of redox species in the electrolyte and the electrical insulator character of GO, had been taken into account. To gain a deeper insight into the charge-transfer properties of the GO-modified electrodes, we carried out additional measurements in the presence of $[Fe(CN)_6]^{3-/4-}$ redox probes (Figs 4.5C & 4.5D). Some of the parameters derived from these experiments, such as peak current densities (j_P), peak-to-peak potential differences (ΔE_P), and apparent charge transfer resistances (R_1), are presented in Table 4.2.

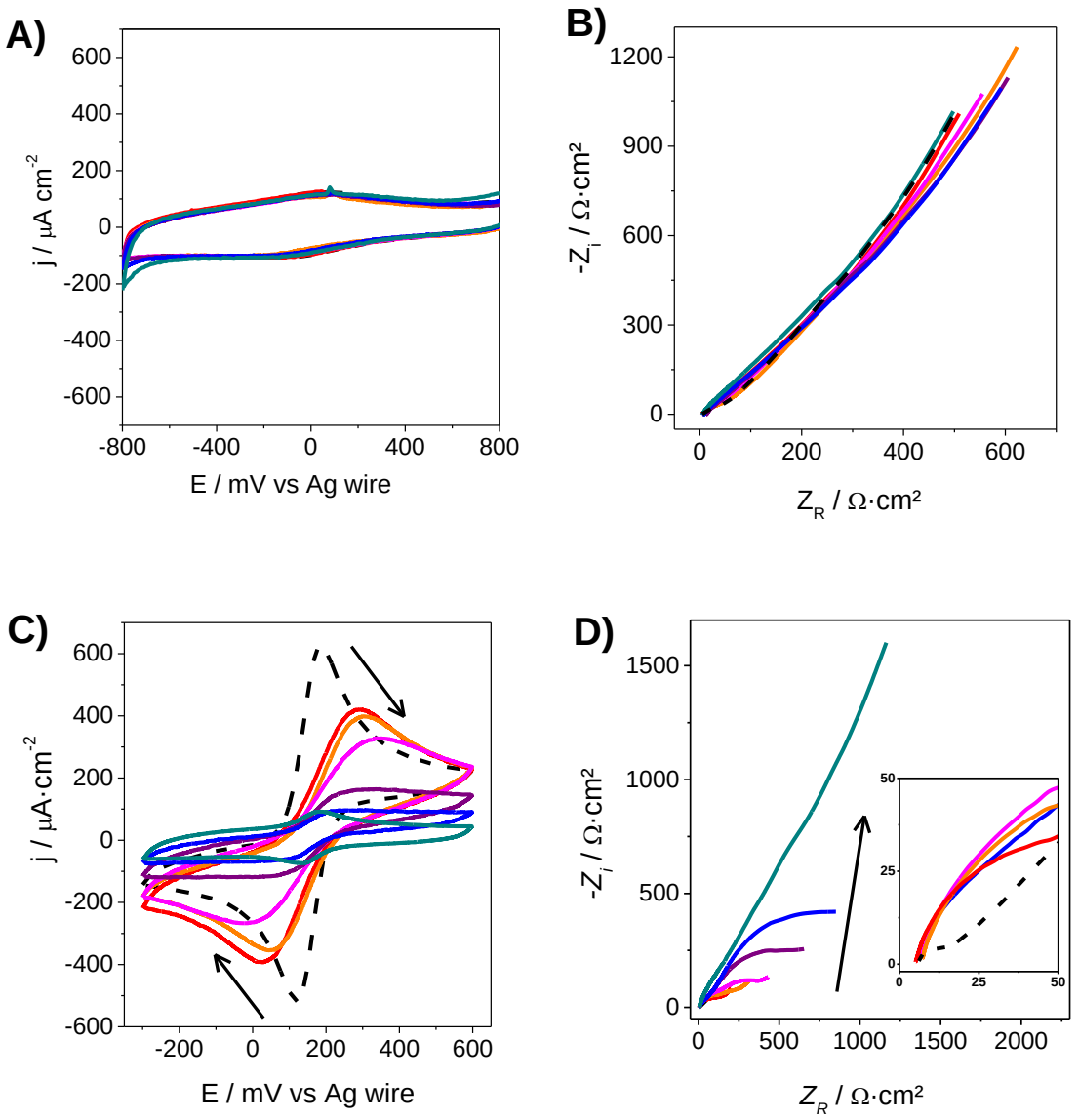

Fig. 4. 5: CVs (**A**, **C**) and Nyquist plots (**B**, **D**) registered in PBS 0.05 M **(A** & **B)** and PBS 0.05 M + 2 mM $[Fe(CN)_6]^{4-/3-}$ **(C** & **D)** for some of the GCE/GO electrodes investigated in Section 4.2.2.1; namely, those prepared with [GO]= 0.5 (red solid line), 5.0 (orange), 10.0 (magenta), 50.0 (purple), 250.0 (blue), 500.0 μg/mL (dark cyan)**.** The curves recorded for the bare GCE (black dashed line) have been included for comparison purposes. The inset in (**D**) features an enlargement of the impedance spectra in the high-medium frequency range. For (**A**) & (**C**), the *scan rate* was 0.05 $V \cdot s^{-1}$ in all cases. The spectra in (**B**) & (**D**) were taken at +0.15 V with an oscillation amplitude (*OA*) of 10 mV.

The voltammetric response recorded for GO#0 (dashed black curve in Fig 4.5C) shows a pair of sharp Faradaic peaks separated by only 64 mV which is very close to the 59 mV expected for a fully reversible one-electron process near room temperature. As best seen in the inset of Fig 4.5D, its impedance spectrum presents a very small semicircle in the mid-high frequency region (dashed black curve). This feature usually reflects the contribution of the ET processes to the total impedance and, therefore, is also related to R_1 in the following manner: the greater the ET resistance, the higher should be both the semicircle diameter and the magnitude of R_1[362].

Returning to sample GO#0, not only its impedance spectrum features the smallest semicircle in the defined region, but also reached the lowest R_1 of all the investigated electrodes (101 Ω; Table 4.2). The low values found for ΔE_P and R_1 confirm the high reversibility of the $[Fe(CN)_6]^{3-/4-}$ pair at the GCE. However, contrary to that observed in pure PBS, the deposition of increasing amounts of GO triggered dramatic changes in the shape of the CVs and Nyquist plots (coloured solid curves).

The voltammetric curves depicted in Fig 4.5C flattened progressively and the anodic peak currents (j_{PA}) dropped from 628 $\mu A \cdot cm^{-2}$ measured for GO#0 to 91 $\mu A \cdot cm^{-2}$ (GO#10). The peak separation grew concomitantly to a maximum ΔE_P of 515 mV for GO#9 (Table 4.2).

Table 4. 2: *Anodic and cathodic peak current densities (j_{PA} & j_{PC}), peak-to-peak potential difference (ΔE_P), and apparent charge transfer resistance (R_1) derived from the CVs and Nyquist plots registered for the different GCE/GO electrodes.*

Electrode	***[GO] / μg·mL^{-1}***	***j_{PA} / μA·cm^{-2}***	***j_{PC} / μA·cm^{-2}***	***j_{PA} / j_{PC}***	***ΔEp / mV***	***R_1 / kΩ***
GO#0	0.0	628	-521	1.2	64	0.10
GO#1	0.1	515	-470	1.1	157	0.92
GO#2	0.5	455	-392	1.2	174	1.68
GO#3	1.0	418	-393	1.0	264	1.77
GO#4	5.0	398	-354	1.1	260	3.64
GO#5	10.0	328	-267	1.2	369	8.25
GO#6	25.0	204	-145	1.4	425	9.65
GO#7	50.0	164	-119	1.4	470	16.75
GO#8	100.0	95	-80	1.2	495	26.83
GO#9	250.0	96	-73	1.2	515	38.20
GO#10	500.0	91	-74	1.2	48	92.50

Despite exhibiting the lowest peak currents in the series, the ΔE_P of GO#10 went below the theoretical value for free-diffusing reversible pairs (48 mV). This response seems to highlight the contribution of surface-confined species (likely trapped within the film) in an electrode that is already significantly towards diffusing probes.

Parallel to these changes, the size of the semicircles in Fig 4.5D did also increase markedly with the rise of [GO]. As expected, R_1 followed the same trend and climbed to a maximum of 92.5 kΩ for GO#10.

These results strongly suggest that the ET processes of the probes get continually hampered as the surface density of GO increases. Such behaviour emerges from a combination of phenomena of steric and/or electrostatic nature taking place simultaneously at the interface:

(1) The adsorption of fluky micron-sized and electrically insulating GO sheets blocks electroactive sites at glassy carbon, thus, introducing a significant hindrance for the probes to reach the electrode surface and transfer charge.

(2) At the working pH, repulsive electrostatic interactions must be established between the redox probes and negatively charged O-groups at the GO sheets, thus, preventing the permeation of the probes through the film and minimizing their concentration near the electrode surface.

The more GO is deposited, the greater will be the fraction of physically blocked electroactive sites and the density of O-groups available for the electrostatic repulsion of the probes. Therefore, any increase in the coverage and thickness of the films (e.g., through the increase of [GO]) will result in an improved contribution of both effects to the blockage of the redox response (just as confirmed by the experimental data in Fig 4.5C & 4.5D and the evolution of the parameters in Table 4.2).

The effect of the scanning rate (υ) was further investigated for samples GO#2, GO#6, and GO#10 (Fig 4.6). In all cases, j_{PA} and j_{PC} showed to grow/decrease linearly with $\upsilon^{1/2}$ just as expected for a reversible ET process (see figure insets). This behaviour indicates that ET processes are governed by the free diffusion of the probes from the bulk electrolyte to the electrode surface and vice versa. This was confirmed upon the linear regression of the data derived from both peaks to straight lines with the formula:

$$j_{PA/PC} = N + M_{A/C} \cdot \upsilon^{1/2} \qquad \textbf{(equation 4.1)}$$

The absolute values of the slopes from the anodic and cathodic fittings, $|M_{A/C}|$, and the corresponding correlation coefficients (R^2) may be found in Table 4.3. $|M_{A/C}|$ declined by about 5 times from sample GO#0 to GO#10. This behaviour indicates a clear departure of the system from the ideal reversibility stated above for sample GO#0 (something that could be already anticipated by the increase of ΔE_P noticed in Fig 4.5 and Table 4.2). The clear dependence of peak potentials on υ (the faster the potential is scanned, the greater the ΔE_P) confirm that, in practical terms, the probes behave at the modified electrodes as a quasi-reversible system (in contrast with their ideal reversibility at GO#0). The AFM evidence in Fig 4.2 allowed us to visualize how the glassy carbon surface gets increasingly covered with island-type features which, finally, coalesce to form a homogeneous GO film. Therefore, could the loss of reversibility evidenced for the probes in Fig 4.6 and Table 4.3 be linked to the contribution of slower diffusion processes taking place across GO-coated domains.

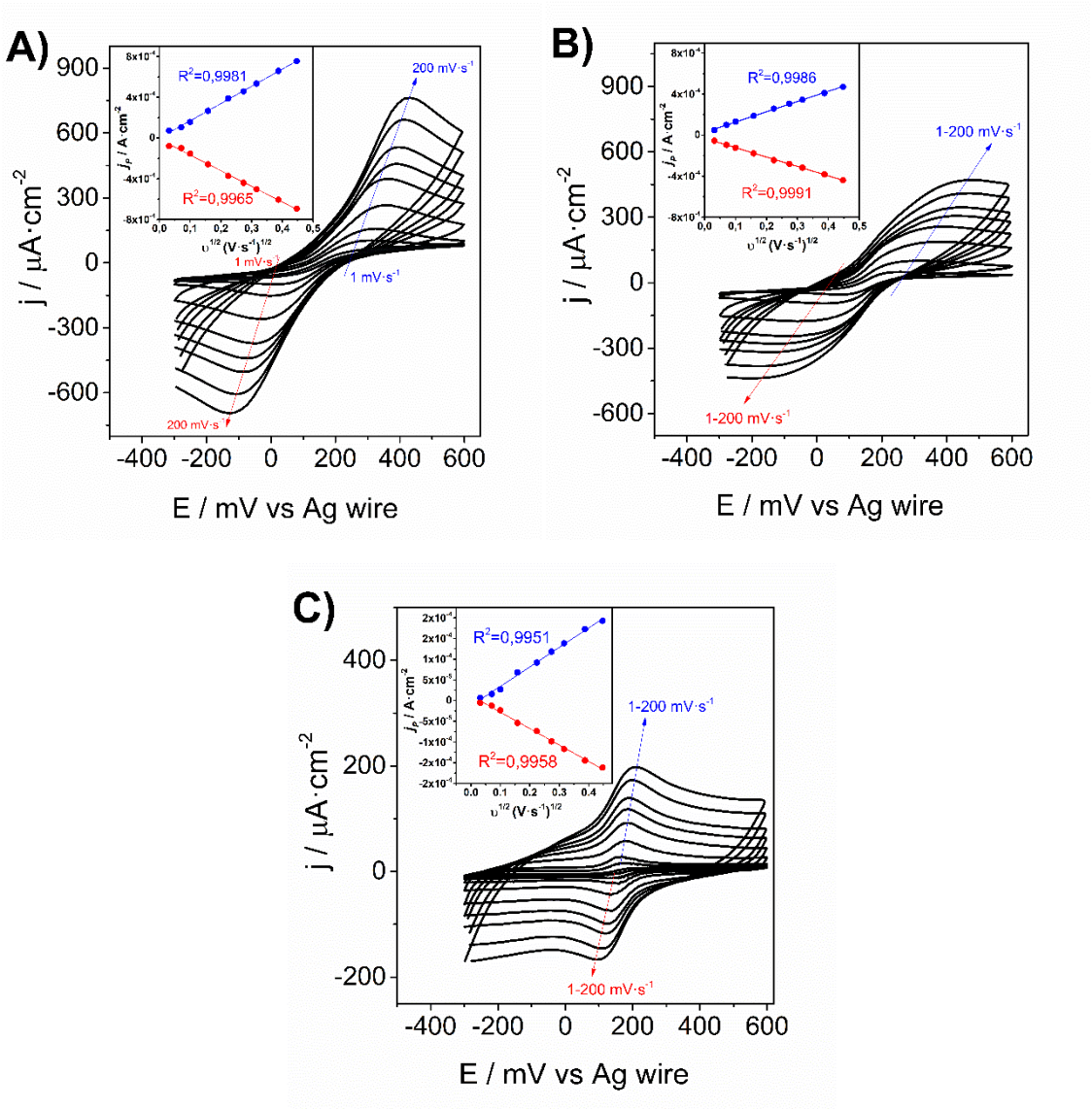

Fig. 4. 6: CVs consecutively registered for some of the electrodes described in Table 4.2, namely GO#2 **(A)**, GO#6 **(B)**, and GO#10 **(C)**; upon variation of the scan rate (υ) in the range 1-200 $mV \cdot s^{-1}$. The insets show the evolution of the anodic (full blue circles) and cathodic (red) peak current densities (j_P) vs. $\upsilon^{1/2}$. The fitting lines obtained by linear regression of these data have been. The electrolyte was PBS 0.05 M (pH 7.4) + 2 mM $[Fe(CN)_6]^{4-/3-}$ in all cases.

Using the Randles-Sevcik formula written at 298 K:

$$j_P=(2.69 \cdot 10^5 \cdot D^{1/2} \cdot n^{3/2} \cdot C) \cdot \upsilon^{1/2} \qquad \textbf{(equation 4.2)}$$

with the numeric constant having units of C mol^{-1} $V^{-1/2}$. *C* the bulk concentration of the oxidized/reduced species ($2 \cdot 10^{-6}$ $mol \cdot cm^3$), *D* their corresponding coefficient of diffusion ($6 \cdot 10^{-6}$ $cm^2 \cdot s^{-1}$)[363] and *n* the number of electrons transferred in the ET process (*n*=1 for this pair).

Using these values, Eq 4.2 supplies j_P in A·cm^2 provided that υ is entered in SI units of V·s^{-1}. By combining Eq 4.1 and 4.2, we could estimate the effective anodic and cathodic coefficients of diffusion for the $[Fe(CN)_6]^{4-/3-}$ species ($D_{A/C}$) as:

$$D_{A/C} = M_{A/C}^2 / (2.69 \cdot 10^5 \cdot C_{O/R})^2 \qquad \textbf{(equation 4.3)}$$

whether $M_{A/C}$ is taken in A·cm^2·s$^{1/2}$·V$^{-1/2}$ units, $D_{A/C}$ may come in cm^2·s^{-1}. As shown in Table 4.3, the calculated values dropped by almost two orders of magnitude from GO#0 to GO#10. This finding strongly supports the departure of the system from ideal reversibility and confirms the progressive hindering of the mass transport phenomena that occur parallel to the rise of the coverage and thickness of GO domains (up to the completion of the full homogeneous film).

Table 4. 3: *Parameters obtained by regression of the experimental data in the insets of Fig 4.6 to Eq 4.1. The absolute values of the slopes of the anodic and cathodic fitting lines ($|M_A|$ and $|M_C|$, respectively) are presented together with their corresponding correlation coefficients (R^2). The anodic and cathodic diffusion coefficients calculated from these data using Eq 4.3 are also presented. The values obtained for the bare GCE (GO#0), ideal reversibility, are included for comparison purposes.*

Electrode	$\|M_A\| \cdot 10^{-4}$ / $A \cdot cm^2 \cdot s^{1/2} V^{-1/2}$	$D_A \cdot 10^{-6}$ / $cm^2 s^{-1}$	R^2	$\|M_C\|$ / $A \cdot cm^2 \cdot s^{1/2} V^{-1/2}$	$D_C \cdot 10^{-6}$ / $cm^2 s^{-1}$	R^2
GO#0	21.3	15.7	0.9915	20.8	14.9	0.9896
GO#2	16.9	9.89	0.9981	15.4	8.18	0.9965
GO#6	9.98	3.44	0.9986	9.16	2.90	0.9991
GO#10	4.71	0.77	0.9951	3.97	0.54	0.9958

4.2.2.2.2. GCE/rGO Electrodes

We also investigated the electrochemical properties of the GCE/rGO electrodes. Fig 4.7A & 4.7B show some of the CVs and EIS registered in the absence of redox pairs. For [rGO] in the range 0.1-100 µg·mL^{-1}, the CVs show a similar response to that exhibited by their GCE/GO counterparts. These feature capacitive currents of the same order that those for bare GCE (RGO#0). However, in marked contrast to that seen in Fig 4.5A, the double-layer current increased dramatically for [rGO]>100 µg·mL^{-1}. That becomes quite evident in the CVs recorded with electrodes RGO#9 and #11 (250 and 500 µg·mL^{-1}, respectively; see Table 4.4).

Consistent with this behaviour, the Nyquist plots exhibited much lower impedances at low-mid ω (blue and dark cyan curves in Fig 4.7B). The Bode plots included in the figure inset unveil the decline of the total impedance (ZT) in the same range of frequencies. All these changes point to the rise of the double-layer electrode capacitance. Such an effect

has been reported before for GCE and other electrode materials modified with non-commercial rGOs [364-364-366].Therefore, it is confirmed as one of the most inherent benefits of rGO-coating treatments observed so far.

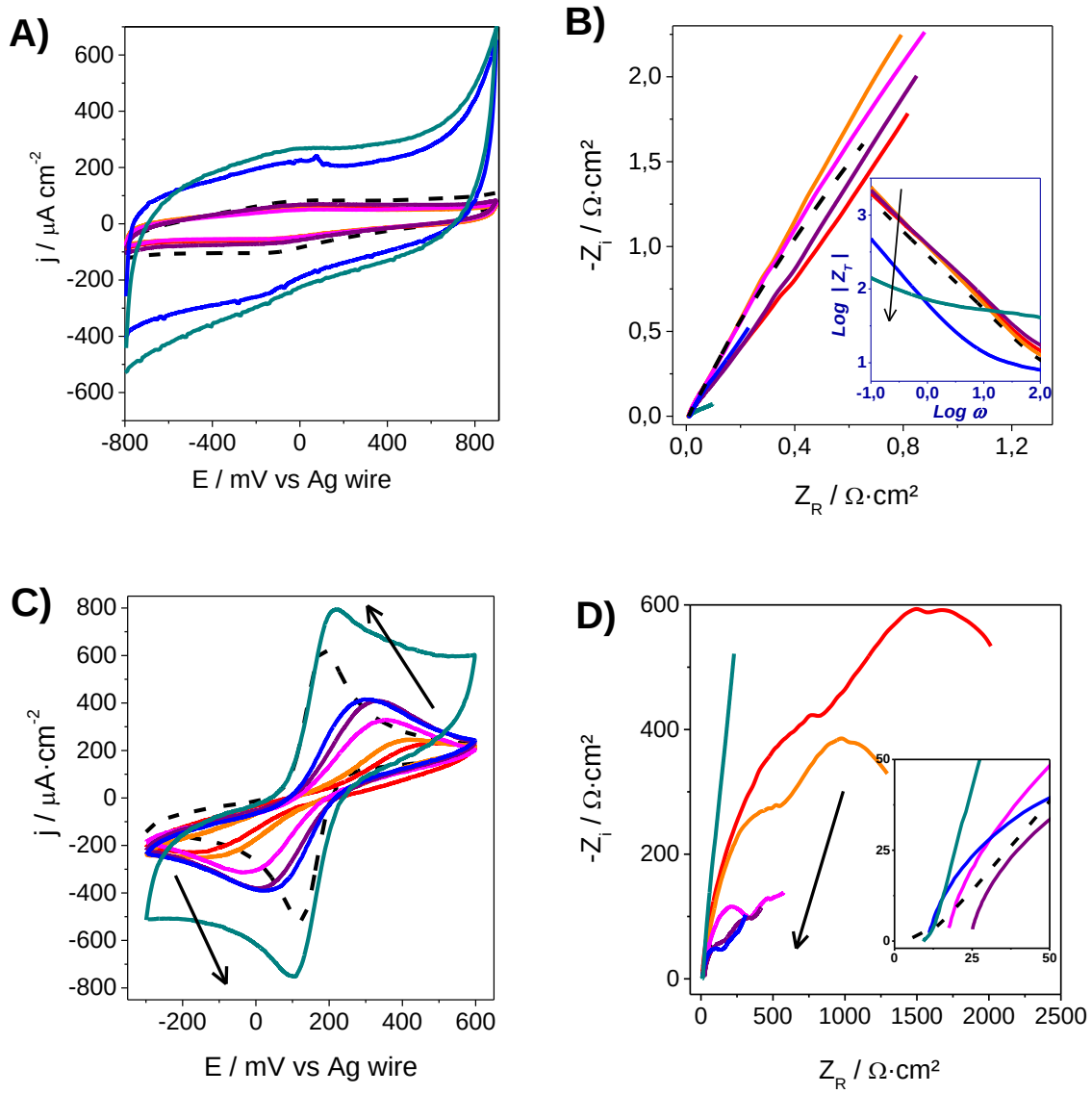

Fig. 4. 7: CVs (**A**, **C**) and Nyquist plots (**B**, **D**) registered in PBS 0.05 M **(A** & **B)** and PBS 0.05 M + 2 mM $[Fe(CN)_6]^{4-/3-}$ **(C** & **D)** for some of the GCE/rGO electrodes investigated in Section 4.2.2.1; namely, those prepared with [rGO]= 0.5 (red solid line), 5.0 (orange), 10.0 (magenta), 50.0 (purple), 250.0 (blue), 500.0 µg·mL^{-1} (dark cyan)**.** The curves recorded for the bare GCE (black dashed line) are included for comparison purposes. The inset in (**B**) presents the equivalent Bode plots (*log* $|Z_T|$ *vs. log* ω). The inset in (**D**) features an enlargement of the Nyquist plots in the region of high-medium ω. For (**A**) & (**C**), the scan rate was 0.05 V·s^{-1}. The spectra in (**B**) & (**D**) were taken at +0.15 V with an *OA* of 10 mV.

Table 4. 4: Anodic and cathodic peak current densities (j_{PA} & j_{PC}), peak-to-peak potential difference (ΔE_P), and the charge transfer resistances (R_1 & R_2) derived from the CVs and Nyquist plots recorded for the GCE/rGO electrodes.

Electrode	*[rGO] / μg·mL^{-1}*	*j_{PA} / μA·cm^{-2}*	*j_{PC} / μA·cm^{-2}*	*ΔEp / mV*	*R_1 / kΩ*	*R_2 / kΩ*
rGO#0	0.0	628	-521	64	0.10	---
rGO#1	0.1	264	-226	569	3.2	19.9
rGO#2	0.5	231	-229	699	10.4	31.7
rGO#3	1.0	237	-205	619	5.32	17.6
rGO#4	5.0	246	-253	579	8.16	19.8
rGO#5	10.0	330	-314	389	5.05	8.01
rGO#6	25.0	355	-300	504	4.13	15.5
rGO#7	50.0	409	-382	328	1.81	7.32
rGO#8	100.0	439	-388	364	1.80	7.95
rGO#9	250.0	415	-391	284	1.83	6.25
rGO#10	400.0	593	-584	144	0.57	10.8
rGO#11	500.0	795	-754	103	0.13	---
rGO#12	600.0	656	-616	129	0.13	---
rGO#13	800.0	481	-458	124	0.75	51.1

In the presence of redox probes, the electrochemical response followed a completely opposite trend to that exhibited by the GCE/GO system. Instead of flattening out, the CVs develop increasingly sharp peaks separated by lower potential differences (Fig 4.7C). The data presented in Table 4.4 offers a quantitative view of these changes. It is worthy to note that the CV of RGO#11 shows the lowest ΔE_P in the series (103 mV, which is still significantly higher than the 64 mV of RGO#0), a substantially enhanced double-layer current (in good agreement with the response depicted in Figs 4.7A), and the most intense peak currents (e.g., j_{PA} reached 795 μA·cm^{-2} vs. the 628 μA·cm^{-2} of RGO#0).

These results indicate that the presence of rGO also facilitates the ET processes of the probes, thus, even allowing to exceed the response of bare GCE for the highest [rGO] investigated. Such a boost in ET performance must have its origins in the vast improvements undergone in double-layer capacitance and probe reversibility (as suggested from the big drop in ΔE_P from 699 to 103 mV).

The Nyquist plots in Fig 4.7D reflect concomitant changes to the impedimetric behaviour of the electrodes. Even for [rGO] as small as 0.5 μg·mL^{-1} (solid red curve), the semicircle region is significantly larger than that observed for RGO#0 (black dashed line in the figure inset). This behaviour evidences a slight hindering of the ET processes due to a partial blockage of sites at the glassy-carbon (GC) surface upon deposition of rGO

sheets and/or their aggregates. With the notable exception of RGO#11, all the spectra show the neat presence of two consecutive semicircles. This feature would strongly suggest that two independent ET processes, characterized by different time constants, are taking place simultaneously. This is also backed by the systematic presence of two waves in the corresponding Bode Phase plots (e.g. check the one for RGO#2 in the right panel of Fig 4.8A; dashed line). Such an impedimetric response is often related to the existence of non-equivalent electroactive sites at the interface.

The AFM and SEM evidence discussed in Section 4.2.2 demonstrated that rGO fails to coat the entire surface of GC even for the highest concentration explored (i.e. RGO#11). Therefore, we attribute both semicircles to the contributions of sites at rGO-coated and bare GC surface domains. Under this hypothesis, the tiny single semicircle spotted in the spectrum of RGO#11 (which is even smaller than that of RGO#0) would indicate that although no full-film is formed under these conditions, rGO-coated sites dominate the electrode response. Such a single time-constant spectrum was fitted to the same Randles-type circuit used for all the GCE/GO and RGO#0 electrodes. Nonetheless, two time-constant systems are better represented by equivalent circuits with the ability to separate both processes in non-arbitrary ways. A popular model employed for the fitting of two-semicircle impedance spectra is the $R_s[Q_1R_1][Q_2R_2]$ circuit depicted in the centred plots of Fig 4.8B (more details in the experimental section)[364, 365]. The impedance data gathered for electrodes RGO#1-RGO#10 were successfully fitted to such a circuit. Some of the fitting curves are presented in Fig 4.8B and the values of R_1 and R_2 are also included in Table 4.4. The qualitative analysis of the spectra in Fig 4.7D allows us to conclude that the rise in [rGO] triggers a continuous reduction in the size of the semicircle region at high-mid ω.

This indicates that the net charge transfer process gets increasingly facilitated. This view is also supported by the drop in the values of R_1 and R_2 (in spite of small oscillations in both parameters, the general trend is quite clear). Just as an example, the former declined about two orders of magnitude from 10.4 (RGO#2) to 0.13 kΩ (RGO#11). It is worthy to note that both R_1 and R_2 reached lower values for RGO#1 than for RGO#2. This is in good agreement with the higher j_{PA} and lower ΔE_P measured from the CVs for that electrode (Table 4.4) and just indicates a lower degree of blockage of the GCE sites. After the initial hindering of the redox response occurring from RGO#0 to RGO#2, the evolution of these data clearly points to a progressive enhancement of the ET processes at both types of sites for [rGO]>0.5 $\mu g \cdot mL^{-1}$.

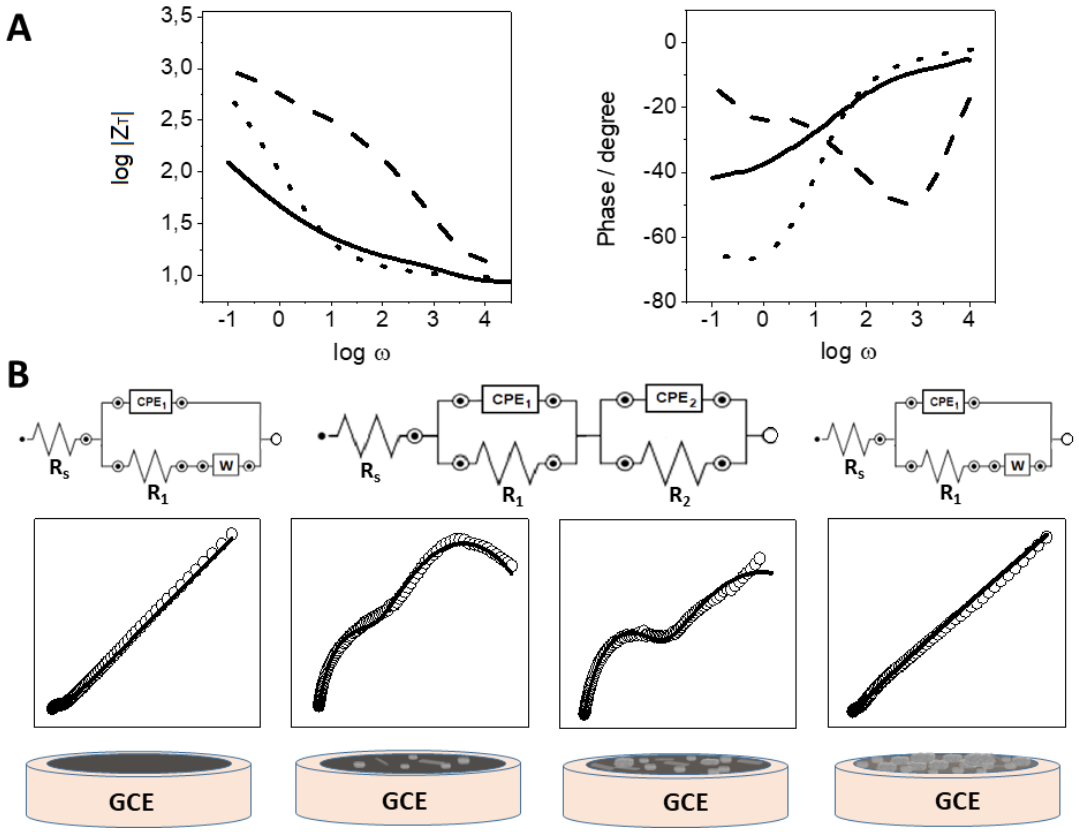

Fig. 4. 8: ***(A)*** *Bode (left) and Bode Phase plot (right) acquired for RGO#0 (solid line), RGO#2 (dashed line), and RGO#11 (dotted line).* ***(B)*** *Art model correlating the shape of some of the impedance spectra in Fig 4.7D (from left to right RGO#0, #2, #8, and #11; empty circles), the equivalent circuit used to fit the data, and the morphological aspect of the electrode surface in each case (as reconstructed from the microscopic evidence in Figs 4.3 and 4.4). The black solid lines represent the fitted spectra.*

Fig. 4.9 shows the effect of υ on the CVs of RGO#2, RGO#6, and RGO#11. As observed in Fig 4.6, the peak currents and their separation in potential grew in all cases upon the increase of υ from 1 to 200 mV·s^{-1}. As shown in the figure insets, j_{PA} and j_{PC} exhibit a linear dependence on $\upsilon^{1/2}$, thus, indicating that the process is diffusion-controlled (just as for the GCE/GO system). This was confirmed upon fitting the data to Eq 4.1. The values of $|M_{A/C}|$ and R^2 derived from the fittings can be found in Table 4.5. $|M_{A/C}|$ declined by about a half from RGO#0 to RGO#2. This is in line with the more hindered CV and EIS responses recorded with the electrodes modified with the lowest [rGO]. However, contrary to that seen for the GCE/GO electrodes, the rise in [rGO] promotes an enhancement in the reversibility of the system.

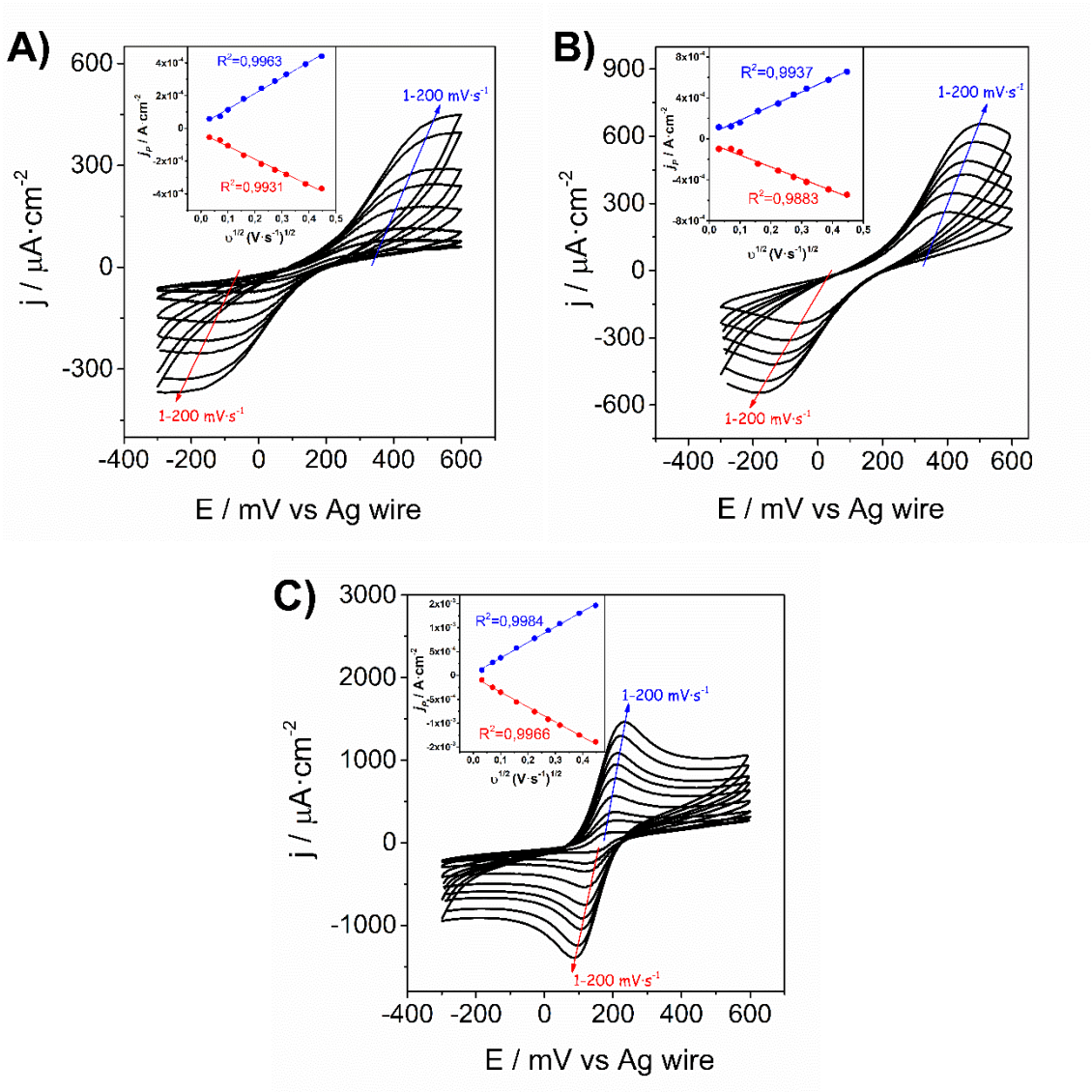

Fig. 4. 9: *CVs consecutively registered for some of the electrodes described in Table 4.4, namely RGO#2* ***(A)****, RGO#6* ***(B)****, and RGO#11* ***(C)****; upon variation of the scan rate (υ) in the range 1-200 mV·s^{-1}. The insets show the evolution of the anodic (full blue circles) and cathodic (red) peak current densities (j_P) vs. $\upsilon^{1/2}$. The fitting lines obtained by linear regression of these data have been included together with the corresponding correlation coefficients (R^2). The electrolyte was PBS 0.05 M (pH 7.4) + 2 mM $[Fe(CN)_6]^{4-/3-}$ in all cases.*

Table 4. 5: Parameters obtained by regression of the experimental data in the insets of Fig 4.9 to Eq 4.1. The absolute values of the slopes of the anodic and cathodic fitting lines ($|M_A|$ and $|M_C|$, respectively) are presented with the correlation coefficients (R^2). The anodic and cathodic diffusion coefficients (D_A and D_C) calculated from these data using Eq 4.3 are also presented. The values for the bare GCE (RGO#0), ideal reversibility, are included for comparison.

Electrode	$\|M_A\|\cdot 10^{-4}$ / $A\cdot cm^2\cdot s^{1/2}V^{-1/2}$	$D_A \cdot 10^{-6}$/ cm^2s^{-1}	R^2	$\|M_C\|$ / $A\cdot cm^2\cdot s^{1/2}V^{-1/2}$	$D_C \cdot 10^{-6}$/ cm^2s^{-1}	R^2
RGO#0	21.3	15.7	0.9915	20.8	14.9	0.9896
RGO#2	9.60	3.20	0.9963	7.90	2.10	0.9931
RGO#6	14.0	6.60	0.9937	11.0	4.70	0.9883
RGO#11	33.0	37.0	0.9984	31.0	34.0	0.9966

This is not only pointed by the increase in the slopes of the curves from RGO#2 to RGO#11, but also by a rise of more than 4 times in $|M_{A/C}|$. In good agreement, the values of $D_{A/C}$ calculated using Eq 4.3 exhibit an identical trend and, thus, point to the same conclusion: i.e. the progressive enhancement in the reversibility of the probes as [rGO] grows from 0.1 to 500 $\mu g \cdot mL^{-1}$ (something already suggested upon the qualitative and quantitative analysis of the CVs and impedance spectra in Fig 4.7C and 4.7D). The fact that both, the $D_{A/C}$ and the slopes derived from the fittings for RGO#11 top those obtained for the blank electrode (e.g. $D_A = 37 \cdot 10^{-6}$ vs $16 \cdot 10^{-6}$ $cm^2 s^{-1}$) is quite striking. Such an improvement in the diffusion coefficients indicates a marked enhancement of mass transport phenomena. Despite this result will deserve further detailed investigation, a temptative hypothesis is that the commercial rGO herein studied could be contaminated (or even residually functionalized) with groups/species that are positively charged under the working pH. In such a context, the attractive electrostatic interactions established with the negatively charge probes could explain the improved mass transport phenomena and overall electrochemical response. Obviously, such an effect would get maximized for the electrodes containing the greater loads of rGO.

Aiming to understand the electrochemical response for higher rGO coverage than those unveiled for RGO#1-RGO#11, we decided to further extend the studies to concentrations up to 800 $\mu g \cdot mL^{-1}$. Above RGO#11, the deposition of additional material clearly hinders ET processes at the interface. The system became more irreversible after deposition of RGO#12 (Fig 4.10C). Anodic peak currents (j_{PA}) were strongly reduced from the 795 $\mu A \cdot cm^{-2}$ measured for GO#11 to 481 $\mu A \cdot cm^{-2}$ (GO#13) and the peak separation grew to a ΔE_P of 124 mV for GO#13 (Table 4.4). Parallel to these changes, the size of the semicircles in Fig 4.10 D did also increase markedly with the rise of [rGO]. As expected, R_1 followed the same trend and increased from 10.8 kΩ for RGO#11 to 51.1 kΩ (RGO#13).

The AFM image revels that increasing the concentration of the casting dispersion to 600 (Fig 4.10A) and 800 $mg \cdot mL^{-1}$ (Fig 4.10B), the coverage is never reached and no continuous film is formed at any stage of the modification process investigated.

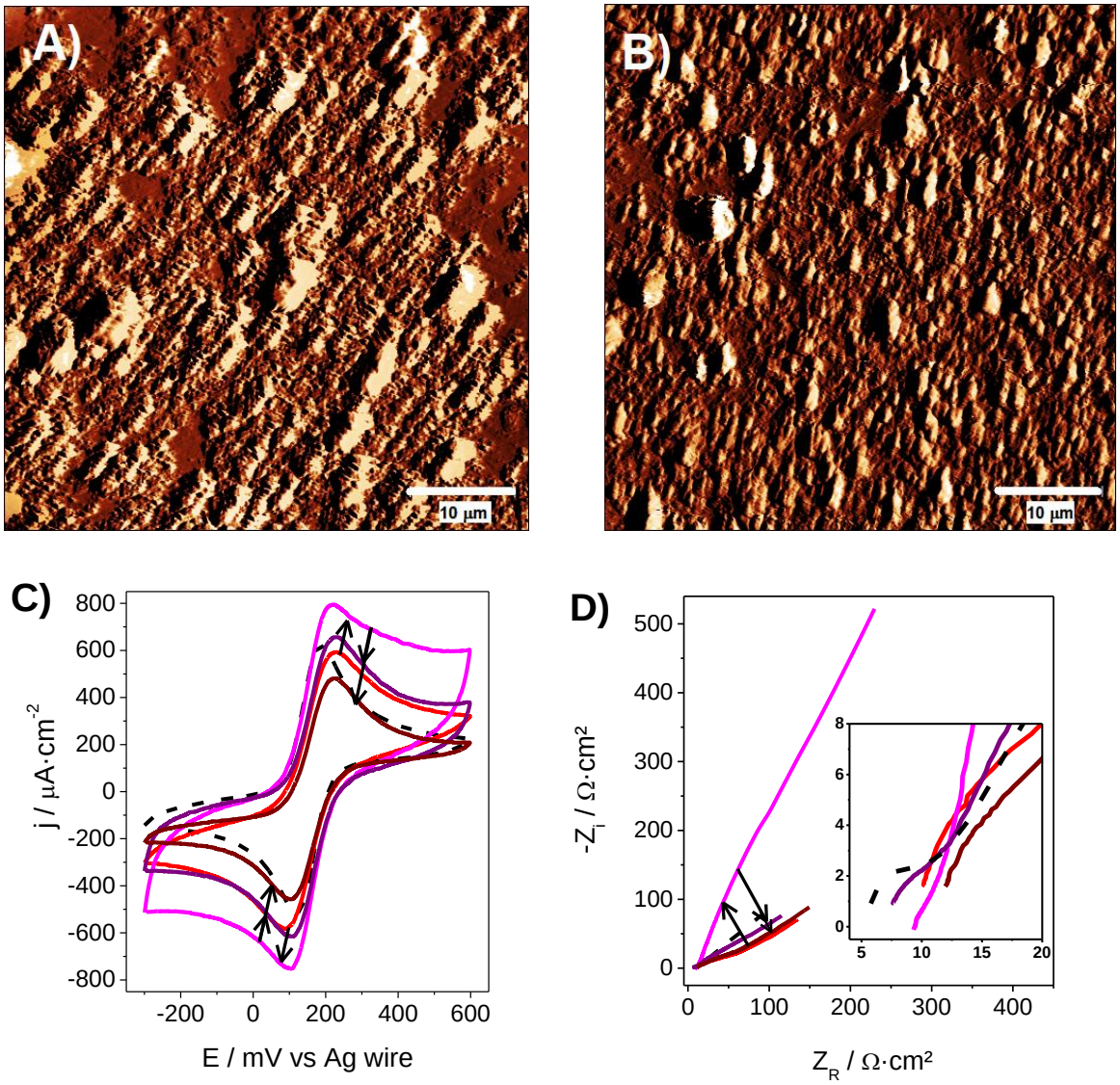

Fig. 4. 10: Amplitude 50 µm × 50 µm AFM images registered in tapping mode for the surfaces of the different GCE/rGO electrodes prepared from dispersions of the following concentrations: **(A)** 600 and **(B)** 800 µg·mL^{-1} rGO. CVs (**C**) and Nyquist plots (**D**) registered in PBS 0.05 M + 2 mM $[Fe(CN)_6]^{4-/3-}$ for GCE/rGO electrodes prepared with [rGO]= 400 (red solid line), 500 (magenta), 600 (purple), and 800.0 µg/mL (wine)**.** The curves recorded for the bare GCE (black dashed line) are included for comparison purposes.

4.2.3. Drop-Casting of rGO-Fe_3O_4 NPs films

4.2.3.1. Microscopy Studies

Fig 4.11 shows a collection of AFM images taken in topography for the surface of the different GCE/ rGO-Fe_3O_4 NPs electrodes (panels A-F). The topographic image (Fig 4.11 A) reveals a significant amount of bright features (ascribed to aggregated forms of the conjugate) on a reddish background (the bare GCE surface).

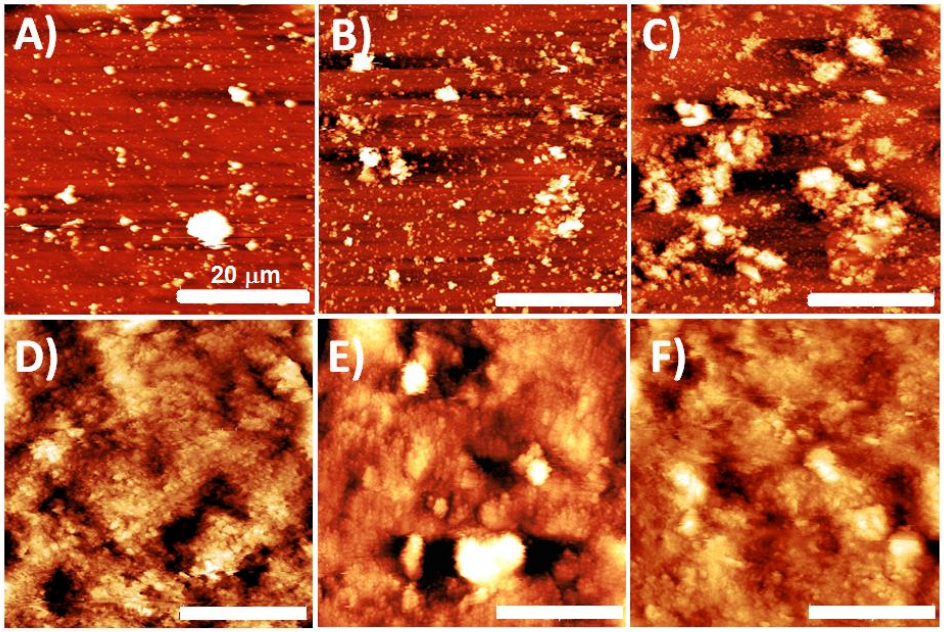

Fig. 4. 11: *AFM images (topography) taken in tapping mode for the GCE surface after casting with 10 µL of 0.2 (**A**), 0.5 (**B**), 1.0 (**C**), 5.0 (**D**), 10.0 (**E**) and 20.0 mg mL^{-1} (**F**) dispersions of rGO-Fe_3O_4 NPs in ethanol. Scan size: 50 µm.*

The preponderance of red domains agrees with a surface which is far from saturation (sub-monolayer regime; SM). Small white dots attributed to NPs as small as 100-200 nm dominate the landscape over much larger colloids of 2-7 µm. By increasing the concentration of the casting dispersion to 0.5 (Fig 4.11 B) and 1.0 mg·mL^{-1} (Fig 4.11 C), the coverage and average size of the imaged particles clearly increase. In good agreement, both the average height (h_{AV}) and surface roughness (R_{MS}) measured from these images also grew significantly (Table 4.6).

Table 4. 6: *Surface roughness (R_{MS})[a] and average height (h_{AV})[a] derived by software analysis of the topographic images presented in Fig 4.11.*

Concentration / mg·mL^{-1}	***h_{AV} / µm***	***R_{MS} / µm***
0.20	0.8	0.09
0.50	0.6	0.12
1.00	1.4	0.22
5.00	1.3	0.21
10.0	1.2	0.20
20.0	1.5	0.30

[a] *Obtained using Gwyddion 2.25 freeware*

However, the reddish domains are still recognizable in the background of Fig 4.11 C, indicating the co-existence of regions heavily loaded with large aggregates and others which are non-covered at all. Such degree of heterogeneity is reflected by

the rise of h_{AV} to 1.4 μm. As seen in Figs 4.11 D-4.11 F, at higher concentrations the films become more homogeneous, smoother, and thicker. This is backed by the drop in h_{AV} and R_{MS} within the range 1.0-10.0 mg·mL^{-1}. The films seem to contain bigger aggregates too. In this sense, the 20 mg·mL^{-1} sample was so loaded that tip-sticking problems made it hard to obtain a relatively sharp image of the surface like that in Fig 4.11 F. In it, particles larger than 20 μm can be spotted. Moreover both, h_{AV} and R_{MS}, reached their maximum values (1.5 and 0.30 μm, respectively) for this sample.

There is a great correlation between the morphological aspect of the films observed by AFM and FESEM (Fig 4.12). Figs 4.12 A depicts the GCE modified with the 0.5 mg·mL^{-1} rGO-Fe_3O_4 NP dispersion. The image shows a distribution of bright dots (aggregated forms of the conjugate) on a rather uncovered dark grey background (bare GCE). Although the major part of the clusters has a size ≤1 μm, these co-exist with a minor amount of much larger particles (2-7 μm). The smallest particles were further investigated by increasing the magnification factor 100 times. Fig 4.12 B displays the zoomed image for one of the individual particles spotted in Fig 4.12 A. Two large clusters (1 μm each) of spherical NPs (size ranging between 15 and 60 nm), apparently supported by a 2D base material, are observed. Such a description fits well with that expected for hybrid species based on 2D sheets of graphene and NPs.

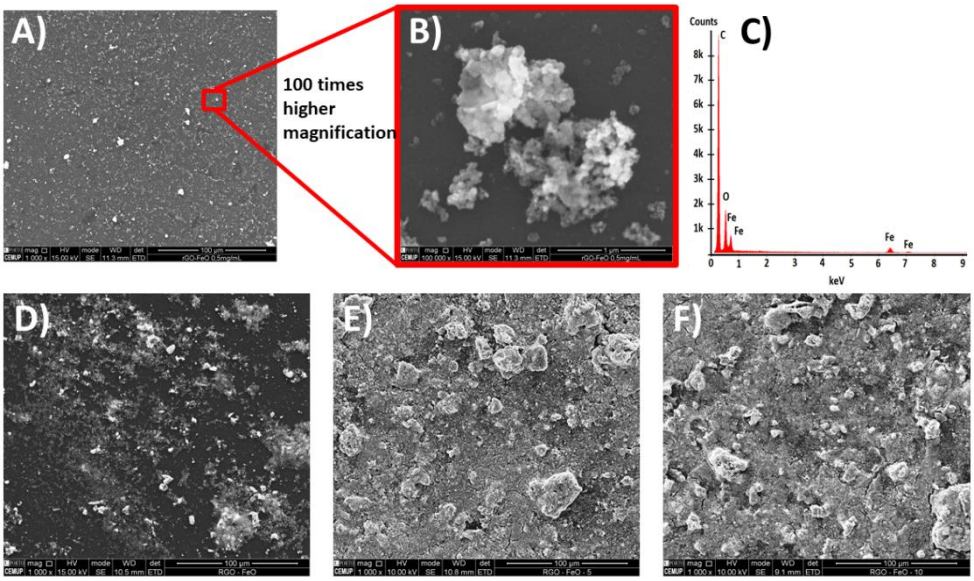

Fig. 4. 12: *FESEM images taken in SE mode (HV: 15 kV) for the GCE surfaces modified with 0.5 (**A**), 1.0 (**D**), 5.0 (**E**), and 10.0 mg mL^{-1} (**F**) dispersions of the rGO-Fe_3O_4 NP conjugate in ethanol (magnification factor, MF: 1,000 X). The red square in panel **A** shows a region investigated in higher detail (MF: 100,000 X; panel **B**). **(C)** EDS spectrum acquired over the isolated island-type feature isolated in the panel B.*

In fact, the NP size range is in excellent agreement with that reported in the literature for Fe_3O_4 NPs[347] and the morphological aspect is almost identical to that observed for other graphene-NP hybrids on the GCE (e.g. rGO-Ni NPs)[116]. The EDX

spectrum acquired at this exact location, confirms the presence of C, O, and Fe atoms (Fig 4.12 C). As discussed for the AFM images, the raise of the concentration to 1, 5, and 10 mg·mL^{-1}, induces a dramatic change in the observed coverage and average particle size. Accordingly, the electrode surface appears completely covered in Figs 4.12 E and 4.12 F and particles as large as 25-50 µm can be identified. From the microscopic inspection of the different rGO-Fe_3O_4 NP-modified GCEs, it follows that the full coverage level must fall somewhere between 1 and 5 mg·mL^{-1}. The results show that thick and compact films of the conjugate are formed for dispersions ≥5 mg·mL^{-1}.

4.2.3.2. Electrochemical Studies

The modified electrodes were also characterized by electrochemical measurements. Fig 4.13 A compares the voltammograms obtained in pure 0.05 M PBS (pH 7.4). In absence of redox probes, none of the registered CVs shows faradaic processes within the potential window investigated. As the concentration of rGO-Fe_3O_4 NPs raised from 0.2 (red solid line) to 10 mg·mL^{-1} (wine), the capacitive current followed a concomitant progressive increase. However, above these levels, it was significantly reduced (20 mg·mL^{-1}; orange line). The current was integrated between 0.1 and 0.4 V in order to estimate the charge density ascribed to double-layer charging (δ_{DL}). As expected from the qualitative analysis of the CVs, δ_{DL} increases linearly with *[rGO-Fe_3O_4]* up to 10 mg·mL^{-1} (blue inset in Fig 4.13 A).

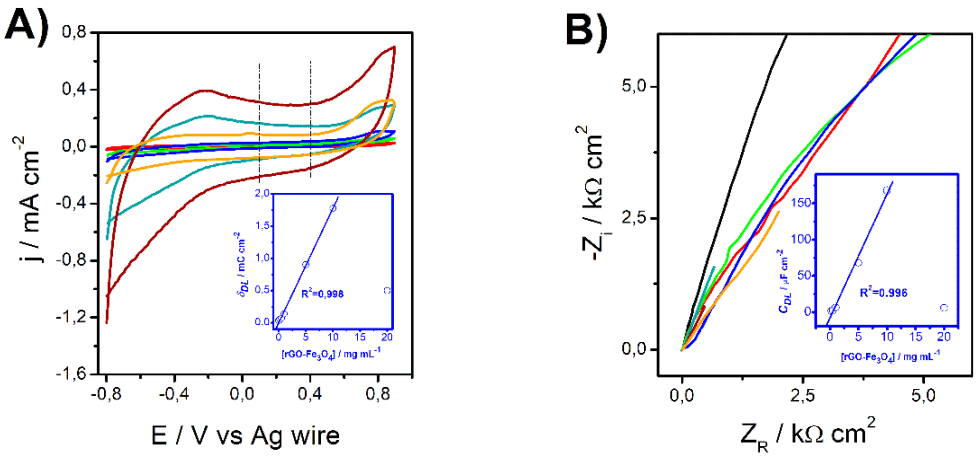

Fig. 4. 13: *CVs* ***(A)*** *and Nyquist plots* ***(B)*** *registered in 0.05 M PBS pH 7.4 for the GCE modified with: 0.2 (red solid line), 0.5 (green), 1.0 (blue), 5.0 (dark cyan), 10.0 (wine), and 20 mg·mL^{-1} (orange) dispersions of rGO-Fe_3O_4 NPs in ethanol. The data recorded for the unmodified GCE is also included (black). The scan rate and oscillation amplitude were 50 mV·s^{-1} and 10 mV, respectively. The double layer charge density (δ_{DL}; panel A) and double layer capacitance (C_{DL}; panel B) are plotted vs the conjugate concentration in the blue insets. The data were fitted to two straight lines (blue) and the corresponding coefficients of correlation have been also included.*

In accordance with the strong blockage of the electrochemical response observed for 20 mg·mL^{-1}, δ_{DL} also dropped by more than 50%. The changes registered in the corresponding Nyquist plots are shown in Fig 4.13 B. Two main effects are observed. Within the range 0.2-1.0 mg·mL^{-1} (SM regime according to the microscopic images), the plots exhibit values of real (Z_R) and imaginary impedances ($-Z_i$) over 5 kΩ. As it could be expected, the impedance is much smaller for the more capacitive electrodes prepared within the range 5.0-20.0 mg·mL^{-1}. This indicates that double-layer charging is more favored on them. In second place, the slope of the linear domains displayed in the figure declined in the whole range of concentrations investigated. The experimental data was fitted to an equivalent circuit ($R_s(CR_1)$) and the double layer capacitance (C_{DL}) was calculated as indicated in the chapter 2, equation 2.23. The C_{DL} *vs [rGO-Fe$_3$O$_4$]* plot in the inset shows a trend almost identical to that followed by δ_{DL}. In this sense, the capacitance also decreased significantly for the 20.0 mg·mL^{-1} electrode. All these results indicate that coating the GCE with the pre-synthesized rGO-Fe_3O_4 NPs favors double-layer charging processes (higher charge densities are passed through and stored at the interface) thereby improving its capacitive behaviour. These properties arise from the excellent surface-to-volume ratio and good conductivity of the rGO-Fe_3O_4 NP conjugate and could find applications in the field of energy storage. The data also indicates the existence of a threshold between 10 and 20 mg·mL^{-1}. Above that level, the deposition of additional material clearly hinders charge storage at the interface. To investigate the effects on faradaic processes, the electrodes were characterized in presence of 2 mM $[Fe(CN)_6]^{3-/4-}$. The recorded CVs can be found in Fig 4.14 A.

The one for bare GCE (black dash line) presents a couple of intense and sharp peaks. Just as expected for such a reversible pair, the peak-to-peak potential difference, ΔE_P, was as low as 79 mV (table 4.7). The system became much more irreversible after deposition of rGO-Fe_3O_4 NPs from the most diluted dispersion. Faradaic currents were strongly reduced (red curve) and the peak separation underwent a huge increase to ΔE_P=652 mV. By increasing *[rGO-Fe$_3$O$_4$]* from 0.2 to 10.0 mg·mL^{-1}, peak currents were progressively recovered (to the point of exceeding those of bare GCE at the 10.0 mg·mL^{-1} electrode) and ΔE_P followed a concomitant decline to 166 mV (table 4.7). Just as occurred with the capacitive currents in Fig 4.14 A, the faradaic processes were also hindered above this level. In this regard, the 20 mg·mL^{-1} electrode (orange curve) exhibited lower current densities and a ΔE_P of 611 mV.

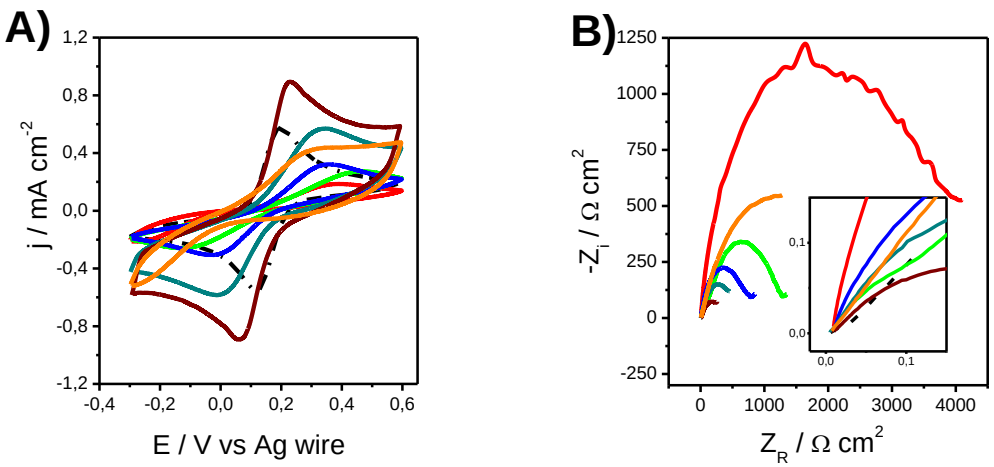

Fig. 4. 14: *CVs* ***(A)*** *and Nyquist plots* ***(B)*** *registered in 0.05 M PBS pH 7.4 + 2 mM $[Fe(CN)_6]^{3-/4-}$ for the GCE modified with: 0.2 (red solid line), 0.5 (green), 1.0 (blue), 5.0 (dark cyan), 10.0 (wine), and 20 mg·mL^{-1} (orange) dispersions of rGO-Fe_3O_4 NPs in ethanol. The curves obtained for the bare GCE are also included (black). The scan rate and oscillation amplitude were 50 mV·s^{-1} and 10 mV, respectively. Impedance spectra were taken at +0.15 V. The peak-to-peak potential difference (ΔE_P; panel A) and charge transfer resistance (R_1; panel B) are plotted vs the conjugate concentration in the blue insets.*

Table 4. 7: *Anodic and cathodic peak current densities (j_{PA} & j_{PC}), peak-to-peak potential difference (ΔE_P), and apparent charge transfer resistance (R_1) derived from the CVs and Nyquist plots registered for the different GCE/GO electrodes.*

Electrode	***[GO] / μg·mL^{-1}***	***j_{PA} / μA·cm^{-2}***	***j_{PC} / μA·cm^{-2}***	***j_{PA} / j_{PC}***	***ΔEp / mV***	***R_1 / kΩ***
GO#0	0.0	565	-555	1,0	79	0,1
GO#1	0.2	188	-222	0,8	652	109
GO#2	0.5	273	-258	1,1	593	41
GO#3	1.0	321	-305	1,1	386	22
GO#4	5.0	569	-584	1,0	382	18
GO#5	10.0	894	-892	1,0	166	6
GO#6	20.0	438	-493	0,9	611	70

Impedance spectra were also taken and the corresponding Nyquist plots are shown in Fig 4.14 B. The absence of linear regions in the plots confirms that the response of the rGO-Fe_3O_4 NP-modified electrodes at the measuring potential is governed by the ET within the entire range of frequencies. The largest semicircle was recorded for the 0.2 mg·mL^{-1} electrode (red curve). This finding agrees with the great blockage of its CV in Fig 4.14 A and indicates that the highest resistance to the ET of the probes is posed by that electrode. Rising *[rGO-Fe_3O_4]* to 10.0 mg·mL^{-1} (wine) produced a continuous decrease in the size of the semicircles which, together with the good recovery of the peaks in Fig 4.14 A, illustrates the positive effects of raising the coverage above the SM regime to the ET processes. In contrast, the semicircle obtained for the 20 mg·mL^{-1} electrode increased its size. This observation fits well with

the reduction of current observed in Fig 4.14 A and confirms the electrode response gets significantly hindered for concentrations over 10 mg·mL^{-1}. For the purposes of quantitative analysis, the experimental data was fitted to the equivalent circuit R_s(Q[R_1W] described in the chapter 2. The values of R_1 obtained from the fittings are present in the table 4.7.

As it can be observed, this parameter followed an analogous trend to that followed by the semicircles size. Accordingly, the highest resistance (109 kΩ) was measured for the 0.2 mg·mL^{-1} electrode and the lowest (6 kΩ) was obtained at 10.0 mg·mL^{-1}. From the data in Figs 4.13 and 4.14, we can conclude that the deposition of rGO-Fe_3O_4 NPs in the range 0.2-10.0 mg·mL^{-1} enhances the electroactivity of GCE. While the capacitance is continuously improved in the range 1-10 mg·mL^{-1}, the ET transfer properties is initially hindered (SM regime) but significantly enhanced with the increase in coverage and thickness of the films. For the thicker films formed above this level, both the faradaic and non-faradaic processes decline importantly which could be due to a drop in conductivity (potentially emerging from a change in the conformation of the assembled hybrid sheets) and/or to the existence of greater difficulties for the diffusion of the probes through them. The concentration of 10.0 mg·mL^{-1} of rGO-Fe_3O_4 NPs was explored as base for constrution of a biosensor (chapter 5).

4.3. Conclusions

The work present in this chapter, describes an assembly of thin GMN, namely GO, rGO and rGO-Fe_3O_4 NP films on GCE surfaces. The structure, morphology and electron transfer properties of these films were evaluated. The films were assembled in a wide range of concentrations and later studied by AFM, FESEM, and electrochemical techniques. The results for the electrode modifications with GO showed a continuous hindering of the ET of the probes as the density of the film increases. This behaviour seems to be related to phenomena of steric and electrostatic type. The AFM images showed that the increased concentration of the GO dispersion results in a homogeneous coverage on the GCE surface.

The modification of electrode surface with rGO and rGO-Fe_3O_4 NPs exhibited a couple of changes in the redox response of the electrodes. However, contrary to that seen for the GCE/GO electrodes, the growth of rGO concentration promotes a progressive enhancement in the reversibility of the system from 0.1 to 500 µg·mL^{-1}. Above this level, the deposition of additional material hinders ET processes and the system became more irreversible.

In the case of rGO- Fe_3O_4 NPs the deposition of rGO-Fe_3O_4 NPs in the range 0.2-10.0 $mg \cdot mL^{-1}$ improves the electroactivity of GCE. The topographic studies reveal that the lower dispersion of conjugate present a significant amount of aggregated on the bare GCE. By increasing the concentration of the casting dispersion, the coverage and average size of the imaged particles clearly increase and a thick and compact films of the conjugate are formed for dispersions ≥5 $mg \cdot mL^{-1}$.

Chapter 5 - A Layered Nanocomposite of Laccase, Chitosan, and Fe3O4 Nanoparticles-Reduced Graphene Oxide for the Nanomolar Electrochemical Detection of Bisphenol A

In this chapter a hybrid conjugate of reduced graphene oxide/ferrous-ferric oxide nanoparticles (rGO-Fe_3O_4 NPs) is characterized and assembled with chitosan and laccase to form a layered functional superstructure. After its characterization by FESEM, EDX, XPS, ATR-FTIRS, CV and EIS, the nanocomposite has been deposited on glassy carbon for the enzyme-mediated electrochemical determination of the endocrine disruptor bisphenol A (BPA). Proof-of-concept assays conducted by CV, EIS, and SWV, reveal that the enzymatic biosensor supplies linear response in a wide range of BPA concentrations (6-228 ppb), very high sensitivities, and excellent durability (over 1-month storage). Under amperometric detection, remarkable sensitivities (2080 $\mu A \cdot \mu M^{-1} \cdot cm^{-2}$) and detection limits (18 nM) are attained. Applications in real samples of bottled water proved feasible with recoveries in the range 107-124%.

The results shown in this chapter have been published as an article in an international peer-reviewed journal. The student performed the all experimental part, as well as writing the first draft of the article.

5.1. Contextualization

The 2,2-bis(4-hydroxyphenyl)propane (*aka* bisphenol A or BPA) is one of the most ubiquitous endocrine disruptors (EDs). Its ability to bind intracellular estrogen receptors (ERα, ERβ, and ERRγ) even at minimal doses[366, 367], may induce reproductive dysfunctions, increased risks of cancer, etc [368, 369], BPA has been found in consumer items (plastic food trays and baby bottles, beverage cans, etc) by solid-phase micro-extraction, gas/liquid chromatography-mass spectrometry, fluorescence spectroscopy, etc[370, 371]. However, other approaches based on miniaturized electroanalytical platforms seem more suitable for any environmental tracing of pollutants due to their low cost, reduced size, portability, high sensitivity, and rapid response. rGO exhibit well balanced surface-to-volume ratio, electrical conductivity, and electrocatalytic activity, to serve as conductivity/charge transfer enhancer in nanostructured coatings to improve the response of classic electrodes[372]. Strong synergies are obtained by conjugation with metallic/semiconducting nanoparticles (NPs) endowed with their own optoelectronic, catalytic, or magnetic, properties[373]. Thereby, the incorporation of rGO-NPs hybrids (NP: Au, Ni, TiO_2, etc) to electrochemical sensors has improved their sensitivity to the levels of laboratory methods based on much more expensive equipment and highly skilled personnel[116, 374, 375]. Non-enzymatic electrochemical sensors have exhibited high sensitivity (*S*) and low limits of detection (*LODs*) in the determination of BPA. For instance, Yu *et al.* reported values of 0.374 $\mu A \cdot \mu M^{-1} \cdot cm^{-2}$ and 8 nM, respectively, using a chitosan-Fe_3O_4 NP composite[376]. The incorporation of rGO or multi-walled carbon nanotubes (MWCNTs) have led to further improvements. Han *et al*. reported a *LOD* of 1.7 nM for a MWCNT-acrylamide composite[377] and Su *et al*. demonstrated an ultrahigh *S*=56.15 $\mu A \cdot \mu M^{-1} \cdot cm^{-2}$ using a film of the hybrid rGO-AuPd NP conjugate[374].

Lower *LOD* in the pM scale was attained with a multilayered superstructure of N-doped rGO and melamine[378]. Using high-capture biological probes (e.g. aptamers[379, 380] or peptides[381]) as receptors, has also led to lower *LOD*s in the pM-aM range. However, high costs and slow response (hours-days) limit their application in commercial portable/disposable solutions. Intrinsically more sensitive electrical/opto-analytical platforms like field-effect transistors (FETs)[382] or fluorescence resonance energy transfer systems (FRET)[383] have also exhibited *LOD*s in the fM-aM scale but these are, by far, less cost-effective. A very common issue in non-biological sensors remains its limited molecular selectivity in complex samples. In this sense, the high efficiency and selectivity of enzymes turns enzymatic biosensors much more desirable. While redox enzymes acting on phenols such as tyrosinases (TYRs) or horseradish peroxidase (HRP) present

low structural stability, self-inhibition issues, or, in the case of HRP, require hydrogen peroxide to perform; laccases are more stable and, like TYRs, oxidize diphenols in presence of oxygen (no additional co-factors required)[384, 385].

Despite these advantages, only a few BPA laccase-based electrochemical sensors (LES) have been reported in the literature[386, 387]. This work introduces a LES for aqueous BPA based on rGO-Fe_3O_4 NPs (nanomagnetites are inexpensive and provide large surface areas and improved biocompatibility)[388, 389], chitosan, and laccase. The layered nanocomposite was assembled onto glassy carbon and tested in cyclic voltammetry (CV), square wave voltammetry (SWV), electrochemical impedance spectroscopy (EIS), and chronoamperometric (CA) assays mediated by $[Fe(CN)_6]^{3-/4-}$ [116, 390, 391]. The good biocompatibility of chitosans is expected to enhance the stability of laccase and the synergistic effects at rGO-Fe_3O_4 NPs should improve the electron transfer (ET) processes/conductivity across the films. The biosensor achieved excellent electroanalytical performance and stability. Good reproducibility and selectivity were attained too. Additional testing in bottled water stocks supplied satisfactory results.

5.2. Results and discussion

5.2.1. Synthesis & Characterization of rGO-Fe_3O_4 NPs

The hybrid conjugate was synthesized following a method reported elsewhere.[347] Briefly, graphite flakes were dispersed in H_2SO_4 and heated at 98 °C (30 min) in presence of $NaNO_3$ and $KMnO_4$ (find more details in the chapter 3 Sections 3.3.1 – 3.3.3).

The composition, morphology, and crystallinity of the synthesized species were characterized by XPS, ATR-FTIRS, FESEM, EDX, and electrochemical techniques. In most of these experiments, the conjugate was deposited onto Si wafers and/or onto a glassy carbon electrode (GCE, Metrohm, 4 mm diameter) from a 10.0 mg mL^{-1} ethanolic dispersion. ATR-FTIR spectra were taken from the pure powder.

5.2.2. Physicochemical Characterization of rGO-Fe_3O_4 NPs

5.2.2.1. ATR-FTIR spectroscopy

Fig 5.1 show the physicochemical characterization of the rGO-Fe_3O_4 NPs conjugate (red line) obtained by ATR-FTIR spectroscopy. The black curve in the spectra corresponds to a commercial rGO powder sample included for comparison. The ATR-FTIR spectrum recorded for the commercial rGO shows no peaks in the range 600-1800 cm^{-1} (black solid line in Fig 5.1). In contrast, the synthesized hybrid (red) exhibits a series of peaks which are assigned as follows: (a) signals at 588 and 667 cm^{-1} due to the stretching of Fe-O bonds in Fe_3O_4 NPs,[392] (b) peaks at 1085, 1115, and 1153 cm^{-1} ascribed to the stretch of hydroxyl-substituted C atoms (C-O and C-C vibrations) in rGO and/or the NP organic shell[393-395], (c) bands at 1395 and 1635 cm^{-1}, also found for GO[396], attributed to stretching in restored sp^2 C atoms (=C-H and C=C, respectively)[397] or to in-plane C-H bending in $–CH_3$ groups at the NP shell (the 1340 cm^{-1} peak would account for analogous bending at skeletal $–CH_2–$ groups)[392].

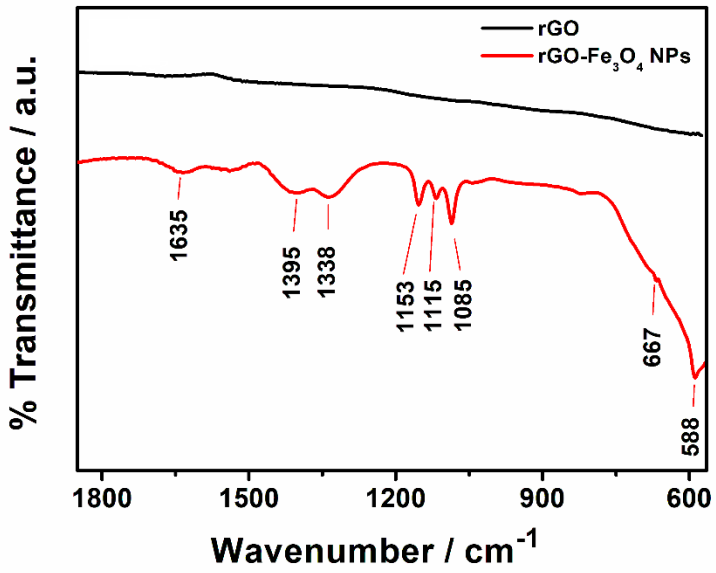

Fig. 5. 1: *ATR-FTIR spectra obtained for the rGO-Fe_3O_4 NPs conjugate. The black curve corresponds to a commercial rGO powder sample included for comparison.*

Other characteristic peaks of GO, e.g. those at 1220 (asymmetric C-O-C stretching in epoxides) and 1730 cm^{-1} (asymmetric stretching of C=O)[79, 394, 398], are not found in the acquired spectrum which confirms a significant reduction to rGO. This interpretation is reinforced by the elemental analysis.

5.2.2.2. XPS spectroscopy

A wide XPS spectra obtained for the rGO-Fe_3O_4 NPs conjugate is present in the Fig 5.2. The XPS spectrum in Fig 5.2A displays bands at: 285 (C 1s), 530 (O 1s), and 710 eV (Fe 2p). The C 1s core level XPS spectrum obtained for the rGO-Fe_3O_4 NPs sample is shown in Fig 5.2B (black solid line). Its de-convolution (coloured curves) resulted in a major peak at 284.5 eV (red curve) and a couple of shoulders at 285.7 and 288.3 eV (green and blue, respectively). In line with that found for rGO-Ni NPs[116], the strongest peak is attributed to graphitic sp^2 C bonding (C=C bonds in the rGO sheets) and the smaller bands to CO bonding in substituent groups (C-O and C=O, respectively). The small intensity of these peaks, suggest a residual content of these species in rGO.

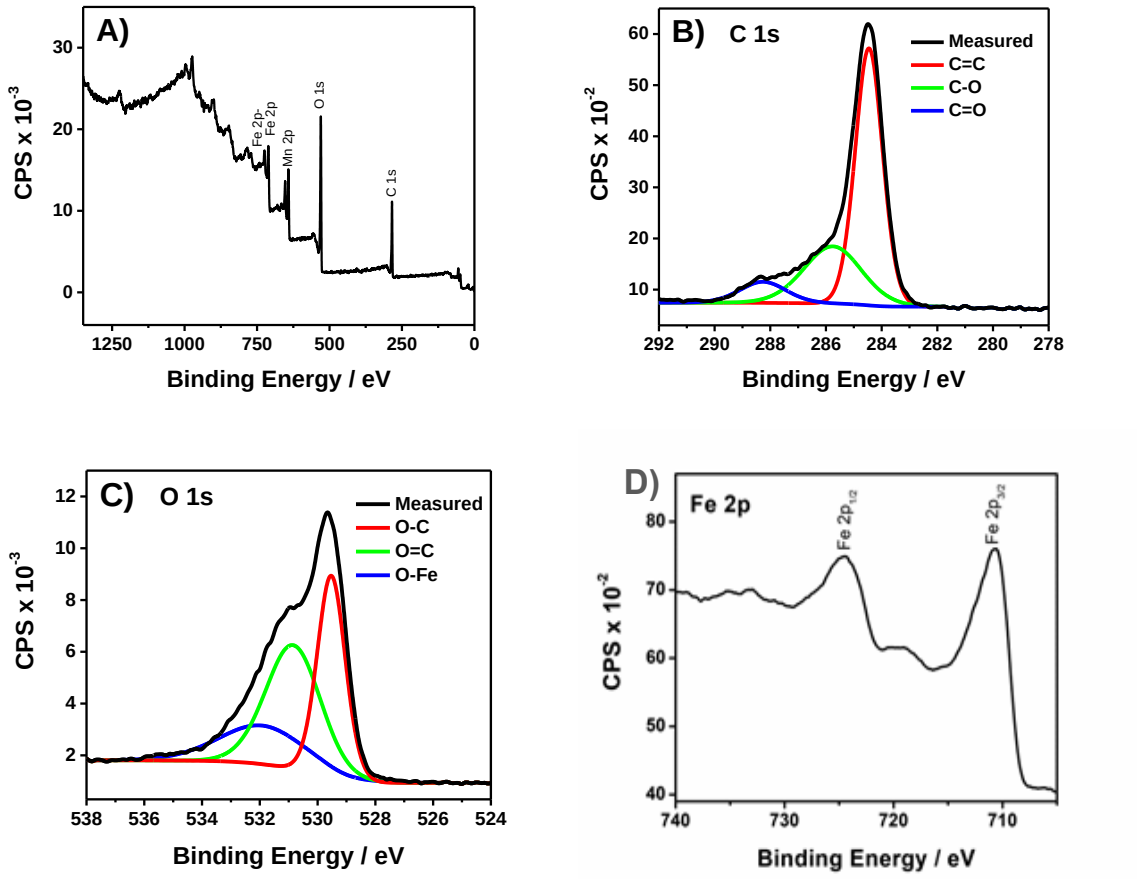

Fig. 5. 2: ***(A)*** *wide XPS spectra obtained for the rGO-Fe_3O_4 NPs conjugate.* ***(B)*** *C 1s core XPS spectra (black) of the rGO-Fe_3O_4 NPs conjugate and their corresponding de-convolution curves (coloured).* ***(C)*** *O 1s core XPS spectra (black) of the rGO-Fe_3O_4 NPs conjugate and their corresponding de-convolution curves (coloured).* ***(D)*** *Fe 2p XPS spectrum obtained for the rGO-Fe_3O_4 NPs conjugate.*

In good, agreement, the de-convolution of the O 1s core spectrum (Fig 5.2C) produced a couple of peaks at 529.5 (red curve) and 530.6 eV (green curve) ascribed to O-C and O=C bonds. Interestingly, their intensity agrees very well with to those found in

the de-convoluted peaks for the same bonds in Fig 5.2B. Hence, it seems that these may also belong to the same residual oxygen-containing substituents in rGO. The third, and less intense, band found at 532.1 eV (blue curve) is due to O-H bonding in those groups[399].

The Fe 2p spectrum in Fig 5.2D displays peaks at 710.4 and 724.3 eV associated to Fe-O bonding. The splitting of the photoemission into the Fe $2p_{1/2}$ and $2p_{3/2}$ components indicates the presence of iron in the Fe(II) and Fe(III) redox states. This finding confirms the presence of Fe_3O_4 in the hybrid conjugate[397].

5.2.2.3. FESEM and EDS spectroscopy

The morphology of GCE modified with rGO-Fe_3O_4 NPs was inspected by FESEM (Fig 5.3).

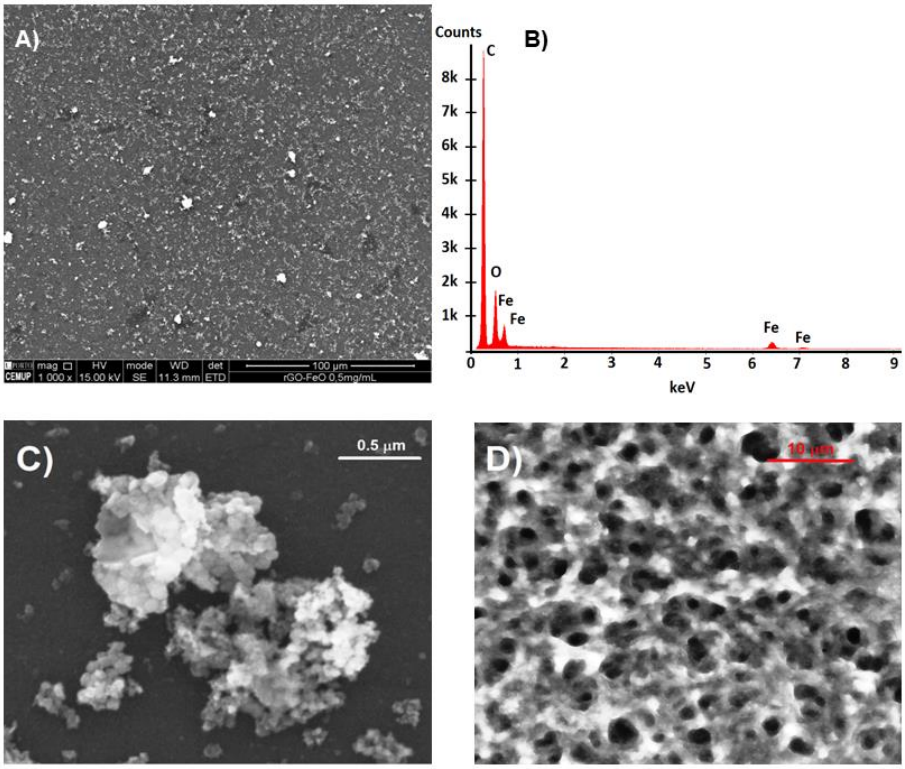

Fig. 5. 3: (A) *top-view of a glassy carbon electrode (GCE) decorated with the rGO-Fe_3O_4 NPs conjugate by adsorption from a diluted suspension in ethanol (0.5 mg mL^{-1}). The magnification factor is 1,000 X.* ***(B)*** *EDX spectrum taken at the individual particle isolated in FESEM image of Fig (D). FESEM top views of the GCE/rGO-Fe_3O_4 NPs* ***(C)*** *and the GCE/rGO-Fe_3O_4NPs/Chit95/TvL* ***(D)*** *modified electrodes (magnification factors: 100,000 X, and 5,000 X, respectively).*

Fig 5.3A shows a top-view of a GCE decorated with the rGO-Fe3O4NPs conjugate by adsorption from a diluted suspension in ethanol (0.5 mg mL^{-1}). In this image, the grey background (i.e. the GCE surface) is homogeneously covered by brighter particles of the synthesized material with coverage under the monolayer. The greatest fraction of these particles displays sizes below 1 µm. By zooming (100 times) on one of the smallest ones

(Fig 5.3C), 2D sheets of graphene loaded with spherical NPs were observed. The NP size (15-60 nm) agrees well with that found in previous studies for Fe_3O_4 NPs[400, 401]. The EDX spectrum taken at this exact location is shown in Fig 5.3B. The strongest peaks at 0.27 and 0.51 keV, support the presence of C and O. From the ratio of intensities measured for those, 4:1, one may have concluded that the original GO was reduced to a significant extent. In addition, two pairs of peaks can be observed at high (6.5 and 7.1 keV) and low energies (0.60 and 0.75 keV). suggest, again, the occurrence of Fe(III) and Fe(II). The position and intensity of those peaks agree quite well with those reported in the literature for Fe_3O_4 NPs[401, 402]. Thus, the EDX data taken over the analyzed particle matches perfectly the composition of rGO-Fe_3O_4 NPs conjugates.

5.3. Biosensor Assembly

The assembly of the rGO-Fe_3O_4NPs/Chit95/TvL nanocomposite was prepared onto a GC electrode cleaned by the procedure describe in de chapter 3 section 3.4.3. The bionanocomposite film was mounted on it following the sequential drop-casting procedure depicted in Scheme 5.1 (find more details in the chapter 3 Section 3.4.3.2).

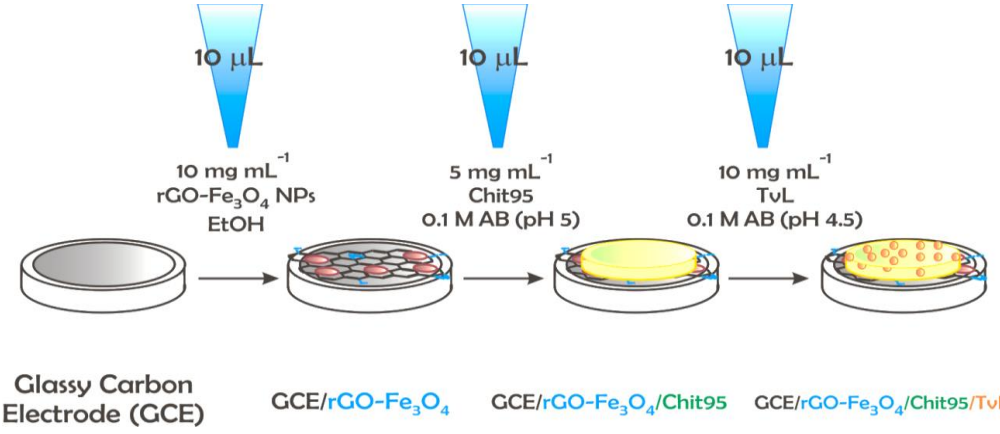

Scheme 5. 1: *Sequential drop-casting procedure followed for the modification of the GCE with rGO-Fe_3O_4NPs/Chit95/TvL nanocomposite films.*

The layer-by-layer construction of the film was monitored by electrochemical measurements in 0.05 M phosphate buffered saline (150 mM NaCl; PBS) and 2 mM $[Fe(CN)_6]^{3-/4-}$ solution in 0.05 M PBS at pH 7.4. CVs were acquired at 0.05 V·s^{-1} in the potential range -0.8/+0.9 V and -0.3/+0.6 V, respectively Impedance spectra were recorded at +0.15 V using a sine wave of 10 mV amplitude and frequency in the range 10^4-10^{-1} Hz. The EIS data were fitted to a R_sQR_1W Randles-type equivalent circuit. Chit95,

TvL, rGO-Fe_3O_4 NPs, and rGO-Fe_3O_4NPs/Chit95 films were also assembled on GCE for comparison purposes.

5.3.1. Results in Pure Buffer

The electrochemical response was acquired in pure buffer after each modification step are shown in Fig 5.4.

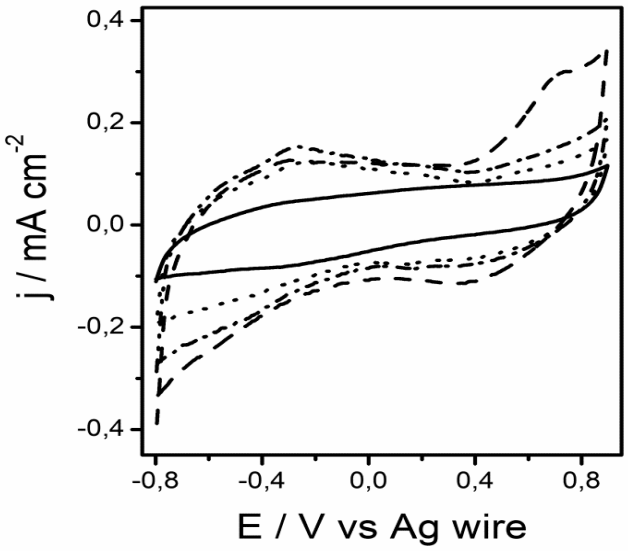

Fig. 5. 4: CVs obtained in PBS 0.05 M (pH 7.4) for the bare GCE (solid line), GCE/rGO-Fe_3O_4 (dashed), GCE/rGO-Fe_3O_4/Chit95 (dash dotted), and GCE/rGO-Fe_3O_4/Chit95/TvL (dotted). The scan rate was 0.05 $V \cdot s^{-1}$ in all cases.

As expected in the absence of redox probes, the bare GCE (solid curve) behaved like an almost pure capacitor. The deposition of the rGO-Fe_3O_4 NPs conjugate (dashed curve) not only increased the capacitive currents but also induced a couple of faradaic peaks (half-wave potential, $E_{1/2}$=+0.55 V). Considering that the tabulated standard potentials (E°) for Fe^{3+}/Fe^{2+} and Fe_2O_3/Fe_3O_4 are in the range +0.57/+0.46 V (vs Ag/AgCl/NaCl sat), the peaks are ascribed to the electroactivity of the rGO-supported NPs. The subsequent deposition of Chit95 and TvL (dash dotted and dotted curves, respectively) resulted in the continuous blockage of those peaks what reflects the increasing passivation of the NP surface after adsorption of the insulating species.

5.3.2. Results in 2 mM $[Fe(CN)_6]^{3-/4-}$

The same electrodes were tested in presence of hexacyanoferrate probes. The electrochemical response of the redox probes at the different stages of modification of the GCE is shown in Fig 5.5.

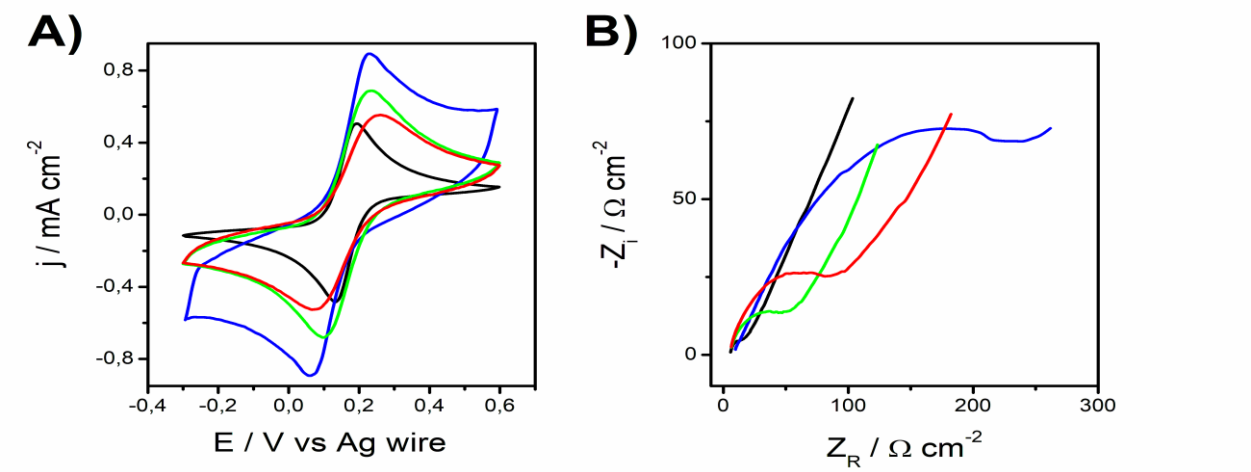

Fig. 5. 5: ***(A)*** *CVs recorded at 0.05 V·s^{-1} in PBS 0.05 M (pH 7.4) + 2 mM $Fe(CN)_6^{3-/4-}$ for: bare GCE (black solid line), GCE/rGO-Fe_3O_4 NPs (blue), GCE/rGO-Fe_3O_4NPs/Chit95 (green), and GCE/rGO-Fe_3O_4NPs/Chit95/TvL (red).* ***(B)*** *Nyquist plots acquired in same conditions at +0.15 V (oscillation amplitude: 10 mV).*

Analyzing the CVs in Fig 5.5A is possible extracted the peak-to-peak potential differences (ΔE_P) and peak anodic current densities (j_{PA}) represents in the table 5.1. In all cases, the measured values of $E_{1/2}$ values match the tabulated standard potential, E°, of the $[Fe(CN)_6]^{3-/4-}$ pair (i.e. +0.16 V vs Ag/AgCl/NaCl sat) so that the peaks are ascribed to the redox activity of the probes. The R_1 data derived from the impedance spectra in Fig 5.5B can also be found in the same table. The circuit used to fit the experimental Z_R *vs* $-Z_I$ plots recorded in this work (the so called Nyquist diagrams) consists of a variation of the well-known Randles circuit[403] which is schematically shown in Fig 5.6. In such a R_sQR_1W circuit, a Constant Phase Element (*CPE or Q*) replaces the typical capacitor in the Randles model to consider for the topological imperfections of the electrode surface. The other elements are: (1) the solution resistance (R_s), (2) the apparent electron transfer resistance (R_1), and (3) a Warburg element, *W,* which accounts for the impedance introduced by the diffusion of the probes from the solution bulk to the electrode surface. All the EIS spectra presented in Fig 5.5B feature a semicircle in the mid-high range of frequencies. In this region, the electron transfer is the rate determining step and, therefore, the impedance is governed by R_1. Hence, the size of the semicircle observed in the Nyquist plots can be directly correlated to the value of R_1: i.e. the larger the semicircle diameter the higher R_1 and vice versa[362].

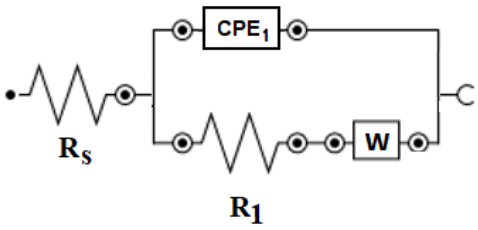

Fig. 5. 6: *Schematic representation of the R_sQR_1W equivalent circuit used to fit the EIS data recorded in this work (a variation of the popular Randles circuit in which the capacitor is replaced by a Constant Phase Element, CPE, to account for the electrode surface roughness).*

Table 5. 1: *Anodic peak current densities (j_{PA}), peak-to-peak potential difference (ΔE_P) and charge transfer resistance (R_1) derived from the experimental data presented in the Fig 5.5).*

Electrode	j_{PA} / mA·cm^{-2}	ΔE_P / mV	R_1 / kΩ
Bare GCE	*0.549*	*60.50*	*0.21*
GCE/rGO-Fe_3O_4 NPs	*0.745*	*171.0*	*11.7*
GCE/rGO-Fe_3O_4NPs/Chit95	*0.657*	*139.0*	*0.89*
GCE/rGO-Fe_3O_4NPs/Chit95/TvL	*0.509*	*187.6*	*1.61*

For the bare GCE, a very small value of ΔE_P (60.5 mV; very close to the theoretical minimum of 59 mV at 25 ºC) was obtained. In good agreement, the smallest R_1 was also estimated for that electrode (210 Ω). These results indicate that the ET of the probes is very fast and highly reversible in the GCE so that the process is limited by mass transport. As observed in pure electrolyte, the faradaic and non-faradaic components of current density (*j*) are reinforced in the CV of GCE/rGO-Fe_3O_4 NPs (blue curve in Fig 5.5A). Nevertheless, both ΔE_P and R_1 soared up to values of 171 mV and 11.7 kΩ, respectively. In addition, no linear domain can be found at low frequencies in its impedance spectrum (a feature that reflects the contribution of mass transport to the impedance). Therefore, the evidence indicates that the ET must be the rate determining step (instead of probe diffusion) governing the redox processes over the entire range of frequencies studied. Therefore, although the redox response must be boosted due to the vast increase in electroactive area (coming from both the high surface to-volume ratio of rGO and the high surface area contributed by the NPs), the adsorption of rGO-Fe_3O_4 NPs species also results in a slight hindering of the ET processes of the probes in the GCE. Interestingly, the deposition of Chit95 drove exactly opposite trends. On one hand, the recorded CV (green lines in Fig 5.5) exhibits a significant decline in the capacitive and faradaic currents compared to GCE/rGO-Fe_3O_4 NPs (although those are still significantly larger than the

observed for bare GCE). In line with this observation, j_{PA} also decreased slightly (Table 5.1). On the other hand, the size of the semicircle in Fig 5.5B became much smaller, R_1 decreased by more than one order of magnitude, and ΔE_P by about 30 mV. While the decreased response is ascribed to a partial passivation of the active sites upon adsorption of an insulating biopolymer, the parallel reinforcement of the ET processes may be explained considering that:

(a) the pK_a of $-NH_2$ groups in chitosans falls around 6.5 [404, 405];

(b) the degree of deacetylation (DD) reaches the 95% in Chit95;

(c) the Chit95 layer is deposited from a solution buffered at pH 5 (i.e. the pH within the scaffold may likely fall below the electrolyte pH)[406].

Then, it seems quite plausible that chitosan chains remain protonated, thus, holding a positive net charge at the working pH (7.4). Under such conditions, the negatively charged probes and other electrolyte anions would diffuse into the chitosan scaffold (with their associated water) to keep the electroneutrality. The electrostatic accumulation of ions within the chitosan layer would not only drive an increase of the electrode capacitance but also boost the apparent ET rate constant. Such an effect has been noticed in other chitosan-based layered electrodes [348, 407] and replicated in the experiments conducted under identical conditions for a GCE/Chit95 electrode (green curves in Fig 5.7). In conclusion, the redox response of GCE/rGO-Fe_3O_4/Chit95 electrode emerges from the balance between the reduction in electroactive area induced by chitosan adsorption and the electrostatic concentration of the probes within the deposited scaffold. The ET processes became slightly more hindered at the fully assembled GCE/rGO-Fe_3O_4NPs/Chit95/TvL electrode. This is supported by the small decrease of the peak currents in Fig 5.5 A (red curve) but also by the increase of ΔE_P and R_1 to values of 188 mV and 1.61 kΩ. (Table 5.1). These changes do support that the accommodation of TvL biomacromolecules within the polymeric network may bring slightly enhanced difficulties to the ET processes (via physical blockage of certain probe diffusion pathways or active sites). However, this is in striking contrast to the strong blockage of the redox response recorded at a GCEs coated with either TvL (red curves in Fig 5.7) or glucose oxidase enzymes[396]. In line with this behaviour, ΔE_P and R_1 were boosted up to values of 450 mV and 18 kΩ, respectively. A similar behaviour has been previously found for other redox enzymes deposited onto GCE (e.g. glucose oxidase, GOx)[116]. In the case of GCE/GOx, a similar blockage of the faradaic processes was noticed and explained as resulting from the formation of a hydrophobic and electrically insulating film following the rapid unfolding of GOx. Hence, the good electroactivity registered by the GCE/rGO-Fe_3O_4NPs/Chit95/TvL in fact demonstrates that the structural stability of TvL is dramatically improved when it is immobilized within the chitosan scaffold. The stabilizing role of Chit95 must be understood

on the base of: (1) the great biocompatibility of high-DD chitosans: the abundant hydroxyl and amino groups in its structure may interact with the hydrophilic outer regions of spheroproteins, thus, favoring their folded states[393, 408]; (2) the space constraints within the polymeric network and its impact on the physical arrest of the structural relaxation of the enzyme. The assembled films were also inspected by FESEM imaging. In this regard, Fig 5.3D shows the surface of a GCE entirely covered by a thick and uniform polymer-like film of spongy morphology (pore size in the range 0.5-4.5 µm).

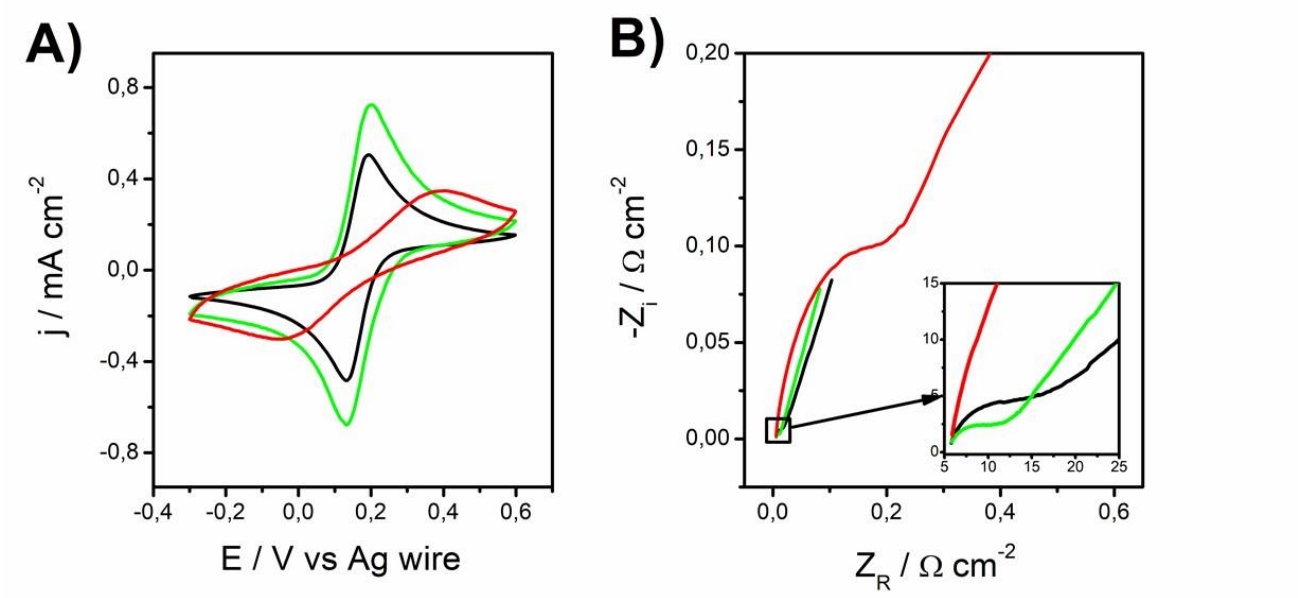

Fig. 5. 7*: (A)** *CV and* ***(B) *EIS curves acquired for the bare GCE (solid black line), GCE/Chit95 (green), and GCE/TvL (red) electrodes in PBS 0.05 M (pH 7.4) + 2 mM $[Fe(CN)_6]^{4-/3-}$. The scan rate and oscillation amplitude were 50 mV·s^{-1} and 10 mV, respectively.*

5.4. Electrochemical determination of BPA

Three independent replicas of the GCE/rGO-Fe_3O_4NPs/Chit95/TvL electrode were prepared and interrogated in 0.1 M AB (pH 4.5) + 2 mM $[Fe(CN)_6]^{3-/4-}$ + BPA (concentration range, [BPA]: 0.05-25 µM) by CV (potential window: -0.3/+0.6 V; scan rate: 0.050 V·s^{-1}), EIS (measurements taken at the cathodic peak potential: i.e. E_{PC}≈0.050 V in all cases; frequency range: 10^4-10^{-1} Hz; amplitude: 10 mV), and SWV (cathodic scans of 1 s duration from +0.6 to-0.3 V; scan rate: 0.015 V·s^{-1}; amplitude: 15 mV). The relevant parameters derived from these measurements (current density, charge transfer resistance, or differential current density), given as mean value ± MSE (standard error of the mean), were plotted against [BPA]. The calibration curves were obtained by linear regression of

the average experimental data and the slopes were taken as the average sensitivity (*S*). The limits of detection (LOD) were estimated from the linear regression data:

$$LOD = 3.3 \times SE_y / S_{sub\text{-}\mu M} \quad \textbf{(equation 5.1)}$$

where SE_y and $S_{sub\text{-}\mu M}$ are the standard error of the y-intercept and the slope in the sub-μM domain, respectively. Chroamperometric (CA) curves were also recorded at +0.15 V in the same electrolyte but in the lower [BPA] range of 0.025-25 nM. In this case, the LOD was estimated as the [BPA] providing a cut-off signal of 3 times the signal-to-noise ratio (*S/N*) (more details in analytical performance section 5.4.2).

5.4.1. Electrochemical response to BPA

Fig 5.8 show the electrochemical response of the GCE/rGO-Fe_3O_4NPs/Chit95/TvL electrode in the presence of BPA. Figs 5.8A-5.8C present the recorded CVs, Nyquist plots, and reverse SWVs.

Laccases are known to catalyze elemental one-electron (1e-) oxidation reactions in p-diphenols and analogues:

$$Lacc + OH\text{-}Ph\text{-}OH \rightarrow Lacc^{-} + HO\text{-}Ph\text{-}O^{-} + H^{+} \quad \textbf{(equation 5.2)}$$

In biological media, molecular O_2 is the typical electron acceptor that regenerates the enzyme. Nevertheless, in the de-aerated electrolytes used in this work, the redox probes play such role. As a consequence, a feed-back loop is established through which a good part of the Fe(III) generated at the anodic peak of Fig 5.8A, is reduced back to Fe(II):

$$TvL^{-} + [Fe(CN)_6]^{3-} \rightarrow TvL + [Fe(CN)_6]^{4-} \quad \textbf{(equation 5.3)}$$

According to this mechanism, any significant increase in [BPA] should lead to an increase of the oxidative current and a decline of the reductive one. This is in full agreement with the results presented in Fig 5.8A: i.e. while the anodic peak current density (j_{PA}) increases slightly, its cathodic counterpart (j_{PC}) experiences a rather steep drop.

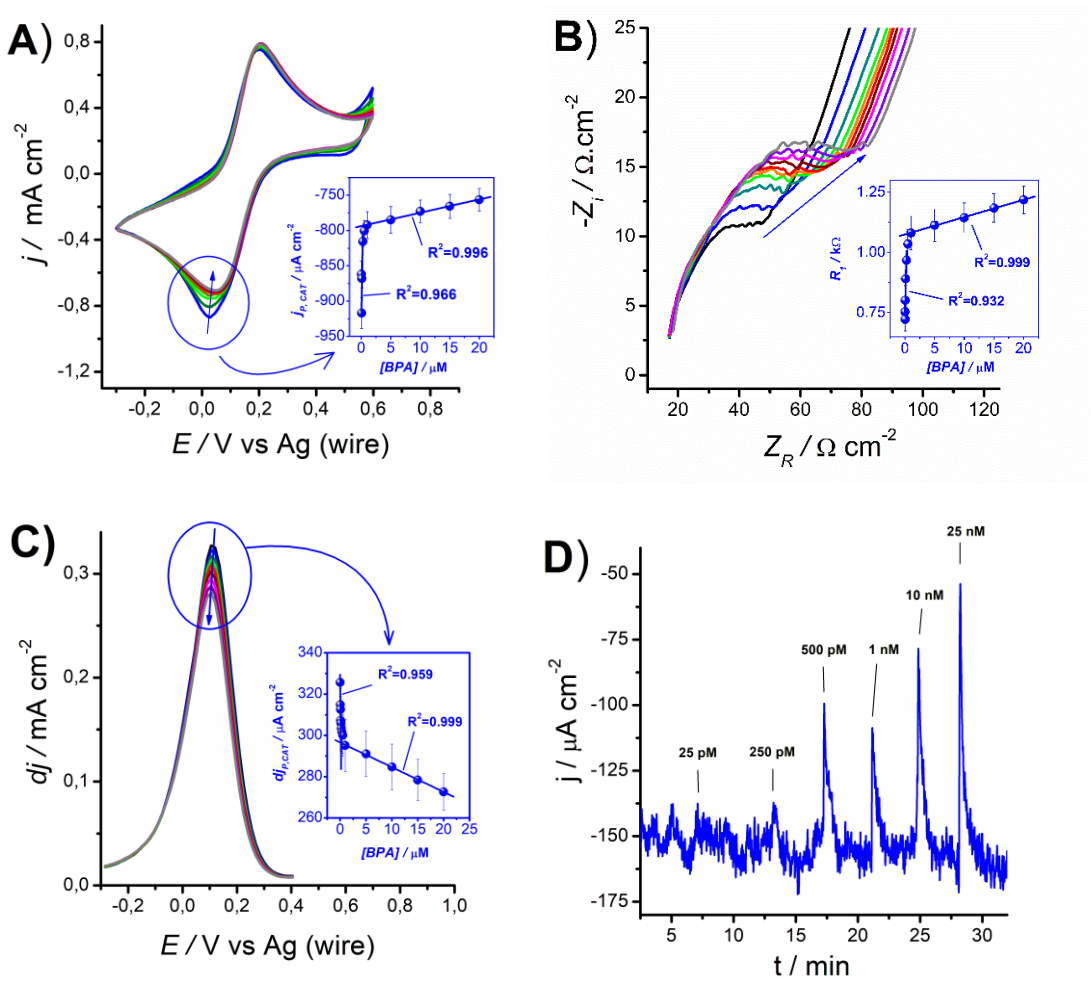

Fig. 5. 8: *CV* ***(A)****, EIS* ***(B)****, and SWV* ***(C)*** *interrogation of the GCE/rGO-Fe_3O_4NPs/Chit95/TvL biosensor in AB 0.1 M (pH 4.5) + 2 mM $Fe(CN)_6^{3-/4-}$ + BPA in the following concentrations: 0.025 (black solid curves), 0.050 (blue), 0.100 (olive), 0.250 (green), 0.500 (orange), 1 (red), 5 (wine), 10 (magenta), 15 (purple), and 20 µM (grey). The means j_{PC}, R_1, and dj_{PC}, with their corresponding error (given as the standard error of the mean; MSE) bars and linear regression curves, are displayed in the blue insets.* ***(D)*** *Chronoamperometric measurements in the same medium at +0.15 V ([BPA]=0.025-25 nM). Scan rate: 0.050 (****A****) and 0.015 mV·s^{-1} (****C****). Amplitude: 10 (****B****) and 15 mV (****C****).*

In this sense, the differential peak current densities (dj_P) derived from the cathodic SWV scans in Fig 5.8C follow an analogous decay. All replicas of the electrode reproduced this behaviour (see quantitative data in the table 5.2) demonstrating a good reproducibility in the preparation the sensor. By plotting the *mean* j_{PC} and *mean* dj_{PC} vs [*BPA*] (blue insets in Figs 5.8A & 5.8C) two linear domains can be identified. The first one operates in the submicromolar (sub-µM) concentration range (0.025-1 µM) and may be exploited in the detection of traces of BPA in water samples (clinical, food, or environmental; e.g. effluent discharges from wastewater treatment plants)[409]. The second covers a broader range of higher concentrations (1-20 µM) what turns it more appropriate for the analysis of concentrated samples (e.g. effluents from plastic manufacturing plants, etc).

The Nyquist plots recorded at the cathodic peak potential (Fig 5.8B) show a concomitant growth of the semicircle at mid-high frequency. As detailed in Section 5.3.2 (fitting Circuit), this feature relates to the value of R_1. In good agreement, the *mean* R_1 *vs* [*BPA*] plot (blue inset) reveals the continuous increase of this parameter along two linear domains identical to those spotted in Figs 5.8A and 5.8C. Hence, both the voltammetric and impedimetric evidence agree on the progressive hindering of the cathodic process when [*BPA*] is increased. As predicted by equations 5.2-5.3, this behaviour confirms that TvL molecules have been immobilized in a fully functional state.

Table 5. 2: *Average cathodic peak current densities (j_{PC}), apparent charge transfer resistance (R_1), and reversed scan peak differential current densities (dj_{PC}) derived from the three replicas of the biosensor (as plotted in the blue insets of Figs 5.8A-5.8C). The data is presented as the mean value at each single concentration ± SEM (the standard error of the mean). For better clarity, the relative standard errors (given as RSEM% = SEM/Mean x 100) are also given.*

[BPA] / µM	***j_{PC} / mA·cm^{-2}***	***RSEM%***	***R_1 / kΩ***	***RSEM%***	***dj_{PC} / mA·cm^{-2}***	***RSEM%***
0.025	*-0.86 ± 0.02*	*2.2*	*0.72 ± 0.05*	*6.9*	*0.31 ± 0.01*	*0.5*
0.050	*-0.92 ± 0.02*	*2.4*	*0.80 ± 0.06*	*7.6*	*0.30 ± 0.01*	*2.6*
0.100	*-0.87 ± 0.01*	*1.5*	*0.89 ± 0.06*	*6.6*	*0.29 ± 0.01*	*3.2*
0.250	*-0.81 ± 0.01*	*0.8*	*0.97 ± 0.05*	*5.4*	*0.29 ± 0.01*	*3.2*
0.500	*-0.80 ± 0.01*	*1.9*	*1.03 ± 0.06*	*5.7*	*0.29 ± 0.01*	*3.5*
1.000	*-0.79 ± 0.02*	*2.4*	*1.08 ± 0.07*	*6.5*	*0.28 ± 0.01*	*4.4*
5.000	*-0.78 ± 0.02*	*2.5*	*1.11 ± 0.07*	*6.0*	*0.28 ± 0.01*	*4.0*
10.00	*-0.77 ± 0.02*	*2.3*	*1.14 ± 0.06*	*5.4*	*0.27 ± 0.01*	*4.1*
15.00	*-0.76 ± 0.02*	*2.5*	*1.18 ± 0.06*	*5.0*	*0.26 ± 0.01*	*3.7*
20.00	*-0.76 ± 0.02*	*2.6*	*1.22 ± 0.06*	*4.7*	*0.26 ± 0.01*	*3.5*

5.4.2. Analytical Performance

Regardless of the mode of operation, the sensitivities attained very high values in both concentration domains (see details Table 5.3). Nevertheless, those in the sub-μM range are consistently two orders of magnitude higher (with a maximum of 471.3 µA·µM^{-1}·cm^{-2} in CV mode). LODs of 24, 15, and 11 ppb (103, 65, and 47 nM) have

been derived from the CV, EIS, and SWV assays, respectively. These figures fall close, or even below, the BPA levels found, for instance, in waters used for the sterilization of polycarbonate (PC) baby bottles (≈50 ppb)[410] or in bottled waters stored under different conditions (5-300 ppb)[411].

The European Food Safety Authority recommends a tolerable daily intake of 4 µg BPA per kg of body weight (bw) in adults. To reach that dosage merely through water consumption, an individual of 70 kg bw would have to drink 2 L per day of a water containing at least 150 ppb of BPA (a level significantly higher than the LODs discussed above). Therefore, the assays in Fig 5.8A – 5.8C show good potential for the assessment of the safety of waters stocked at shops, warehouses, logistic centers, etc.

Table 5. 3: *Parameters derived by fitting the average data in the sub-µM and µM domains (insets of Fig 5.8A – 5.8C) to straight lines with formula $Y = A \pm S \cdot [BPA]$, where Y accounts for either j_{PC}, R_1, or dj_{PC}; A is the y-intercept; S the slope; and R^2 the correlation coefficient.*

Mode	***Domain***	***[BPA] / µM***	***S / µA·µM $^{-1}$·cm^{-2}***	***A / µA·cm^{-2}***	***R^2***
CV	*Sub-µM*	0.025-1	471.3	-930	0.966
CV	*µM*	1-20	1.890	-794	0.997
SWV	*Sub-µM*	0.025-1	228.7	329	0.959
SWV	*µM*	1-20	1.200	297	0.999
			S / Ω·µM $^{-1}$	***A / Ω***	***R^2***
EIS	*Sub-µM*	0.025-1	950.5	746.8	0.936
EIS	*µM*	1-20	7.180	1075	0.999

Such a performance constitutes a solid demonstration of the biosensor concept and, in addition, it can be taken as excellent if the following aspects are considered: A) The inherent limitations of electroanalytical methods (compared to other more sensitive electrical/optical platforms based on field effect transistors, FETs; localized surface plasmon resonance; etc); B) The absence of analyte pre-accumulation steps or signal amplification schemes; C) The limited enzyme loading capacity of a single rGO-Fe_3O_4NPs/Chit95-TvL bilayer; D) The heterogeneous distribution of resistivity across the films (good electrical properties are mostly localized at the inner rGO-Fe_3O_4 NPs layer); and E) The limited stability of proteins at solid surfaces and its impact on the outcome of enzymatic biosensors.

The biosensor response was also investigated in a lower concentration range by CA (Fig 5.8D). A measurable signal was registered even at BPA levels as low as 5.7 ppt (25 pM). This is relevant since the disruption of cellular processes is triggered at very low exposure (at levels of ppt)[367]. However, the peaks recorded in

this region are statistically indistinguishable from noise and the LOD was calculated by the signal-to-noise method. This method is recommended by the European Pharmacopeia[412] and the International Conference on Harmonization (ICH)[413]. It is very popular for techniques that exhibit baseline noise, e.g. chromatography, and has been applied to the chronoamperometric determination in Fig 5.9A. The peak-to-peak noise around the analyte signals (*N*) is measured and the LOD is estimated as the [BPA] that produces a signal-to-noise ratio of S/N=3. In Fig 5.9A, *N* (30.4 $\mu A \cdot cm^{-2}$) and the intensity of the peaks (S_i, green lines) are measured. The S_i/N data are plotted vs [BPA] (Fig 5.9B) and fitted to a straight line (red). The LOD was interpolated from this line as the [BPA] for which $S_i/N=3$ (blue dashed line). A very low LOD of 18 nM (4 ppb) was obtained in this way. Despite the good responsiveness shown in the 25-250 pM range (peaks 1-3), these signals cannot be statistically distinguished from the noise with high confidence.

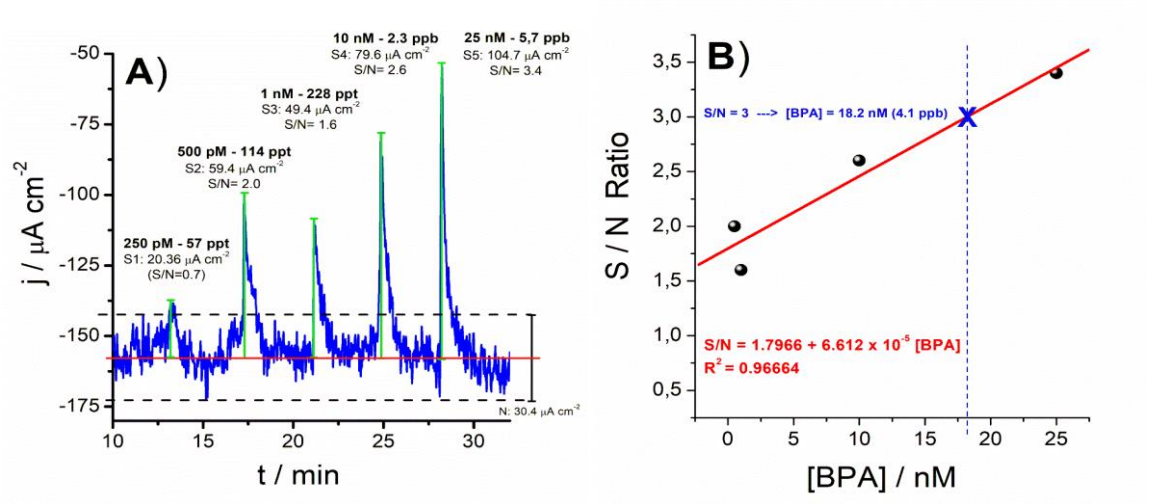

Fig. 5. 9: (A) *Amperometric curve registered at 0.17 V for a freshly prepared GCE/rGO-Fe_3O_4/Chit95/TvL biosensor after the consecutive injection of: 0.25 (13 min), 0.5 (17 min), 1 (22 min), 10 (25 min), and 25 nM BPA (28 min). The value of N was taken as the peak-to-peak difference in the background noise (black dashed lines). The signal for each peak, S_i, was measured from the half-height of the baseline (red solid line) to the peak maximum (green lines).* ***(B)*** *S/N ratio vs [BPA] plot derived from the data in panel A. The data was fitted to a straight line (fitting curve and parameters provided in red). The [BPA] value for a S/N of 3 was interpolated from the fitting curve and taken as the corresponding LOD (blue dotted line and inset).*

These results compare very well to those reported for other electrochemical sensors based on rGO/GO, MWCNTs, polymers, and/or inorganic NPs as signal transducers or supporting materials. In this regard, Table 5.4 presents the output registered by a number of devices (both, enzymatic and non-enzymatic) built off these nanomaterials. In all cases, the reported sensitivities are much lower than those discussed above (the highest one is about 4 and 37 times lower than those derived from SWV and CA, respectively). Tyrosinase-based enzymatic sensors (TES, entries 5th-7th) attain LDRs very similar to those verified for the GCE/rGO-Fe_3O_4NPs/Chit95/TvL biosensor under CV,

EIS, or SWV. However, the latter shows extended linearity down to the pM scale (Fig 5.8D) and LODs amongst those reported for the TES in the table (1-33 nM). This is important because TvL provides lower self-inhibition, better stability, and the ability to perform in absence of peroxide or oxygen acceptors. To our best knowledge, the best performing laccasse-based sensor (LES) reported so far (8th entry in Table 5.4) exhibits a LOD 4-11 times higher than those discussed for the GCE/rGO-Fe_3O_4NPs/Chit95/TvL biosensor and a more limited range of linearity (down to only 500 nM).

Table 5. 4: *Sensitivity (S), limit of detection (LOD), and linear dynamic range (LDR) reported in the literature for the detection of BPA using different enzymatic (E) and non-enzymatic (NE) electrochemical sensors.*

Technique	***Sensor***	***Type***	***S / μA·μM^{-1} cm^{-2}***	***LOD/ nM***	***LDR /μM***	***Ref.***
DPV[a]	GCE/Chit[b]/Fe_3O_4 NPs	NE	0.374	8.000	0.050-30	376
DPV	GCE/rGO-Fe_3O_4 NPs	NE	0.256	17.00	0.060-11	414
DPV	GCE/rGO-AuPd NPs	NE	56.15	8.000	0.050-10	374
CV	GCE/MWCNT[c]/PAAM[d]	NE	30.40	1.700	0.005-20	377
DPV	GCE/rGO-AuNP/Chit/Tyr[e]	E	50.89	1.000	0.025-3	415
CV	GCE/NGP[f]-Chit-Tyr	E	3.108	33.00	0.100-2	416
CA	SPCE/Fe_3O_4NPs/Tyr	E	3.199	8.300	0.027-40	417
CA	SPCE/CB[g]/Thio[h]/TvL	E	0.071	200.0	0.500-50	418
DPV	GCE/3DGN[i]/Cu/Fe_3O_4/TvL	E	5.014	1700	7.200-18	387
SWV	**GCE/rGO-Fe_3O_4NPs/Chit95/TvL**	**E**	**228.7**	**47.00**	**0.025-20**	**This work**
CA			**2080**	**18.10**	**2.5x10^{-5}-0.025**	
EIS			**950.5 Ω μM^{-1}**	**65.00**	**0.025-20**	

[a] *Differential Pulse Voltammetry;* [b] *Chitosan;* [c] *Multiwalled Carbon Nanotubes;* [d] *Polyacrylamide;* [e] *Tyrosinase;* [f] *Nanographene;* [g] *Carbon Black;* [h] *Thionine;* [i] *3D Graphene*

5.5. Reproducibility and Durability

Three independent replicas of the electrode were prepared. The error bars in the insets of Fig 5.8 represent relative standard errors of 1-3% (CV), 5-8% (EIS), and 2-4% (SWV) (Table 5.2). Taking into account the large amount of synthetic and assembly steps comprising the fabrication of the investigated biosensor, these values are very low and indicate a good degree of reproducibility. No signal degradation was observed during the registration of 100 consecutive CVs with a freshly prepared biosensor (Fig 5.10A). The relative standard deviation (*RSD*) of j_{PA} in these experiments fell below 1.5%, thus, showcasing the excellent repeatability and structural integrity of the biosensor under

continuous operation. As a proof of its good durability, the j_{PA} only declined by 18% after one month of storage at 4 ºC in AB 0.1 M (Fig 5.10B).

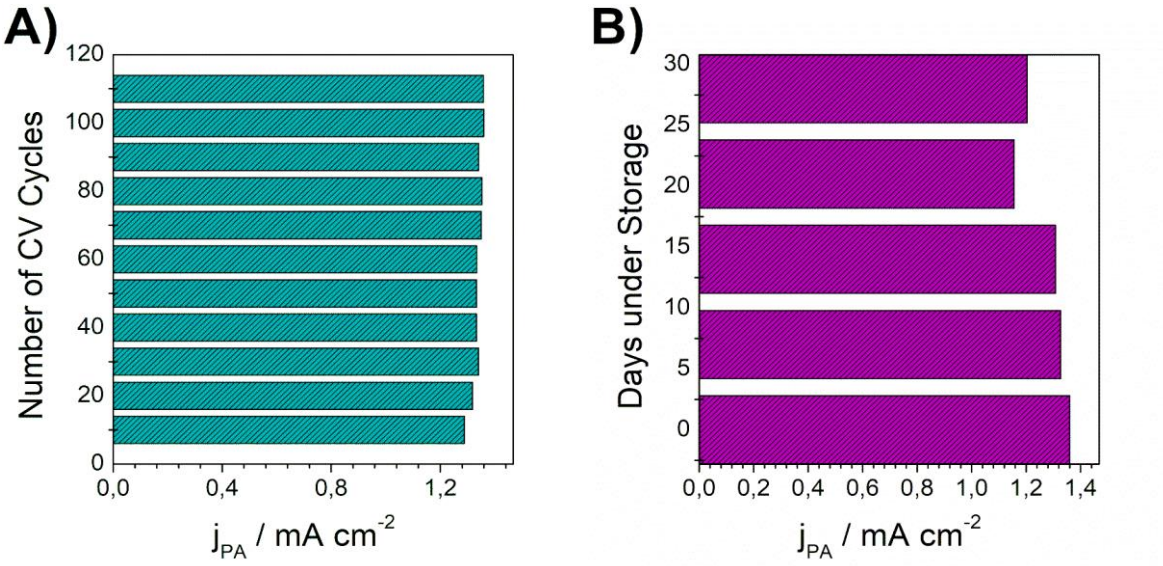

Fig. 5. 10: (A) *Anodic peak current densities (j_{PA}) measured every 10 CV-cycles for a freshly prepared GCE/rGO-Fe_3O_4/Chit95/GOx electrode (total nº cycles: 112).* ***(B)*** *j_{PA} derived from the CVs weekly recorded during one month for an analogous electrode stored in AB 0.1 M (pH 4.5). All CVs were registered at 50 mV·s^{-1} in AB 0.1 M (pH 4.5) + 2 mM $Fe(CN)_6^{3-/4-}$.*

5.6. Interferences

The impact of potentially interfering species (PIS) such as catechol (CC, an o-diphenol), ascorbic acid (AA), uric acid (UA), glucose (G), 1-naphthol (1-NTHL), 4-nitrophenol (4-NPHL), and benzene (BZ), was investigated in AB 0.1 M + $[Fe(CN)_6]^{3-/4-}$ 2 mM + BPA 10 µM + PIS 0.01-10 µM. By increasing [CC], a very small and symmetric decrease was observed in both redox peaks (*RSD* for j_{PC}: 5.5%, Fig 5.11A). A similar effect is found in Figs 5.11C, 5.11E, 5.11G, 5.11I, 5.11K, and 5.11M for AA (*RSD:* 0.4%), UA (6.2%), G (9.3%), 1-NTHL (1.8%), 4-NPHL (1.5%), and BZ (2.0%). Very minor changes are also observed in the registered Nyquist plots (Figs 5.11B, 5.11D, 5.11F, 5.11H, 5.11J, 5.11L, and 5.11N). Hence, only glucose seems to pose a really small but significant interference to the biosensor response (relative error well above ±6%).

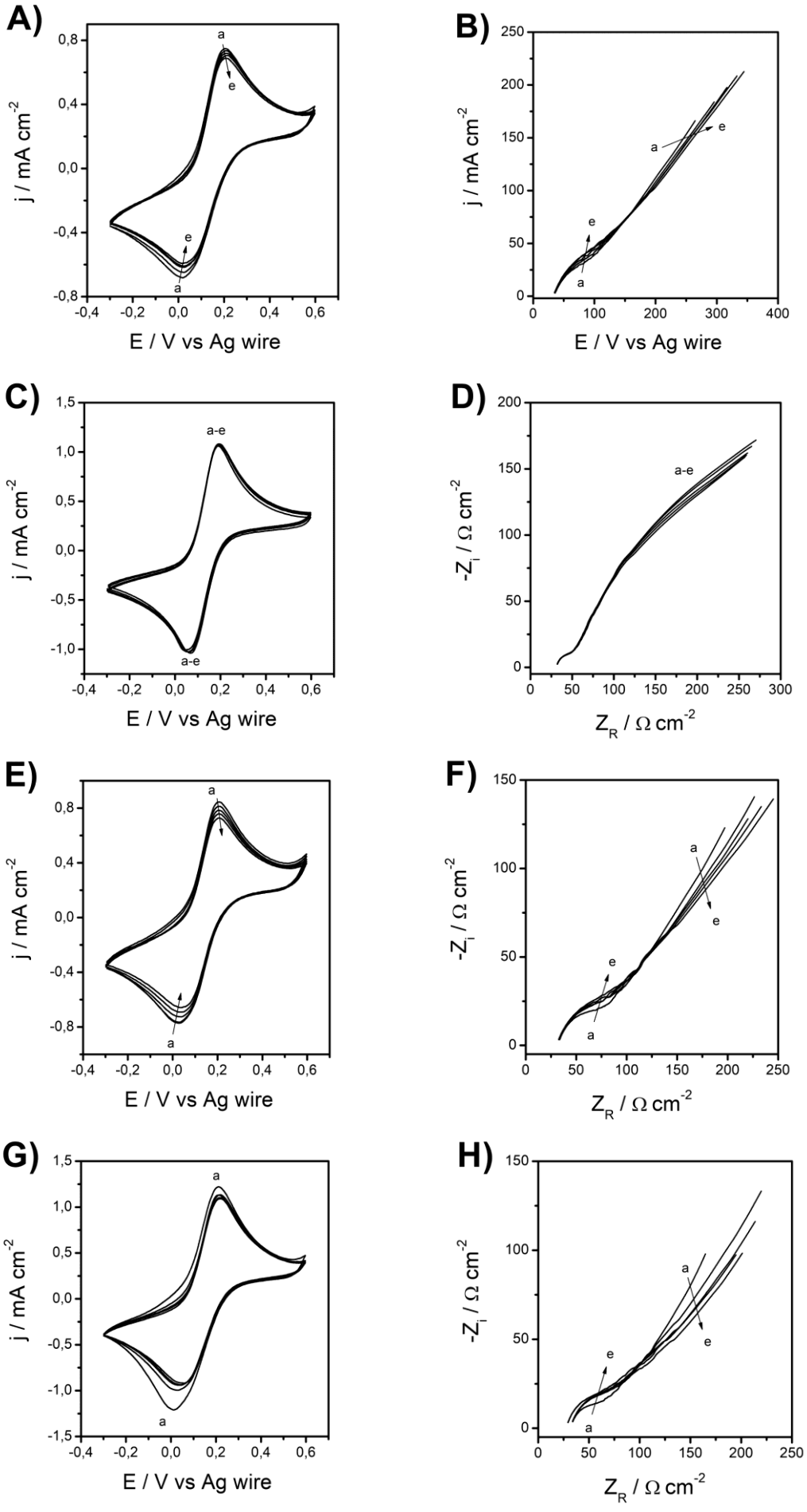
A)
j / mA cm-2
E / V vs Ag wire
a
e
B)
j / mA cm-2
E / V vs Ag wire
C)
j / mA cm-2
E / V vs Ag wire
a-e
D)
-Zi / Ω cm-2
ZR / Ω cm-2
E)
j / mA cm-2
E / V vs Ag wire
F)
-Zi / Ω cm-2
ZR / Ω cm-2
G)
j / mA cm-2
E / V vs Ag wire
H)
-Zi / Ω cm-2
ZR / Ω cm-2

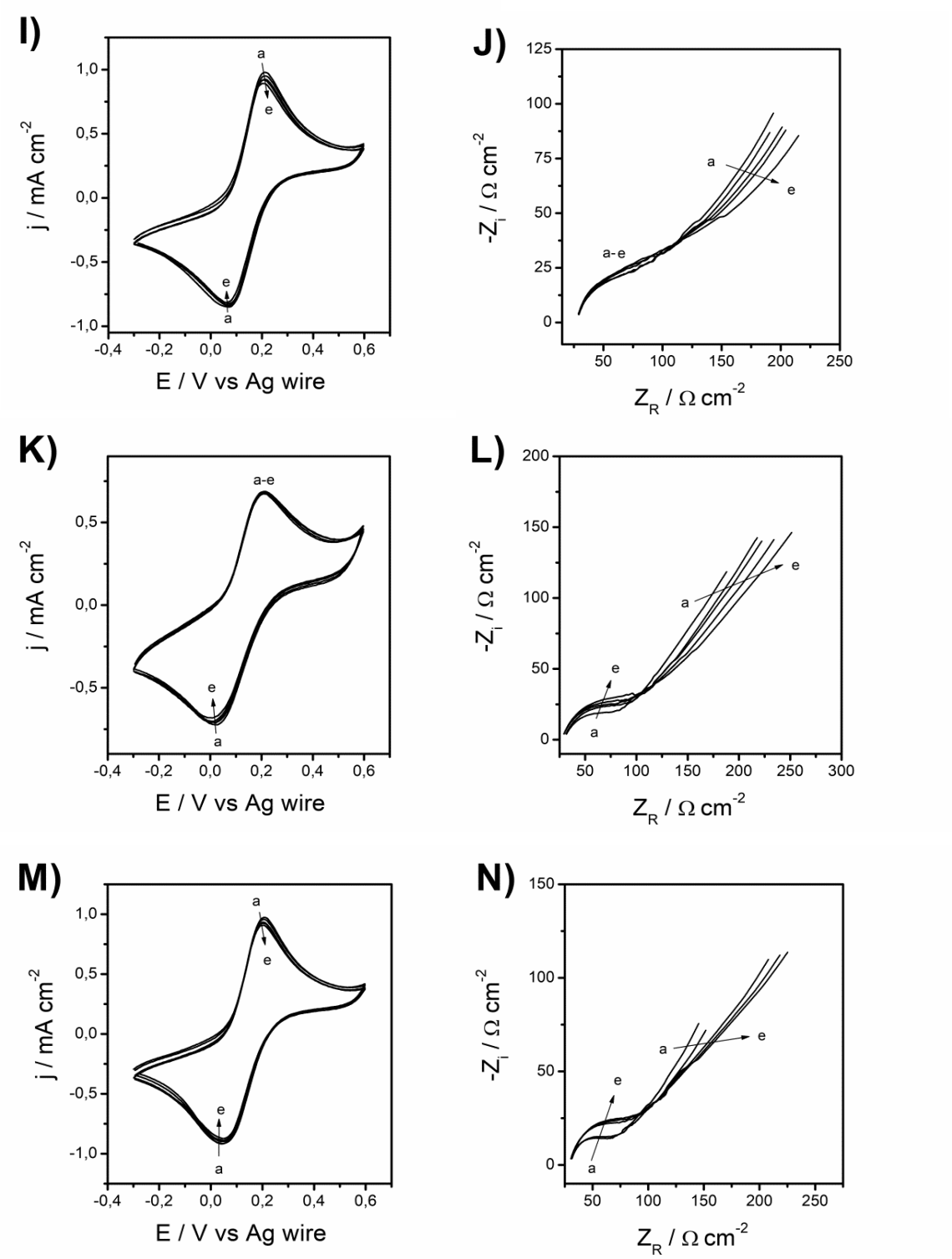

Fig. 5. 11: *CVs* ***(A, C, E, G, I, K, and M)*** *and Nyquist plots (****B, D, F, H, J, L, and N****) recorded for freshly prepared GCE/rGO-Fe_3O_4/Chit95/TvL electrodes in AB 0.1 M (pH 4.5) + 2 mM $Fe(CN)_6^{3-/4-}$ + 10 µM BPA after the injection of chatechol (****A, B****), ascorbic acid (****C, D****), uric acid (****E, F****), glucose (****G, H****), 1-naphtol (****I, J****), 4-nitrophenol (****K, L****), and benzene (****M, N****) in increasing concentrations: 0.01 (curve a), 0.10 (b), 1.00 (c), 5.00 (d) and 10.0 µM (e). The scan rate was 50 mV·s^{-1} and the oscillation amplitude 10 mV.*

5.7. Practical Application

To explore the potential of the GCE/rGO-Fe_3O_4NPs/Chit95/TvL electrode in real-life applications, commercial sport PC-bottles (1 L) were filled with ultrapure water and warmed at 100 ºC in a lab oven for two weeks. Afterwards, aliquots were added to an equal volume of working electrolyte (pH 4.5 in presence of 0.1 M AB+2 mM $[Fe(CN)_6]^{3-/4-}$) for later analysis by EIS. Three parallel determinations were performed in each case. The average concentration of endogenous BPA determined is 4.94 µM which falls within the range reported in the literature for aqueous samples incubated with BPA-leaching plastics under similar conditions (4-6 µM)[376, 377, 411].

BPA content was also determined after spiking the samples with 15 and 20 µM obtaining recoveries of 124 and 107%, respectively (RSD=1.7 and 2.2%). Although further optimization must be required for operation in real samples, the results demonstrate that the biosensor can detect harmful levels of BPA in waters stored in PC-bottles.

5.8. Conclusions

The work present in this chapter, describes an approach to the immobilization of TvL with a high surface area graphene-nanomagnetite conjugate (signal transducer) and a high-DD chitosan (biocompatible support). The nanocomposite has been tested towards the electrochemical detection of BPA at low potential (<0.2 V) without pre-accumulation or signal amplification schemes. Under these conditions, the GCE/rGO-Fe_3O_4/Chit95/TvL biosensor exhibits ultrahigh sensitivity (minimum LOD of 4 ppb BPA), wide linearity and rapid response. To our best knowledge, this is the best performing LES reported so far in the literature. Good reproducibility, durability, and an excellent operational stability have been registered. Among all the investigated PIS, only glucose interferes significantly with the biosensor response (although in a very limited and likely manageable way). At this stage, applications to the analysis of real waters (tap, bottled, stored, effluents from plastic manufacturing industries, etc) are more feasible than those for more complex samples (e.g. sugar-containing drinks, reconstituted foods, blood serum, etc). In any case, there is plenty of room for improvements in cross-sensitivity and analytical performance (e.g. through the engineering of more homogenous films, rGO-Fe_3O_4NPs/Chit95-TvL multilayers, and so on). Integration with miniaturized electrochemical technology may bring future solutions for testing the safety of real foods/drinks at a point-of-need.

Chapter 6 - Reduced Graphene Oxide-Nickel Nanoparticles/Biopolymer Composite Films for Sub-Millimolar Detection of Glucose

In this chapter the characterization of a rGO-Ni NPs conjugate and the preparation of nanocomposite films with chitosan (a deacetylated derivative of the abundant chitin polysaccharide which is used in graphene composites due to its excellent film forming abilities and biocompatibility) and glucose oxidase (GOx), is described. Applications as a glucose biosensor were explored in proof-of-concept assays mediated by $[Fe(CN)6]^{3-/4-}$ redox probes. This approach brings the advantages of the enhanced surface area and balanced electrical/electrochemical properties of the rGO-Ni NPs conjugate, the excellent biocompatibility and enhanced density of enzyme molecules accommodated in the chitosan scaffold, and the excellent selectivity of GOx.

The results shown in this chapter have been published as an article in an international peer-reviewed journal. The student performed all electrochemical experiments.

6.1. Contextualization

The disorders of carbohydrate metabolism are often regarded as the pandemics of the modern times. Only *Diabetes Mellitus* affected to 2.8% of the world population in 2000 (figures which could double by 2030)[419]. To date, the self-management of blood glucose levels has been the best proven approach to delay clinical complications[420]. In this sense, different generations of glucose sensors have been commercially available since the 60s. Biosensors, which take benefit from the high specificity of enzymatic processes (catalytic or enzymatic biosensors: e.g. glucose sensors)[421] and molecular recognition phenomena (affinity biosensors: e.g. immunosensors[422], DNA/RNA aptasensors[423], or molecularly imprinted polymers)[424], have expanded from healthcare to environmental monitoring, food safety, homeland security, etc; reaching a predicted market value of $20 billion by 2020[425].

Electrochemical sensors present inherent advantages such as good sensitivity, rapid and reliable response, and no need of laborious sample pretreatment or labeling. Furthermore, low-cost miniaturized chips and portable hand-held electrochemical readers put this technology ahead of their competitors for the development of wearable analytical tools that enable the self-management of different conditions[423, 426]. Despite their excellent selectivity, the sensitivity of biosensors is often limited by:

(a) Low coverage of biomolecules (enzymes, antibodies, and so on) immobilized on a 2D supports.

(b) Poor conformational stability of surface-attached biomolecules.

(c) Insulating or semiconducting nature of the most common supports (polymers, hydrogels, inorganic scaffolds, etc).

Nanotechnology has shrunk the dimensions of the main sensor elements for enhanced signal-to-noise (S/N) ratios. Nanostructured transducers and/or supporting matrices, exhibit much higher surface-to-volume ratios to improve the density of attached biomolecules. Regarding point (b), covalent immobilization typically leads to low coverage and/or reduced biological activity (due to the conformational changes triggered by the coupling chemistries). Oppositely, passive adsorption improves coverage but makes it harder to control molecular orientation and the organization of the layers. In parallel, protein unfolding is favored on many surfaces which further limits the activity of the attached biomolecules[427].

Conductivity enhancers such as redox mediators[428], conductive polymers[429], metal nanoparticles (MNPs)[430], and carbon nanomaterials, have been addressed to solve point (c). In this sense, carbon nanotubes (CNTs) allowed the direct electron

ET between redox enzymes and electrodes[431]. More recently, graphene (a one atom thick 2D sheet of honeycomb carbon easily prepared from graphite[138] or by vapor deposition)[38] has also been explored[231, 432]. Compared to CNTs, graphene has larger surface area, fewer impurities, and superior mechanical and electrical properties[138]. Indeed, water-processable chemically modified forms of graphene, e.g. GO are obtained in bulk quantities by functionalization and exfoliation of graphite.

GO has been explored as a membrane material[64] and a mechanical reinforcer[65]. Despite its poor electron conductivity, it presents good electrocatalytic properties[63] due to a high density of functional groups and structural defects[62]. After reduction to rGO, the conductivity is partially restored but, unavoidably, certain amount of functional groups and defects, remain in the structure. Therefore, rGO is a better balanced material for electrochemical applications. More recently, hybrid conjugates of rGO and metallic/semiconducting NPs (rGO-MNPs/SNPs) have been explored for energy storage, catalysis, analysis, and so on[52, 393, 433-440]. So far the most investigated conjugates in electroanalytical applications include MNPs of Au[433, 438], Cu[437, 441], and Pt[440]. While the use of Ni NPs may bring similar advantages in terms of surface-to-volume area, Ni is a cheaper and less toxic metal than the previous. Despite these advantages, the rGO-Ni hybrid conjugate has been only explored in a handful of non-enzymatic sensors for the detection of glucose (and other carbohydrates)[434, 435] and, to our best knowledge, no glucose biosensor based on this enhancer has been demonstrated to date.

In this chapter, the synthesis and characterization of a rGO-Ni NPs conjugate and the preparation of nanocomposite films with chitosan (a deacetylated derivative of the abundant chitin polysaccharide which is used in graphene composites[433, 440] due to its excellent film forming abilities and biocompatibility[391, 407, 442] and glucose oxidase (GOx), is described. Applications as a glucose biosensor were explored in proof-of-concept assays mediated by $[Fe(CN)_6]^{3-/4-}$ redox probes[443, 444]. This approach brings the advantages of the enhanced surface area and balanced electrical/electrochemical properties of the rGO-Ni NPs conjugate, the excellent biocompatibility and enhanced density of enzyme molecules accommodated in the chitosan scaffold, and the excellent selectivity of GOx.

6.2. Synthesis & Characterization of the rGO-Ni NPs Conjugate

GO was synthesized from graphite powder through a modified Hummers method[61]. Hybrid sheets of rGO-Ni NPs were grown *in situ* as reported in detail in the chapter 3 section 3.3.4.

The composition, morphology, and crystallinity of the synthesized species were characterized by XPS, ATR-FTIRS, FESEM, EDX, and electrochemical techniques. In most of these experiments, the conjugate was deposited onto Si wafers and/or onto a glassy carbon electrode (GCE, Metrohm, 4 mm diameter) from a 1,0 mg mL^{-1} ethanolic dispersion. ATR-FTIR spectra were taken from the pure powder.

6.3. Physicochemical Characterization of rGO-Ni NPs

6.3.1. XRD patterns

The XRD patterns of GO and rGO-Ni NPs are shown in Fig 6.1.

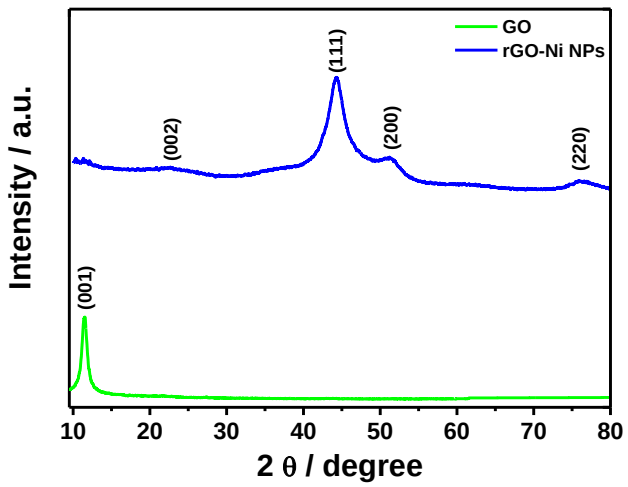

Fig. 6. 1: XRD patterns obtained for GO (green curves) and rGO-Ni NPs (blue) powder samples.

For GO, a virtually flat diffractogram dominated by one single spike at 2θ=11°, which is typically ascribed to its (001) basal plane[395, 445], was registered (green curve). The d-spacing was d_{001}=0.81 nm which agrees well with the interlayer distance in GO (typical values for graphite flakes are ≈0.33 nm). Such an increase in the distance between graphitic sheets indicates a successful introduction of functional groups and solvent

molecules. In big contrast, the diffractogram of rGO-Ni NPs featured a series of bands at 2θ>20° (blue curve). The small band at 23° is due to the (002) crystallographic plane of rGO[445]. From its low intensity, it is strongly suggested that rGO sheets are covered by a different material. The rest of peaks matched well the typical pattern of Ni crystals with face centered cubic structure (fcc) [JCPDS card No. 04-0850]. In this sense, the intense band at 44.4° (ascribed to diffraction by Ni (111) facets) confirms the good crystallinity of the grown NPS.

6.3.2. ATR-FTIR Spectroscopy

Deeper insights on the composition of the hybrid were obtained by ATR-FTIR sprectrum presents in Fig 6.2. The spectrum of GO exhibited a series of bands (green curve). While the main of these peaks, registered at 1625 cm^{-1}, involves a variety of possible vibrations (asymmetric stretching in deprotonated carboxyls, $\nu_{COO,AS}$; stretching in ketones, $\nu_{C=O}$[446], or O-H bending in adsorbed H_2O); the peak at 1730 cm^{-1} is precisely ascribed to symmetric carbonyl stretching in edge carboxyl groups, ν_{COOH}. Other bands were also found at 1220 cm^{-1} (C-O-C asymmetric stretching in epoxides), 1415 cm^{-1} (combined carbonyl stretching and in-plane C-O-H bending in protonated carboxyls, ν_{C-OH}), and the small shoulder at 1810 cm^{-1} (carbonyl stretching in chloride acids)[79, 395, 445, 446].

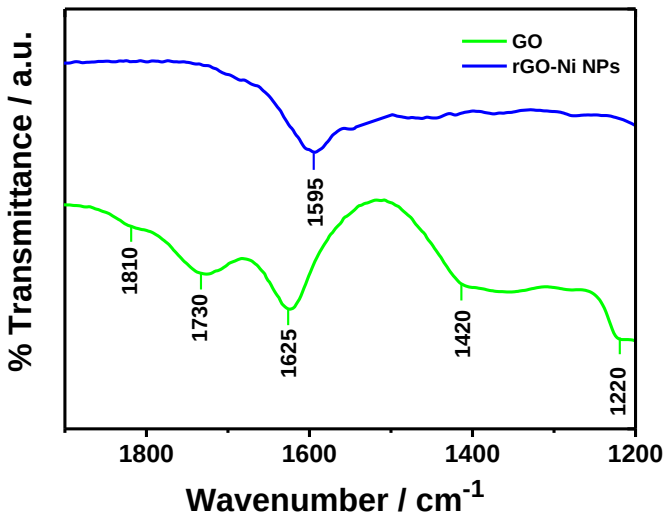

Fig. 6. 2: *ATR-FTIR spectra obtained for GO (green curves) and rGO-Ni NPs (blue) powder samples.*

For rGO-Ni, significant absorption only took place at 1595 cm^{-1} which may involve: (1) largely restored sp^2–hybridized C=C aromatic vibrations[79], (2) residual carboxyl or ketone groups (literature has shown that a complete reduction of GO is difficult to achieve even by high-temperature annealing)[79], or (3) adsorbed H_2O. In summary, not only most

of the vibrations related to oxygen-based functional groups vanished from the spectrum but no new peaks accounting for distinct functional groups were also observed. These results strongly support that, through the described method, a high degree of reduction of the original GO sheets to rGO was achieved. This view was additionally confirmed by XPS.

6.3.3. XPS Spectroscopy

Fig 6.3 show the C 1s XPS spectrum measured for rGO-Ni NPs (black) and its corresponding de-convolution curves (coloured). While the major peak at 284.9 eV is attributed to the sp^2 C=C bond (graphitic carbon bonding), the peaks at 286.6 eV and 288.5 eV are assigned to carbon-attached remaining oxygen functionalities (C-O and C=O, respectively)[116]. The small intensity of these peaks, propose a residual content of these species in rGO.

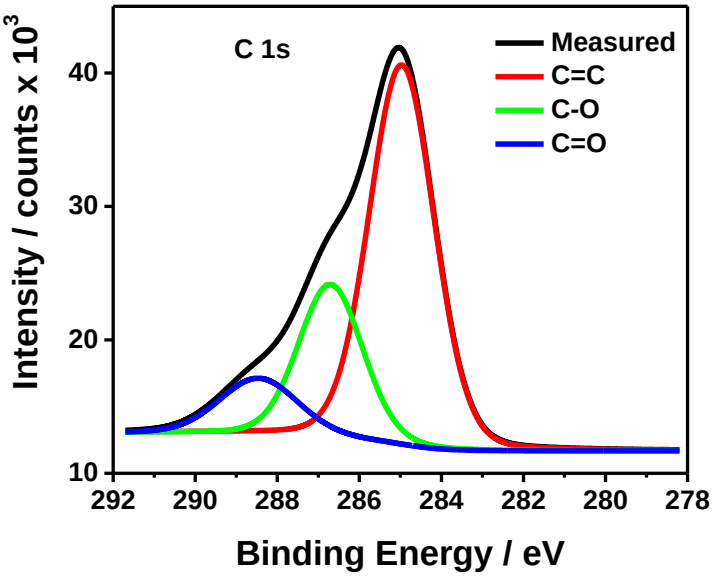

Fig. 6. 3: *The C 1s XPS spectrum measured for rGO-Ni NPs (black) and its corresponding de-convolution curves (coloured).*

6.1.1. SEM and TEM Characterization

The morphology of the rGO-Ni NPs conjugate was inspected by FESEM (Fig 6.4a) and HRTEM (Fig 6.4b). The image of FESEM displays a bright spherical clusters of particles with size below the micron which seem deposited onto a surface apparently covered by 2D sheets of graphene. More details were obtained with the HRTEM technique.

Fig 6.4b displays a 2D sheet of rGO decorated with a homogeneous distribution of NPs (5-10 nm size). Despite the good degree of isolation of the NPs in this sample, clusters of about 3-5 NPs (size: 15-20 nm) are also found in this image.

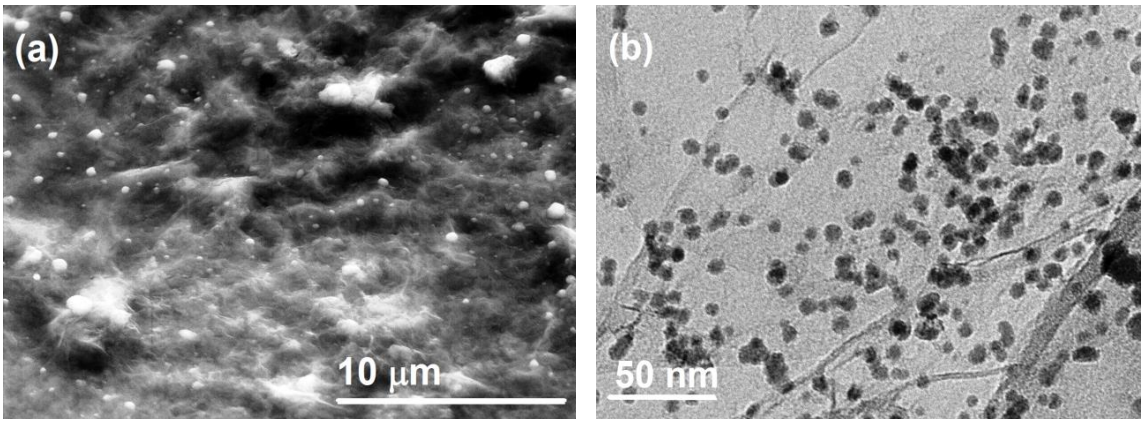

Fig. 6. 4: *(a) SEM and (b) HRTEM images taken for the rGO-Ni NPs powder.*

6.2. Fabrication of the Composite Films

The rGO-Ni/Chit95/GOx composite films were deposited onto a glassy carbon electrode by sequential drop-casting. Previously, the GCE was polished and consecutively washed. Cyclic voltammetry (CV) in H_2SO_4 0.5 M was used to assess the cleanliness of the electrode. Then, it was modified in three sequential steps (Scheme 6.1) (more details are available in chapter 3, section 3.4.3).

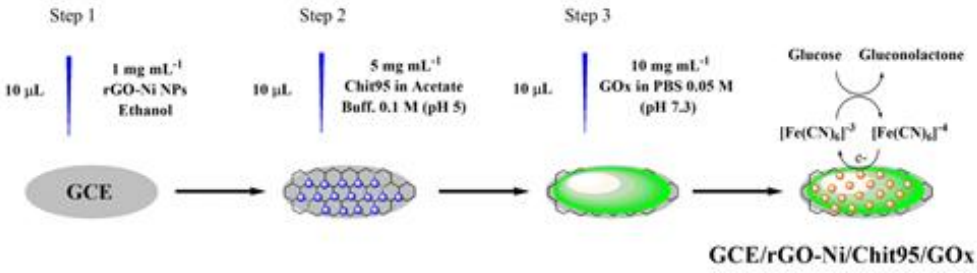

Scheme 6. 1: *Artistic illustration showing the different steps applied for the preparation of a rGO-Ni/Chit95/GOx nanocomposite film onto a clean GCE.*

The build-up process was followed by electrochemical measurements in PBS (Fig 6.5). Panel A presents the CVs registered for bare GCE, GCE/GOx, GCE/Chit95, GCE/Chit95/GOx, and GCE/rGO-NiNPs. Interestingly the capacitive current exhibited by the bare GCE (black solid curve) was significantly blocked after adsorption of GOx (red solid curve).

The hypothetical unfolding of GOx molecules on GCE to form a hydrophobic blocking layer, would result in a significant reduction of the electrode capacitance. Hence, the evidence points to a poor conformational stability of GOx onto glassy carbon. In great contrast, the capacitive current of GCE/Chit95 (green solid curve) overtook that exhibited by the bare GCE.

The pK_a of $–NH_2$ groups in chitosan falls around 6.5. Hence, chitosan exhibits positive charge at pHs ranging from acidic to neutral. Due to the high DD of Chit95, and because it was deposited since AB pH 5 (i.e. the pH at the electrode surface may be slightly inferior to that at the electrolyte)[447], it would not be surprising that it remained partially protonated under the working conditions (pH 7.3).

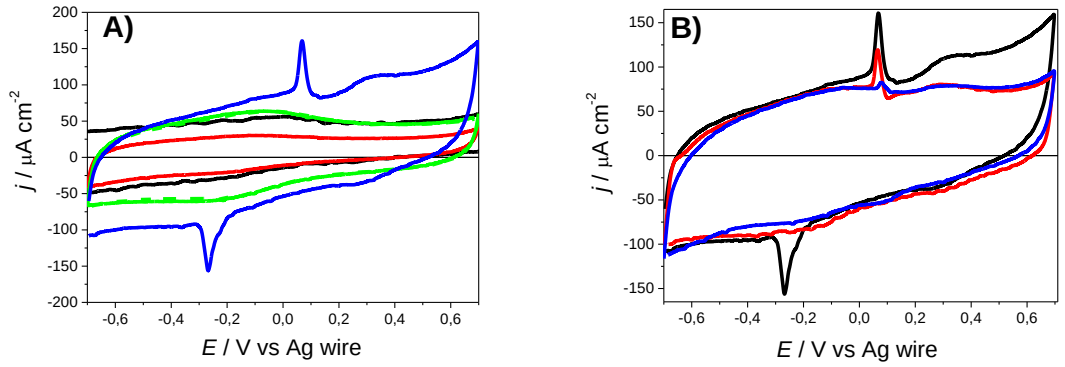

Fig. 6. 5: (A) *CVs obtained for bare GCE (black solid line), GCE/GOx (red), GCE/Chit95 (green), GCE/Chit95/GOx (green dashed line), and GCE/rGO-Ni NPs (blue) in PBS 0.05 M (pH 7.3).* ***(B)*** *Evolution of the CV for GCE/rGO-Ni NPs (black curve) after its sequential modification to GCE/rGO-Ni/Chit95 (red) and GCE/rGO-Ni/Chit95/GOx (blue). The scan rate was 50 mV·s^{-1} in all cases.*

In such a case, solution anions (and their associated water molecules) would diffuse within the biopolymer matrix to keep the electroneutrality. As a consequence, the capacitance of the electrode should increase as it is reflected in the recorded CV.

Contrary to behaviour of GCE/GOx, the CV of GCE/Chit95/GOx (green dashed line) presented negligible changes compared to GCE/Chit95. This may be due to: (1) the GCE surface is densely covered by Chit95 and no direct adsorption of GOx onto the GCE surface occurs, or (2) the biopolymer surface area is much higher than that for uncovered GCE so that the impact of GOx unfolding on the average electrochemical response is nearly negligible. In any case, the result confirms an improved stability of GOx when supported by Chit95. For GCE/rGO-Ni (blue solid line), a large increase of the non-faradaic current was noticed throughout the whole potential range. Moreover, a pair of sharp peaks were identified at +0.07 and -0.27 V. The enlarged double layer is typical of graphene-modified electrodes (and attributed to its high surface-to-volume ratio and the consequent increase in the amount of storable interfacial charge). G. Chen *et al*. reported an analogous

pair of peaks for a magnetically assembled rGO-Ni NPs electrode[448]. Despite differences in CV-shape and peak potentials (which may originate from the different synthesis and electrode preparation), a broad peak-to-peak potential separation ($\Delta EP \geq 320$ mV) was found in both cases. Chen assigned the peaks to the electroactivity of the $NiOOH/Ni(OH)_2$ redox pair. Given the absence of redox probes in our experiments, the faradaic peaks in Fig 6.5A must be ascribed to the Ni NPs species in the hybrid conjugate. Further coating of the GCE/rGO-Ni NPs electrode (black curve in Fig 6.5B) with Chit95 caused a very slight decrease of the non-faradaic currents (red curve). However, the subsequent deposition of GOx (blue curve) resulted in an important blockage of the faradaic processes. These results evidence a continuous passivation of the Ni NPs surface after deposition of the biopolymer and the enzyme layers.

6.3. Structure and Composition of the film

The morphology of the rGO-Ni/Chit95/GOx films was inspected by FESEM. Fig 6.6A shows a wide view at the borders of the electrode surface and its housing. The GC surface is covered by a thick, smooth, and uniform film which looks like a hydrogel. Over the electrode housing, a cracked region revealed the polymeric structure of polyether ether ketone (PEEK) below the detached film. At the right end of the crack, the film was twisted so that its entire cross-section was exposed. From this particular feature, the film thickness could be roughly estimated in 3-4 μm. Some microns to the left, a bunch of graphene sheets appeared wrapped in the film (see a higher magnification image in the red inset).

Fig 6.6B shows another snapshot taken at a different location in which a part of the film was intentionally removed. The induced step allowed for the direct comparison between the composite-covered (brighter region on the left) and the bare GCE surface (right). In the latter, a number of bright features with island-type morphology were observed in the vicinities of the induced step. Their closer inspection with higher magnification (red inset) unveiled individual sheets of rGO (of about 2 μm width) loaded with bright clusters of particles with size ranging between 20 and 60 nm in (in good agreement with the shape and size of the few-NP aggregates shown in Fig 6.4b).

An EDS spectrum taken over one of these islands showed that these are mainly composed of carbon, oxygen, and nickel (Fig 6.6C) The absence of N peaks, allowed discarding the presence of colloidal forms of chitosan. Therefore, the combination of FESEM and EDS support the observation of isolated 2D sheets of rGO-Ni NPs. It might be also concluded that the structure of the composite film consists of a base layer of the

rGO-Ni NPs hybrid covered by chitosan hydrogel (which contains the GOx). This structure not only agrees with the changes shown in Fig 6.5 but also fits the order of assembly followed in the preparation of the composite.

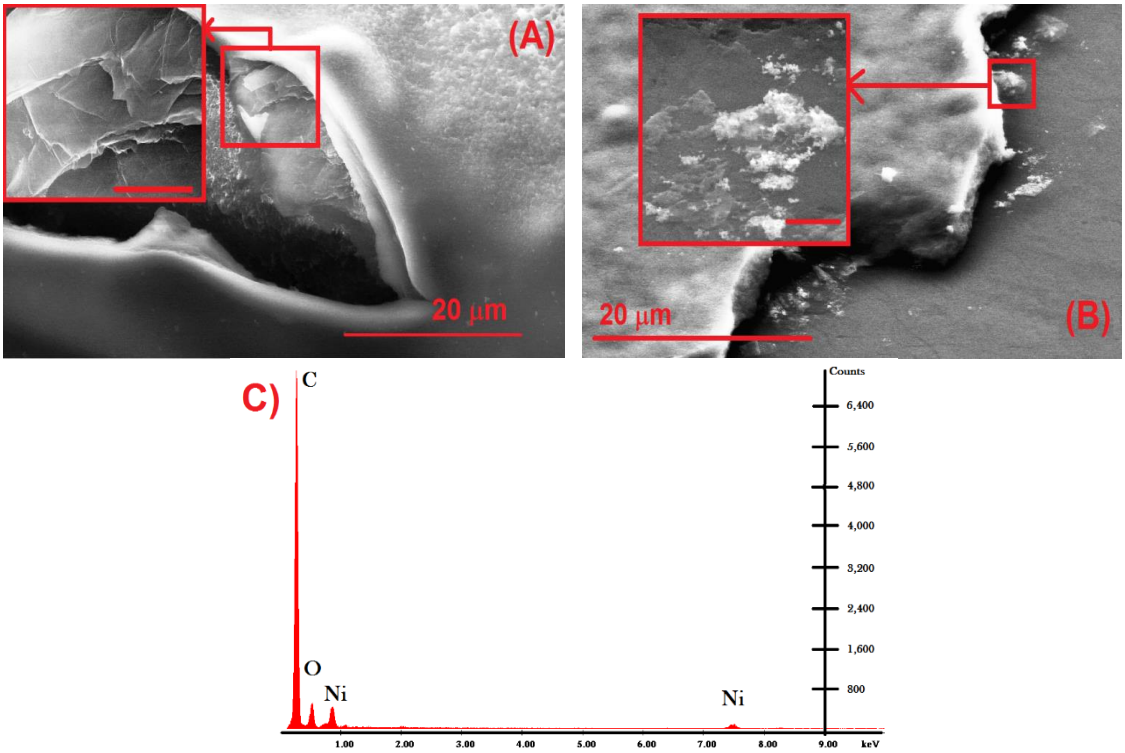

Fig. 6. 6: (A, B) *FESEM images taken at two different locations over the GCE/rGO-Ni/Chit95/GOx surface. The red insets display areas re-scanned with higher magnification (the width of the red bar is 2 µm in both cases).* ***(C)*** *EDS spectrum acquired over the isolated island-type feature isolated in the inset of Fig 6.6B.*

6.4. Stability and Catalytic Activity of GOx

The stability of GOx was investigated by testing its catalytic activity in presence of glucose. Figure 6.7 presents the interrogation tests conducted by CV (panel A) and EIS (panel B) for bare GCE, GCE/GOx, GCE/Chit95/GOx, and GCE/rGO-Ni/Chit95/GOx in 1 mM glucose. Blank measurements in its absence have been also included for comparison purposes. In the absence of glucose, the adsorption of GOx (red solid curve in Fig 6.7A) resulted in a great blockage of the reversible faradaic processes seen for bare GCE (as also occurred with the capacitive currents in Fig 6.5A). Accordingly, the anodic peak current density (j_{PA}) dropped by almost 0.5 $mA \cdot cm^{-2}$ and ΔE_P grew to 800 mV (see Table 6.1). Its corresponding Nyquist plot (red solid curve in Fig 6.7B) exhibited a semicircle at high-medium frequencies whose diameter was, by far, the largest amongst all the investigated electrodes. In this frequency region, the total impedance is controlled

by the apparent charge transfer resistance (R_1) so that, the wider the observed semicircle registered the higher is R_1[362].

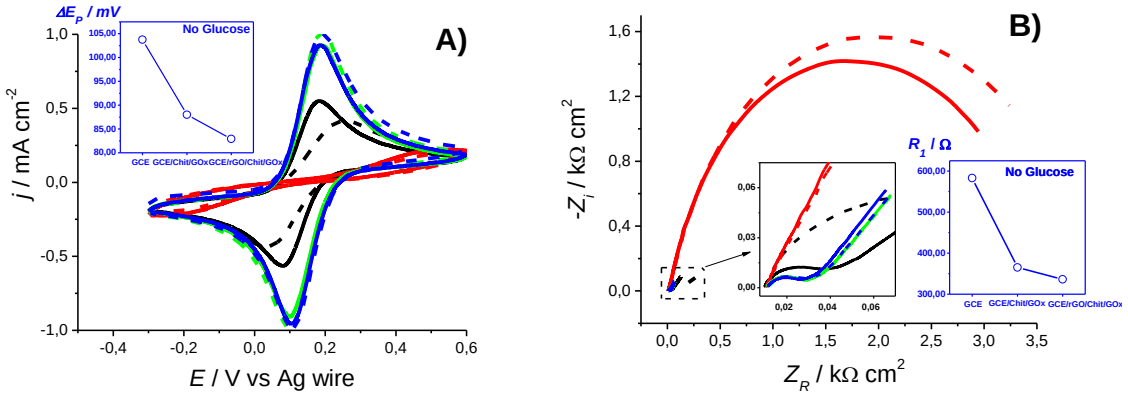

Fig. 6. 7: *Redox response registered for bare GCE (black), GCE/GOx (red), GCE/Chit95/GOx (green) and GCE/rGO-Ni/Chit95/GOx electrodes (blue) in PBS 0.05 M (pH 7.3) + 2 mM $[Fe(CN)_6]^{-3/-4}$ + 1 mM D-glucose (dashed lines). The curves in the absence of glucose are also included for comparison (solid lines).* ***(A)*** *CVs recorded at 50 mV·s^{-1}.* ***(B)*** *Nyquist plots collected at 0.15 V (oscillation amplitude: 10 mV). The black inset features an enlargement of the impedance spectra in the high-medium frequency range. The blue insets display the evolution of ΔE_P and R_1.*

Table 6. 1: Anodic peak current densities (j_{PA}), peak-to-peak potential difference (ΔE_P) and apparent charge transfer resistance (R_1) derived from the responses registered in Fig 7 for GCE/rGO-Ni/Chit95/GOx in the presence and absence of 1 mM glucose.

Electrode	***[G] / mM***	***j_{PA} / mA· cm^{-2}***	***ΔE_P / V***	***R_1 / kΩ***
Bare GCE	0	0.583	104	0.583
GCE/GOx	0	0.104	800	60.2
GCE/Chit95/GOx	0	0.916	88	0.365
GCE/rGO-Ni/Chit95/GOx	0	0.956	83	0.336
Bare GCE	1	0.418	209	2.68
GCE/GOx	1	0.089	800	68.0
GCE/Chit95/GOx	1	1.023	93	0.363
GCE/rGO-Ni/Chit95/GOx	1	1.047	88	0.353

Agreeing with this qualitative interpretation, R_1 (determined in this case from the fittings to a R_sQR_1 circuit; Fig 6.8) increased by two orders of magnitude (60.2 kΩ) since the 583 Ω measured for bare GCE. Hence, both the data in Fig 6.7 and Table 6.1 indicate that the ET is strongly hindered at the GCE/GOx electrode which, as discussed above, may be due to the poor conformational stability of GOx onto GCE. As reported for an anodized carbon electrode[449], the unfolding of GOx should form a blocking layer on GCE that seriously limits its charge storage capabilities and the ET kinetics. In big contrast, a pair of sharp peaks (and current densities well above those for bare GCE) was observed in the CV of GCE/Chit95/GOx (green solid line). As shown in Table 6.1, j_{PA} soared to

916 μA·cm^{-2} and ΔEP fell to 88 mV. In line with this behaviour, its Nyquist exhibited a semicircle even narrower than that exhibited by bare GCE. The very low value of R_1 obtained from the fittings, 365 Ω, confirmed this view.

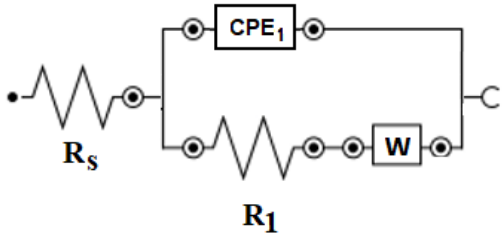

Fig. 6. 8: *Typical Randles circuit, it includes a Constant Phase Element (CPE or Q) which accounts for the topological imperfections of the electrode surface. R_s is the solution resistance, R_1 is the charge transfer resistance, and W is the Warburg diffusion impedance. When the charge transfer is the rate determining step (for instance, for the GCE/GOx electrode), the Warburg element can be neglected and the system is electrically equivalent to a R_sQR_1 circuit.*

Hence, immobilizing GOx on chitosan not only did not block of the ET processes of the $[Fe(CN)6]^{3-/4-}$ species but, oppositely, they were slightly favoured. The main conclusions are:

(1) When supported on chitosan, the conformational stability of GOx is superior. Chit95 is rich in hydroxyl and amino groups which interact with the hydrophilic residues in the outer regions of GOx (protein cores are usually hydrophobic) to help keeping the biomolecules in its folded state[436, 442].

(2) The enhanced redox response is consistent with the enhanced capacitive currents recorded in pure buffer (Fig 6.5A). As already discussed, the Chit95 matrix may be partially charged so that negatively charged anions and redox probes may be attracted into it and rise their concentrations over those at the bulk electrolyte (thus, explaining the enhanced response).

Although the most important enhancement in the ET occurred after deposition of the Chit95/GOx hydrogel, the incorporation of rGO-Ni NPs sheets at the base of this construct gave a further boost (see insets of Fig 6.7). Accordingly, j_{PA} and ΔE_P improved to 956 μA·cm^{-2} and 83 mV, respectively. Furthermore, the semicircle diameter followed a concomitant decrease. This was additionally confirmed by a minimum R_1 of 335 Ω. Hence, due to the synergies described in the introduction, the GCE/rGO-Ni/Chit95/GOx electrode exhibited the best electroactivity within the investigated series.

Not surprisingly, the response of bare GCE and GCE/GOx was slightly hampered in 1 mM glucose (black and red dashed lines, respectively). Supporting this view, j_{PA} decreased by a 28% (bare GCE) and 14% (GCE/GOx) compared to the response in absence of glucose. In good agreement, R_1 increased by a 360 % and 13%, respectively. These results indicate that:

(1) None of these electrodes exhibited apparent catalytic activity towards glucose.

(2) Glucose seemed to induce a partial blockage of the ET.

A reasonable hypothesis to explain these results considers the blockage of electroactive sites by glucose molecules. The adsorption of glucose onto carbon materials has been scarcely explored[450, 451] and, to our best knowledge, nothing has been published about its adsorption on GCE. Then, to check this phenomenon, we took CV and EIS measurements under the same working conditions within a wide range of glucose concentrations [*G*]=0.05-13 mM (see Fig 6.9).

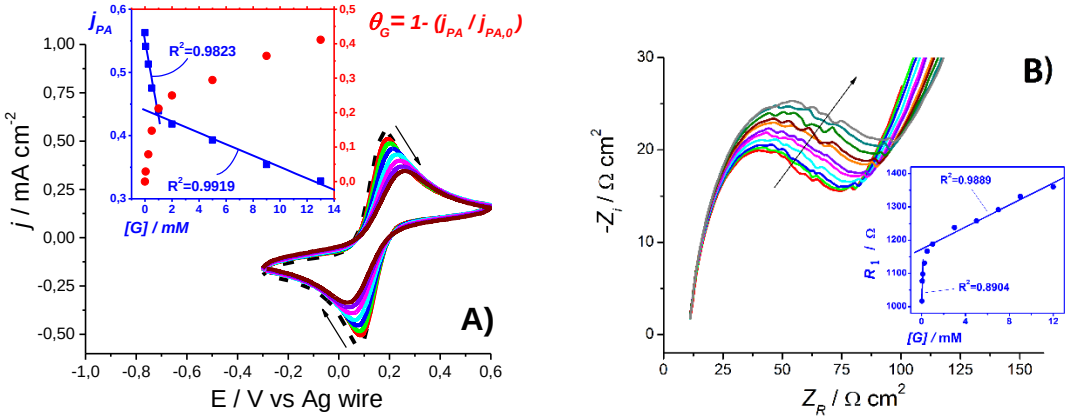

Fig. 6. 9: A) *CVs for bare GCE in PBS 0.05 M (150 mM NaCl; pH 7.3) + 2 mM $[Fe(CN)_6]^{-3/-4}$ in the absence (black dashed line) and presence (coloured solid lines) of increasing concentrations of D-glucose ([G]): 0.05 (red solid line), 0.25 (green), 0.50 (blue), 1.00 (cyan), 5.00 (magenta), 9.00 (violet), and 13.00 mM (wine). The changes in anodic peak currents (j_{PA}; blue y-axis) and the surface coverage (estimated as $\theta_G = 1 - [j_{PA}/j_{PA,0}]$, with $j_{PA,0}$ being registered in absence of glucose; red y-axis) are plotted versus [G] in the inset. The scan rate was 50 mV· s^{-1}.* ***B)*** *Nyquist plots measured at the half wave potential ($E_{1/2}$=+0.15 V) in the range 10^4 - 10^{-1} Hz (oscillation amplitude: 10 mV). The R_1 values derived from the fittings to the R_sQR_1W circuit are plotted versus [G] in the inset (calibration curves and correlation factors are also included).*

By increasing [G], j_{PA} declined continuously and R_1 followed a concomitant increase. The j_{PA}/R_1 vs [G] curves clearly resembled to the reported adsorption isotherms of glucose on mesoporous carbons[451]. From this experiment the maximum coverage of glucose on GCE was estimated to be below half a monolayer (θ_G=0.4). As discussed above, the GCE/GOx electrode must be blocked by a layer of denaturated enzyme so that any additional blocking (due to glucose adsorption) would have a very small impact on the ET (as confirmed in Fig 6.7). In great contrast with this behaviour, the CVs of GCE/Chit95/GOx and GCE/rGO-Ni/Chit95/GOx exhibited enhanced peak currents (green and blue dashed lines in Fig 6.7A). The integrated anodic charge (Q_A) increased by a 13% and 15%, respectively, but the values of ΔE_P and R_1 barely changed.

The Nyquist plots for both electrodes in absence and presence of glucose virtually overlapped each other. Although no evidence of direct ET from GOx was found, the consistently enhanced peak currents observed for the GOx-modified electrodes may be

attributed to the catalytic activity of the enzyme. GOx is known to selectively oxidize β-D-glucose to D-glucono-1,5-lactone as follows:

$$\beta\text{-D-Glucose} + \text{GOx-FAD} \rightarrow \text{D-glucono-1,5-lactone} + \text{GOx-FADH}_2 \quad \textbf{(equation 6.1)}$$

In presence of O_2, the flavin adenine dinucleotide redox cofactor (FAD, the initial acceptor of two electrons and two protons) is regenerated:

$$GOx\text{-}FADH_2 + O_2 \rightarrow GOx\text{-}FAD + H_2O_2 \quad \textbf{(equation 6.2)}$$

Hydrogen peroxide oxidation, constitutes the detection principle in “first generation” electrochemical biosensors. Alternatively, redox mediators have been used as electron acceptors to reduce their high operating potentials (second generation). In our experiments, the electrolyte contains no O_2 and, thus, the mediator must be the initial electron acceptor:

$$GOx\text{-}FADH_2 + 2[Fe(CN)_6]^{3-} \rightarrow GOx\text{-}FAD + 2[Fe(CN)_6]^{4-} + 2H^+ \quad \textbf{(equation 6.3)}$$

By balancing eq. 1 and 3:

$$\beta\text{-}D\text{-}Glucose + 2[Fe(CN)_6]^{3-} \rightarrow D\text{-}glucono\text{-}1,5\text{-}lactone + 2[Fe(CN)_6]^{4-} + 2H^+ \quad \textbf{(equation 6.4)}$$

Therefore, the enzymatic activity of GOx results in an increased concentration of $[Fe(CN)_6]^{4-}$. As its oxidation to $[Fe(CN)_6]^{3-}$ occurs at the anodic peak, the activity of the enzyme establishes a feed-back loop due to GOx which results in enhanced oxidation peaks.

6.5. Calibration Curves

Encouraged by these results, the GCE/rGO-Ni/Chit95/GOx electrode was further interrogated in a wide range of [*G*] (0.025-12 mM) (Fig 6.10). Accordingly, the proof-of-concept experiments were recorded in triplicate. As shown in Fig 6.10A, the CVs did not follow great changes in shape. However, the peak currents followed a slight but progressive decrease (red inset). The average j_{PA} vs [*G*] plot (blue inset) confirmed this view and exhibited two linear domains which were fitted to a couple of straight lines. The widest region, 1-12 mM, covers normal blood glucose levels in healthy humans (3.9-6.5 mM) and most cases of hypo and hyperglycemia in diabetics.

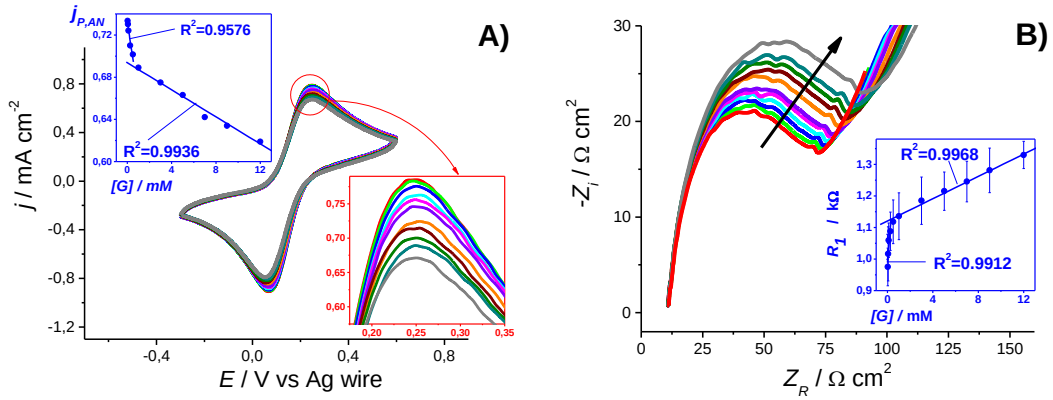

Fig. 6. 10: *Electrochemical interrogation of the biosensor in the presence of increasing concentrations of glucose [G]: 0.025 (red), 0.050 (green), 0.100 (blue), 0.250 (cyan), 0.500 (magenta), 1 (purple), 3 (orange), 5 (wine), 7(olive), 9 (dark cyan), and 12 mM (grey).* ***(A)*** *CVs recorded at 50 mV·s^{-1}. The changes in the anodic peak are shown with higher detail in the red inset.* ***(B)*** *Nyquist plots collected at +0.15 V and oscillation amplitude of 10 mV. The average changes in j_{PA} and R_1 for three GCE/rGO-Ni/Chit95/GOx electrodes are shown in the blue insets with the corresponding calibration curves. The error bars represent the standard deviations. The electrolyte was PBS 0.05 M (pH 7.3) + 2 mM $Fe(CN)_6^{3-/4-}$.*

The second is much narrower (0.025-1 mM) but more sensitive (as inferred from its greater slope). The EIS interrogation showed a continuous growth of the semicircle diameter (Fig 6.10B) upon the increase of [*G*]. Remarkably, two identical linear domains were also spotted in the average R_1 *vs* [*G*] plot (blue inset). The quantitative average data in Table 6.2 confirms both the decline of j_{PA} and the growth of R_1. Both the CV and EIS calibration is consistent with a progressive hindering of the ET as the amount of glucose is increased.

Table 6. 2: Average anodic peak current densities (j_{PA}) and apparent charge transfer resistance (R_1) plotted in the blue insets of Fig 6.10. The errors correspond to the standard deviation of the three experiments.

[G] / mM	***j_{PA} / mA· cm^{-2}***	***R_1 / kΩ***
0.025	0.73 ± 0.04	0.97 ± 0.06
0.050	0.73 ± 0.04	1.02 ± 0.09
0.100	0.72 ± 0.04	1.06 ± 0.05
0.250	0.71 ± 0.03	1.09 ± 0.06
0.500	0.70 ± 0.04	1.12 ± 0.07
1.000	0.69 ± 0.03	1.13 ± 0.07
3.000	0.67 ± 0.03	1.18 ± 0.07
5.000	0.66 ± 0.03	1.21 ± 0.06
7.000	0.64 ± 0.03	1.24 ± 0.06
9.000	0.63 ± 0.03	1.28 ± 0.07
12.00	0.62 ± 0.02	1.33 ± 0.04

To get deeper insights on the responsiveness of the biosensor, the GCE/rGO-Ni/Chit95/GOx electrode was potentiostatically interrogated. Figure 6.11 presents an amperometric interrogation of a GCE/RGO-Ni/Chit95/GOx electrode at the anodic peak potential (+0.20 V vs Ag wire) in PBS 0.05 M (150 mM NaCl; pH 7.3) + 2mM $[Fe(CN)_6]^{-3/-4}$.

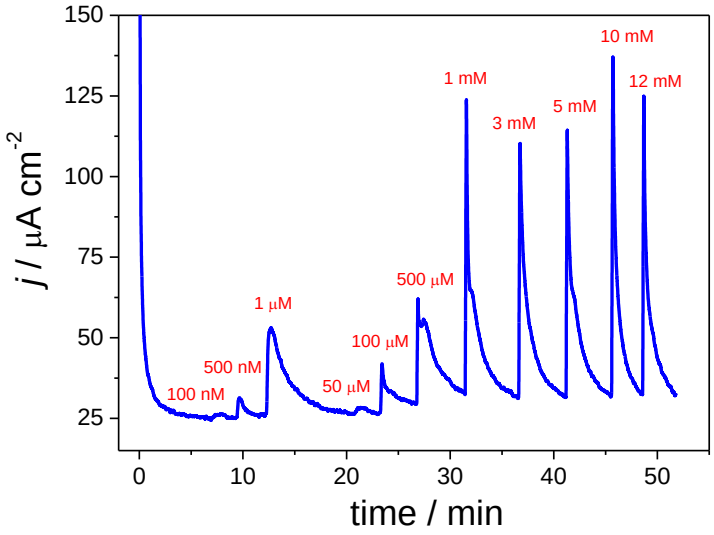

Fig. 6. 11: *Amperometric interrogation of a GCE/RGO-Ni/Chit95/GOx electrode at the anodic peak potential (+0.20 V vs Ag wire) in PBS 0.05 M (150 mM NaCl; pH 7.3) + 2 mM $[Fe(CN)_6]^{-3/-4}$. Aliquots of D-glucose were consecutively injected to cover a range of concentration between 25 nM and 12 mM.*

Aliquots of D-glucose were consecutively injected to cover a range of concentration between 25 nM and 12 mM. At the anodic peak potential, the $[Fe(CN)_6]^{4-}$ probe is continuously oxidized to $[Fe(CN)_6]^{3-}$. Under this approach the probes are solution species with finite concentration (2 mM) vs the bulky surface MNPs/SNPs used in most non-enzymatic sensors. Hence, the concentration of $[Fe(CN)_6]^{4-}$ is depleted causing the current to fall until a diffusion limited current density is reached (≈25 μA·cm^{-2}). When glucose is injected, the activity of GOx regenerates $[Fe(CN)_6]^{4-}$ and its re-oxidation generates the peaks. The regenerated probe is readily reoxidized so that the current follows a fast decline and no plateau is achieved. For this reason, we have not used these data to build a calibration curve. However, they demonstrate the high responsiveness of the biosensor even for [*G*] as low as 0.1 μM glucose.

6.6. Electroanalytical Performance and Detection Mechanism

The average sensitivity of the biosensor in the sub-millimolar ($\hat{S}_L$) and millimolar ($\hat{S}_H$) domains was derived from the slopes of the fitting curves in Fig 6.10 (Table 6.3).

Table 6. 3: *Parameters obtained by fitting the average data in the blue insets of Fig 6.10 to straight lines defined by the equation Y = A + S · [G], with Y being j_{PA} and R_1, A the y-intercept, and S the slope.*

Mode	***[G] / mM***	***S / μA· cm^{-2}·mM^{-1}***	***A / μA·cm^{-2}***	***R^2***
CV	0.025-1	68	732	0.958
CV	1-12	6	694	0.994
	[G] / mM	***S / Ω · mM^{-1}***	***A / Ω***	***R^2***
EIS	0.025-1	262	1004	0.925
EIS	1-12	17	1121	0.997

Under the voltammetric determination, these achieved values of $\hat{S}_L$=68 μA·cm^{-2}·mM^{-1} and $\hat{S}_H$=6 μA·cm^{-2}·mM^{-1}. These data suggest a superior sensitivity of the biosensor in the sub-millimolar range. While the sensitivity of the individual GCE/rGO-Ni/Chit95/GOx electrodes in the millimolar scale (S_H) were very close to $\hat{S}_H$ (*c.a.* 6-7 μA·cm^{-2}·mM^{-1}), the maximum S_L achieved by the biosensor was about twice the $\hat{S}_L$ (129 μA·cm^{-2}·mM^{-1}). In good agreement with these findings, the impedimetric determination showed to be about 15 times more sensitive in the submillimolar domain (Table 6.3). The limits of detection (*LOD*) were evaluated for both methods considering a S/N ratio of 3. Thus, minimum values of 390 and 254 μM were obtained from the voltammetric and impedometric methods, respectively. These results suggest that the impedometric determination is slightly more sensitive. Compared to other enzymatic biosensors based on GOx and graphene-MNPs/SNPs conjugates (e.g. rGO-Cu[452], rGO-TiO_2[453], rGO-Au[433], GO-Pt[28], and rGO-hydroxyapatite[398], 2nd-6th entries in Table 6.4), the GCE/rGO-Ni/Chit95/GOx electrode exhibited the highest sensitivity (a close performance was only achieved by the GCE/GO-Pt/Chit/GOx sensor) [454].

The same conclusion was reached by comparison with other biosensors based on GOx and undecorated forms of graphene (rGO[454,395], GO[455], and graphene nanosheets, GNS[456], see Table 6.4).

In fact, the best sensitivity attained by these sensors was 48 μA·cm^{-2}·mM^{-1} (GCE/GNS/Nafion/GOx)[456], which is 20 μA·cm^{-2}·mM^{-1} below the average sensitivity demonstrated in our results. Non-enzymatic sensors based on graphene-CuO have also exhibited linear response in the sub-millimolar range and a better combination of LODs and Sensitivity[457, 458]. The few number of non-enzymatic sensors based on the rGO-Ni NPs hybrid have presented low LODs (0.1-1 μM)[434, 435, 448, 459, 460]. On the other hand, while the GCE/rGO-Ni sensors reported by Y. Zhang *et al.*[459] and Z. Wang *et al.*[435] exhibited sensitivities around 10^3 μA·cm^{-2}·mM^{-1}, the other three were less sensitive than the GCE/rGO-Ni/Chit95/GOx biosensor.

Table 6. 4: *Sensitivity (S), limit of detection (LOD), and linear dynamic range (LDR) reported in the literature for the electrochemical detection of glucose using different graphene-based sensors.*

Sensor	*Type*	*Method*	*S*	*LOD/ µM*	*LDR/ mM*	*Ref.*
GCE/rGO-Ni/Chitosan/GOx	E[a]	CV EIS	129 µA·cm^{-2}·mM^{-1} 497 Ω·mM^{-1}	390 254	0.025-1	This work
GCE/rGO-Cu/Nafion/GOx	E	CV	34 µA·cm^{-2}·mM^{-1}	5.00	0.05-12	[452]
GCE/rGO-TiO_2/Nafion/GOx	E	CV	6 µA·cm^{-2}·mM^{-1}	–	Up to 8	[453]
GCE/rGO-Hap[b]/GOx	E	CV	17 µA·cm^{-2} ·mM^{-1}	30.0	0.1-11	[398]
GCE/GO-Pt/Chitosan/GOx	E	CA[c]	113 µA·cm^{-2}·mM^{-1}	0.6	0.001-2.25	[454]
Au/rGO-Au/Chitosan/GOx	E	CV	0.55 µA·mM^{-1}	180	2.0-10	[433]
GCE/rGO/Chitosan/GOx	E	CV	38 µA·cm^{-2}·mM^{-1}	20.0	0.08-12	[454]
GCE/rGO/GOx	E	CA	1.85 µA·cm^{-2}·mM^{-1}	–	0.1-27	[395]
GCE/GNS[d]/Nafion/GOx	E	CV	48 µA·cm^{-2}·mM^{-1}	–	0.2-1.4	[456]
Pt/GO/GOx	E	CA	8 µA·cm^{-2}·mM^{-1}	–	0.1-20	[455]
CPE[e]/rGO-Ni	NE [f]	CA	1.1 µA·cm^{-2}·mM^{-1}	0.47	0.001-1	[434]
AER[g] /rGO-Ni	NE	CA	82 µA·cm^{-2}·mM^{-1}	1.05	0.001-1	[448]
GCE/rGO-Ni	NE	CA	1020 µA·cm^{-2}·mM^{-1}	0.1	0.002-2.1	[459]
GCE/rGO/PANI[h]/Ni	NE	CA	30 µA·cm^{-2}·mM^{-1}	0.1	0.0001-1	[460]
GCE/rGO-Ni	NE	CA	813 µA·cm^{-2}·mM^{-1}	-	0.001-0.110	[435]
GCE/rGO-CuO	NE	CA	2221 µA·cm^{-2}·mM^{-1}	0.1	0.0004-3	[457]
GCE/SG[i]-CuO	NE	CA	1299 µA·cm^{-2}·mM^{-1}	0.08	0.1-10.5	[458]

[a] Enzimatic; [b] Hydroxyapatite; [c] Chronoamperometry; [d] Graphene Nanosheets; [e] Carbon Paste Electrode; [f] Non-enzymatic; [g] Anion Exchange Resin Microspheres; [h] Polyaniline; [i] Sulfur-Doped Graphene

From this broad comparison it is concluded that non-enzymatic graphene-MNPs/SNPs sensors, which are based on different working and detection principles and operate at pHs well above the physiological level, present enhanced electroanalytical performance compared to their enzymatic counterparts. Beyond the good electrocatalytic properties of MNPs/SNPs, the results unavoidably evoke the idea of a still limited stability/loading of enzyme in those systems (further investigation will be required to ascertain this point). In any case, the presented results demonstrate an important improvement in the stability of GOx when supported on Chit95 and, as a result, the achieved sensitivities are amongst the finest reported for glucose biosensors based upon GOx and graphene. In fact, good responsiveness was not only noticed for the lowest [*G*] studied in these experiments (25 µM), which is close to the detection limit reported for GCE/rGO/Chitosan/GOx (20 µM) [454], but even at a much lower *[G]* of 100 nM as shown in Fig 6.11. The progressive hindering of the redox response in Fig 6.10, as opposed to the enhanced current densities evidenced in Fig 6.7, is a clear indication that the activity of

GOx is not the only phenomenon making part of the sensing mechanism. We must recall that the adsorption of glucose on bare GCE was demonstrated in Fig 6.9. Hence, a hybrid enzymatic/non-enzymatic detection mechanism is proposed to explain the net response in Fig 6.10. The progressive blockage of uncovered GCE surface sites in presence of increasing amounts of glucose molecules, may counter-balance the enhanced response of the biosensor due to the activity of GOx. Hence, a net deterioration of the ET kinetics is observed in the interrogation tests. Although further research is required to confirm this point, the behaviour in Fig 6.10 is strongly suggested to be controlled by the progressive adsorption of glucose (in fact, the shape of the R_1/j_{PA} *vs* [*G*] plots remind a typical two-step adsorption isotherm).

6.7. Reproducibility and Stability Studies

The errors presented in Table 6.2, correspond to relative standard deviations (*RSD*) in the range 4-6%. In good agreement, the *RSD* of the j_{PA} registered in 1 mM glucose for three electrode samples was 4.9%. Taking into account the variety of synthetic and assembly steps involved in the preparation of the biosensor, these results evidence a good degree of reproducibility. The RSD of five consecutive measurements taken with a freshly prepared electrode fell below 1.3% (see the curves in Fig 6.12) which indicates an excellent repeatability. The stability of the biosensor towards continuous cycling was judged upon collecting 100 consecutive CVs. Although the j_{PA} followed an important decrease, the biosensor was still operative.

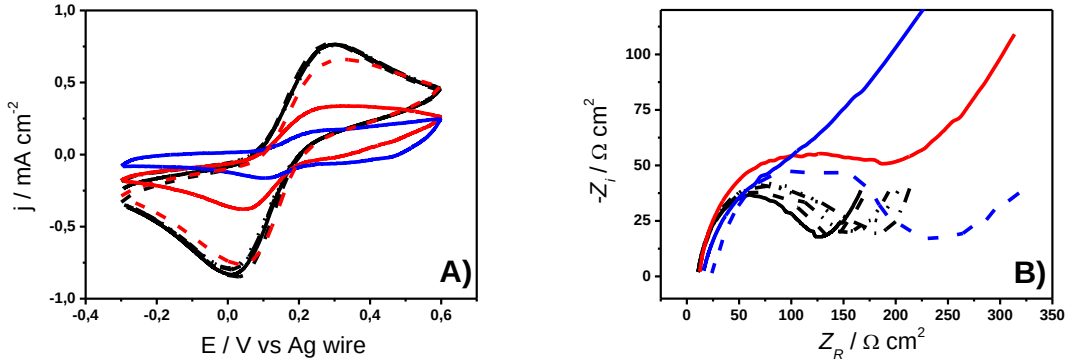

Fig. 6. 12: *CVs* ***(A)*** *and Nyquist plots* ***(B)*** *recorded for a GCE/rGO-Ni/Chit95/GOx in PBS 0.05 M (150 mM NaCl; pH 7.3) + 2 mM* $[Fe(CN)_6]^{-3/-4}$ *+ 1 mM D-glucose. The first five CVs/Nyquist plots consecutively registered for this electrode, are presented as black curves: 1st (solid), 2nd (dashed), 3rd (dash dotted), 4th (dash dot dotted), and 5th (dotted). From the additional 95 voltammograms and impedance spectra registered, only the curves for the 100th are shown (solid red). The CVs for other freshly prepared electrodes stored for three weeks at 4ºC under either dry (blue solid curves) or wet conditions (blue dashed curves) are also included. The scan rate was 50 mV· s-1 and the impedance spectra were taken at +0.15 V (oscillation amplitude: 10 mV).*

Its durability was evaluated for a period of one month. After 3 weeks storage, a dramatic decrease of the electroactivity was observed (Fig 6.12). At first glance, the electrode surface looked like cracked and scaly. This evidence suggests that the drying of the hydrogel film results in a great loss of performance (indeed, as also seen in the figure, the situation improved when storage was performed under appropriate conditions of hydration).

6.8. Interference Studies

Ascorbic acid (AA) and uric acid (UA) are some of the most important species interfering in the electrochemical detection of glucose in plasma samples (although ten times more diluted, these oxidize in simultaneous with H_2O_2 in first generation biosensors). To investigate this effect, additional interrogation tests were conducted in PBS 0.05 M + 2 mM $[Fe(CN)_6]^{3-/4-}$ + 1 mM glucose after successive additions of AA and UA to concentrations of 50, 75, and 100 µM (Fig 6.13).

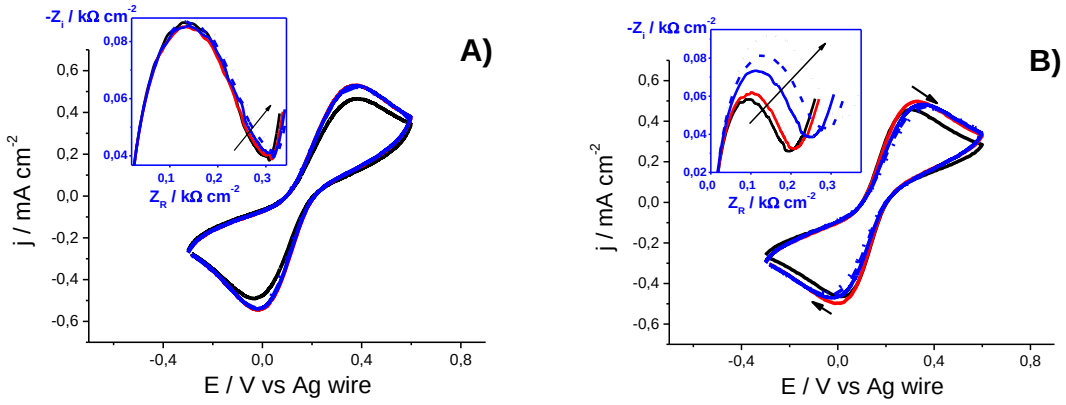

Fig. 6. 13: *CVs Interference tests in presence of ascorbic acid (AA) and uric acid (UA) (blue lines).* ***(A)*** *CVs registered for the GCE/rGO-Ni/Chit95/GOx biosensor in PBS 0.05 M (pH 7.3) + 2 mM $Fe(CN)_6^{3-/4-}$ + 1 mM D-glucose (red line) after addition of AA to final concentrations of 50 (solid), 75 (dashed), and 100 µM (dotted). The voltammetric profile obtained in absence of glucose is also included for comparison (black line). The impedance spectra obtained under identical conditions are included in the blue inset.* ***(B)*** *Analogous experiments were carried out by addition of UA (same line styles and color keys apply). The scan rate was 50 $mV \cdot s^{-1}$ in all cases.*

The addition of AA, led to total variations in j_{PA} and ΔE_P within the measurement error (1.7% and 1%, respectively) and to negligible changes in the Nyquist plots. Oppositely, UA induced a decrease in j_{PA} of *ca.* 6.6% and ΔE_P increased more than 10% (the changes in the Nyquist also became more evident as seen in the inset of Fig 6.13B). These results indicate that while AA has a negligible effect in the response of the biosensor, UA poses

a significant interference which may slightly overestimate the analytical signal. Since the oxidation of AA and UA in bare GCE occurs at E>0.35 V vs Ag/AgCl,[61] competitive adsorption is suggested as a possible interference mechanism.

6.9. Conclusions

Sheets of reduced graphene oxide (rGO) decorated with clusters, or isolated NPs, of Ni were synthesized through the one-pot reduction of GO and Ni^{2+}. rGO-Ni/Chit95/GOx nanocomposite films, constituted by a base layer of the conjugate and a GOx-containing chitosan hydrogel on top, were deposited onto a GCE. The interrogation of the modified electrode in dilute glucose solutions demonstrated a significant activity of the enzyme supported on Chit95. Further interrogation in a wider range of [*G*], demonstrated the feasibility of the system as a second generation electrochemical biosensor with good linearity found in the millimolar and sub-millimolar scales (both under voltammetric and impedimetric mode). Good reproducibility and short-term repeatability upon consecutive measurements were also demonstrated. Tests in presence of AA and UA showed a negligible effect of the first and a small (and likely manageable) interference of the latter in the response of the biosensor. The stability towards continuous cycling and storage under dry conditions were limited.

Part D - Concluding Remarks & Future Perspectives

Chapter 7 – Concluding Remarks & Future Perspectives

In this chapter the main conclusions and remarks regarding the whole work carried out during this PhD thesis are presented. Besides, suggestions for future work are also provided.

7.1. Concluding Remarks

The aim of this thesis was to study the role of the assembly of GNMs on solid surfaces for application as electrochemical biosensors. The results reported in this work described the preparation, characterization, and optimization of thin films of GNMs deposited onto glassy carbon for the enzyme-mediated electrochemical determination of BPA and Glucose.

The results reported in *Chapter 4* described the preparation, physical characterization and electron transfer properties of solid electrodes modified with thin films of 2D GNMs, namely GO, rGO and RGO-NPs. The films were assembled in a wide range of concentrations and subsequently studied by AFM, SEM, and electrochemical techniques in the presence of $Fe(CN)_6^{3-/4-}$ redox probes. The results unveiled the continuous hindering of the ET of the probes while increasing the surface density of GO at the solid-liquid interface. This behaviour might be assigned to the contribution of both steric and electrostatic-type phenomena. The modification of the electrode surface with either rGO or rGO-NPs denoted a couple of changes in the redox response of the electrodes. However, contrary to that was observed for the GCE/GO electrodes, the increase in the concentration of rGO from 0.1 to 500 $\mu g \cdot mL^{-1}$ promoted a progressive enhancement in the reversibility of the system. Moreover, the deposition of additional material (above 500 $\mu g \cdot mL^{-1}$) hindered the ET processes and the system became more irreversible. The deposition of rGO-Fe_3O_4 NPs in the range 0.2-10.0 $mg \cdot mL^{-1}$ improved the ET process. The excellent electroanalytical efficacy found for 10.0 $mg \cdot mL^{-1}$ of rGO-Fe_3O_4 NPs had been explored for the detection of BPA via electrochemical techniques.

In the *chapter 5*, the assembly of a graphene-nanomagnetite conjugate with a high-DD chitosan and TvL (GCE/rGO-Fe_3O_4/Chit95/TvL) composite was explored for the electrochemical detection of BPA at low potential (<0.2 V). Under these conditions, the GCE/rGO-Fe_3O_4/Chit95/TvL biosensor exhibited an ultrahigh sensitivity (minimum LOD of 4 ppb BPA), wide linearity and rapid response. Good reproducibility, durability, and an excellent operational stability have been registered. Among all the investigated interfering species, only glucose interferes significantly with the biosensor response, although in a very limited and likely manageable way. Applications in real samples of water stored in PC-bottles proved feasible with recoveries in the range between 107-124%. The results demonstrated that the biosensor could detect harmful levels of BPA in this kind of sample.

The results in the *Chapter 6* showed the construction of rGO-Ni/Chit95/GOx nanocomposite films encompassing a base layer of rGO sheets decorated with clusters,

or isolated Ni-NPs and a GOx-containing chitosan hydrogel on top. The rGO-Ni/Chit95/GOx nanocomposite films were deposited onto a GCE and interrogated in dilute glucose solutions. The results demonstrated a significant activity of the enzyme supported on Chit95. The interrogation in a wider range of [*G*], demonstrated the feasibility of the system as a second generation electrochemical biosensor with good linearity found in the millimolar and sub-millimolar scales. A good reproducibility and short-term repeatability upon consecutive measurements of the biosensor were registered. The results of stability towards continuous cycling and storage under dry conditions were limited. The interferences' studies showed a negligible effect in the presence of AA and a small interference of UA in the response of the biosensor.

7.2. Future Perspectives

The preliminary results presented in the *Chapter 4* for the assembly of different kind of GNMs on solid surfaces need further studies. It is generally recognised that the amazing properties of graphene might enhance the effects of NPs in the composite material. To this end, the immobilization of nanoparticles (metal and metal oxide) on the two simple forms of 2D graphene (GO & rGO) via different methods should be further explored. The immobilization of metallic nanoparticles on a surface of GCE modified with GO and RGO via drop casting method has already started (these results were not presented in this thesis because the study was at a very early stage). Other strategies such as electrochemical reducing a metal salt in the presence of GO need be further explored too.

Finally, this thesis highlighted the need to continuously investigate the impact of assembling solid electrodes modified with 2D GNMs for the successful application of these materials as biosensors.

References

1. V. B. Mohan, K.-t. Lau, D. Hui, and D. Bhattacharyya, *Composites Part B: Engineering*, 2018, **142**, 200-220.
2. M. Sharon and M. Sharon: 'The History of Graphene', in book Graphene: An Introduction to the Fundamentals and Industrial Applications, 2015, 1-15.
3. A. H. Castro Neto, F. Guinea, N. M. R. Peres, K. S. Novoselov, and A. K. Geim, *Reviews of Modern Physics*, 2009, **81**, 109-162.
4. G. Yang, L. Li, W. B. Lee, and M. C. Ng, *Science and technology of advanced materials*, 2018, **19**, 613-648.
5. Z. Zhen and H. Zhu: '1 - Structure and Properties of Graphene', in 'Graphene', (eds. H. Zhu, et al.), Academic Press, 2018, 1-12.
6. T. Kuilla, S. Bhadra, D. Yao, N. H. Kim, S. Bose, and J. H. Lee, *Progress in Polymer Science*, 2010, **35**, 1350-1375.
7. N. A. A. Ghany, S. A. Elsherif, and H. T. Handal, *Surfaces and Interfaces*, 2017, **9**, 93-106.
8. P. R. Wallace, Phys. Rev., 1947, **71**, 622-634.
9. D. P. DiVincenzo and E. J. Mele, *Physical Review B*, 1984, **29**, 1685-1694.
10. J. W. McClure, *Physical Review*, 1956, **104**, 666-671.
11. R. E. Peirls, *Helv. Phys. Acta*, 1934, **7**, 81-83.
12. H. P. Boehm, A. Clauss, G. O. Fischer, and U. Hofmann, *Zeitschrift für anorganische und allgemeine Chemie*, 1962, **316**, 119-127.
13. H. P. Boehm, R. Setton, and E. Stumpp, Pure Appl. Chem., 1994, **66**, 1893-1890.
14. K. S. Novoselov, A. K. Geim, S. V. Morozov, D. Jiang, Y. Zhang, S. V. Dubonos, I. V. Grigorieva, and A. A. Firsov, *Science*, 2004, **306**, 666-669.
15. A. K. Geim, *Physica Scripta*, 2012, **T146**, 014003.
16. F. Bonaccorso, A. Lombardo, T. Hasan, Z. Sun, L. Colombo, and A. C. Ferrari, *Materials Today*, 2012, **15**, 564-589.
17. S. Deng and V. Berry, *Materials Today*, 2016, **19**, 197-212.
18. E. P. Randviir, D. A. C. Brownson, and C. E. Banks, *Materials Today*, 2014, **17**, 426-432.
19. J. M. Tour, *Chemistry of Materials*, 2014, **26**, 163-171.
20. S. S. Shams, R. Zhang, and J. Zhu, *Materials Science-Poland*, 2015, **33**, 566-578.
21. X.-Y. Wang, A. Narita, and K. Müllen, *Nature Reviews Chemistry*, 2017, **2**, 1-10.
22. J. E. Crowell, *Journal of Vacuum Science & Technology A*, 2003, **21**, S88-S95.
23. E. K. Broadbent, *Journal of Vacuum Science & Technology B: Microelectronics Processing and Phenomena*, 1987, **5**, 1661-1666.
24. G. Reina, J. M. González-Domínguez, A. Criado, E. Vázquez, A. Bianco, and M. Prato, *Chemical Society Reviews*, 2017, **46**, 4400-4416.
25. B. H. Min, D. W. Kim, K. H. Kim, H. O. Choi, S. W. Jang, and H.-T. Jung, *Carbon*, 2014, **80**, 446-452.
26. J. Campos-Delgado, A. R. Botello-Méndez, G. Algara-Siller, B. Hackens, T. Pardoen, U. Kaiser, M. S. Dresselhaus, J.-C. Charlier, and J.-P. Raskin, *Chemical Physics Letters*, 2013, **584**, 142-146.
27. P. W. Sutter, J.-I. Flege, and E. A. Sutter, *Nature Materials*, 2008, **7**, 406-411.
28. P. Suvarnaphaet and S. Pechprasarn, *Sensors (Basel)*, 2017, **17**, 1-24
29. D. Farías, A. M. Shikin, K. H. Rieder, and Y. S. Dedkov, *Journal of Physics: Condensed Matter*, 1999, **11**, 8453-8458.
30. E. Loginova, N. C. Bartelt, P. J. Feibelman, and K. F. McCarty, *New Journal of Physics*, 2008, **10**, 1-16.
31. X. Li, W. Cai, J. An, S. Kim, J. Nah, D. Yang, R. Piner, A. Velamakanni, I. Jung, E. Tutuc, S. K. Banerjee, L. Colombo, and R. S. Ruoff, *Science*, 2009, **324**, 1312-1314.

32. P. W. Sutter, P. M. Albrecht, and E. A. Sutter, *Applied Physics Letters*, 2010, **97**, 213101-3.
33. Z. Wang, Z. Xue, M. Zhang, Y. Wang, X. Xie, P. K. Chu, P. Zhou, Z. Di, and X. Wang, *Small*, 2017, **13**,1-8.
34. A. Reina and J. Kong: 'Graphene Growth by CVD Methods', in 'Graphene Nanoelectronics: From Materials to Circuits', MA, Springer US (ed. R. Murali), Boston, 2012, 167-203.
35. P. R. Somani, S. P. Somani, and M. Umeno, *Chemical Physics Letters*, 2006, **430**, 56-59.
36. A. Reina, S. Thiele, X. Jia, S. Bhaviripudi, M. S. Dresselhaus, J. A. Schaefer, and J. Kong, *Nano Research*, 2009, **2**, 509-516.
37. Z.-Y. Juang, C.-Y. Wu, C.-W. Lo, W.-Y. Chen, C.-F. Huang, J.-C. Hwang, F.-R. Chen, K.-C. Leou, and C.-H. Tsai, *Carbon*, 2009, **47**, 2026-2031.
38. A. Reina, X. Jia, J. Ho, D. Nezich, H. Son, V. Bulovic, M. S. Dresselhaus, and J. Kong, *Nano Letters*, 2009, **9**, 30-35.
39. Z.-Y. Juang, C.-Y. Wu, A.-Y. Lu, C.-Y. Su, K.-C. Leou, F.-R. Chen, and C.-H. Tsai, *Carbon*, 2010, **48**, 3169-3174.
40. Y. Wang, Y. Zheng, X. Xu, E. Dubuisson, Q. Bao, J. Lu, and K. P. Loh, *ACS Nano*, 2011, **5**, 9927-9933.
41. B. Gupta, M. Notarianni, N. Mishra, M. Shafiei, F. Iacopi, and N. Motta, *Carbon*, 2014, **68**, 563-572.
42. M. Bhatnagar and B. J. Baliga, *IEEE Transactions on Electron Devices*, 1993, **40**, 645-655.
43. X. J. Lee, B. Y. Z. Hiew, K. C. Lai, L. Y. Lee, S. Gan, S. Thangalazhy-Gopakumar, and S. Rigby, *Journal of the Taiwan Institute of Chemical Engineers*, 2019, **98**, 163-180.
44. N. Mishra, J. Boeckl, N. Motta, and F. Iacopi, *physica status solidi (a)*, 2016, **213**, 2277-2289.
45. C. Riedl, C. Coletti, and U. Starke, *Journal of Physics D: Applied Physics*, 2010, **43**, 374009.
46. A. Tzalenchuk, S. Lara-Avila, A. Kalaboukhov, S. Paolillo, M. Syväjärvi, R. Yakimova, O. Kazakova, T. J. B. M. Janssen, V. Fal'ko, and S. Kubatkin, *Nature nanotechnology*, 2010, **5**, 186-189.
47. F. Mitsuhashi, M. Okada, Y. Tateno, T. Nakabayashi, M. Ueno, H. Nagasawa, H. Fukidome, and M. Suemitsu, *MRS Advances*, 2017, **2**, 51-56.
48. X. Lu, M. Yu, H. Huang, and R. S. Ruoff, *Nanotechnology*, 1999, **10**, 269-272.
49. K. Parvez, S. Yang, X. Feng, and K. Müllen, *Synthetic Metals*, 2015, **210**, 123-132.
50. Y. Hernandez, V. Nicolosi, M. Lotya, F. M. Blighe, Z. Sun, S. De, I. T. McGovern, B. Holland, M. Byrne, Y. K. Gun'Ko, J. J. Boland, P. Niraj, G. Duesberg, S. Krishnamurthy, R. Goodhue, J. Hutchison, V. Scardaci, A. C. Ferrari, and J. N. Coleman, *Nature Nanotechnology*, 2008, **3**, 563-568.
51. J.-H. Ding, H.-R. Zhao, and H.-B. Yu, *Scientific Reports*, 2018, **8**, 5567, 1-8.
52. J. Chen, W. Shi, Y. Chen, Q. Yang, M. Wang, B. Liu, Z. Tang, M. Jiang, D. Fang, and C. Xiong, *Applied Physics Letters*, 2016, **108**, 073105.
53. N. Margaryan, N. Kokanyan, and E. Kokanyan, *Journal of Saudi Chemical Society*, 2019, **23**, 13-20.
54. F. Torrisi, T. Hasan, W. Wu, Z. Sun, A. Lombardo, T. S. Kulmala, G. W. Hsieh, S. Jung, F. Bonaccorso, P. J. Paul, D. Chu, and A. C. Ferrari, *ACS Nano*, 2012, **6**, 2992-3006.
55. N.-W. Pu, C.-A. Wang, Y. Sung, Y.-M. Liu, and M.-D. Ger, *Materials Letters*, 2009, **63**, 1987-1989.
56. D. Rangappa, K. Sone, M. Wang, U. K. Gautam, D. Golberg, H. Itoh, M. Ichihara, and I. Honma, *Chemistry – A European Journal*, 2010, **16**, 6488-6494.
57. G. Yoon, D.-H. Seo, K. Ku, J. Kim, S. Jeon, and K. Kang, *Chemistry of Materials*, 2015, **27**, 2067-2073.
58. D. Konios, M. M. Stylianakis, E. Stratakis, and E. Kymakis, *Journal of Colloid and Interface Science*, 2014, **430**, 108-112.

59. M. S. Khan, A. Shakoor, G. T. Khan, S. Sultana, and A. Zia, *Journal of the Chemical Society of Pakistan*, 2015, **37**, 62-67.
60. B. C. Brodie, *Philosophical Transactions of the Royal Society of London*, 1859, **149**, 249-259.
61. W. S. Hummers and R. E. Offeman, *J. Am. Chem. Soc.*, 1958, **80**, 1339-1339.
62. C. Gómez-Navarro, J. C. Meyer, R. S. Sundaram, A. Chuvilin, S. Kurasch, M. Burghard, K. Kern, and U. Kaiser, *Nano Letters*, 2010, **10**, 1144-1148.
63. T. J. Davies, M. E. Hyde, and R. G. Compton, *Angewandte Chemie International Edition*, 2005, **44**, 5121-5126.
64. R. K. Joshi, S. Alwarappan, M. Yoshimura, V. Sahajwalla, and Y. Nishina, *Applied Materials Today*, 2015, **1**, 1-12.
65. H. Fan, L. Wang, K. Zhao, N. Li, Z. Shi, Z. Ge, and Z. Jin, *Biomacromolecules*, 2010, **11**, 2345-2351.
66. S. Stankovich, D. A. Dikin, R. D. Piner, K. A. Kohlhaas, A. Kleinhammes, Y. Jia, Y. Wu, S. T. Nguyen, and R. S. Ruoff, *Carbon*, 2007, **45**, 1558-1565.
67. V. H. Pham, T. V. Cuong, T.-D. Nguyen-Phan, H. D. Pham, E. J. Kim, S. H. Hur, E. W. Shin, S. Kim, and J. S. Chung, *Chemical Communications*, 2010, **46**, 4375-4377.
68. S. Park and R. S. Ruoff, *Nature Nanotechnology*, 2009, **4**, 217-224.
69. N. Mohanty, A. Nagaraja, J. Armesto, and V. Berry, *Small*, 2010, **6**, 226-231.
70. R. Muszynski, B. Seger, and P. V. Kamat, *The Journal of Physical Chemistry C*, 2008, **112**, 5263-5266.
71. Y. Si and E. T. Samulski, *Nano Letters*, 2008, **8**, 1679-1682.
72. W. Chen, L. Yan, and P. R. Bangal, *The Journal of Physical Chemistry C*, 2010, **114**, 19885-19890.
73. X. Mei and J. Ouyang, *Carbon*, 2011, **49**, 5389-5397.
74. Y. Liu, Y. Li, M. Zhong, Y. Yang, W. Yuefang, and M. Wang, *Journal of Materials Chemistry*, 2011, **21**, 15449-15455.
75. Z. Khosroshahi, M. Kharaziha, F. Karimzadeh, and A. Allafchian, *AIP Conference Proceedings*, 2018, **1920**, 020009.
76. X. Zhou, J. Zhang, H. Wu, H. Yang, J. Zhang, and S. Guo, *The Journal of Physical Chemistry C*, 2011, **115**, 11957-11961.
77. V. H. Pham, H. D. Pham, T. T. Dang, S. H. Hur, E. J. Kim, B. S. Kong, S. Kim, and J. S. Chung, *Journal of Materials Chemistry*, 2012, **22**, 10530-10536.
78. M. Acik, G. Lee, C. Mattevi, M. Chhowalla, K. Cho, and Y. J. Chabal, *Nature Materials*, 2010, **9**, 840-845.
79. M. Acik, G. Lee, C. Mattevi, M. Chhowalla, K. Cho, and Y. Chabal, *Nature materials*, 2010, **9**, 840-845.
80. A. Bagri, C. Mattevi, M. Acik, Y. J. Chabal, M. Chhowalla, and V. B. Shenoy, *Nat Chem*, 2010, **2**, 581-587.
81. Y. H. Wu, T. Yu, and Z. X. Shen, *Journal of Applied Physics*, 2010, **108**, 071301-38.
82. M. J. McAllister, J.-L. Li, D. H. Adamson, H. C. Schniepp, A. A. Abdala, J. Liu, M. Herrera-Alonso, D. L. Milius, R. Car, R. K. Prud'homme, and I. A. Aksay, *Chemistry of Materials*, 2007, **19**, 4396-4404.
83. H. C. Schniepp, J.-L. Li, M. J. McAllister, H. Sai, M. Herrera-Alonso, D. H. Adamson, R. K. Prud'homme, R. Car, D. A. Saville, and I. A. Aksay, *The Journal of Physical Chemistry B*, 2006, **110**, 8535-8539.
84. Z.-S. Wu, W. Ren, L. Gao, B. Liu, C. Jiang, and H.-M. Cheng, *Carbon*, 2009, **47**, 493-499.
85. X. Li, X. Wang, L. Zhang, S. Lee, and H. Dai, *Science*, 2008, **319**, 1229-1232.
86. X. Li, G. Zhang, X. Bai, X. Sun, X. Wang, E. Wang, and H. Dai, *Nature Nanotechnology*, 2008, **3**, 538-542.

87. S. R. Dhakate, N. Chauhan, S. Sharma, J. Tawale, S. Singh, P. D. Sahare, and R. B. Mathur, *Carbon*, 2011, **49**, 1946-1954.
88. Y. Zhu, S. Murali, M. D. Stoller, K. J. Ganesh, W. Cai, P. J. Ferreira, A. Pirkle, R. M. Wallace, K. A. Cychosz, M. Thommes, D. Su, E. A. Stach, and R. S. Ruoff, *Science*, 2011, **332**, 1537-1541.
89. I. Janowska, K. Chizari, O. Ersen, S. Zafeiratos, D. Soubane, V. D. Costa, V. Speisser, C. Boeglin, M. Houllé, D. Bégin, D. Plee, M.-J. Ledoux, and C. Pham-Huu, *Nano Research*, 2010, **3**, 126-137.
90. Z.-S. Wu, W. Ren, L. Gao, J. Zhao, Z. Chen, B. Liu, D. Tang, B. Yu, C. Jiang, and H.-M. Cheng, *ACS Nano*, 2009, **3**, 411-417.
91. W. Qian, R. Hao, Y. Hou, Y. Tian, C. Shen, H. Gao, and X. Liang, *Nano Research*, 2009, **2**, 706-712.
92. J. Zheng, C.-a. Di, Y. Liu, H. Liu, Y. Guo, C. Du, T. Wu, G. Yu, and D. Zhu, *Chemical Communications*, 2010, **46**, 5728-5730.
93. Q. Du, M. Zheng, L. Zhang, Y. Wang, J. Chen, L. Xue, W. Dai, G. Ji, and J. Cao, *Electrochimica Acta*, 2010, **55**, 3897-3903.
94. M. Jin, H.-K. Jeong, T.-H. Kim, K. P. So, Y. Cui, W. J. Yu, E. J. Ra, and Y. H. Lee, *Journal of Physics D: Applied Physics*, 2010, **43**, 275402, 1-7.
95. A. Kaniyoor, T. T. Baby, and S. Ramaprabhu, *Journal of Materials Chemistry*, 2010, **20**, 8467-8469.
96. W. Lv, D.-M. Tang, Y.-B. He, C.-H. You, Z.-Q. Shi, X.-C. Chen, C.-M. Chen, P.-X. Hou, C. Liu, and Q.-H. Yang, *ACS Nano*, 2009, **3**, 3730-3736.
97. H.-B. Zhang, J.-W. Wang, Q. Yan, W.-G. Zheng, C. Chen, and Z.-Z. Yu, *Journal of Materials Chemistry*, 2011, **21**, 5392-5397.
98. N. Liu, F. Luo, H. Wu, Y. Liu, C. Zhang, and J. Chen, *Advanced Functional Materials*, 2008, **18**, 1518-1525.
99. J. Lu, J. X. Yang, J. Wang, A. Lim, S. Wang, and K. P. Loh, *ACS Nano*, 2009, **3**, 2367-2375.
100. C.-Y. Su, A.-Y. Lu, Y. Xu, F.-R. Chen, A. N. Khlobystov, and L.-J. Li, *ACS Nano*, 2011, **5**, 2332-2339.
101. I. Janowska, O. Ersen, T. Jacob, P. Vennégues, D. Bégin, M.-J. Ledoux, and C. Pham-Huu, *Applied Catalysis A: General*, 2009, **371**, 22-30.
102. K. I. Bolotin, K. J. Sikes, Z. Jiang, M. Klima, G. Fudenberg, J. Hone, P. Kim, and H. L. Stormer, *Solid State Communications*, 2008, **146**, 351-355.
103. C. Lee, X. Wei, J. W. Kysar, and J. Hone, *Science*, 2008, **321**, 385-388.
104. H. K. Chae, D. Y. Siberio-Pérez, J. Kim, Y. Go, M. Eddaoudi, A. J. Matzger, M. O'Keeffe, and O. M. Yaghi, *Nature*, 2004, **427**, 523-527.
105. R. R. Nair, P. Blake, A. N. Grigorenko, K. S. Novoselov, T. J. Booth, T. Stauber, N. M. R. Peres, and A. K. Geim, *Science*, 2008, **320**, 1308.
106. A. A. Balandin, S. Ghosh, W. Bao, I. Calizo, D. Teweldebrhan, F. Miao, and C. N. Lau, *Nano Letters*, 2008, **8**, 902-907.
107. Z. Xu and C. Gao, *Macromolecules*, 2010, **43**, 6716-6723.
108. D. A. Nguyen, Y. R. Lee, A. V. Raghu, H. M. Jeong, C. M. Shin, and B. K. Kim, *Polymer International*, 2009, **58**, 412-417.
109. X. Wang, L. Zhi, and K. Müllen, *Nano Letters*, 2008, **8**, 323-327.
110. J. Wu, M. Agrawal, H. A. Becerril, Z. Bao, Z. Liu, Y. Chen, and P. Peumans, *ACS Nano*, 2010, **4**, 43-48.
111. S. Pang, H. N. Tsao, X. Feng, and K. Müllen, *Advanced Materials*, 2009, **21**, 3488-3491.
112. Z. Liu, K. Parvez, R. Li, R. Dong, X. Feng, and K. Müllen, *Advanced Materials*, 2015, **27**, 669-675.

113. S. Bae, H. Kim, Y. Lee, X. Xu, J.-S. Park, Y. Zheng, J. Balakrishnan, T. Lei, H. Ri Kim, Y. I. Song, Y.-J. Kim, K. S. Kim, B. Özyilmaz, J.-H. Ahn, B. H. Hong, and S. Iijima, *Nature Nanotechnology*, 2010, **5**, 574.
114. Z.-S. Wu, K. Parvez, A. Winter, H. Vieker, X. Liu, S. Han, A. Turchanin, X. Feng, and K. Müllen, *Advanced Materials*, 2014, **26**, 4552-4558.
115. Z.-S. Wu, W. Ren, L. Wen, L. Gao, J. Zhao, Z. Chen, G. Zhou, F. Li, and H.-M. Cheng, *ACS Nano*, 2010, **4**, 3187-3194.
116. R. Krishna, J. M. Campiña, P. M. V. Fernandes, J. Ventura, E. Titus, and A. F. Silva, *Analyst*, 2016, **141**, 4151-4161.
117. M. Khan, M. M. Khan, and M. H. Cho, *Nanoscale*, 2018, **10**, 9427-9440.
118. D. G. Papageorgiou, I. A. Kinloch, and R. J. Young, *Progress in Materials Science*, 2017, **90**, 75-127.
119. C. Lee, X. Wei, J. W. Kysar, and J. Hone, *Science*, 2008, **321**, 385-388.
120. R. J. T. Nicholl, H. J. Conley, N. V. Lavrik, I. Vlassiouk, Y. S. Puzyrev, V. P. Sreenivas, S. T. Pantelides, and K. I. Bolotin, *Nature communications*, 2015, **6**, 8789, 1-7.
121. Z. Li, I. A. Kinloch, R. J. Young, K. S. Novoselov, G. Anagnostopoulos, J. Parthenios, C. Galiotis, K. Papagelis, C.-Y. Lu, and L. Britnell, *ACS Nano*, 2015, **9**, 3917-3925.
122. W. Chen, X. Gui, B. Liang, M. Liu, Z. Lin, Y. Zhu, and Z. Tang, *ACS applied materials & interfaces*, 2016, **8**, 10977-10984.
123. J. Vejpravova, B. Pacakova, J. Endres, A. Mantlikova, T. Verhagen, V. Vales, O. Frank, and M. Kalbac, *Scientific reports*, 2015, **5**, 15061.
124. W.-K. Lee, J. Kang, K.-S. Chen, C. J. Engel, W.-B. Jung, D. Rhee, M. C. Hersam, and T. W. Odom, *Nano letters*, 2016, **16**, 7121-7127.
125. P. Y. Chen, J. Sodhi, Y. Qiu, T. M. Valentin, R. S. Steinberg, Z. Wang, R. H. Hurt, and I. Y. Wong, *Advanced materials*, 2016, **28**, 3564-3571.
126. T. Hallam, A. Shakouri, E. Poliani, A. P. Rooney, I. Ivanov, A. Potie, H. K. Taylor, M. Bonn, D. Turchinovich, and S. J. Haigh, *Nano letters*, 2015, **15**, 857-863.
127. J. Zang, S. Ryu, N. Pugno, Q. Wang, Q. Tu, M. J. Buehler, and X. Zhao, *Nature materials*, 2013, **12**, 321.
128. K. Sampathkumar, C. Androulidakis, E. N. Koukaras, J. Rahova, K. Drogowska, M. Kalbac, A. Vetushka, A. Fejfar, C. Galiotis, and O. Frank, *Carbon*, 2019, **146**, 772-778.
129. H. Qin, Y. Sun, J. Z. Liu, and Y. Liu, *Carbon*, 2016, **108**, 204-214.
130. P. Zhang, L. Ma, F. Fan, Z. Zeng, C. Peng, P. E. Loya, Z. Liu, Y. Gong, J. Zhang, and X. Zhang, *Nature communications*, 2014, **5**, 3782, 1-7.
131. G. Jung, Z. Qin, and M. J. Buehler, *Extreme Mechanics Letters*, 2015, **2**, 52-59.
132. M.-N. Ky and Y.-J. Yum, *Journal of Mechanical Science and Technology*, 2014, **28**, 3645-3652.
133. K. S. Kim, Y. Zhao, H. Jang, S. Y. Lee, J. M. Kim, K. S. Kim, J.-H. Ahn, P. Kim, J.-Y. Choi, and B. H. Hong, *Nature*, 2009, **457**, 706-710.
134. J. Wang, F. Ma, W. Liang, and M. Sun, *Materials Today Physics*, 2017, **2**, 6-34.
135. P. Avouris, Z. Chen, and V. Perebeinos: 'Carbon-based electronics', in 'Nanoscience And Technology: A Collection of Reviews from Nature Journals', 174-184; 2010, World Scientific.
136. Y. Zhang, Y.-W. Tan, H. L. Stormer, and P. Kim, *nature*, 2005, **438**, 201-204.
137. A. K. Geim and K. S. Novoselov: 'The rise of graphene', in 'Nanoscience and Technology: A Collection of Reviews from Nature Journals', 11-19; 2010, World Scientific.
138. K.S. Novoselov, D. Jiang, F.Schedin, T.J. Booth, V.V. Khotkevich, S.V. Morozov, and G. AK., *Two-dimensional atomic crystals.* Proc Natl Acad Sci U S A., 2005, 10451-10453.
139. X.-Y. Fang, X.-X. Yu, H.-M. Zheng, H.-B. Jin, L. Wang, and M.-S. Cao, *Physics Letters A*, 2015, **379**, 2245-2251.

140. Y. Xu, K. T. He, S. W. Schmucker, Z. Guo, J. C. Koepke, J. D. Wood, J. W. Lyding, and N. R. Aluru, *Nano Letters*, 2011, **11**, 2735-2742.
141. J.-H. Chen, C. Jang, S. Xiao, M. Ishigami, and M. S. Fuhrer, *Nature Nanotechnology*, 2008, **3**, 206-209.
142. P. Norton, T. Braggins, and H. Levinstein, *Physical Review B*, 1973, **8**, 5632-5653.
143. T. Dürkop, S. A. Getty, E. Cobas, and M. S. Fuhrer, *Nano Letters*, 2004, **4**, 35-39.
144. M. Ishigami, J. H. Chen, W. G. Cullen, M. S. Fuhrer, and E. D. Williams, *Nano Letters*, 2007, **7**, 1643-1648.
145. Y. Zhu, S. Murali, W. Cai, X. Li, J. W. Suk, J. R. Potts, and R. S. Ruoff, *Advanced Materials*, 2010, **22**, 3906-3924.
146. E. H. Hwang, S. Adam, and S. D. Sarma, *Physical Review Letters*, 2007, **98**, 186806.
147. A. A. Sagade, D. Neumaier, D. Schall, M. Otto, A. Pesquera, A. Centeno, A. Z. Elorza, and H. Kurz, *Nanoscale*, 2015, **7**, 3558-3564.
148. M. Calandra, G. Profeta, and F. Mauri, *physica status solidi (b)*, 2012, **249**, 2544-2548.
149. A. Di Bernardo, O. Millo, M. Barbone, H. Alpern, Y. Kalcheim, U. Sassi, A. K. Ott, D. De Fazio, D. Yoon, M. Amado, A. C. Ferrari, J. Linder, and J. W. A. Robinson, *Nature Communications*, 2017, **8**, 14024.
150. A. M. Dimiev, L. B. Alemany, and J. M. Tour, *ACS Nano*, 2013, **7**, 576-588.
151. F. Wang, Y. Zhang, C. Tian, C. Girit, A. Zettl, M. Crommie, and Y. R. Shen, *Science*, 2008, **320**, 206-209.
152. C. H. Lui, K. F. Mak, J. Shan, and T. F. Heinz, *Physical Review Letters*, 2010, **105**, 127404.
153. Z. Wang, H. Zeng, and L. Sun, *Journal of Materials Chemistry C*, 2015, **3**, 1157-1165.
154. Z. H. Ni, H. M. Wang, J. Kasim, H. M. Fan, T. Yu, Y. H. Wu, Y. P. Feng, and Z. X. Shen, *Nano letters*, 2007, **7**, 2758-2763.
155. E. Pop, V. Varshney, and A. K. Roy, *MRS Bulletin*, 2012, **37**, 1273-1281.
156. Y. Fu, J. Hansson, Y. Liu, S. Chen, A. Zehri, M. K. Samani, N. Wang, Y. Ni, Y. Zhang, Z.-B. Zhang, Q. Wang, M. Li, H. Lu, M. Sledzinska, C. M. S. Torres, S. Volz, A. A. Balandin, X. Xu, and J. Liu, *2D Materials*, 2019, **7**, 012001.
157. G. Fugallo, A. Cepellotti, L. Paulatto, M. Lazzeri, N. Marzari, and F. Mauri, *Nano letters*, 2014, **14**, 6109-6114.
158. K. M. F. Shahil and A. A. Balandin, *Nano letters*, 2012, **12**, 861-867.
159. E. Pop, D. Mann, Q. Wang, K. Goodson, and H. Dai, *Nano Letters*, 2006, **6**, 96-100.
160. T. R. Anthony, W. F. Banholzer, J. F. Fleischer, L. Wei, P. K. Kuo, R. L. Thomas, and R. W. Pryor, *Physical Review B*, 1990, **42**, 1104-1111.
161. J. H. Seol, I. Jo, A. L. Moore, L. Lindsay, Z. H. Aitken, M. T. Pettes, X. Li, Z. Yao, R. Huang, D. Broido, N. Mingo, R. S. Ruoff, and L. Shi, *Science*, 2010, **328**, 213-216.
162. B. Qiu and X. Ruan, *Applied Physics Letters*, 2012, **100**, 193101.
163. J. Haskins, A. Kınacı, C. Sevik, H. Sevinçli, G. Cuniberti, and T. Çağın, *ACS Nano*, 2011, **5**, 3779-3787.
164. Z. Aksamija and I. Knezevic, *Applied Physics Letters*, 2011, **98**, 141919.
165. F. Hao, D. Fang, and Z. Xu, *Applied Physics Letters*, 2011, **99**, 041901.
166. W. Liu and M. Asheghi, *Journal of Applied Physics*, 2005, **98**, 123523.
167. R. Chen, A. I. Hochbaum, P. Murphy, J. Moore, P. Yang, and A. Majumdar, *Physical Review Letters*, 2008, **101**, 105501.
168. P. A. Denis and F. Iribarne, *The Journal of Physical Chemistry C*, 2013, **117**, 19048-19055.
169. A. Eftekhari and P. Jafarkhani, *The Journal of Physical Chemistry C*, 2013, **117**, 25845-25851.
170. G. Diankov, M. Neumann, and D. Goldhaber-Gordon, *ACS Nano*, 2013, **7**, 1324-1332.
171. M. T. Hasan, B. J. Senger, P. Mulford, C. Ryan, H. Doan, Z. Gryczynski, and A. V. Naumov, *Nanotechnology*, 2017, **28**, 065705.

172. H. He, T. Riedl, A. Lerf, and J. Klinowski, *The Journal of Physical Chemistry*, 1996, **100**, 19954-19958.
173. A. Lerf, H. He, M. Forster, and J. Klinowski, *The Journal of Physical Chemistry B*, 1998, **102**, 4477-4482.
174. R. Larciprete, P. Lacovig, S. Gardonio, A. Baraldi, and S. Lizzit, *The Journal of Physical Chemistry C*, 2012, **116**, 9900-9908.
175. C. Gómez-Navarro, M. Burghard, and K. Kern, *Nano Letters*, 2008, **8**, 2045-2049.
176. R. Aradhana, S. Mohanty, and S. K. Nayak, *Polymer*, 2018, **141**, 109-123.
177. W.-S. Hung, S.-M. Chang, R. L. G. Lecaros, Y.-L. Ji, Q.-F. An, C.-C. Hu, K.-R. Lee, and J.-Y. Lai, *Carbon*, 2017, **117**, 112-119.
178. D. S. Shin, H. G. Kim, H. S. Ahn, H. Y. Jeong, Y.-J. Kim, D. Odkhuu, N. Tsogbadrakh, H.-B.-R. Lee, and B. H. Kim, *RSC Advances*, 2017, **7**, 13979-13984.
179. M. T. Hasan, B. Senger, P. Mulford, C. Ryan, H. Doan, Z. Gryczynski, and A. Naumov, *Nanotechnology*, 2017, **28**, 065705.
180. M. Enayati, A. Nemati, A. Zarrabi, and M. A. Shokrgozar, *Journal of Alloys and Compounds*, 2019, **784**, 134-148.
181. J. Rosas, R. Gutiérrez, A. Escobedo Morales, and E. Chigo, *Journal of molecular modeling*, 2011, **17**, 1133-1139.
182. D. Wei, Y. Liu, Y. Wang, H. Zhang, L. Huang, and G. Yu, *Nano Letters*, 2009, **9**, 1752-1758.
183. H. Xu, L. Ma, and Z. Jin, *Journal of Energy Chemistry*, 2018, **27**, 146-160.
184. R. Lv, Q. Li, A. R. Botello-Méndez, T. Hayashi, B. Wang, A. Berkdemir, Q. Hao, A. L. Elías, R. Cruz-Silva, H. R. Gutiérrez, Y. A. Kim, H. Muramatsu, J. Zhu, M. Endo, H. Terrones, J.-C. Charlier, M. Pan, and M. Terrones, *Scientific Reports*, 2012, **2**, 586, 1-8.
185. Y. J. Cho, H. S. Kim, S. Y. Baik, Y. Myung, C. S. Jung, C. H. Kim, J. Park, and H. S. Kang, *The Journal of Physical Chemistry C*, 2011, **115**, 3737-3744.
186. S. Seo, Y. Yoon, J. Lee, Y. Park, and H. Lee, *ACS Nano*, 2013, **7**, 3607-3615.
187. L. Sun, L. Wang, C. Tian, T. Tan, Y. Xie, K. Shi, M. Li, and H. Fu, *RSC Advances*, 2012, **2**, 4498-4506.
188. C. H. Choi, S. H. Park, M. W. Chung, and S. I. Woo, *Carbon*, 2013, **55**, 98-107.
189. H. N. Tien and S. H. Hur, *Materials Letters*, 2015, **161**, 399-403.
190. C. Liang, Y. Wang, and T. Li, *Carbon*, 2015, **82**, 506-512.
191. Y. Su, Y. Zhang, X. Zhuang, S. Li, D. Wu, F. Zhang, and X. Feng, *Carbon*, 2013, **62**, 296-301.
192. X. a. Chen, X. Chen, X. Xu, Z. Yang, Z. Liu, L. Zhang, X. Xu, Y. Chen, and S. Huang, *Nanoscale*, 2014, **6**, 13740-13747.
193. S. Abdelaal, E. K. Elmaghraby, A. M. Abdelhady, M. Youssf, A. M. Rashad, I. I. Bashter, and A. I. Helal, *Diamond and Related Materials*, 2020, **101**, 107613.
194. K. Gong, F. Du, Z. Xia, M. Durstock, and L. Dai, *Science*, 2009, **323**, 760-764.
195. M. Sahoo, K. P. Sreena, B. P. Vinayan, and S. Ramaprabhu, *Materials Research Bulletin*, 2015, **61**, 383-390.
196. X. Mu, X. Wu, T. Zhang, D. B. Go, and T. Luo, *Scientific Reports*, 2014, **4**, 3909, 1-10.
197. H. Yan, X. Tao, Z. Yang, K. Li, H. Yang, A. Li, and R. Cheng, *J Hazard Mater*, 2014, **268**, 191-198.
198. D. V. Stergiou, E. K. Diamanti, D. Gournis, and M. I. Prodromidis, *Electrochemistry Communications*, 2010, **12**, 1307-1309.
199. G. Maccaferri, C. Zanardi, Z. Y. Xia, A. Kovtun, A. Liscio, F. Terzi, V. Palermo, and R. Seeber, *Carbon*, 2017, **120**, 165-175.
200. A. Lherbier, A. Botello-Méndez, and J.-C. Charlier, *Nano letters*, 2013, **13**, 1446–1450.
201. D. J. Late, A. Ghosh, K. S. Subrahmanyam, L. S. Panchakarla, S. B. Krupanidhi, and C. N. R. Rao, *Solid State Communications*, 2010, **150**, 734-738.
202. R. Maiti, A. Midya, C. Narayana, and S. K. Ray, *Nanotechnology*, 2014, **25**, 495704.
203. Y. Wang, Y. Shao, D. W. Matson, J. Li, and Y. Lin, *ACS Nano*, 2010, **4**, 1790-1798.

204. Z.-S. Wu, W. Ren, L. Xu, F. Li, and H.-M. Cheng, *ACS nano*, 2011, **5**, 5463-5471.
205. O. S. Kwon, S. J. Park, J.-Y. Hong, A. R. Han, J. S. Lee, J. S. Lee, J. H. Oh, and J. Jang, *ACS Nano*, 2012, **6**, 1486-1493.
206. Y. Sun, C. Du, M. An, L. Du, Q. Tan, C. Liu, Y. Gao, and G. Yin, *Journal of Power Sources*, 2015, **300**, 245-253.
207. L. Chen, J. Feng, H. Zhou, C. Fu, G. Wang, L. Yang, C. Xu, Z. Chen, W. Yang, and Y. Kuang, *Journal of Materials Chemistry A*, 2017, **5**, 7403-7415.
208. J. O. Hwang, J. S. Park, D. S. Choi, J. Y. Kim, S. H. Lee, K. E. Lee, Y.-H. Kim, M. H. Song, S. Yoo, and S. O. Kim, *ACS nano*, 2012, **6**, 159-167.
209. H. Li, J. He, S. Li, and A. P. F. Turner, *Biosensors and Bioelectronics*, 2013, **43**, 25-29.
210. L. Zhang and Z. Xia, *The Journal of Physical Chemistry C*, 2011, **115**, 11170-11176.
211. Z. Lin, G. H. Waller, Y. Liu, M. Liu, and C.-p. Wong, *Nano Energy*, 2013, **2**, 241-248.
212. L. Qu, Y. Liu, J.-B. Baek, and L. Dai, *ACS Nano*, 2010, **4**, 1321-1326.
213. S. Wang, L. Zhang, Z. Xia, A. Roy, D. W. Chang, J. B. Baek, and L. Dai, *Angew Chem Int Ed Engl*, 2012, **51**, 4209-4212.
214. S. Yang, L. Zhi, K. Tang, X. Feng, J. Maier, and K. Müllen, *Advanced Functional Materials*, 2012, **22**, 3634-3640.
215. M. D. Esrafili, *Chemical Physics Letters*, 2018, **705**, 44-49.
216. B. Xiong, Y. Zhou, Y. Zhao, J. Wang, X. Chen, R. O'Hayre, and Z. Shao, *Carbon*, 2013, **52**, 181-192.
217. Z.-S. Wu, S. Yang, Y. Sun, K. Parvez, X. Feng, and K. Müllen, *Journal of the American Chemical Society*, 2012, **134**, 9082-9085.
218. N. Kurita, *Carbon*, 2000, **38**, 65-75.
219. L. S. Panchakarla, K. S. Subrahmanyam, S. K. Saha, A. Govindaraj, H. R. Krishnamurthy, U. V. Waghmare, and C. N. R. Rao, *Advanced Materials*, 2009, **21**, 4726-4730.
220. B. Huang, *Physics Letters A*, 2011, **375**, 845-848.
221. M. D. Slater, D. Kim, E. Lee, and C. S. Johnson, *Advanced Functional Materials*, 2013, **23**, 947-958.
222. H. W. Lee, H. S. Moon, J. Hur, I. T. Kim, M. S. Park, J. M. Yun, K. H. Kim, and S. G. Lee, *Carbon*, 2017, **119**, 492-501.
223. H. Liu, M. Jia, B. Cao, R. Chen, X. Lv, R. Tang, F. Wu, and B. Xu, *Journal of Power Sources*, 2016, **319**, 195-201.
224. J. Xu, M. Wang, N. P. Wickramaratne, M. Jaroniec, S. Dou, and L. Dai, *Advanced Materials*, 2015, **27**, 2042-2048.
225. J. Zhang, C. Li, Z. Peng, Y. Liu, J. Zhang, Z. Liu, and D. Li, *Scientific Reports*, 2017, **7**, 4886, 1-7.
226. H. M. Jeong, J. W. Lee, W. H. Shin, Y. J. Choi, H. J. Shin, J. K. Kang, and J. W. Choi, *Nano Letters*, 2011, **11**, 2472-2477.
227. Y. Qiu, X. Zhang, and S. Yang, *Physical Chemistry Chemical Physics*, 2011, **13**, 12554-12558.
228. Y. Seekaew, O. Arayawut, K. Timsorn, and C. Wongchoosuk: 'Chapter Nine - Synthesis, Characterization, and Applications of Graphene and Derivatives', in 'Carbon-Based Nanofillers and Their Rubber Nanocomposites', (eds. S. Yaragalla, et al.), 2019, 259-283, Elsevier.
229. A. Hulanicki, S. Głab, and F. Ingman, Pure&App/. Chern., 1991, **63**, 1247-1250.
230. J. Peña-Bahamonde, H. N. Nguyen, S. K. Fanourakis, and D. F. Rodrigues, *Journal of nanobiotechnology*, 2018, **16**, 75-75.
231. M. Pumera, *Materials Today*, 2011, **14**, 308-315.
232. Y. Song, Y. Luo, C. Zhu, H. Li, D. Du, and Y. Lin, *Biosensors and Bioelectronics*, 2016, **76**, 195-212.
233. C. N. R. Rao, A. K. Sood, K. S. Subrahmanyam, and A. Govindaraj, *Angewandte Chemie International Edition*, 2009, **48**, 7752-7777.

234. N. Chauhan, T. Maekawa, and D. N. S. Kumar, *Journal of Materials Research*, 2017, **32**, 2860-2882.
235. C. S. Park, H. Yoon, and O. S. Kwon, *Journal of Industrial and Engineering Chemistry*, 2016, **38**, 13-22.
236. S. Korkut, J. D. Roy-Mayhew, D. M. Dabbs, D. L. Milius, and I. A. Aksay, *ACS Nano*, 2011, **5**, 5214-5222.
237. L. Xu, Y. Wen, S. Pandit, V. R. S. S. Mokkapati, I. Mijakovic, Y. Li, M. Ding, S. Ren, W. Li, and G. Liu, *BMC Chemistry*, 2019, **13**:112, 1-12.
238. S. Taniselass, M. K. M. Arshad, and S. C. B. Gopinath, *Biosensors and Bioelectronics*, 2019, **130**, 276-292.
239. J. M. George, A. Antony, and B. Mathew, *Microchimica Acta*, 2018, **185**, 358, 1-26.
240. S. K. Krishnan, E. Singh, P. Singh, M. Meyyappan, and H. S. Nalwa, *RSC Advances*, 2019, **9**, 8778-8881.
241. D. Chauhan, Pooja, V. Nirbhaya, C. M. Srivastava, R. Chandra, and S. Kumar, *Microchemical Journal*, 2020, **155**, 104697.
242. S. Nazarpour, R. Hajian, and M. H. Sabzvari, *Microchemical Journal*, 2020, **154**, 104634.
243. F. Xiao, H. Li, X. Yan, L. Yan, X. Zhang, M. Wang, C. Qian, and Y. Wang, *Analytica Chimica Acta*, 2020, **1103**, 84-96 .
244. H. Liang, Y. Zhao, H. Ye, and C.-P. Li, *Journal of Electroanalytical Chemistry*, 2019, **855**, 113487.
245. L. Fu, G. Lai, D. Zhu, B. Jia, F. Malherbe, and A. Yu, *ChemCatChem*, 2016, **8**, 2975-2980.
246. Y. Zhou, M. Ma, H. He, Z. Cai, N. Gao, C. He, G. Chang, X. Wang, and Y. He, *Biosensors and Bioelectronics*, 2019, **146**, 111751.
247. G. B. V. S. Lakshmi, A. Sharma, P. R. Solanki, and D. K. Avasthi, *Nanotechnology*, 2016, **27**, 345101.
248. N. Agnihotri, A. D. Chowdhury, and A. De, *Biosensors and Bioelectronics*, 2015, **63**, 212-217.
249. S. Alexander, P. Baraneedharan, S. Balasubrahmanyan, and S. Ramaprabhu, *European Polymer Journal*, 2017, **86**, 106-116.
250. A. Rengaraj, Y. Haldorai, C. H. Kwak, S. Ahn, K.-J. Jeon, S. H. Park, Y.-K. Han, and Y. S. Huh, *Journal of Materials Chemistry B*, 2015, **3**, 6301-6309.
251. R. Ponnusamy, R. Venkatesan, A. Gangan, R. Samal, B. Chakraborty, D. J. Late, and C. S. Rout, *Applied Surface Science*, 2019, **495**, 143588.
252. Y. Xue, B. Tian, M. Wang, T. Zhai, R. Li, and L. Tan, *Colloids and Surfaces A: Physicochemical and Engineering Aspects*, 2020, **591**, 124549.
253. C. Wang, Y. Sun, X. Yu, D. Ma, J. Zheng, P. Dou, Z. Cao, and X. Xu, *Journal of Materials Science: Materials in Electronics*, 2016, **27**, 9370-9378.
254. S. Yang, L. Liu, G. Wang, G. Li, D. Deng, and L. Qu, *Journal of Electroanalytical Chemistry*, 2015, **755**, 15-21.
255. K. Dhara, T. Ramachandran, B. G. Nair, and T. G. Satheesh Babu, *Journal of Electroanalytical Chemistry*, 2015, **743**, 1-9.
256. J. Lu, X. Zhang, N. Liu, Z. Yu, and T. Duan, *Journal of Electroanalytical Chemistry*, 2016, **769**, 21-27.
257. H. Teymourian, A. Salimi, and S. Khezrian, *Electroanalysis*, 2017, **29**, 409-414.
258. K. D. Kıranşan, E. Topçu, and M. Alanyalıoğlu, *Journal of Applied Polymer Science*, 2017, **134**, 45139.
259. S. Sakthinathan, H. F. Lee, S. M. Chen, and P. Tamizhdurai, *Journal of Colloid and Interface Science*, 2016, **468**, 120-127.
260. J. Gao, P. He, T. Yang, L. Zhou, X. Wang, S. Chen, H. Lei, H. Zhang, B. Jia, and J. Liu, *Journal of Electroanalytical Chemistry*, 2019, **852**, 113516.

261. P. Salazar, I. Fernández, M. C. Rodríguez, A. Hernández-Creus, and J. L. González-Mora, *Journal of Electroanalytical Chemistry*, 2019, **855**, 113638.
262. S. Bozkurt, B. Tosun, B. Sen, S. Akocak, A. Savk, M. F. Ebeoğlugil, and F. Sen, *Analytica Chimica Acta*, 2017, **989**, 88-94.
263. X. Yang, Y. Ouyang, F. Wu, Y. Hu, Y. Ji, and Z. Wu, *Sensors and Actuators, B: Chemical*, 2017, **238**, 40-47.
264. B. Amanulla, S. Palanisamy, S. M. Chen, V. Velusamy, T. W. Chiu, T. W. Chen, and S. K. Ramaraj, *Journal of Colloid and Interface Science*, 2017, **487**, 370-377.
265. Z. Yao, X. Yang, F. Wu, W. Wu, and F. Wu, *Microchimica Acta*, 2016, **183**, 2799-2806.
266. B. Sun, X. Gou, R. Bai, A. A. A. Abdelmoaty, Y. Ma, X. Zheng, and F. Hu, *Materials Science and Engineering C*, 2017, **74**, 515-524.
267. Y. Xu, W. Zhang, J. Shi, X. Zou, Y. Li, T. Haroon Elrasheid, X. Huang, Z. Li, X. Zhai, and X. Hu, *Food Chemistry*, 2017, **237**, 423-430.
268. C. D. Mendonça, T. M. Prado, F. H. Cincotto, R. T. Verbinnen, and S. A. S. Machado, *Sensors and Actuators, B: Chemical*, 2017, **251**, 739-745.
269. Z. Zhao, Z. Xia, C. Liu, H. Huang, and W. Ye, *Electrochimica Acta*, 2017, **256**, 146-154.
270. Y. Zuo, J. Xu, F. Jiang, X. Duan, L. Lu, H. Xing, T. Yang, Y. Zhang, G. Ye, and Y. Yu, *Journal of Electroanalytical Chemistry*, 2017, **801**, 146-152.
271. H. Yu, X. Feng, X. X. Chen, S. S. Wang, and J. Jin, *Journal of Electroanalytical Chemistry*, 2017, **801**, 488-495.
272. T.-W. Chen, J. Princy Merlin, S.-M. Chen, S. Anandaraj, M. S. Elshikh, T.-W. Tseng, K. Wang, D. Qi, and J. Jiang, *Ultrasonics Sonochemistry*, 2020, **64**, 104717.
273. P. Bollella, G. Fusco, C. Tortolini, G. Sanzò, G. Favero, L. Gorton, and R. Antiochia, *Biosensors and Bioelectronics*, 2017, **89**, 152-166.
274. L. Fritea, M. Tertis, R. Sandulescu, and C. Cristea: 'Chapter Eleven - Enzyme–Graphene Platforms for Electrochemical Biosensor Design With Biomedical Applications', in 'Methods in Enzymology', (ed. C. V. Kumar), 2028, 293-333, Academic Press.
275. C. Karunakaran, T. Madasamy, and N. K. Sethy: 'Chapter 3 - Enzymatic Biosensors', in 'Biosensors and Bioelectronics', (eds. C. Karunakaran, et al.), 2015, 133-204, Elsevier.
276. V. Gaudin, *Biosensors and Bioelectronics*, 2017, **90**, 363-377.
277. M. Thangamuthu, K. Y. Hsieh, P. V. Kumar, and G.-Y. Chen, *International journal of molecular sciences*, 2019, **20**, 2975.
278. J.-H. Lee, S.-J. Park, and J.-W. Choi, *Nanomaterials*, 2019, **9,** 297.
279. A. Soozanipour and A. Taheri-Kafrani: 'Chapter Fourteen - Enzyme Immobilization on Functionalized Graphene Oxide Nanosheets: Efficient and Robust Biocatalysts', in 'Methods in Enzymology', (ed. C. V. Kumar), 2018, 371-403, Academic Press.
280. S. Pakapongpan and R. P. Poo-arporn, *Materials Science and Engineering: C*, 2017, **76**, 398-405.
281. X. You and J. J. Pak, *Sensors and Actuators B: Chemical*, 2014, **202**, 1357-1365.
282. D. Maity, M. C.R, and R. K. R.T, *Materials Science and Engineering: C*, 2019, **105**, 110075.
283. Y. Yuan, Y. Wang, H. Wang, and S. Hou, *Journal of Electroanalytical Chemistry*, 2019, **855**, 113495.
284. X. Feng, H. Cheng, Y. Pan, and H. Zheng, *Biosensors and Bioelectronics*, 2015, **70**, 411-417.
285. M. Zhang, C. Liao, C. H. Mak, P. You, C. L. Mak, and F. Yan, *Scientific Reports*, 2015, **5**, 8311.
286. Z. Kang, K. Jiao, X. Xu, R. Peng, S. Jiao, and Z. Hu, *Biosensors and Bioelectronics*, 2017, **96**, 367-372.
287. X. Shen, X. H. Xia, Y. L. Du, W. C. Ye, and C. M. Wang, *Journal of the Electrochemical Society*, 2017, **164**, B285-B291.
288. B. Çakıroğlu and M. Özacar, *Electroanalysis*, 2017, **29**, 2719-2726.
289. M. F. Hossain and J. Y. Park, *Scientific Reports*, 2016, **6**, 21009.
290. M. Qi, Y. Zhang, C. Cao, Y. Lu, and G. Liu, *RSC Advances*, 2016, **6**, 39180-39187.

291. K. Vijayaraj, S. W. Hong, S.-H. Jin, S.-C. Chang, and D.-S. Park, *Analytical Methods*, 2016, **8**, 6974-6981.
292. D. B. T. Mascagni, C. M. Miyazaki, N. C. da Cruz, M. L. de Moraes, A. Riul, and M. Ferreira, *Materials Science and Engineering: C*, 2016, **68**, 739-745.
293. S. Wu, F. Su, X. Dong, C. Ma, L. Pang, D. Peng, M. Wang, L. He, and Z. Zhang, *Applied Surface Science*, 2017, **401**, 262-270.
294. Y. Liu, X. Zhang, D. He, F. Ma, Q. Fu, and Y. Hu, *RSC Advances*, 2016, **6**, 18654-18661.
295. A. Halder, M. Zhang, and Q. Chi, *Biosensors and Bioelectronics*, 2017, **87**, 764-771.
296. Y. Wang, X.-y. Liu, X. Xu, Y. Yang, L.-h. Huang, Z.-y. He, Y.-h. Xu, J.-j. Chen, and Z.-s. Feng, *Materials Research Bulletin*, 2018, **101**, 340-346.
297. N. Mansouri, A. A. Babadi, S. Bagheri, and S. B. A. Hamid, *International Journal of Hydrogen Energy*, 2017, **42**, 1337-1343.
298. R. Devasenathipathy, V. Mani, S.-M. Chen, S.-T. Huang, T.-T. Huang, C.-M. Lin, K.-Y. Hwa, T.-Y. Chen, and B.-J. Chen, *Enzyme and Microbial Technology*, 2015, **78**, 40-45.
299. S. Palanisamy, S. K. Ramaraj, S.-M. Chen, T. C. K. Yang, P. Yi-Fan, T.-W. Chen, V. Velusamy, and S. Selvam, *Scientific Reports*, 2017, **7**, 41214.
300. B. Thirumalraj, S. Palanisamy, S.-M. Chen, C.-Y. Yang, P. Periakaruppan, and B.-S. Lou, *RSC Advances*, 2015, **5**, 77651-77657.
301. N. Haghighi, R. Hallaj, and A. Salimi, *Materials Science and Engineering: C*, 2017, **73**, 417-424.
302. E. Povedano, F. H. Cincotto, C. Parrado, P. Díez, A. Sánchez, T. C. Canevari, S. A. S. Machado, J. M. Pingarrón, and R. Villalonga, *Biosensors and Bioelectronics*, 2017, **89**, 343-351.
303. L.-P. Mei, J.-J. Feng, L. Wu, J.-Y. Zhou, J.-R. Chen, and A.-J. Wang, *Biosensors and Bioelectronics*, 2015, **74**, 347-352.
304. C. Lou, T. Jing, J. Zhou, J. Tian, Y. Zheng, C. Wang, Z. Zhao, J. Lin, H. Liu, C. Zhao, and Z. Guo, *International Journal of Biological Macromolecules*, 2020, **149**, 1130-1138.
305. I. Vasilescu, S. A. V. Eremia, M. Kusko, A. Radoi, E. Vasile, and G.-L. Radu, *Biosensors and Bioelectronics*, 2016, **75**, 232-237.
306. Z. Fan, Q. Lin, P. Gong, B. Liu, J. Wang, and S. Yang, *Electrochimica Acta*, 2015, **151**, 186-194.
307. S. K. Pandey, S. Sachan, and S. K. Singh, *Materials Science for Energy Technologies*, 2019, **2**, 676-686.
308. J. Liu, T. Wang, J. Wang, and E. Wang, *Electrochimica Acta*, 2015, **161**, 17-22.
309. N. Zou, X. Wei, Z. Zong, X. Li, Z. Wang, and X. Wang, *Journal of Chemical Sciences*, 2019, **131**, 1-8.
310. K. Pramanik, P. Sarkar, D. Bhattacharyay, and P. Majumdar, *Electroanalysis*, 2018, **30**, 2719-2730.
311. Z. Li, C. Xie, J. Wang, A. Meng, and F. Zhang, *Sensors and Actuators B: Chemical*, 2015, **208**, 505-511.
312. S. Komathi, N. Muthuchamy, K. P. Lee, and A. I. Gopalan, *Biosensors and Bioelectronics*, 2016, **84**, 64-71.
313. R. Rawal, N. Chauhan, M. Tomar, and V. Gupta, *Biochemical Engineering Journal*, 2017, **125**, 238-245.
314. G. Aydoğdu Tığ, *Talanta*, 2017, **175**, 382-389.
315. R. Jirakunakorn, S. Khumngern, J. Choosang, P. Thavarungkul, P. Kanatharana, and A. Numnuam, *Microchemical Journal*, 2020, **154**, 104624.
316. J. Wang: '*Analytical Electrochemistry*' 2000, NY, Wiley-VCH.
317. Bard, A. J., and L. R. Faulkner, *Electrochemical methods – Fundamentals and Applications*. 2001, John Wiley & Sons, Inc.: New York.

318. C. Brett and A. M. Brett: 'Electrochemistry: principles, methods, and applications'; 1993, Oxford, UK, Oxford university press.
319. A. Fick, *On Liquid Diffusion*. **1855**, P*hil. Mag*. p. 30–39.
320. T. Erdey-Gruz and M. Volmer, *Zur theorie der wasserstoffu berspannung*. 1930, Z Phys Chem. p. 203–213.
321. J. A. V. Butler, *Transactions of the Faraday Society*, 1924, **19**, 729-733.
322. W. H. Reinmuth, *Journal of Electroanalytical Chemistry and Interfacial Electrochemistry*, 1972, **34**, 297-311.
323. H. Helmholtz, *Annalen der Physik*, 1853, **165**, 211-233.
324. M. Gouy, J. Phys. Theor. Appl., **1910**, 9,457-468
325. D. L. Chapman, *The London, Edinburgh, and Dublin Philosophical Magazine and Journal of Science*, 1913, **25**, 475-481.
326. O. Stern, *Zeitschrift für Elektrochemie und angewandte physikalische Chemie*, 1924, **30**, 508-516.
327. J. E. B. Randles, *Transactions of the Faraday Society*, 1948, **44**, 327-338.
328. A. Ševčík, *Collection of Czechoslovak Chemical Communications*, 1948, **13**, 349-377.
329. M. E. Orazem, Tribollet, and B.: 'E*lectrochemical Impedance Spectroscopy*'; 2**008**, New Jersey, USA,, The Electrochemical Society Series, John Wiley & Sons, Inc., Hoboken.
330. E. M. Barsoukov and J. R.: 'I*mpedance Spectroscopy; Theory, Experiment, and Applications*'; 2005, New Jersey, USA, John Wiley & Sons, Inc., Hoboken.
331. G. Instruments, *The Basics of Electrochemical Impedance Spectroscopy*. 2019, Gamry Instruments.
332. S. Rao and K. D. Costa: '2 - Atomic Force Microscopy (AFM) in biomedical research', 'Biomedical Imaging', (ed. P. Morris),2014, 41-64, Woodhead Publishing.
333. G. Binnig, C. F. Quate, and C. Gerber, *Physical Review Letters*, 1986, **56**, 930-933.
334. P. Eaton, J. C. Fernandes, E. Pereira, M. E. Pintado, and F. Xavier Malcata, *Ultramicroscopy*, 2008, **108**, 1128-1134.
335. D. A. Campos, A. C. Ribeiro, E. M. Costa, J. C. Fernandes, F. K. Tavaria, F. B. Araruna, C. Eiras, P. Eaton, J. R. S. A. Leite, and M. Manuela Pintado, *Carbohydrate Polymers*, 2012, **90**, 270-274.
336. G. Kada, F. Kienberger, and P. Hinterdorfer, *Nano Today*, 2008, **3**, 12-19.
337. P. Eaton and P. West: 'Atomic Force Microscopy'; 2010, Oxford Scholarship Online
338. A. K. Singh: 'Chapter 4 - Experimental Methodologies for the Characterization of Nanoparticles', in 'Engineered Nanoparticles', (ed. A. K. Singh), 2016, 125-170, Boston, Academic Press.
339. G. E. Amidon, P. J. Meyer, and D. M. Mudie: 'Chapter 10 - Particle, Powder, and Compact Characterization', in 'Developing Solid Oral Dosage Forms (Second Edition)', (eds. Y. Qiu, et al.), 2017, 271-293, Boston, Academic Press.
340. Nanoscience. 'Scanning Electron Microscopy', [viewed October 2019]; Available from: https://www.nanoscience.com/techniques/scanning-electron-microscopy/.
341. D. J. Stokes: 'Principles of SEM. In Principles and Practice of Variable Pressure/Environmental Scanning Electron Microscopy'; 2008, Royal Microscopical Society.
342. D. A. Skoog, D. M. West, F.J. Holler, Crouch, and S. R. '*Fundamentals of Analytical Chemistry*'; 2004, USA, Thomson Brooks/Cole, Inc.
343. D. Skoog, J. Holler, and T. Nieman: '*Principles of Instrumental Analysis*'; 1998, Tomothy Thomson Learning, Inc.
344. A. Barron and P. Raja: 'Physical Methods in Chemistry and Nano Science'; 2012, Connexions, Rice University.
345. P. G. Zambonin and E. Desimoni: 'X-Ray Photoelectron Spectroscopy: Principles, Instrumentation, Data Processing and Molten Salt Applications', in 'Molten Salt Chemistry:

An Introduction and Selected Applications', (eds. G. Mamantov, et al.)1987, 425-445, Dordrecht, Springer Netherlands.
346. R. Gurwitz, R. Cohen, and I. Shalish, *Journal of Applied Physics*, 2014, **115**, 033701.
347. R. Krishna, C. Dias, J. Ventura, and E. Titus, *Materials Today: Proceedings*. 2016, **3**, 2807-2813.
348. R. Krishna, E. Titus, L. Costa, J. Menezes, M. Correia, S. Pinto, J. Ventura, J. Araujo, J. Cavaleiro, and J. Gracio, J. Mater. Chem. 2012, **22**, 10457-10459.
349. W. Zhang, S. Zhu, R. Luque, S. Han, L. Hu, and G. Xu, *Chemical Society Reviews*, 2016, **45**, 715-752.
350. R. C. Carvalho, C. Gouveia-Caridade, and C. M. A. Brett, *Analytical and Bioanalytical Chemistry*, 2010, **398**, 1675-1685.
351. Y. Xu, M. Cao, H. Liu, X. Zong, N. Kong, J. Zhang, and J. Liu, *Talanta*, 2015, **139**, 6-12.
352. T. Gan and S. Hu, *Microchimica Acta*, 2011, **175**, 1-19.
353. D. A. C. Brownson, L. J. Munro, D. K. Kampouris, and C. E. Banks, *RSC Advances*, 2011, **1**, 978-988.
354. M. S. Goh and M. Pumera, *Analytical Chemistry*, 2010, **82**, 8367-8370.
355. D. K. Kampouris and C. E. Banks, *Chemical Communications*, 2010, **46**, 8986-8988.
356. D. A. C. Brownson, D. K. Kampouris, and C. E. Banks, *Chemical Society Reviews*, 2012, **41**, 6944-6976.
357. S. J. Rowley-Neale, D. A. C. Brownson, and C. E. Banks, *Nanoscale*, 2016, **8**, 15241-15251.
358. P. M. Hallam and C. E. Banks, *Electrochemistry Communications*, 2011, **13**, 8-11.
359. M. Ciszewski, A. Mianowski, P. Szatkowski, G. Nawrat, and J. Adamek, *Ionics*, 2014, **21**, 557–563.
360. C. Hu, Y. Liu, Y. Yang, J. Cui, Z. Huang, Y. Wang, L. Yang, H. Wang, Y. Xiao, and J. Rong, *Journal of Materials Chemistry B*, 2013, **1**, 39-42.
361. J. R. Macdonald, *Annals of Biomedical Engineering*, 1992, **20**, 289-305.
362. A. Campiña J.MMartins, Fernando, The Journal of Physical Chemistry C., 2007, **111**, 5351-5362.
363. S. J. Konopka and B. McDuffie, *Analytical Chemistry*, 1970, **42**, 1741-1746.
364. L. Wang, J. Zhao, X. He, J. Gao, J. Li, C. Wan, and C. Jiang, *International journal of electrochemical science*, 2012, **7**, 345-353.
365. B. E. McNealy and J. L. Hertz, *Solid State Ionics*, 2014, **256**, 52-60.
366. M. A., Kakuta Y, Teramoto T, Koshiba T, Liu X, Okada H, Tokunaga T, Kawabata S-I, Kimura M, and S. Y, *J. Biochem,* . 2007, **142**, 517-524.
367. F.S. Vom Saal and H. C, *Environ Health Perspect* 2005, **113**, 926-933.
368. L.F. Doherty, J. G. Bromer, Y. Zhou, T.S. Aldad, H.S. Taylor, *Horm Canc*. 2010, **1**, 146-155.
369. P. Tarapore, J. Ying, B. Ouyang, B. Burke, B. Bracken, and H. SM, *PLoS One,* 2014, **9**, e90332.
370. X.L. Cao and C. J, *J Agric Food Chem*., 2008, **56**, 6378-6381.
371. Z. Brenn-Struckhofova and C.-M. M, *Food Addit Contam,* 2006, **23**, 1227-1235.
372. Y. Yang, A.M. Asiri, Z. Tang, D. Du, and Y. L., *Mater Today* 2013, **16**, 365-373.
373. M.C. Dalfovo, G.I. Lacconi , M. Moreno, M.C. Yappert, G.U. Sumanasekera, R.B. Salvarezza, and I. FJ, *ACS Appl Mater Interfaces,* 2014, **6**, 6384-6391.
374. B. Su, H. Shao, N. Li, X. Chen, Z. Cai, and C. X, *Talanta*, 2016, **166**, 6384-6391.
375. J.A.V. Albelda, A.Uzunoglu, G.N.C. Santos, and S. LA, *Biosens Bioelectron*, 2017, **89**, 518-524.
376. C. Yu, L. Gou, X. Zhou, N. Bao, and G. H, *C, Electrochim Acta*, 2011, **56**, 9056- 9063.
377. J. Han, F. Li, L. Jiang, K. Li, Y. Dong, and L. Y, *Anal Methods,* 2015, **7**, 8220-8226.
378. J. Qin, J. Shen, X. Xu, Y. Yuan, G. He, and C. H, *Microchim. Acta,* 2018, **185**, 1-8.
379. H. Mirzajani, C. Cheng, J. Wu, J. Chen, S. Eda, E.N. Aghdam, and G. HB, *Biosens Bioelectron,* 2017, **89**, 1059-1067.

380. A.A. Ensafi, M. Amini, and R. B, *Microchim. Acta,* 2018, **185**, 1-7.
381. K.S. Kim, J. R. Jang, W. S. Choe, and Y. PJ, *Biosens Bioelectron,* 2015, **71**, 214-221.
382. S. G. Kim, J. S. Lee, J. Jun, D. H. Shin, and J. J, *ACS Appl Mater Interfaces,* 2016, **8**, 6602-6610.
383. Y. Zhu, Y. Cai, L. Xu, L. Zheng, L. Wang, B. Qi, and X. C, *ACS Appl Mater Interfaces,* 2015, **7**, 7492-7496.
384. J. Abdullah, M. Ahmad, L.Y. Heng, N. Karuppiah, and S. H, *Anal Bioanal Chem,* 2006, **386**, 1285–1292.
385. M.M. Rodríguez-Delgado, G.S. Alemán-Nava, J. M. Rodríguez-Delgado, G. Dieck-Assad, S.O. Martínez-Chapa, D. Barceló, and P. R, *TrAC-Trend Anal Chem*, 2015, **74**, 21-45
386. E. Casero, M.D. Petit-Domínguez, L. Vázquez, I. Ramírez-Asperilla, A.M. Parra-Alfambra, F. Pariente, and L. E, *Talanta*, 2013, **115**, 401-408.
387. C. Lou, T. Jing, J. Tian, Y. Zheng, J. Zhang, M. Dong, C. Wang, C. Hou, J. Fan, and G. Z, *J Mater Res,* 2019, **34**, 2964-2975.
388. L. Dishlyuk, M. Novoselova, and T. Rozalyonok, *Foods and Raw Materials*, 2013, **1**, 85-88.
389. O.S. Godage, A.B. Bucharskaya, N.A. Navolokin, G.N. Maslyakova, S.V. German, Gorin, and DA, *J Nanomed Res,* 2017, **5**, 00119, 1-3.
390. J. Borges, J.M. Campiña, and A.F. Silva, *J Mater Chem B* 2013, **1**, 500-511.
391. J. Borges, J.M. Campiña, and A.F. Silva, *J Mater Chem B* 2013, **1**, 500-511.
392. J. Wang, G. Meng, K. Tao, M. Feng, X. Zhao, Z. Li, H. xu, D. Xia, and Y. Lu, *PloS one*, 2012, **7**, e43478.
393. B. Li and H. Cao, *Journal of Materials Chemistry*, 2011, **21**, 3346-3349.
394. D. Lin-Vien, N. B. Colthup, W. G. Fateley, and J. G. Grasselli: 'Preface', in 'The Handbook of Infrared and Raman Characteristic Frequencies of Organic Molecules', (eds. D. Lin-Vien, et al.), xv-xvi; 1991, San Diego, Academic Press.
395. B. Unnikrishnan, S. Palanisamy, and S.-M. Chen, *Biosensors and Bioelectronics*, 2013, **39**, 70-75.
396. R. E. Peierls, *Helv. Phys. Acta*, 1934, **7**, 81-83.
397. T. N. Narayanan, Z. Liu, P. R. Lakshmy, W. Gao, Y. Nagaoka, D. Sakthi Kumar, J. Lou, R. Vajtai, and P. M. Ajayan, *Carbon*, 2012, **50**, 1338-1345.
398. G. Bharath, R. Madhu, S.-M. Chen, V. Veeramani, A. Balamurugan, D. Mangalaraj, C. Viswanathan, and N. Ponpandian, *Journal of Materials Chemistry B*, 2015, **3**, 1360-1370.
399. F. Liu, C. Chen, H. Guo, M. Saghayezhian, G. Wang, L. Chen, W. Chen, J. Zhang, and E.W. Plummer, Surface Science, 2017, **665,** 25-30.
400. M. A. Ghasemzadeh, M. H. Abdollahi-basir, and M. Babaei, *Green Chemistry Letters and Reviews*, 2015, **8**, 40-49.
401. Y. Bagbi, A. Sarswat, D. Mohan, A. Pandey, and P. R. Solanki, *Journal of Environmental Chemical Engineering*, 2016, **4**, 4237-4247.
402. M. A. Ghasemzadeh, M. H. Abdollahi-Basir, and M. Babaei, *Green Chemistry Letters and Reviews*, 2015, **8**, 40-49.
403. J. E. B. Randles, Discuss. Faraday Soc., 1947, **1**, 11-19.
404. K. M. Vårum, M. H. Ottøy, and S. O., Carbohydrate Polymers, 1994, **25**, 65-70.
405. M. W. Anthonsen and O. Smidsrød, Carbohydrate Polymers, 1995, **26**, 303-305.
406. Q. Z. Wang, X. G. Chen, N. Liu, S. X. Wang, C. S. Liu, X. H. Meng, and C. G. Liu, Carbohydrate Polymers, 2006, **65**, 194-201.
407. J. Borges, J. Campiña, H. Souza, M. Gonçalves, and A. F. Silva, Soft Matter, 2011, **8**, 1190-1201.
408. J. Borges, J. Campiña, and A. F. Silva, The journal of physical chemistry. B, 2013, **117**, 16565-16576.

409. J. Corrales, L. Kristofco, W. Steele IV, B. Yates, C. Breed, E. Spencer, B. Brooks, and C. Williams, *Review and Analysis of Its Occurrence and Bioaccumulation*, 2015, **13**, 1559325815598308.
410. S. Biedermann-Brem and K. Grob, European Food Research and Technology, 2009, **228**, 679-684.
411. J. Biles, T. McNeal, T. Begley, and H. Hollifield, Journal of Agricultural and Food Chemistry, 1997, **45**, 3541-3544.
412. E. Pharmacopeia, *European Directorate for the Quality of Medicines*, 6th ed, Strasburg, Council of Europe, UK distributor, Stationery Office, 2007.
413. ICH, *International Conference on Harmonization of Technical Requirements for the Registration of Pharmaceuticals for Human Use, Validation of analytical procedures: Text and Methodology.* 1996: Genova.
414. Y. Zhang, Y. Cheng, Y. Zhou, B. Li, W. Gu, X. Shi, and Y. Xian, Talanta, 2013, **107**, 211-218.
415. D. Pan, Y. Gu, H. Lan, Y. Sun, and H. Gao, Analytica chimica acta, 2015, **853**, 297-302.
416. L. Wu, D. Deng, J. Jin, X. Lu, and J. Chen, Biosens Bioelectron, 2012, **35**, 193-199.
417. R.S. Alkasir, M. Ganesana, Y.H. Won, L. Stanciu, and S. Andreescu, Biosens Bioelectron, 2010, **26**, 43-49.
418. M. Portaccio, D. Tuoro, F. Arduini, D. Moscone, M. Cammarota, D. Mita, and M. Lepore, Electrochimica Acta, 2013, **109**, 340-347.
419. S. Wild, G. Roglic, A. Green, R. Sicree, H. King, Diabetes Care, 2004, **27**, 1047-1053.
420. R. R. Holmam, S. K. Paul, M.A. Bethel, D.R. Matthews, and N. HA., N Engl J Med, 2008, **359**, 1577-1589.
421. J. Wang, Chem. Rev, 2008, **108**, 814-825.
422. B. Hock, Anal. Chim. Acta, 1997, **347**, 177–186.
423. E. Katz, I. Willner, Electroanalysis, 2003, **15**, 913-947.
424. K. Haupt, K. Mosbach, Chem Rev, 2000, **100**, 2495-2504.
425. Press Release by Persistence Market Research Pvt. Ltd., 2014, New York City; http://www.persistencemarketresearch.com/mediarelease/biosensor-market.asp .
426. J. Wang, Biosens Bioelectron, 2006, **15**, 1887-1892.
427. M. Rabe, D. Verdes and S. Seeger, *Adv. Colloid Interface Sci.*, 2011, **162**, 87-106.
428. F. W. Scheller, F. Schubert, B. Neumann, D. Pfeiffer, R. Hintsche, I. Dransfeld, U. Wollenberger, R. Renneberg, A. Warsinke, G. Johansson, M. Skoog, X. Yang, V. Bogdanovskaya, A. Bückmann and S. Y. Zaitsev, Biosens. Bioelectron., 1991, **6**, 245-253.
429. B. D. Malhotra, A. Chaubey and S. P. Singh, Anal. Chim. Acta, 2006, **578**, 59-74.
430. X. L. Luo, A. Morrin, A. J. Killard, and M. R. Smyth, *Electroanalysis*, 2006, **18**, 319-326.
431. J. Liu, A. Chou, W. Rahmat, M. N. Paddon-Row, and J. J. Gooding, Electroanalysis, 2005, **17**, 38-46.
432. A. Bonanni, A. H. Loo, and M. Pumera,: TrAC - Trends in Analytical Chemistry, 2012, **37**, 12-21.
433. C. Shan, H. Yang, D. Han, Q. Zhang, I. A., and L. Niu. Biosens. Bioelectron, 2010, **15**, 1070-1074.
434. W. Qu, L. Zhang, and G. Chen, Biosens. Bioelectron, 2013, **42**, 430-433.
435. Z. Wang, Y. Hu, W. Yang, M. Zhou, and X. Hu, Sensors, 2012, **12**, 4860-4869.
436. B. J. Li and H. Q. Cao. 2011: J. Mater. Chem, 2011, **21**, 3346-3349.
437. K. and Zhang, *Appl. Surf. Sci.*, 2012, **258**, 7327 -7329.
438. K. Turcheniuk, R. Boukherroub, and S. Szunerits, *J. Mat. Chem. B*, 2015, ***3***, 4301-4324.
439. Y. Zhang, X. Xiao, Y. Sun, Y. Shi, H. Dai, P. Ni, J. Hu, Z. Li, Y. Song, L., and Wang, *Electroanalysis*, 2013, **25**, 959 - 966.
440. H. Wu, J. Wang, X. Kang, C. Wang, D. Wang, J. Liu, I. A. Aksay, and Y. Lin, *Talanta*, 2009, **80**, 403-406.
441. K-J. Huang, L. Wang, J. Li, T. Gan, and Y-M. Liu, *Measurement*, *2013*, ***46***, 378 -383.

442. J. Borges, J. M. Campiña, and S. A. F., J. Phys. Chem. B., 2013, **117**, 16565-16576.
443. H. Qi, C. Wang, and N. Cheng, *Microchim. Acta*, 2010, **170**, 33 -38.
444. M. K.mPatel, M. A. Ali, S. Srivastava, V. V. Agrawal, S. G. Ansari, and B. D. Malhotra, *Biosens. Bioelectron*, 2013, **50**, 406-413.
445. G. Bharath, R. Madhu, S.-M. Chen, V. Veermani, A. Balamurugan, D. Mangalaraj, and N. Ponpandian, J. Mater. Chem. A., 2015, **3**, 15529-15539.
446. C. Mattevi, G. Eda, S. Agnoli, S. Miller, K. A. Mkhoyan, O. Celik, D. Mastrogiovanni, G. Granozzi, G. E., and M. Chhowalla, Adv. Funct. Mater, 2009, **19**, 2577-2583.
447. Q. Z. Wang, X. G. Chen, N. Liu, S. X. Wang, C. S. Liu, M. X. H., and L. C. G, Carbohydr. Polym, 2006, **65**, 194-201.
448. R. Zhang, S. Lu, L. Zhang, and G. Chen. 2014: J. Chromatogr. A., 2014, **1374**, 261-267.
449. Q. Chi, J. Zhan, S. Dong, and E. Wang, Electrochim. Act, 1994, **39**, 2431-2438.
450. T. L. Blaney, O. Lindan, and R. E. Sparks, Trans. Amer. Soc. Artif. Int. Organs, 1966, **12**, 7-12.
451. P.-W. Chung, A. Charmot, O. M. Gazit, and A. Katz. Langmuir, 2012, **28**, 15222–15232.
452. K.-J. Huang, L. Wang, J. Li, T. Gan, and Y.-M. Liu. Measurement, 2013, **46**, 378-383.
453. H. D. Jang, S. K. Kim, H. Chang, K.-M. Roh, J.-W. Choi, and J. Huang, Biosens. Bioelectron, 2012, **38**, 184-188.
454. X. Kang, J. Wang, H. Wu, I. A. Aksay, J. Liu, and Y. Lin, Biosens. Bioelectron, 2009, **25**, 901-905.
455. Y. Liu, D. Yu, C. Zeng, Z. Miao, and L. Dai, Langmuir, 2010, **26**, 6158-6160.
456. C. Fu, W. Yang, X. Chen, and D. G. Evans, Electrochem. Commun, 2009, **11**, 997-1000.
457. X. Wang, E. Liu, and X. Zhang, Electrochim. Acta, 2014, **130**, 253-260.
458. Y. Tian, Y. Liu, W.-P. Wang, X. Zhang, and W. Peng, Electrochim. Acta, 2015, **156**, 244-251.
459. Y. Zhang, X. Xiao, Y. Sun, Y. Shi, H. Dai, P. Ni, J. Hu, Z. Li, Y. Song, and L. Wang, Electroanalysis, 2013, **25**, 959-966.
460. B. Zhang, Y. He, B. Liu, and D. Tang, Microchim. Acta, 2015, **182**, 625-631.